UNIVERSITY OF BIRMINGHAM

Integration of a Solid Oxide Fuel Cell System with a Heat Driven Refrigeration System for Refrigerated Transportation Application

---

by

BHARGAV PANDYA

A Thesis submitted to the University of Birmingham for the

Degree of Doctor of Philosophy

Supervisor:
Prof. Robert Steinberger-Wilckens

Co-supervisor:
Dr Yousif Al-sagheer

This work was performed at:
Centre for Fuel Cell and Hydrogen Research
School of Chemical Engineering
College of Engineering and Physical Sciences
University of Birmingham
December 2022

Dedicated to my late grandfather, who was the first teacher and most caring person in my life.

“Everything should be made as simple as possible, but not simpler”

- Albert Einstein

Abstract

This study investigates a novel combined cooling and power concept with a Solid Oxide Fuel Cell (SOFC) driven Vapour Absorption Refrigeration System (VARS) for automotive transportation. The novel concept is focused on future powertrain designs where the fuel cell electrically contributes to both tractive force and auxiliary loads, with the heat generated used to operate a VARS. This thesis therefore focuses on the integration of an SOFC system with a VARS for automotive transportation applications. To prove the feasibility of such a concept, the work is divided into two categories, namely: an experimental approach and a simulation approach. In order to gain confidence in in the feasibility of SOFC integrated VARS concept, experiments were carried out on a laboratory set-up. It appeared that it was possible to achieve freezing temperatures down to -8^{o}C with the laboratory set-up.

A detailed steady state and transient simulation model of the SOFC and VARS combined system was then developed. In the first step of steady state simulation, the performance of different SOFC system configurations to power a VARS were compared. The best SOFC system layout and operating conditions to obtain optimised performance of the combined system were identified. The selection of the operating envelope of the SOFC system to power a VARS is not a straightforward process as it appeared that a balance had to be struck between the need for refrigeration load, power density, emissions, and the overall efficiency of the system. Hence, a comprehensive thermodynamic performance analysis was carried out to select the preferred operating envelope for the SOFC system considering several crucial performance parameters.

A detailed 0D SOFC, and a 1D VARS transient model were prepared to analyse the different operational phases of the integrated system during truck operating hours. The transient simulation concept of predicting SOFC integrated VARS performance under load following conditions for automotive application has been explored here for the first time. The system level transient simulation was carried out for the hottest and coldest day of a calendar year to observe the SOFC system response in matching the varying refrigeration load. It was observed that the SOFC system could deal with load following conditions without violating any operating constraints.

Acknowledgements

The last four years has been a magnificent academic journey. I was fortunate enough to work on cutting edge technology focused on automotive transportation which might contribute to reduce environmental impact of transportation. I am thankful to a lot of people who have contributed in many different ways through this journey. First, I would like to express my gratitude to Prof. Robert Steinberger-Wilckens for his unwavering support throughout this research study. He constantly motivated me to go beyond the boundaries to strive for high academic standards. It has been a pleasure working with him; he has been a great supervisor, mentor, and advisor. I would also like to thank Dr. Yousif Al-sagheer for being a supportive co-supervisor. He provided critical and valuable feedback to develop control software for the experimental facility. I am also incredibly thankful to Dr. Ahmad El-kharouf, who was my co-supervisor during the initial phase of the study. He guided exceptionally well in establishing the direction of this research study. His concise feedback helped to kick off this work effectively and efficiently.

This work at the University of Birmingham would not have been possible without funding from the Commonwealth Scholarship Commission, Government of UK. I am also thankful to programme officers Mr. James Goldsmith and Ms. Nighat Anwar from the Commonwealth Scholarship Commission.

I want to convey my appreciation to Chyntol Kanhimbe and Manzo Brown for their support in lab-related activities. To John Hooper, Lynn Draper, and Sarah Brookes, these admirable people made my life easy whenever I had any issues with administrative procedures. Thank you very much, guys for your helping hand. Thank you, Dr. Vikrant Venkataraman, for all the

interesting discussion and support on the experimental facility. I also thank Dr. Anurag Goyal for his support and feedback on refrigeration system modelling.

This work would also not be possible without colleagues and friends at the Center for Fuel Cell and Hydrogen Research. I would like to thank my dearest friends – Sathish, Marcus, Chris, Naser, Liam, Abdul, Abu, Pushpa, Sam, and everyone in our research group. A special thanks to Marcus for always being available to solve any open points related to simulation. Chris and Sathish, thanks for your valuable feedback on the thesis writing.

Finally, last but not least, I am grateful to my family and friends back in India. I could not have accomplished this work without their enormous support. I want to thank my parents from the bottom of my heart for their trust, unconditional love, and faith in me. Most importantly, I would like to thank my wife, Shreya. She has been incredibly supportive, patient, and calm throughout this journey. I am fortunate to pursue my endeavours with her constant moral support.

List of Publications

Journal Publications

1. **Pandya B**, El-Kharouf A, Venkataraman V, Steinberger-Wilckens R. Comparative study of solid oxide fuel cell coupled absorption refrigeration system for green and sustainable refrigerated transportation. Applied Thermal Engineering. 2020 Jun 1;179p.:115597. DOI: 10.1016/j.applthermaleng.2020.115597.
2. Venkataraman V, El-Kharouf A, **Pandya B**, Amakiri E, Steinberger-Wilckens R. Coupling of engine exhaust and fuel cell exhaust with vapour absorption refrigeration/air conditioning systems for transport applications: A review. Thermal Science and Engineering Progress. 2020 Aug 1;18p.:100550. DOI: 10.1016/j.tsep.2020.100550

Conference proceedings

1. **Pandya B**, El-Kharouf A, Steinberger-Wilckens R. Transient analysis of a solid oxide fuel cell coupled with an absorption refrigeration system for refrigerated transportation. In: 14th European SOFC & SOE Forum, 20-23 Oct, Lucerne Switzerland. 2020. pp. 277–86.
2. **Pandya B**, Venkataraman V, El-Kharouf A, Steinberger-Wilckens R. "Carbon footprint and economic analysis of fuel cell assisted road transport refrigeration system. International Conference on Applied Energy 2019, Aug 12-15, 2019, Västerås, Sweden (paper ID: 0350).

Table of Contents

List of Figures

Chapter 1:

Chapter 2:

Chapter 3:

Chapter 4:

Chapter 5:

Chapter 6:

List of Tables

Chapter 2:

Chapter 3:

Chapter 4:

Chapter 5:

Chapter 6:

List of Abbreviations

ATR	Auto Thermal Reforming
APU	Auxiliary Power Unit
BoP	Balance of Plant
CF	Coupling Fluid
CNG	Compressed Natural Gas
DIR	Direct Internal Reforming
EES	Engineering Equation Solver
FCH JU	Fuel Cells and Hydrogen Joint Undertaking
GHG	Greenhouse Gases
GWP	Global Warming Potential
IIR	Indirect Internal Reforming
LNG	Liquefied Natural Gas
LCO_2	Liquid Carbon Dioxide
LN_2	Liquid Nitrogen
LMTD	Log Mean Temperature Difference
NRMM	Non-Road Mobile Machinery
PM	Particulate Matter
POX	Partial Oxidation
PEFC	Polymer Electrolyte Fuel Cell
RHX	Refrigerant Heat Exchanger
RR	Recirculation Rate
REXP	Refrigerant Expansion Valve
SOFC	Solid Oxide Fuel Cell
SHX	Solution Heat Exchanger

SRU	Single Repeating Unit
SMR	Steam Methane Reforming
SP	Solution Pump
SR	Steam Reforming
SC	Steam to Carbon
SEXP	Solution Expansion Valve
TRU	Truck Refrigeration Unit
VARS	Vapour Absorption Refrigeration System
VARS	Vapour Absorption Refrigeration System
VCRS	Vapour Compression Refrigeration System
WGS	Water Gas Shift

Chapter 1: *Introduction*

This chapter provides a brief introduction and background to fuel cell technology and heat driven refrigeration technology. It also introduces the need to develop an alternative technology for refrigerated transportation. The research objectives, scope and research questions are introduced along with the outline of the thesis.

1.1 Introduction

Refrigerated transportation is one of the crucial elements of the cold chain. A refrigerated carrier controls the temperature of the transported goods, mostly food, within the tolerance limits that will ensure high-quality shelf life. Refrigerated transportation also plays a vital role in vaccine transportation across the globe. The total number of refrigerated vehicles worldwide is estimated to reach 15.5 million by 2025, up from less than 3 million in 2013 [1]. In 2019, the market value of refrigerated transportation was 15.5 billion USD globally [2]. However, the widespread application of refrigerated carriers also has also a negative environmental impact. In the UK, commercial food transport is accountable for 12MtCO2e [3] in which one-third of food transportation is temperature controlled. Truck refrigeration units (TRUs) employ Vapour Compression Refrigeration Systems (VCRS) to produce a refrigeration effect. Most VCRS are powered by an auxiliary diesel engine or via the vehicle main engine to power the VCRS [3]. It was found that the TRU employed on a truck powered by an auxiliary diesel engine emit six times more NOx and 29 times more Particulate Matter (PM) than a Euro VI diesel engine [4]. In 2015, one million TRUs in Europe emitted 40,000 tonnes of NOx, equivalent to 26 million Euro 6 diesel cars, 5,000 tonnes of PM, equivalent to 56 million Euro 6 diesel cars and 13 MtCO2e [4]. The primary reason for the high number of emissions from TRUs is that the EU emissions restriction policy does not restrict the emissions from TRUs. TRUs are covered under Non-Road Mobile Machinery (NRMM) regulations. Current NRMM only covers emission restrictions on auxiliary diesel engines having a capacity greater than 19 kW. Most diesel engines used for TRUs have around or less than 19 kW. TRUs employed on the truck also suffer from poor overall efficiency, approximately 25% [5]. Moreover, these VCRS employ hydrofluorocarbon refrigerants with great Global Warming Potential (GWP), such as R134a and R404a with 1430 and 3922, respectively. The annual leakage rate of the refrigerant from the TRUs can be as high as 15% to 25% [3]. These data confirm that

conventional TRUs are inefficient and harmful to the environment, and there is a need to develop sustainable energy conservation technology to reduce both the emission of Greenhouse Gases (GHGs) and hazardous air pollutants from refrigerated road transportation. In response, the California Air Resource Board has announced that development of novel refrigerated transportation technologies that can reduce GHG emissions by 40% by 2030, 80% by 2050 and PM emissions by 85% by 2030 to meet climate change mitigation goals [6]. This long-term objective includes developing novel TRUs technology with zero or near-zero emissions.

1.2 Decarbonisation of Refrigerated Transportation

Fossil fuel is the leading energy provider in conventional TRUs. GHG emissions can be reduced from the TRU if the auxiliary engine is fuelled by Compressed Natural Gas (CNG) or Liquefied Natural Gas (LNG) to power VCRS on the truck without substantial changes to the current technology. However, it was determined that CNG and LNG-powered TRUs only reduce the overall emissions rate by 25% and 12%, respectively [6]. Hence, CNG and LNG-powered auxiliary diesel engines are not favourable long-term solutions to make carbon-neutral TRUs. Cryogenic transportation systems using Liquid Carbon Dioxide (LCO_2) and Liquid Nitrogen (LN_2) have recently emerged as potential technology to replace conventional diesel driven TRUs [7]. Cryogenic TRUs share 0.5% of the total market in Europe, although the cost of cryogenic fuels is comparable with diesel. Cryogenic TRUs technology is only feasible where cryogenic fuels are readily available with refuelling infrastructure, which is not widespread across the globe. Rai and Tassou [3] compared the environmental impacts of cryogenic transportation systems using LN_2 and LCO_2 with conventional diesel driven VCRS large refrigerated trucks. The authors concluded that all the technologies emitted similar GHG emissions. Hence, cryogenic transportation is also not a viable option to decarbonise refrigerated transportation. Electric battery-operated TRUs have the potential to become an

alternative to refrigerated transportation. All-electric battery-operated TRUs on vans and small trucks are already employed in Europe. However, for large long-haul trucks, all-electric battery-operated TRUs have yet to be developed due to the requirement of large and bulky batteries, which sacrifices the truck's payload capacity. Also, plug-in infrastructure for long-haul trucks and all-electric battery-operated TRUs is minimal globally [6]. In the current scenario, the all-electric TRUs concept is in the early commercialisation stage for vans and small trucks. Long-haul trucks are in pilot-scale development, needing further attention and action to employ the idea for real-world applications.

In the recent decade, there has been an increasing interest in adopting fuel cells in automobiles to make them more environmentally friendly and to either replace the conventional diesel engine or reduce the engine load. Fuel cells on board the vehicle have been used as part of the power train and as an Auxiliary Power Unit (APU). Fuel cell technology has recently penetrated heavy-duty transportation applications as a favourable alternative to all-electric battery-operated technology [8]. Fuel cells directly convert chemical energy of the fuel into electricity. Hence, the fuel cell produces electricity with higher efficiency. The fuel cell can generate carbon-neutral and emissions-free electricity if it is powered by green hydrogen (H_2) (for instance delivered via electrolysis driven by renewable electricity). Even if the fuel cell is powered by fossil fuel, it can significantly reduce GHG emissions, NOx emissions and PM emissions due to the higher efficiency [9]. The California Air Resource Board has identified fuel cell powered TRUs as one of the most promising technologies for future sustainable TRUs [6]. Fuel cell TRUs are not commercially available as the concept is still in pilot-scale development. However, it is predicted that fuel cell TRUs can be pushed into the early commercialisation phase within the next five to ten years [6]. Polymer Electrolyte Fuel Cell (PEFC) and Solid Oxide Fuel Cell (SOFC) technology are identified as potential fuel cell

technologies that will take over most market share. Remarkable attention has been given to PEFCs by automobile industries as possible successors to internal combustion (IC) engines due to quick start-up times, high power density and ability to switch to steady-state operation rapidly [10]. However, widespread green hydrogen infrastructure with comparable cost are the primary requirements for successfully commercialising PEFC-driven TRUs. SOFCs are preferred for stationary combined heat and power applications, with 25,000 units accounting for approximately 85 MW employed since 2017 [11]. Most employed units have been fuelled by the existing natural gas infrastructure. Hence, it is unclear whether fuel cell system will be compatible with the TRUs in the near future and if so, which type of fuel cell system will be the best candidate. Unfortunately, the attention seized by PEFCs technology has overshadowed the possible application of other types of fuel cells in automobile applications. For instance, high durability, high efficiency, high-quality residual heat, and fuel flexibility make SOFC an attractive technology for satisfying the energy requirements of diverse end-use applications [12]. The available high-quality residual heat from the SOFCs can be utilised further for cooling and refrigeration applications with heat-driven refrigeration cycles. Heat-driven Vapour Absorption Refrigeration Systems (VARS) have been employed in commercial applications since the 1950s [13]. In recent years, heat-driven refrigeration technologies have gained significant interest from researchers to overcome emerging environmental challenges in the cooling and refrigeration sector. Most heat-driven refrigeration technologies use an environmentally friendly refrigerant with zero GWP. Furthermore, heat-driven refrigeration technologies can utilise waste heat as input energy leading to waste heat recovery and energy-saving opportunities.

Therefore, the integration of SOFCs and VARS may play an essential role in the refrigerated road transportation energy transition. Thus, this dissertation provides insight into the

characteristics and operating strategy of SOFC integrated VARS combined systems for refrigerated transportation applications.

1.3 Overview of Solid Oxide Fuel Cell Technology

The SOFC is a high-temperature fuel cell that operates at 500 to 900°C [12]. Since SOFCs use higher temperatures, they are less sensitive to fuel impurities compared to PEFC and can deal with various fuels such as methane, carbon monoxide and ammonia [14]. Amongst the various types of nonconventional energy systems, SOFC systems have been identified as an emerging energy generation system since they can produce electric power with high energy efficiency and negligible emissions of NOx and no emissions of SOx and PM from methane/natural gas [15]. Therefore, a brief review of the working principle of SOFCs and the SOFC system is presented next.

1.3.1 Working principle of SOFC

A typical SOFC Single Repeating Unit (SRU) consists of four major components: the cell made of an anode, an electrolyte, and a cathode, and the interconnect between individual SRUs. SOFCs are constructed with two porous electrodes separated by an oxygen ion conducting electrolyte (for instance, yttrium-doped zirconium oxide). Electrolyte materials can only conduct ions at a higher temperature. Therefore, SOFCs must be operated at a high working temperature of 500 to 900°C. Higher temperature accelerates the electrochemical reactions and improves contaminant resistance and electrical efficiency. The anode is mostly made of a mixture of ceramic electrolyte and nickel catalyst, and the cathode of perovskite material, for instance lanthanum strontium manganite or lanthanum strontium cobaltite ferrite. In a typical SOFC, fuel is continuously fed to the anode and oxidant (normally air) is provided to the

cathode. Under load, oxygen ionisation takes place at the cathode surface. Oxide ions travel through the solid electrolyte to the anode, oxidising the fuel (e.g., hydrogen), which releases electrons, heat and water. As the electrolyte is a material with (ideally) zero electronic conductivity, electrons are directed through the interconnect and connected load towards the cathode, as shown in Figure 1-1. In the case of methane as an inlet fuel, different chemical reactions, namely Steam Methane Reforming (SMR) and Water Gas Shift (WGS) reaction, take place in the anode [16].

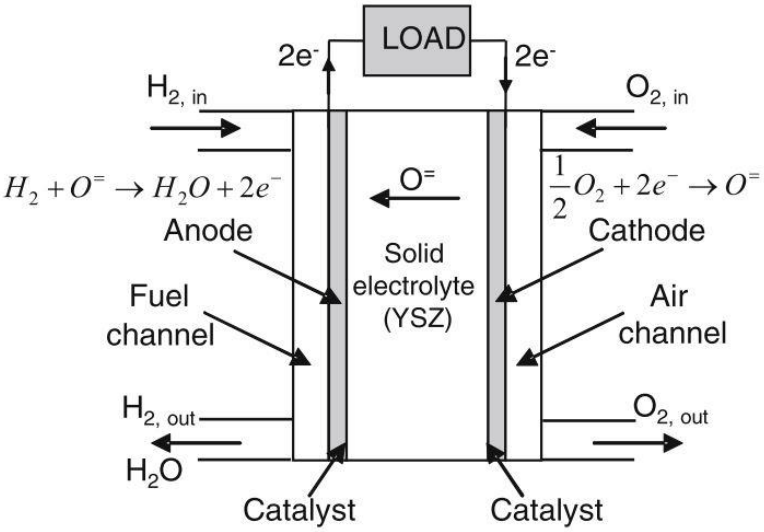

Figure 1-1 : SOFC working principle [16].

1.3.2 SOFC system

The schematic of the SOFC system fed by hydrocarbons is shown in Figure 1-2. A SOFC system consists of an SOFC stack, and the Balance of Plant (BoP), including anode and cathode pre-heater, air blower, fuel blower, water feed pump, and catalytic afterburner. The inlet fuel is mixed with high-temperature steam before entering a pre-reformer, where the water and fuel reform into a hydrogen gas-rich mixture. The inlet air is also pre-heated before it enters the SOFC stack. The exhaust gases enter an afterburner to combust any unreacted fuel from the

stack. The high-temperature exhaust gas mixture generated from the afterburner is used to pre-heat the anode and cathode inlet gas streams. Usually, an external reformer is used in SOFC systems to convert hydrocarbon fuels into a hydrogen-rich gas mixture (fuel reforming). However, it is also possible to carry out the fuel reforming process on the nickel-based anode catalyst, known as Direct Internal Reforming (DIR) [17]. SOFCs can deliver (net) electrical efficiencies of 60 % and beyond [18]. If the high residual heat is being further utilised for co-generation (combined heating and power or combined cooling and power), the SOFC system can achieve a combined efficiency over 80 % [19].

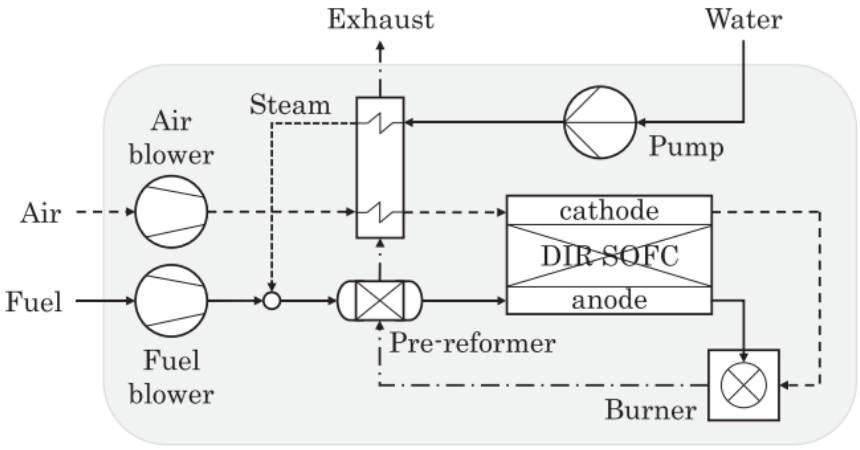

Figure 1-2 : SOFC system fuelled with hydrocarbon fuel [12].

1.4 Overview of Vapour Absorption Refrigeration System

The VARS concept is the most used heat-operated refrigeration system. The VARS is one of the oldest refrigeration concepts, having been invented in the 1700s. It involved making ice by evaporating water in the presence of sulphuric acid in a vacuum container [20]. The working fluid in a VARS is a binary solution that consists of a mixture of refrigerant and absorbent. LiBr-H_2O and NH_3-H_2O are the widely used pairs for VARS [21]. The LiBr-H_2O team is used for cooling and air conditioning, whilst the NH_3-H_2O pair is used for refrigeration. Therefore,

the NH_3-H_2O couple is considered for the VARS in this work. In the NH_3-H_2O pair, NH_3 acts as a refrigerant and H_2O as an absorbent. A schematic of a single-stage aqua-ammonia VARS is depicted in Figure 1-3. The main components of the single-stage aqua-ammonia VARS are a desorber, absorber, rectifier, evaporator, condenser, a Solution Heat Exchanger (SHX), a Refrigerant Heat Exchanger (RHX), and the Solution Pump (SP).

In a VARS, the refrigerant flows throughout the system while the absorbent only circulates between the absorber and the desorber. A thermal compressor and an absorbent replace the mechanical compressor of the conventional VCRS. A VARS operates between high and low-pressure levels. The desorber, condenser, expansion valve, solution heat exchanger, and rectifier operate at high pressure, and the absorber, evaporator and refrigerant heat exchanger operate at low pressure. An expansion valve integrated into the system controls high and low pressure. A robust solution (with high ammonia concentration) is pumped from the absorber through the SHX to the desorber at elevated pressure. Thermal energy is supplied to the desorber to separate the NH_3-H_2O binary solution. Ammonia and water vapour enter the rectifier, where the ammonia vapour is purified from any water vapour. Then it enters the condenser, where the ammonia is condensed. The condensate is passed through the RHX and throttle valve to the evaporator and absorbs the heat from the external source at low pressure. High temperature and pressurised weak solution (solution with low ammonia concentration) enter the SHX from the desorber, which rejects heat to the high-pressure solution from the absorber. The low-temperature weak solution finally enters the absorber from the SHX, where it absorbs the refrigerant (ammonia) vapour from the evaporator. The primary function of the SHX is to preheat the strong solution to a certain degree which will minimise the heat required to boil the solution at the desorber. The advantage of employing an RHX in the system is that

the liquid refrigerant (ammonia) is cooled down further, accelerating the evaporator's cooling capacity.

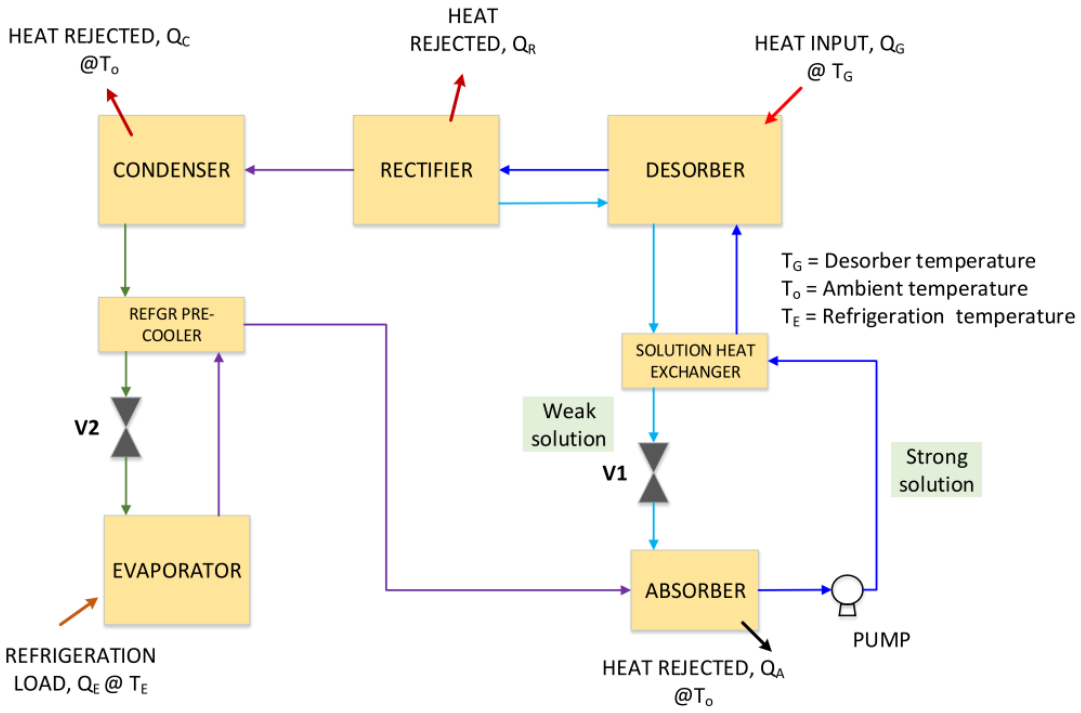

Figure 1-3 : Schematic diagram of vapour absorption refrigeration system [22].

Diesel combustion technology currently dominates the refrigerated transportation market due to its technical maturity, low cost and operational flexibility, reliability, and available infrastructure for refuelling. However, the United Kingdom is following an emissions reduction strategy and action to improve urban air quality, reduce heavy-duty vehicle emissions, and noise levels. Therefore, heavy-duty vehicles and bus and truck operators are encouraged to switch to alternative propulsion technology with zero or ultra-low carbon emissions. Diesel engine powered TRUs can contribute as high as 40% to the total GHG emissions of the vehicle [23]. Hence, even if TRUs can be replaced by alternative sustainable technology, a considerable amount of GHG emissions could be reduced from refrigerated vehicles.

1.5 Research Objectives and Scope

The broad objective of the study is to predict the performance of SOFC exhaust driven absorption refrigeration systems for refrigerated automotive transportation. The ultimate goal is to make refrigerated transportation more environmentally friendly or/and completely green with SOFC technology. The research objectives and scope of the current study are as follows:

1. Feasibility of the concept of SOFC integrated VARS via an experimental approach.
    - A laboratory setup was developed to couple the absorption refrigeration system with an SOFC exhaust. It supported the evaluation of the viability of coupling an SOFC exhaust with an absorption refrigeration system.
2. Development of a simplified SOFC system simulation methodology.
    - The goal here was to develop an SOFC system level model with least number of input parameters required to solve it. A simplified and generic SOFC model helped in predicting the system level performance to match the trade-off between accuracy and computational effort.
3. Development of a steady state and transient model for the combined SOFC-VARS system.
    - Steady state modelling was required to estimate the energy and mass flows in the system. The steady state model provided insight into the system performance. This data was needed later to develop the transient model of the system.
4. Identification of an optimised operating strategy for an SOFC driven absorption refrigeration system for refrigerated transportation.
    - The SOFC-VARS system encounters different operational phases during operation. Different strategies need to be developed based on feedback from

transient and steady state simulation to obtain an efficient performance of the system.

5. Identification of the system transient response to load following conditions.
    - This was required to determine the capability of the SOFC system to match refrigeration load following conditions over a variety of ambient conditions.

In addition, following research question were also addressed in the current study.

1. Between SOFC and VARS systems, which system's performance is more crucial to enhance overall efficiency of the combined system?
2. Does conventional SOFC system layout/architecture offer optimised performance for a concept of combined cooling and power?
3. Should SOFC be operated to maximise electrical or thermal power? What should be the optimised operating envelope (temperature, fuel utilisation, current density, and anode gas recirculation) of the SOFC system to power the VARS?
4. To what extent the proposed system can contribute to decarbonise refrigerated transportation?
5. How long does the heat-up time for the SOFC last? If the heat-up time of the SOFC is longer, would it affect the suitability of an SOFC system for refrigerated transportation applications?
6. How long can SOFC maintain temperature above its minimum activation temperature during non-operative hours of a truck? Does SOFC need to heat-up often after short/long breaks during the journey?
7. How does the refrigeration load following operation affect the SOFC operating envelope?

The current study considers both experimental and simulation approaches to assess the system performance. However, the simulation and modelling aspect contributes significantly to the current study. It is mainly carried out to better understand steady-state and transient performance of the SOFC integrated VARS. The outcome of the modelling can be utilised further to develop matured SOFC integrated VARS system for real life application.

1.6 Thesis Organisation

The current study is organised as follows:

Following the Introduction in Chapter 1:, Chapter 2: provides a comprehensive literature review on the current status of SOFC and VARS technologies for automotive applications. It also highlights available opportunities to integrate VARS with the SOFC exhaust. This chapter also covers various simulation methodologies in developing a mathematical model of the SOFC and VARS systems. This will provide the reader with a clear understanding of progress that has been done in the field and technical challenges involved.

Chapter 3: outlines the research methodology adopted. All detail on laboratory setup is presented in this chapter. A detailed methodology to build the steady state and transient simulation of the combined system is presented here. The governing equations and modelling assumptions are discussed in this chapter.

Chapter 4: highlights the experimental approach and results from the experiments carried out on the laboratory setup. The absorption refrigeration system experimental data was used to validate the transient model of the VARS.

Chapter 5: offers a detailed study of the steady state operation of the combined system. First, the cooling load requirement of refrigerated truck is identified. This information serves as an input to characterise the VARS steady state performance. These inputs are fed to the SOFC steady state model. SOFC model data has been validated with literature studies. A detailed simulation is carried to characterise SOFC system for different types of refrigerated trucks and applications.

Chapter 6: describes the transient response of the combined system in different operational phases. The system is subjected to load following conditions in this chapter. This chapter also addresses crucial research questions (questions 5 to 7) that have been considered in the study, including SOFC heat-up, start-up, and cool-down transient characteristics.

Chapter 7: summarises important findings/conclusions from the current study, including an outlook on future research work.

Chapter 2: *State of the Art and Literature Review*

A detailed literature survey relating to the thesis topic is presented in the current chapter. A brief introduction on reforming concept in SOFCs is represented. The current literature review focuses on highlighting activities carried out with SOFC system and absorption refrigeration system for automotive transportation. The importance of modelling and why modelling from scratch is required to simulate the system behaviour for such a concept is also included. The focus of the literature survey then presents different modelling methodologies to simulate the performance of both systems (SOFC and VARS). In addition, the main challenges and opportunities are outlined for SOFC integrated absorption systems for automotive transportation application.

Note: Certain sections of this chapter was published in Thermal Science and Engineering Progress 2020;Volume 18:100550. DOI: 10.1016/j.tsep.2020.100550 [24].

2.1 Reforming in SOFC

It is essential to understand the different reforming concept with hydrocarbon fuelled SOFC system. The SOFC system layout and performance greatly depends upon the type of reforming being considered. Hence, a brief introduction is provided in this chapter on different reforming concept with SOFCs. Reforming is the extensively used chemical process to convert hydrocarbon fuels into a hydrogen-rich synthetic gas mixture, often known as syngas, by several methods such as Steam Reforming (SR), Partial Oxidation (POX), and Auto Thermal Reforming (ATR) [25]. All three processes are briefly explained in the following section.

2.1.1 Steam reforming

The endothermic steam reforming reaction between steam and a hydrocarbon produces a hydrogen-rich syngas in the following chemical equilibrium reaction: .

$$C_nH_m + nH_2O \leftrightarrow (n + \frac{m}{2})H_2 + nCO \qquad 2.1$$

In the case of methane, the fuel reacts with steam to produce hydrogen and carbon monoxide, known as steam methane reforming (SMR):

$$CH_4 + H_2O \leftrightarrow CO + 3H_2 \qquad \Delta H^0_{SMR}=206.1 \text{ kJ/mol} \qquad 2.2$$

ΔH^0 represents the standard enthalpy of reaction. A positive sign indicates energy being consumed and negative sign indicates energy being released [26].

Additionally, Carbon monoxide reacts with steam to produce hydrogen, known as the water gas shift reaction (WGS), an exothermic reaction:

$$CO + H_2O \leftrightarrow CO_2 + H_2 \qquad \Delta H^0_{WGS} = -41.1 \text{ kJ/mol} \qquad 2.3$$

In the presence of a nickel catalyst, the temperature required to initiate the SR reaction is between 500 and 600ºC as shown in Figure 2-1 [27]. The effect of reforming temperature on the equilibrium hydrogen yield is shown in Figure 2-1. The equilibrium hydrogen yield increases with the reforming temperature. The maximum hydrogen yield can be achieved at 800 ºC as shown in Figure 2-1.

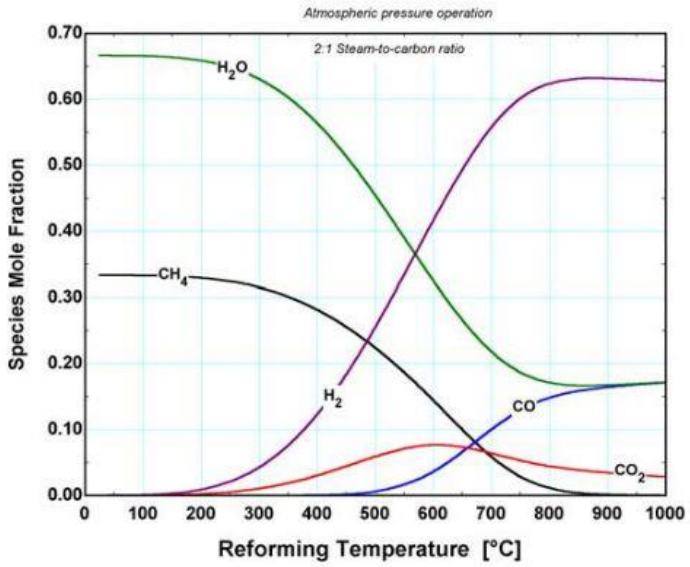

Figure 2-1 : Effect of reforming temperature on the equilibrium hydrogen yield [10].

In an SOFC system two different SR configurations are possible, external reforming and internal reforming. Further, internal reforming can be divided into Indirect Internal Reforming (IIR) and direct internal reforming (DIR). These SR configurations are depicted in Figure 2-2. The external reformer configuration requires a separate dedicated reformer that needs an external heat source to power the endothermic SMR. The internal reforming concept utilises the heat released due to the fuel and CO oxidation reaction inside the SOFC. The internal reforming concept does not require an external reformer, IIR physically separates the

electrochemical response of the reforming process. The required heat to activate SMR is provided using direct physical contact between the SOFC structure and the reforming unit [10]. In DIR, the inlet hydrocarbon fuel reforming process occurs on the nickel-based anode surface. An endothermic SMR absorbs the heat released by electrochemical reaction inside the SOFC stack, thus acting as a heat sink which reduces the cooling air required to maintain the stack temperature, hence it also reduces the air blower power of the SOFC system, which improves the overall efficiency of the SOFC system. It was determined that the DIR concept with SOFC required 50% less cooling air, which improved system efficiency by 8.5% compared to external reforming [10].

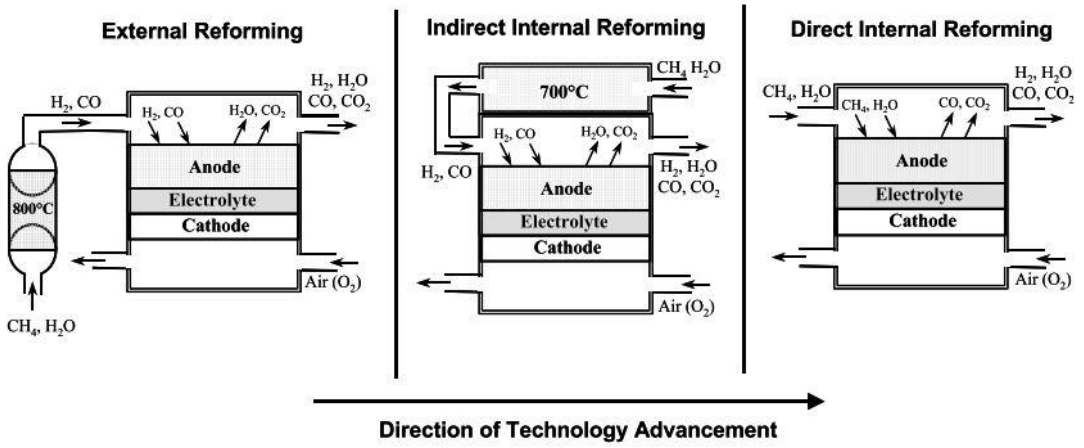

Figure 2-2 : Different SR configurations [10].

Carbon deposition is one of the major concerns associated with SMR. Avoiding carbon deposition on the porous catalyst layer is required as it deactivates the catalyst [25]. Carbon deposition can be avoided by increasing the steam-to-carbon (SC) ratio of the inlet fuel. The effect of the SC ratio on the equilibrium hydrogen yield is depicted in Figure 2-3. Hydrogen content decreases with the SC ratio, which is not a favourable condition for the SOFC. Hence, an optimal SC ratio must be selected to match the trade-off between carbon deposition and the

equilibrium hydrogen concentration in the gas stream. For SOFC systems with DIR, the SC ratio is generally kept above 2 to avoid carbon deposition [25].

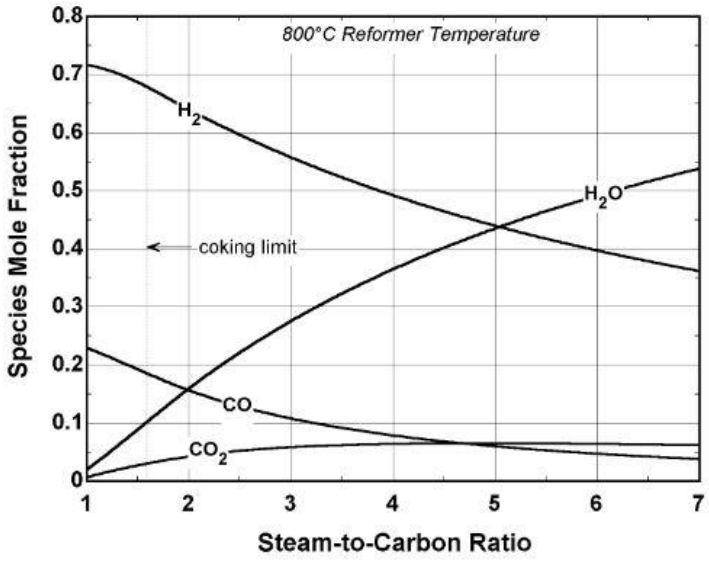

Figure 2-3 : Effect of SC ratio on equilibrium hydrogen yield [10].

2.1.2 Partial oxidation

Partial oxidation is a simple reforming process which relies on the oxidation of hydrocarbon fuel with sub-stochiometric oxygen. Partial oxidation is an exothermic process shown by eqn.2.4. Oxygen is supplied to the POX reformer, which produces a carbon monoxide and hydrogen mixture:

$$CH_4 + \frac{1}{2}O_2 \leftrightarrow CO + 2H_2 \quad \Delta H^0_{POX} = -36 kJ/\,mol \qquad 2.4$$

The operating temperature of POX reformers differs widely. In the absence of a catalyst, the operating temperature of POX varies between 1100 to 1500ºC. These high temperatures require unique materials and remarkable system preheating. Using a Ni/Al_2O_3 catalyst (catalyst POX - CPOX) can significantly reduce the operating temperature to as low as 550 to 600 ºC [28].

The required oxygen is supplied via air, which further dilutes the hydrogen fraction by the amount of nitrogen in the air, which results in a reduction of the SOFC voltage. CPOX yields less hydrogen per mole of methane (or hydrocarbon fuel) than SMR. However, CPOX reformers are simple and compact, and do not require a steam generator and heat exchangers, making the SOFC system more compact.

2.1.3 Autothermal reforming

Autothermal reforming is a hybrid concept that combines SR and CPOX. Methane (or in general: hydrocarbon fuel) is partially oxidised with air, and heat released due to the exothermic reaction of CPOX is utilised to supply energy to the endothermic SMR reaction. ATR does not need any additional heat source to power the chemical reaction, but it still requires a steam generator. The operating temperature of ATR is lower than with CPOX and higher than with SMR. ATR offers a higher hydrogen mole fraction and higher efficiency compared to CPOX.

2.1.4 Important findings

Overall, SMR has several advantages over CPOX and ATR, such as high fuel conversion efficiency (80 % to 95 %) and avoiding the diluting effect of nitrogen on the hydrogen mole fraction. In addition, SMW with DIR concept offers several advantages for the SOFC system, which are as follows:

Electrical efficiency: DIR minimises the requirement of cooling air, reducing the power required to operate the air blower (parasitic losses). It allows SOFC operation at higher fuel utilisation as high burner temperatures are not required to power an external reformer for conversion of the inlet hydrocarbon fuel [29].

Thermal Efficiency: An external reformer is one of the significant sources of heat loss from the SOFC system due to higher surface temperature. Eliminating the external reformer leads to reduced heat losses from the SOFC system, thus allowing more opportunity to recover the waste heat from the SOFC. DIR is preferred for SOFC-powered co-generation (combined cooling, heating and power generation) applications [29].

Cost: DIR potentially reduces the cost of the SOFC system as it does not require an external reformer and associated extensive insulation. DIR requires lower airflow, meaning the Balance of Plant (BOP) components, such as air pre-heater, can be reduced in size, thus reducing cost and volume.

Power density: Due to fewer and more compact BoP components involved in the system, DIR also improves the volumetric density of the SOFC system.

Faster transient response: Larger size and thermal mass of an external reformer result in a slower transient response of the SOFC to load following conditions. However, a faster transient response is predicted with DIR due to the proximity of electrochemical and reforming processes and the reduced thermal mass of the system [30].

Therefore, DIR offers benefits over external reforming for the efficient performance of the SOFC system. DIR also makes the SOFC system compact, which is favourable for automobile applications due to space constraints.

2.2 Experience of SOFC for Transportation Application

Several research and industrial projects have been carried out in the last two decades to demonstrate SOFC systems as an APU for heavy-duty vehicles. The most remarkable projects are briefly discussed in this section.

The US National Energy Technology Laboratory and Pacific Northwest National Lab carried out a project in the year 2000 to develop a 5 kW SOFC stack for military and heavy-duty trucks powered by petrol [31]. The developed SOFC stack obtained 420 mW/cm^2 power density at 0.7 V cell voltage at 750°C. The project's ultimate aim was to significantly reduce the usage of petrol fuel by utilising the power produced by the SOFC stack to reduce engine idling and the residual heat available from the SOFC for heating the vehicle cabin [31]. Figure 2-4 shows the SOFC APU developed, which had a volume of 50 litres. The APU contained two SOFC stacks connected in series and ancillary components such as a reformer, cathode heat exchanger and afterburner. The authors found that the start-up time of this APU was about an hour to reach the operating temperature of the stack, which is not favourable for automobile applications. The authors concluded that the required compactness of the SOFC APU was achieved, however rapid start-up remained a critical challenge that needed to be addressed.

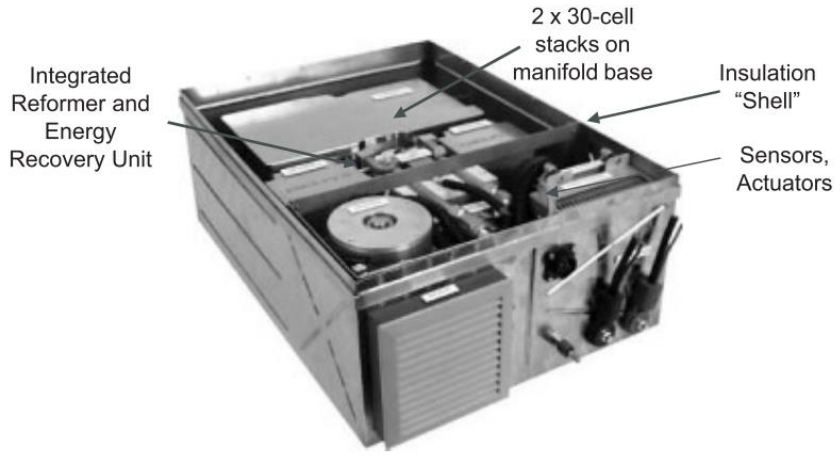

Figure 2-4 : SOFC APU system developed by Delphi and BMW with 50 litres volume.

Lawrence and Boltze [32] carried out a similar study with H.C. Starck GmbH and Fraunhofer IKTS in which a 1 kW SOFC APU consisting of 30 cells and a partial catalytic oxidation (CPOX) diesel reformer for military vehicles and trucks was developed, as shown in Figure 2-5. The authors chose the CPOX reformer technology to eliminate the requirement of water

supply onboard, which is required for steam methane reforming (SMR). The APU was able to deliver electric power after 3 hours of warm-up phase. It was found that the SOFC APU showed 30% electrical efficiency, which was found to be better compared to conventional engine driven APUs. If the residual heat from the SOFC APU was recovered and utilised, the combined efficiency could reach up to 60 %. The developed SOFC APU successfully demonstrated vital properties such as; thermal self-sustainability, ability to tolerate dynamic behaviour of a vehicle drive profile and sudden shut-down process and start-up without external electrical heating.

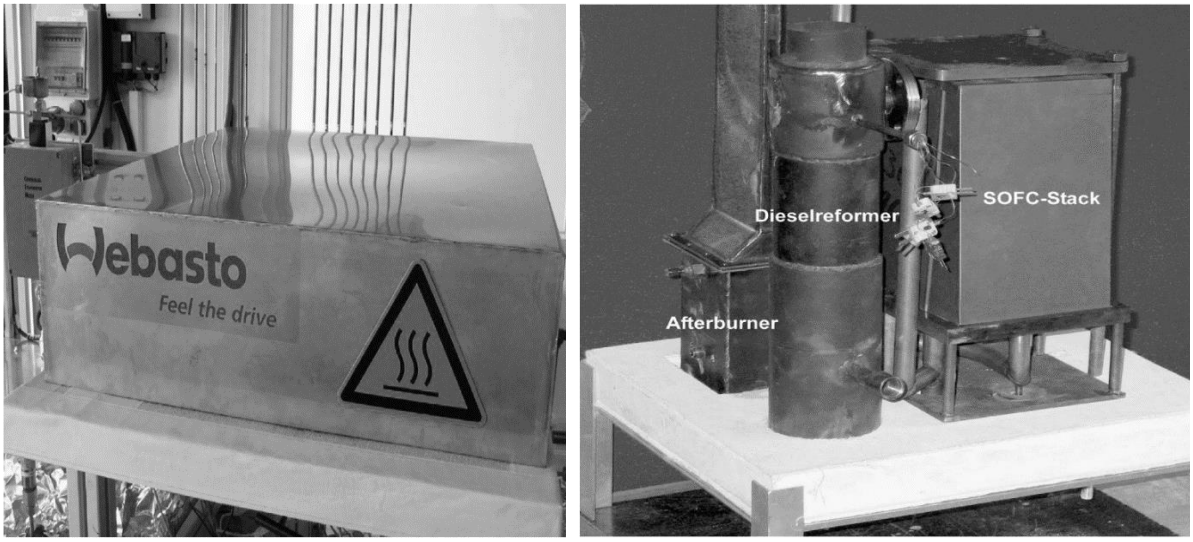

(a) Developed SOFC APU (b) Internal components of SOFC-APU

Figure 2-5 : 1 kW SOFC APU with CPOX reformer developed by Webasto [32].

Delphi Automotive demonstrated a 3.5 kW of SOFC APU on the Hybrid Truck user forum, USA, in 2010 as shown in Figure 2-6 [33,34]. The primary function of the SOFC-APU was to deliver power to the cab air conditioner, refrigerator, and other auxiliary components of the truck. The SOFC APU could operate on natural gas, diesel, or propane. Delphi Automotive claimed that the developed SOFC APU achieved 50% higher efficiency than conventional

diesel-driven APU. The report highlighted that the SOFC APU offers an advantage in reducing truck emissions and fuel usage. It was recommended to utilise waste heat from SOFC system into a liquid coolant loop in the vehicle for cabin heat, and truck oil heating in cold climate.

Figure 2-6 : 3.5 kW SOFC APU developed by Delphi automotive system [34].

In 2012, the DESTA project demonstrated the first European SOFC APU on a heavy-duty truck funded by the European Union Fuel Cells and Hydrogen Joint Undertaking (FCH JU) shown in Figure 2-7 [35]. The critical functions of the APU included supplying electrical power to the auxiliary components of the truck, such as; air conditioning, refrigerator, and television during the vehicle idling. The APU produced 10 kW of thermal power, which could be utilised for waste heat recovery. This SOFC APU provided 35% net electrical efficiency. The total volume and weight of the SOFC APU were 75 L and 60 kg, respectively. The APU system was able to convert conventional diesel fuel to a syngas mixture utilised by the SOFC stack. It was concluded that the SOFC APU consumed 75% less fuel compared to conventional diesel driven units. The SOFC APU emitted 73% less CO_2 emissions compared to conventional diesel APU during engine idling. In addition, it did not have environmentally harmful emissions such as NOx, $PM_{2.5}$ and PM_{10}.

(a) Demonstrated truck (b) Demonstrated APU

Figure 2-7 : SOFC APU developed in DESTA project [35].

Kendall et al. [36] carried out a research project called SAFARI (SOFC APU for Auxiliary Road-Truck Installations, FCH JU funded) in which a micro-tubular SOFC APU operated with liquid natural gas was developed for truck applications, as shown in Figure 2-8. A 16-tube micro SOFC stack was developed to generate 100 W of electric power and 600 W of heat, which could be used to heat or cool the cabin. It was concluded that the innovative concept of micro-tubular SOFC APUs for trucks was feasible and can be developed for real-world application. Unfortunately, the project was terminated before it delivered any results.

Figure 2-8 : SOFC APU developed in SAFARI project [36].

Apart from the application of SOFC as an APU, the Japanese automaker; Nissan demonstrated a 5 kW SOFC stack powered by bioethanol as a range extender, as depicted in Figure 2-9 for battery-operated vehicles in Brazil [37]. This technology offers an opportunity for environmentally friendly transportation and regional energy generation. In Brazil, bioethanol is readily available without the need to establish new infrastructure. Bioethanol fuel is also safe to handle compared to other fuels.

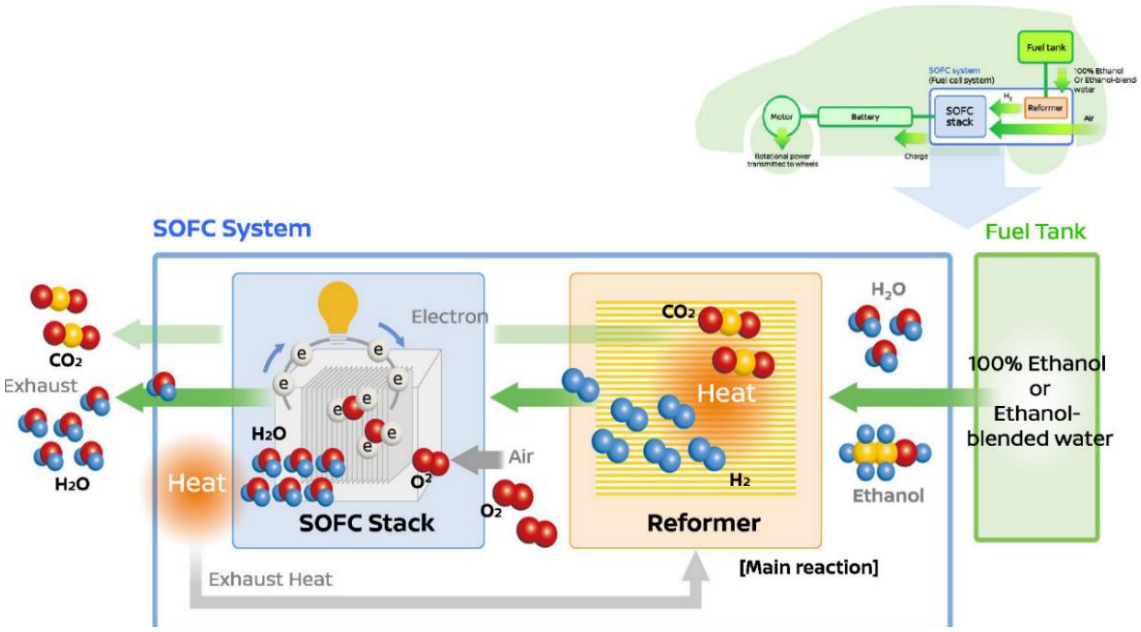

Figure 2-9 : Concept of e-Bio SOFC APU developed by Nissan [38].

Benveniste et al [39] investigated the environmental impacts of SOFC-APU fuelled by liquefied propane gas (LPG), which were developed to deliver power to recreational vehicles. The authors evaluated the system using a life cycle assessment following the ISO 14040-44 standard to assess the environmental impacts from the system manufacturing to system decommissioning. This study concluded that employing SOFC APU reduced the primary energy demand by 80% and global warming potential (GWP) output by 45% compared to conventional diesel-powered APUs. It was noted that a diesel-powered APU emits 555 kg of

CO2 eq., while an LPG powered SOFC APU emits 300 kg of CO_2 eq. Hence, a significant amount of CO_2 emissions can be reduced with SOFC APU.

Ballard et al. [40] developed natural gas/hydrogen fuelled 1 kW, 5 kW, 10 kW and 10's of kW SOFC systems for transportation and stationary applications. They developed compact 5 kW and 10 kW SOFC systems to obtain high power outputs with improved efficiency, as shown in Figure 2-10. A 10 kW SOFC system used two SOFC stacks of 5 kW at the bottom of the unit, as shown in Figure 2-10 (b). The overall volume of the unit was 1.4 m^3 (with dimensions of 0.6 m × 1.25 m × 1.90 m). The net electrical efficiency of up to 60% was achieved in a 5 kW SOFC system fuelled with natural gas, with the potential to further improve performance. This study also demonstrated the concept model for a 30 kW SOFC system as a range extender for electric buses. A 30 kW SOFC system consists of six modules of 5 kW SOFC stacks. This technology proved to have several prerequisites required for transportation applications, such as its robust nature (ability to deal with the vibration of the vehicle), a rapid start-up from ambient temperatures, and compactness. Leah et al. [29] demonstrated the feasibility of a 5 kW with this SOFC technology operating with complete internal reforming of methane. It was concluded that future SOFC technology could be demonstrated without an external reformer which also reduces the size and cost of the system. Direct internal reforming also facilitates SOFC systems with high electrical efficiency (>65%), making SOFC technology a favourable alternative to conventional combustion engines for road transportation applications.

(a) 5kW SOFC stack (b) 10kW SOFC system

Figure 2-10 : SOFC stacks developed by Ballard et al. [40].

Udomsilp et al. [41] developed a metal supported SOFC with an exceptionally high power and current density of up to 2 W/cm^2 and 2.8 A/cm^2, respectively. The primary focus of the research was to develop an SOFC as a range extender for battery electric vehicles. The metal supported SOFC demonstrated rapid start-up time, mechanical robustness and acceptable manufacturing cost, which are favourable characteristics for the automobile application. The authors concluded that the concept of SOFC as a range extender for electric vehicles lowered the weight, size and cost of the battery with fast refuelling and an improved driving range.

Pirou et al. [42] presented a metal based monolithic SOFC stack design for automotive transportation applications to achieve high volumetric power density and specific power. An initial SOFC testing revealed that the monolithic design could achieve a volumetric power density of 5.6 kW/litre at a current density of 0.6 A/cm^2 . The authors concluded that the monolithic SOFCs could be manufactured with cost-effective and scalable manufacturing

processes. Hence, metal based monolithic SOFC stacks could provide the next generation advanced SOFC systems with efficient performance.

Ample projects and research studies have been carried out to support the possible application of SOFCs for automobile applications. All the projects and studies considered SOFCs as an APU or range extender. However, there has yet to be evidence of commercial/research projects considered complete SOFC-driven vehicles. All the projects were focused on the hybridisation of SOFC with a combustion engine, or electric battery system as a main power source. A summary of the project work focused on SOFC APU is reported in Table 2-1.

Table 2-1 : Summary of SOFC projects for automotive transportation application.

Project Lead/ Funding Body	**Year**	**Logistic fuel**	**Application**	**References**
Pacific Northwest National Lab & US National Energy Technology Laboratory	2000	Diesel	Military Vehicles and Trucks	[43]
H.C. Starck GmbH and Fraunhofer IKTS	2005	Diesel	Trucks and Cars	[32]
Delphi automotive	2010	Diesel, natural gas, or propane	Trucks	[33]
Fuel Cells and Hydrogen Joint Undertaking	2016	Diesel	Heavy duty trucks	[35]
Adelan Ltd	2016	Natural Gas	Heavy duty trucks	[36]
Nissan	2016	Ethanol	Range extender for battery operated vehicle	[37]
Ceres Power	2019	Natural Gas	Range extender for electric passenger buses	[40]
Plansee SE and AVL	2020	Hydrogen	Range extender for electric passenger buses	[41]
Lawrence Berkeley National Laboratory and Nissan	2020	Ethanol	Automobile	[44]

Most projects demonstrated in the past decades considered diesel as a logistic fuel for SOFC-APU applications. This concept proved to be complicated due to the possibility of sulphur accumulation and poisoning of the anode of the SOFC stack. Also, the use of diesel does not help reduce GHG emissions, as diesel production-related emissions are as high as 0.926 $kgCO_2e$ / litre [3]. There has been significant development in the area of natural gas fuelled SOFC systems during the past decade. Recently the focus has shifted to using natural gas/methane as the logistic fuel for SOFC transportation applications, as mentioned in the studies carried out by Ballard et al. [40], Leah et al. [29] and Kendall et al. [36]. The overall efficiency of the SOFC APU system can be further enhanced if waste heat is utilised for heating or cooling, as described by Lawrence and Boltze [32] and Kendall et al. [36]. Unfortunately, publications reporting on a methane/hydrocarbon fuelled SOFC integrated combined cooling and power concept for automotive transportation are scarce. Hence, it is worth exploring the possible application of SOFC-powered co-generation (power and cooling) for refrigerated automotive carriers.

For the successful commercialisation of the NH_3-H_2O VARS for automotive applications, developing a more compact small-scale unit that can be housed within the available packaging volume on the different types of vehicles is essential. Hence, it will be useful to present work on compact absorption technology, experience of VARS with automotive transportation, and integration of a refrigeration system with a fuel cell for truck refrigeration units (TRUs). Therefore, studies focused on demonstrating these applications are summarised in the following section.

2.3 Experience with Compact Absorption Technology

Determan and Garimella [45] demonstrated the first-ever microscale monolithic NH_3-H_2O absorption refrigeration system for miniaturised and mobile applications. The plan was designed to obtain a 300 W nominal cooling capacity with an overall volume of 0.0013 m^3 (with dimensions of 0.20 m × 0.20 m × 0.034 m) and 7 kg of mass, as shown in Figure 2-11.

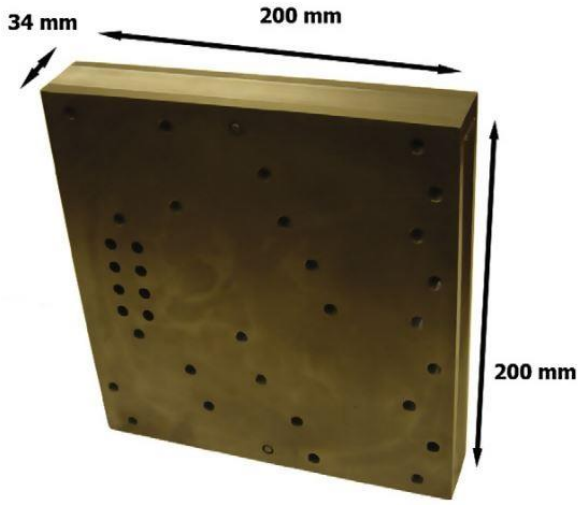

Figure 2-11 : Microscale monolithic NH_3-H_2O absorption chiller by Determan and Garimella [45].

Thin metal sheets with headers and fluid channels were bonded to fabricate the monolithic absorption heat pump. It significantly reduced the possibility of leakage of the working fluid, which is necessary while working with ammonia refrigerant. The system was designed to deliver chilled water at 7ºC. A coefficient of performance (COP) was achieved between 0.25 and 0.43 under the variation of heat input to the system from 500 W to 800 W, respectively. The cooling-to-mass ratio of this compact VARS was found to be between 85 and 120 W/kg. The developed microscale monolithic NH_3-H_2O VARS technology could be easily scaled-up to achieve a cooling capacity of up to 10 kW through minor changes in the component geometry. The modular nature of these units facilitated the operation of these units with a wide

range of source temperatures to achieve a wide range of refrigeration temperatures and loads. The authors concluded that applications such as cogeneration systems (combined heating/cooling power), automotive, marine and refrigerated transportation could benefit from the developed monolithic microscale NH_3-H_2O absorption system.

In a next step, monolithic microchannel technology demonstrated by Determan and Garimella[45] shown in Figure 2-11 was scaled up to 7 kW by Staedter and Garimella [46] for residential applications to deliver chilled water at the temperature of 7.9ºC as shown in Figure 2-12.

Figure 2-12 : Compact NH_3-H_2O VARS developed by Staedter and Garimella [46].

Microchannel heat and mass exchangers were integrated with monolithic blocks to form the core of the absorption chiller. Desorber, evaporator, condenser and evaporator microchannel heat exchangers were coupled with hydronic coupling fluids to make the system highly compact. Heat exchanger coupling with hydronic fluid reduces the working fluid volume to a great extent, which also reduces the refrigerant charge in the system. Therefore, an air heat

exchanger (i.e., radiator) was incorporated in the system as the heat sink for the combined absorber and condenser in an amalgamation with a hydronic coupling fluid circuit. The absorption chiller was powered by Paratherm™ heat transfer fluid coupled with a natural gas combustion module. The system achieved a COP of 0.51. The overall volume of the developed unit was 0.28 m^3 (with dimensions of 0.66 m × 0.66 m × 0.66 m). Thus, this system delivered cooling power with approximately 25 kW/m^3 of volumetric cooling density.

Du et al. [47] developed an engine exhaust coupled NH_3-H_2O absorption chiller for freezing application, as shown in Figure 2-13. The whole system was divided into two sub-divisions: the separation unit and the combined absorption-condensation unit. The condenser and absorber were assembled in a single unit and cooled with water. Heat exchangers with a large specific area and small diameter tubes were employed to make the system compact. The evaporator was coupled with ethylene glycol aqueous solution (acting as a secondary refrigerant with 45% mass fraction). Particular attention was given to maximising the internal heat recovery in the system to improve the COP. The system had an overall volume footprint of 0.57 m^3. The system achieved 33.8 kW of refrigeration capacity with 0.53 of COP under the input temperature conditions of cooling water 26.1ºC, evaporation temperature -19ºC, secondary refrigerant -15.2ºC, and engine exhaust temperature 567ºC. Therefore, these results from the developed prototype proved the feasibility of the compact and efficient absorption refrigeration cycle for freezing applications.

Figure 2-13 : NH_3-H_2O absorption chiller prototype developed by Du et al[47].

In light of the studies mentioned above, it seems feasible to develop a compact, efficient and reliable NH_3-H_2O absorption chiller to support the thermally activated absorption refrigeration system in replacing the conventional compression systems for refrigerated transportation. Internal heat recovery and microchannel heat exchangers are critical strategies for successfully implementing heat-driven absorption chillers.

A brief review of the absorption refrigeration technology development for transport applications is presented in the following section to provide a holistic view of the topic.

2.4 Experience of VARS for Automobile Application

Many researchers have explored the idea of implementing VARS for automobile air conditioning and refrigeration applications [48–56]. In all reported studies, VARS was coupled with the vehicle engine exhaust. The exhaust from the typical diesel engine is in the temperature

range of 250 to 490 °C temperature [57] which is suitable to drive VARS. Venkataraman et al. [24] conducted a comprehensive literature review on engine exhaust-coupled VARS. As a detailed literature search has therefore already been performed on the engine exhaust coupled VARS, only the conclusion is mentioned here to avoid repetition. It was noted that heat captured from the engine exhaust is sufficient to obtain the required refrigeration load when the vehicle operates within a specific RPM range. During idling, however, the exhaust heat is insufficient to supply the cooling load. Also, the engine performance is greatly influenced by the back pressure generated due to the coupling of the engine exhaust to the VARS, an issue that needs to be considered. Another problem is the corrosion effect caused by the hydrocarbon and NOx present in the exhaust gas. It was concluded that flat terrain or long-distance highway transport is the most suitable for VARS as the engine runs on continuous RPM. In city driving, the engine needs to often idle. Therefore, heat delivered by the engine exhaust varies and is often insufficient. Therefore, engine exhaust coupled VARS without an auxiliary burner and control mechanism are unreliable and challenging [27].

Hence, it is worth exploring alternate configurations to replace TRUs on conventional diesel engine-powered trucks. Therefore, the following section briefly explains literature focusing on integrating fuel cells with absorption or compression refrigeration technology.

2.4.1 VARS with SOFC for transportation application

As per the author's best knowledge, there is a scarcity of available sources reporting the application of fuel cells for refrigerated transportation. The available research studies and projects on the application of fuel cells for TRUs are discussed in the following.

Venkataraman et al. [22,58] conducted a detailed simulation for hydrogen-fuelled SOFC-coupled NH_3-H_2O VARS for refrigerated truck transportation. This study demonstrated a simulated study of the concept of SOFC powered VARS. It was observed that the performance of the combined system of SOFC-VARS greatly depended upon the operating conditions along the polarisation curve (I-V) of the SOFC. The authors found that the available thermal energy from the stack could be increased by operating the stack at a higher current density. Therefore, the operating condition for the SOFC-VARS configuration should be selected to balance electrical power and thermal power generated from the stack. The authors carried out a simulation to determine SOFC stack size to supply for the refrigeration load of different refrigerated vehicles at different refrigeration temperatures, as shown in Figure 2-14. Initial results depicted by the authors suggested that the novel system promised 80% combined efficiency. However, the study assumed coupling the SOFC cathode exhaust to the VARS via a heat recovery exchanger without considering preheating the SOFC reactants, which is necessary for the SOFC operation.

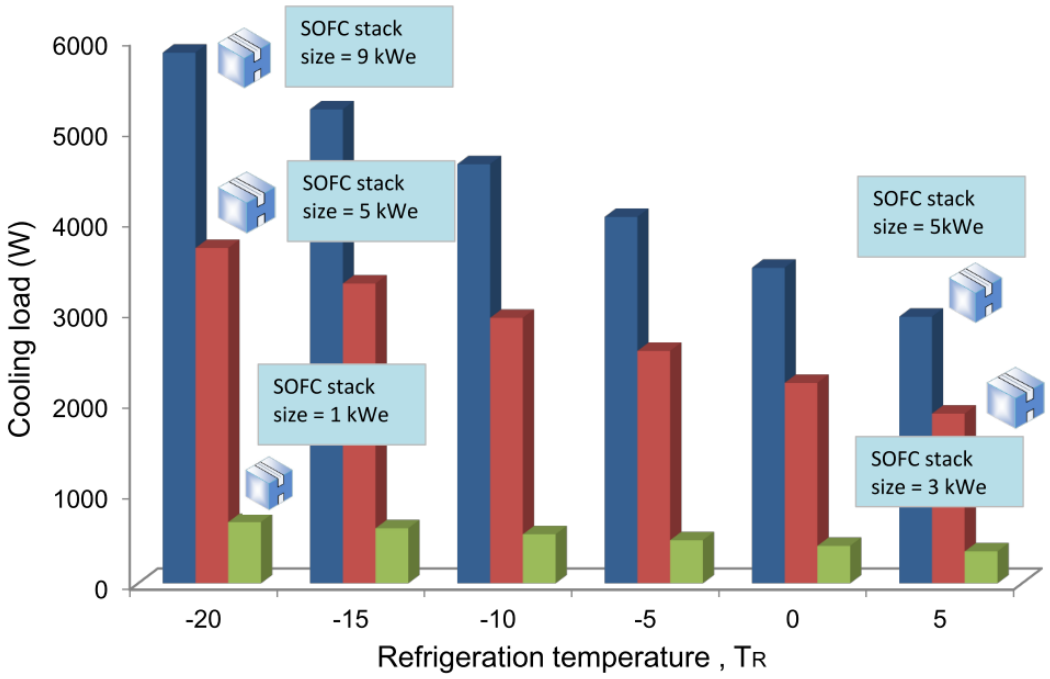

Figure 2-14 : SOFC stack size for different truck size [22].

Amakiri [59] demonstrated a small-scale NH_3-H_2O absorption refrigeration prototype coupled with simulated SOFC exhaust for refrigerated transportation applications. The prototype was equipped with an electric heater to simulate the SOFC exhaust. An internally finned tube-in-tube heat exchanger with thermal oil was used to couple the absorption system with an SOFC exhaust. The hot air flow rate and temperature were kept at 24 L/s and 600ºC to heat the 16 g/s of thermal oil flow rate to 200ºC. It was determined that 1.84 kW of heat was recovered from 5 kW of hydrogen fuelled SOFC exhaust. The recovered heat was able to cater for the 1 kW of refrigeration load at 4ºC of evaporator temperature with 0.52 COP. The study's main aim was to identify the feasibility of coupling an SOFC exhaust flow to a VARS and the minimum evaporator temperature that could be achieved, hence not much attention was paid to optimising the system operating conditions. The primary focus was on the system-level modelling of the absorption system side, and no information on the SOFC system was provided in the study.

Hauth et al [60] demonstrated a 5 kW NH_3-H_2O absorption chiller integrated with 6 kW SOFC system for a maritime transport application, as shown in Figure 2-15. The high temperature (> 200°C) SOFC exhaust was directly used to drive the heat operated absorption chiller. Diesel was used as a fuel to power the SOFC-coupled system. The SOFC stack was operated at 0.27 A/cm^2 current density and 75% fuel utilisation. The SOFC system demonstrated 60% net electrical efficiency. If the VARS was to be operated by the SOFC exhaust only, it would need at least a 19 kW SOFC system, hence remaining heat load was provided by an additional amount of fuel in the burner. 11 kW of diesel burner was equipped to the system to deliver the necessary amount of heat during the heat-up phase of the SOFC system. The absorption system produced 5 kW of cooling at an ambient temperature below 30°C. The authors found electric power to cooling capacity ratios for cooling application (6°C) of 5.6, sub-zero application (-

29°C) of 36, and air conditioning application (15°C) of 3.8. The SOFC system generated 320 gCO_2/kW, considerably lower than combustion engine-driven generators and compression refrigeration systems (600 gCO_2/kW). It was found that the SOFC exhaust cooled down to 79°C by the effect of the absorption chiller. An additional 1.3 kW of heat was recovered by cooling down the SOFC exhaust from 79°C to 40°C. The system showed overall 90% efficiency including the cooling and heating effect from its exhaust.

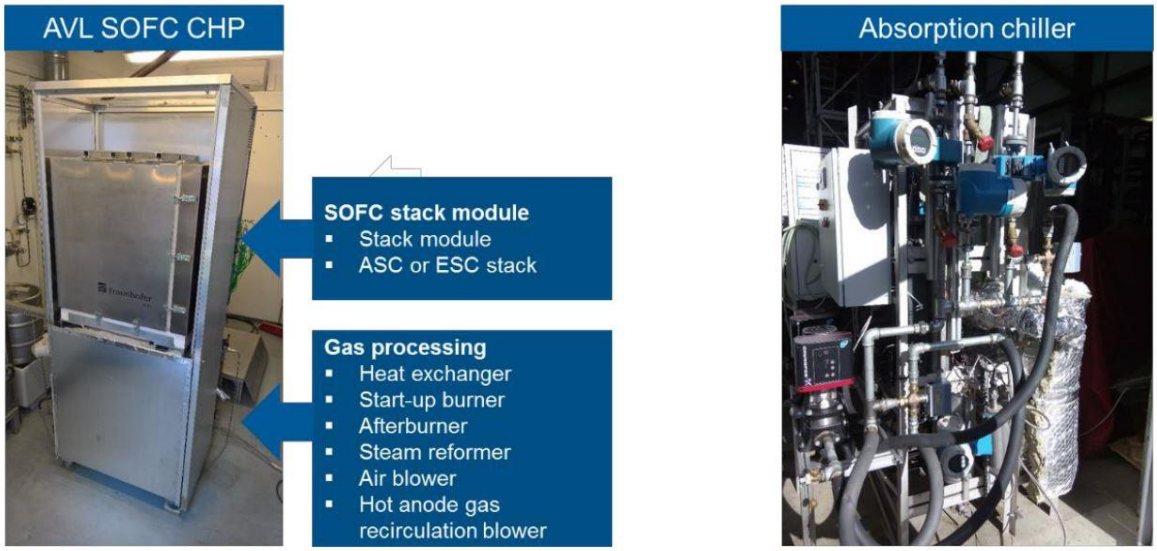

Figure 2-15 : SOFC powered absorption chiller for a maritime transport application [60].

In the past decade, only few projects have yet to be carried out concerning fuel cell coupled refrigeration systems. Recent developments in fuel cells and compact VARS support the consideration of absorption refrigeration technology for automotive transportation. However, this concept is still novel and requires critical insights, which the system-level transient simulation should supplement before the prototype development of the system.

SOFCs for applications in combined cooling and power generation for automotive transportation is in its infancy, forcing the designer to start from scratch to explore all the possible design configurations to satisfy the requirements of refrigerated transportation application, SOFC and VARS system likely to encounter load following conditions through all operating modes. Hence, knowledge of the transient characteristics plays a significant role in determining the need for any auxiliary storage device, such as a battery, in dealing with load following conditions. The design and modelling of an SOFC-powered VARS system require multidisciplinary knowledge across various disciplines, including electrochemistry, chemical engineering, electrical engineering, thermodynamics, and refrigeration. In an SOFC-VARS combined system, the SOFC is a prime mover to run the system. Therefore, successfully demonstrating an SOFC powered VARS concept requires the optimised selection of operating conditions of the SOFC system such as current density, working temperature, and fuel utilisation. Analysing the transient characteristics of the combined system also helps to understand the system capability to load following conditions. Therefore, the technical literature review in the upcoming section is primarily focused on the modelling methodology of both systems (SOFC and VARS).

2.5 SOFC Modelling

Mathematical modelling is the first and essential step in designing power generation systems. The complexity involved in SOFC modelling can be explained based on electrochemical reactions, ion conduction, electric conduction and heat transfer simultaneously taking place within the SOFC control volume [61]. Complexity increases even further with DIR SOFCs due to SMR and WGS chemical reactions and electrochemical reactions within the SOFC when powered by hydrocarbon fuels.

The mathematical model of any power generation system can be divided into steady state and transient state models from the perspective of whether the system dynamics are considered or not. The range of these models can vary from zero-dimensional (0D) to three-dimensional (3D) depending upon the spatial aspect that has been considered in the modelling. The 3D and two-dimensional (2D) modelling approaches are physical models which consider detailed heat and mass transfer phenomena within the fuel cell control volume [62]. Various electrochemical parameters, material properties, geometrical parameters and other cell structure details are required for higher dimensional models (3D and 2D), which may not always be accessible. On the contrary, 0D and one-dimensional (1D) are low-dimensional modelling approaches that require significantly less information. Research objectives and aims determine the complexity and dimension of the model. 3D and 2D models are aimed at cell or stack design development/modifications, while 0D and 1D are used for system-level analysis and control strategy development of the SOFC system [63].

High-dimensional physical models (3D and 2D) models are able to provide a detailed profile of temperature, pressure, and species concentration which have great significance to understand the operation of SOFCs [62]. The development of high-dimensional models begins with a set of partial differential equations (PDEs), which describe the space and time evolution of the system. These so-called PDEs are solved by computational fluid dynamics (CFD) simulation technology[64].

1D models consider spatial variation only in one dimension. Generally, the spatial variable is considered either along the fuel flow direction or along the thickness direction of the cell assembly [62]. A typical 1D model divides the SOFC control volume into a number of interconnected discretised control segments. 1D models contain several sets of PDEs

(conservation equations of mass, energy and momentum). These can be solved with the finite difference method. The control and diagnostic simulation may for instance be performed with 1D modelling to determine temperature gradient distribution within the SOFC control volume [16].

0D models are the most straightforward approach to perform the system-level analysis without considering spatial variations of the system parameters. Such models are applicable when the primary characteristics of the system are known, e.g., when a system prototype is available [16]. For 0D SOFC modelling, missing physical information is extracted from the higher-dimensional physical models or experiments. Therefore, the 0D models incorporate data from experimental and empirical information. Mathematical equations in the 0D model are still based on energy and mass conservation between the inlet and outlet of the SOFC. The 0D models are characterised by a particular set of so-called ordinary differential equations (ODEs), which demonstrate the system's time evolution over a given period. The 0D SOFC models are frequently implemented when the fuel cell is viewed as a single component of a larger and integrated systems for evaluating system behaviour and performance where detailed physical and chemical parameter variations are not so relevant. However, system performance in energy output (power and heat) and energy (fuel) input requirements are still main areas of interest. It also prompts fast computation with reasonable accuracy of the model [63].

In general, an SOFC model can be developed with three approaches: white, black and grey box. Physical high-dimensional (3D and 2D) models follow the white box approach, which requires primary data to solve well-established physical principle equations [65]. On the other hand, the black-box approach only requires a mathematical description of the process obtained from the experimental data. Therefore, the black box approach does not rely on physical

variables and does not need to solve ODEs or PDEs, considerably reducing computational time. The accuracy of the black box approach entirely depends upon the data being extracted from the experiments [65]. The Grey box approach falls between the white and black boxes. It exploits both the physical parameters and experimental data. The 0D or lumped models are an example of the grey box approach.

Figure 2-16 depicts the impact of the modelling approach on the required experimental burden for the validation of the model. The white method requires few experimental data for the validation, while the black box approach needs a considerable amount of empirical data for identification and testing. Especially, SOFC manufacturing industries use high-dimensional physical models (white box approach) to improve SOFC geometries for efficient SOFC performance [25].

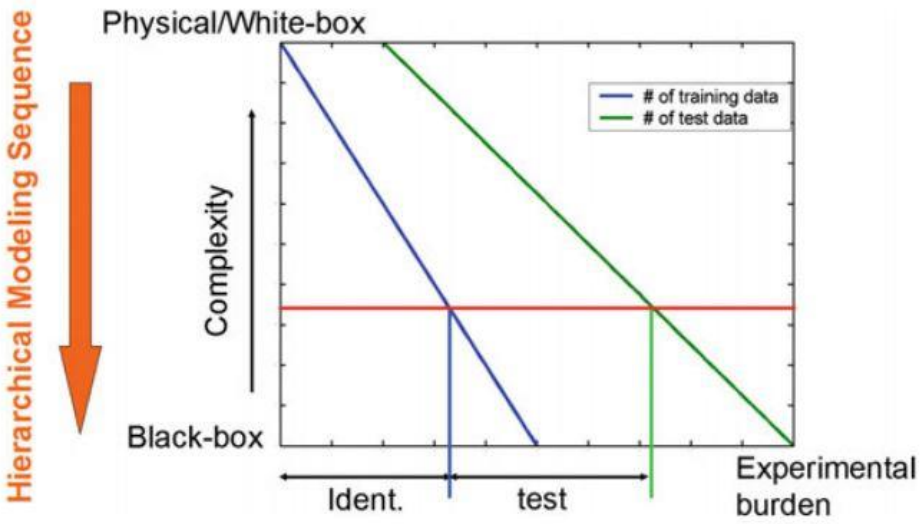

Figure 2-16 : Impact of modelling approach on required experimental burden [16].

As far as system-level analysis of SOFC is concerned, it is advisable to incorporate some reduced 0D/lumped-capacitance type SOFC models that can take key aspects of SOFC system operation into account and avoid having to solve highly complex models. This approach meets the trade-off between acceptable accuracy and reasonable computational time for the analysis of SOFC co-generation systems. Thus, reviewing research studies focused on high-dimensional physical models does not make sense. Therefore, research studies focused on 0D/lumped modelling approaches only are presented in the following section.

2.5.1 SOFC stack/system modelling

Marra et al. [66] developed a grey box modelling approach based on a 0D lumped transient model for an SOFC stack operating with direct internal reforming. The authors validated the steady state temperature profile with the experiments. Assumptions made in the study were as follows: (i) the pressure drop across the cell was neglected, (ii) negligible variation in gases sensible heat, (iii) methane was assumed to be wholly reformed inside the stack, and (iv) anode and cathode streams exit the fuel cell at the same temperature as the solid. Non-adiabatic conditions with conduction, convection and radiation heat exchange mechanisms were applied for thermal transient modelling of the SOFC. Thermal performance of the SOFC was characterised by using the mass and energy conservation governing equation between the inlet and outlet of the stack. A mixed grey/black approach was adopted to model heat exchanges between the stack and its surroundings, where the temperature difference between the stack and furnace was extracted with the help of the black box approach. The results obtained from the modelling confirmed that the convection heat mechanism dominated the heat transfer inside the stack, thus allowing the opportunity to neglect the radiation and conduction heat transfer mechanisms. The adopted 0D model reproduced a similar stack outlet temperature profile from experimental results. Hence, the 0D modelling approach was proven effective and efficient to

characterise an SOFC under various operating conditions, and it could be further extended to formulate control strategies.

Sorrentino et al. [67] demonstrated a hierarchical modelling approach to characterise transient and steady-state SOFC stack model for APU applications. The first step in the approach was to develop a 1D steady-state model of the SOFC to determine an accurate spatial variation of SOFC performance parameters such as local current densities, temperature, and gas molar fraction along the direction of the flow channel. Adiabatic conditions were applied to cell boundaries, and only heat transfer due to mass flow was considered for heat exchange, thus neglecting the radiation and conduction heat transfer. This study only considered thermal dynamics, mass dynamics and electrochemistry dynamics assumed to be rapid. Later, outputs of the 1D steady-state model, such as voltage, were used in the 0D lumped modelling approach. The adiabatic conditions were assumed in building the 0D lumped transient SOFC model to determine thermal dynamics. The 0D model was found accurate to reproduce temperature and voltage dynamics with the data supplied by in the steady state 1D model. Finally, the authors concluded that the proposed hierarchical modelling approach could also be applied to BoP components and system level analysis.

Saarinen et al. [68] developed a 0D dynamic model of a 5 kW SOFC-powered combined heat and power system. The authors used the area-specific resistance (ASR) approach to calculate SOFC stack voltage to avoid the complex physical information needed to calculate the SOFC electrochemistry model. It was found that the ASR approach allowed meeting the trade-off between accuracy in SOFC voltage calculation and the requirement of complex physical parameters for the 0D lumped model. This study considered complete conversion of methane inside the SOFC stack to avoid the complexity involved in calculating the reaction rate of SMR.

The radiative and convective heat transfer were considered to determine the heat exchange in the SOFC stack. The model developed by the authors is a typical example of the grey box approach, where conservation equations have been applied for thermal dynamics and experimental data used to determine ASR and voltage calculation. However, the authors did not detail the methodology for building the heat exchanger and air blower models. A burner model was built by assuming complete conversion of combustible gases entering the burner. It was determined that the ASR model presented inaccuracy to predict SOFC performance in the simulated results outside the current and fuel utilisation range for which the ASR function had been formulated. However, the SOFC system always operates within a specific range of current and fuel utilisation. Therefore, the ASR model can provide sufficiently accurate results for standard operational conditions. It was concluded that the 0D SOFC model reproduced accurate validated results, and it was the preferred modelling approach for system level analysis.

Sorrentino and Pianese [69] implemented a 0D lumped transient model of an SOFC system for APU applications. The authors used the grey box approach. The SOFC voltage was determined by using the equation developed by Sorrentino et al. [67]. The adiabatic boundary conditions were assumed for the SOFC stack and BoP components with only heat transfer due to mass flows considered. A complete conversion of combustible gases was assumed for the burner modelling. The air blower model was quasi-static. A zero-heat capacity approach with constant heat transfer coefficient was adopted to model the heat exchangers. In this approach, the thermal capacitance of the solid heat exchanger (wall mass) was added to the hot fluid side. Thermal transients due to mass flows were considered, thus neglecting radiation and conduction heat transfer. The 0D lumped capacity model was demonstrated to outline the response of SOFC stack and heat exchangers to the load following conditions.

Gallo et al. [70] developed a versatile 0D lumped model for an SOFC system for system-level analysis. A transient 0D lumped approach was developed to model the thermal dynamics of the SOFC stack, heat exchangers and afterburner. This modelling approach considered only thermal dynamics, neglecting mass and electrochemistry dynamics. In addition, pressure loss in the components was also neglected. Energy and mass conservation equations were applied between the inlet and outlet of the SOFC stack, heat exchangers and afterburner control volume. The effectiveness of the heat exchanger was assumed to be independent of the fluid temperature and set to 0.85 for simplification of heat exchanger transient modelling. Afterburner modelling included an assumption of complete adiabatic oxidation of combustible gases from the SOFC stack. In this approach, methane was assumed to be completely reformed in the SOFC stack to overcome the need for a complex reaction kinetics model, which would have required detailed physical parameters of the stack. The authors considered all three heat transfer modes: conduction, convection and radiation to simulate heat exchanges in the SOFC stack. The authors also concluded that the assumption of adiabatic boundary conditions (no heat loss) with heat transfer due to mass flows was sufficient to model the SOFC transient behaviour while maintaining a trade-off between model accuracy and computational time. The ASR approach was adopted to compute the SOFC voltage and demonstrated accurate results of stack voltage. It was concluded that the ASR approach guaranteed the electrochemical model to be closer to actual SOFC stack behaviour. The 0D lumped modelling approach simulated accurate voltage and temperature profile results with a maximum relative error of 4% and 5% against experimental data in transient and steady-state conditions, respectively. Hence, the 0D lumped approach with ASR concept was found to be effective and efficient in predicting SOFC system behaviour.

Marra et al. [71] developed a 0D lumped transient model of a 10 kW SOFC system for APU and CHP applications. Different chemical reactions (SMR, WGS and hydrogen oxidation) taking place in the SOFC stack were assumed to be at equilibrium. Also, the stack was assumed adiabatic, and the pressure drop across the cell was neglected. Heat transfer was only considered due to mass flow, thus neglecting radiation, convection, and conduction heat transfer. The methodology to build BoP components was not presented explicitly. The results of the 0D lumped model were validated against the experimental data available from an SOFC stack prototype. The 0D model simulated accurate transient characteristics of the SOFC with a relative maximum error of less than 1 %.

Wu and Chen [72] developed a 0D lumped transient model to theoretically simulate a methane fuelled SOFC system powered adsorption refrigeration system (combined cooling and power system). This 0D lumped model considered both mass and thermal dynamics, however electrochemistry dynamics were assumed rapid. The SMR reaction rate was determined with reaction kinetics first principles, however the WGS reaction was assumed at equilibrium. Temperature, pressure and gas species in the stack and BoP components were determined by applying energy and mass conservation equations and the ideal gas law between the inlet and outlet of the components. Adiabatic boundary conditions were applied to the SOFC stack, and heat transfer inside the SOFC by radiation, convection and conduction mechanisms was neglected. This study only considered heat transfer due to mass flow. The heat exchangers were resolved with constant heat transfer coefficient between hot and cold fluid. Pressure loss in the components was neglected. The authors validated the steady-state I-V curve with the experimental data with a maximum relative error of 5%.

Kang et al. [73] investigated the transient behaviour of a methane fuelled direct internal reforming SOFC stack with a 1D modelling approach. Spatial variations of SOFC parameters (temperature, gas species concentration, cell voltage and local current density) along the flow channel direction were determined in the modelling. The thermal and mass dynamics were considered in the modelling. Pressure loss was neglected in the SOFC stack. This model considered heat transfer due to convection, conduction and mass flow for the thermal transients, however, radiation heat transfer was neglected in the modelling. The WGS reaction was considered at equilibrium, and the SMR reaction rate was computed with a reaction kinetics equation. The International Energy Agency (IEA) benchmark test was used to validate the steady state results from the model, and model predictions were found to be quite close to the IEA benchmark test. The current density and cell voltage dynamics were found to be rapid, but the thermal dynamics were slow.

Xi and Sun [74] formulated a 1D transient model for methane fuelled SOFC to represent the spatial variations of key performance parameters such as temperature, current density and gas species concentration. In the baseline 1D model, SOFC was divided into a number of interconnected discretised units along the fuel flow direction. The transient behaviour of the SOFC was determined by applying energy and mass conservation equations to each discretised control volume. Each discretisation control volume was simulated with three sub-models: mass balance, energy balance and electrochemical model. Heat transfer considered in the 1D model included conduction in the solid layer of SOFC and convection between fuel flowing in the channel and its surroundings. It was mentioned that a baseline model accuracy greatly relied upon the number of discretised control volumes. Modelling with a higher number of discretised control volumes depicts more accurate spatial variations of SOFC parameters. However, it also increased computational time substantially. It was found that thermal dynamics (stable

temperature) dominate the transient behaviour of the SOFC. Thus, it should be solved dynamically while mass conservation and electrochemical principle equations developed quasi-static. Mass dynamics were found to be rapid due to the high velocity of the fuel flow in flow channels. Hence, these dynamics achieved their steady states instantaneously (quasi-static relation). Therefore, authors have developed a low-order iterative modelling approach that solves mass and energy balance equations with a quasi-static approach. The low-order model adopted only stack temperature variation from 1D transient model, and remaining energy and mass balance equations were resolved with steady state approach. It was concluded that the low-order modelling approach closely matches the transient 1D model and requires 50 % less computational time.

Braun [10] presented a detailed steady state analysis to predict the performance of SOFC powered combined heat and power systems for small-scale stationary application. The SOFC stack was built with a 1D steady state approach, however BoP component modelling was based on a 0D steady state approach. This study was among the few examples in the literature that presented all required data and information to build SOFC system modelling. This study also described the detailed approach to build BoP components models. Convection, radiation and conduction heat transfer were considered to determine heat exchange discretised control volumes. The SMR reaction rate in the SOFC was computed using reaction kinetics, however, the WGS reaction was considered to be at equilibrium. Adiabatic conditions were applied to the SOFC stack. Air and fuel heat exchanges were modelled with constant effectiveness assumptions. The pressure loss was considered for each component in the study. The author mentioned the pressure drop at nominal design point, and the pressure loss in off-design operation was determined by establishing the relation of pressure loss with gas flow. The burner model assumed complete conversion of combustible gases. Air blower, fuel compressor and

water pump were simulated with constant isentropic efficiency, however the mechanical efficiency was varied according to component manufacturer data. The modelling results were compared with IEA benchmark results, where it was observed that the model reproduced results with great accuracy.

Uva et al. [75] presented a transient model of an SOFC system for maritime applications. The authors developed a 1D transient model for the SOFC stack and 0D lumped transient model for BoP components. The SMR and WGS reaction kinetics were included in the SOFC 1D transient modelling. Convective and conduction heat transfer were considered in the 1D transient stack model, but radiation heat transfer was ignored in the model. Heat loss was considered for the stack modelling; however, it was neglected for BoP components modelling. The SOFC system blowers (air blower, recirculation blower) were modelled with constant isentropic and mechanical efficiency. Air and fuel heat exchangers were modelled with a zero-capacity approach and constant heat transfer coefficient assumption. This study applied adiabatic boundary conditions to the burner and assumed complete combustion of combustible gases entering the burner. The 1D SOFC stack model produced comparable results against experimental data, however the results from BoP components modelling were now validated with experimental results.

Murshed et al. [76] built a 0D transient model for a methane fuelled SOFC system. The 0D transient model was based on energy and mass conservation equations and electrochemical principles. Mass and thermal dynamics were considered in developing a 0D transient model. Adiabatic conditions were assumed in building the SOFC system model. Two different types of 0D models namely: a lumped model and a detailed model were developed for the SOFC stack. The lumped model considered uniform temperature distribution for the entire stack. The

detailed model considered different temperatures for fuel electrode, air electrode, interconnector, air and fuel side gases. The lumped model did not take convection, conduction and radiation heat transfer into account; however, the detailed model considered all heat transfer modes to evaluate heat exchange. The BoP components were modelled with only the 0D lumped approach. The transient model of heat exchangers considered a constant heat transfer coefficient. It was found that at lower current loads, electrodes and electrolyte temperatures did not differ much, thus assuming uniform temperature distribution throughout the stack was a legit assumption. However, at higher current loads and higher operation temperature, stack component temperatures differed in magnitude, hence the uniform temperature distribution assumption may not be valid. Hence, a detailed model must be incorporated to simulate the SOFC system at higher current load at elevated temperature. It should be noted that both models depicted significant variation in the SOFC stack temperature when the SOFC was operated with an air inlet temperature above 950ºC. However, both models reproduced similar SOFC stack working temperature and steady state results when the SOFC stack was operated below 950ºC of air inlet temperature. The authors did not present a model validation in the study.

Table 2-2 summarises the key modelling methodologies and key points derived from the research studies discussed in the section.

.

Table 2-2 : Overview of modelling methodology for SOFC stack/system.

Modelling approach	Authors	SOFC stack/ system	Remarks
0D lumped transient	Marra et al [66]	Stack	• Complete conversion of methane in the SOFC stack. • Thermal dynamics were considered, mass and electrochemistry dynamics were assumed rapid. • Convection heat transfer mechanism dominates the heat transfer inside the stack • Multiple linear regression based black box approach was developed to map heat exchange processes.
1D steady state and 0D lumped transient	Sorrentino et al [67]	Stack	• 1D steady state model was used to establish the relation between performance parameters with operating parameters. • Adiabatic conditions were assumed, only heat transfer due to mass flow was assumed in the SOFC stack. • Mass and electrochemistry dynamics were neglected in 0D lumped transient model.
0D transient	Saarinen et al [68]	System	• Simplified ASR approach was adopted to calculate cell voltage. • BoP components transient modelling methodology were not presented. • Complete conversion of methane was assumed in SOFC stack. • Convection and radiation heat transfer mechanism were considered for the thermal transient modelling. • Mass and electrochemistry dynamics were neglected in 0D lumped transient model.

0D lumped transient	Sorrentino and Pianese [69]	System	• Mass and electrochemistry dynamics were neglected in 0D lumped transient model. • Adiabatic conditions were assumed for stack and BoP components with only heat transfer due to mass flow was considered to determine heat exchange. • Heat exchangers were solved with a zero-heat capacity approach. • Air blower model was steady state. • Burner model was built with assumption of complete conversion of combustible gases.
0D lumped transient	Gallo et al [70]	System	• Methane was assumed to be completely reformed in the stack. • ASR approach was adopted for voltage calculation. • Transient model considered only thermal dynamics, mass and electrochemistry dynamics were neglected. • Conduction, convection, and radiation heat transfer modes were considered for heat transfer computational model. • Heat exchangers were modelled with constant effectiveness approach. • Pressure loss in the components was neglected. • Burner model was built with assumption of complete conversion of combustible gases.
0D lumped transient	Marra et al [71]	System	• This approach only considered heat transfer due to mass flows, thus neglecting heat transfer by conduction, convection, and radiation heat transfer. • Chemical reactions were considered at equilibrium. • Pressure drop was neglected in components. • BoP modelling methodology found missing.

0D lumped transient	Wu and Chen[72]	System	• Heat transfer by radiation, convection and conduction mechanisms was neglected. • Pressure loss was neglected in the SOFC system components. • WGS reaction was considered at equilibrium. • Thermal and mass dynamics were considered. • Heat exchangers model assumed constant heat transfer coefficient.
1D transient	Kang et al. [73]	Stack	• Heat transfer due to convection, conduction, and mass flows was considered, radiation heat transfer was neglected. • Thermal and mass dynamics were considered. • Pressure loss was neglected. • WGS reaction was assumed at equilibrium.
1D transient	Xi and Sun [74]	Stack	• Convective and conduction heat transfer was considered in the model. Radiation heat transfer was neglected. • Mass dynamics was found rapid and achieved its steady state values instantaneously. • Low order model was developed with quasi-static approach to solve mass and • Low order model was found to be accurate and reliable.
1D and 0D steady state	Braun [10]	System	• Stack was modelled with 1D model and BoP components were modelled with 0D model. • 1D stack model considered radiation, convection, and conduction heat transfer to evaluate heat exchange in SOFC control volume. • Heat exchangers were modelled with constant effectiveness value. • Constant isentropic efficiency was assumed for electricity driven components.

1D transient and 0D lumped transient	Uva et al. [75]	System	• 1D and 0D transient models were developed for SOFC stack and BoP components respectively. • Stack model considered convection, conduction and radiation heat transfer. BoP components model consider heat transfer only due to mass flows. • Heat loss was considered for stack; however, it was neglected for BoP components. • A zero-capacity approach was considered with constant heat transfer coefficient for heat exchanger modelling. • Blowers were modelled with constant isentropic and mechanical efficiency.
0D Transient	Murshed et al [76]	No	• 0D lumped and detail model were developed for the SOFC stack. • 0D lumped model considered uniform temperature distribution, while detail model considered different temperature among electrode, interconnector, and gas flow. • Detailed model considered convective, radiative, and conduction heat transfer, lumped model considered heat transfer due to mass flows only. • BoP components were built with 0D lumped approach. • 0D lumped model reproduced comparable results detail approach when SOFC operated with air inlet temperature lower than 950ºC.

2.5.2 Lesson learnt

The application of lumped models includes a system-level analysis where the main interest is not on single system components but in analysing the interplay between system components. Regarding system level analysis, lumped models are a better choice than detailed physical and highly computationally intensive models. Therefore, most studies focused on the SOFC system level analysis relied on the simplified lumped-capacitance models to avoid the complexity involved in building electrochemical higher-dimensional modelling. The lumped model often neglects the mass and electrochemistry dynamics and only considers thermal dynamics for the transient model. It was also observed that the radiation heat transfer within the SOFC stack was mostly ignored in the lumped model. Adiabatic boundary conditions were often applied to the SOFC stack in the lumped models, eliminating the effort required to build the convection heat transfer model between stack and its surroundings. Therefore, the lumped models mainly account for the energy carried by flowing mass to evaluate the thermal transients of the SOFC stack. Lumped modelling studies focused on system level analysis often assumed complete reformation of methane in the SOFC stack and chemical reactions at equilibrium in order to avoid the complexity of calculating the reaction rate inside the stack. The ASR approach to calculate cell voltage was found to be an effective tool to match the trade-off between accuracy and computational burden, which becomes a crucial aspect of the modelling, especially when dealing with the transient analysis of SOFC integrated co-generation systems. As far as BoP components modelling is concerned, all studies build heat exchanger models either with the constant effectiveness approach or with constant heat transfer coefficient assumptions with the adiabatic boundary assumption. The burner modelling always assumed complete conversion of combustible gases with adiabatic boundary implementation. Electricity driven components (blower, compressor and pump) were always solved with a steady state approach with assumption of constant isentropic efficiency.

The transient modelling of the SOFC-integrated absorption refrigeration system is complicated, lengthy and sensitive to inaccuracies. Therefore, the 0D lumped modelling approach combined with the ASR approach can deliver essential highlights of the transient SOFC system operation while considerably reducing computational and high dimensional modelling effort.

2.6 Absorption Refrigeration System Modelling

Transient simulation of the vapour absorption refrigeration system (VARS) is critical to understand the time evolution of the system and its response under load following conditions. The development of a model of the VARS is a complex process as the heat exchangers in the system encounter multi-phase fluids and binary mixtures. The transient model of the VARS contains a set of non-linear conservation equations that can be solved using several approaches ranging from simplified lumped approaches to detailed discretised high-dimensional physical models [77]. A simplified 0D lumped approach and 1D discretised modelling approach are often used for the absorption system-level transient analysis [77]. Therefore, studies focused on simplified lumped and discretised methods are presented briefly in the current literature review.

Tiji et al [78] investigated a transient simulation to of an NH_3-H_2O VARS with a 0D lumped approach for stationary application. This study did not consider modelling of the rectifier due to the complexity involved in its operation. In addition, the NH_3 refrigerant concentration leaving the desorber was assumed to have a constant value of 0.9996, and the pressure loss across the components was neglected. The refrigerant phase was assumed to be a saturated liquid at the condenser outlet, and saturated vapour at the evaporator outlet. Mass and energy conservation equations were applied to heat exchangers of the absorption system. The system's

high and low side pressure was determined by applying a momentum equation, and characteristic curves of the solution pump supplied by the manufacturer. The authors did not validate the modelling results in this study.

Kim and Park [79] developed a 0D lumped transient model of a commercially available 10.5 kW NH_3-H_2O VARS. The system was developed for a stationary application. The model was formulated by applying energy and mass conservation equations to each component. This study considered a two-phase mixture at thermodynamic equilibrium. It was assumed that the enthalpy of a binary NH_3-H_2O mixture varied linearly along the stream direction in the heat exchanger, however the concentration of ammonia was assumed constant. The authors assumed a constant overall heat transfer coefficient for each heat exchanger. Thermal capacitance of the desorber was only considered in the simulation while it was neglected for other system components. Quasi-steady state was assumed for the refrigerant heat exchanger (RHX) due to its relatively low volume compared to other system parts. This study considered frictional pressure drop in the components, determined by standard equations. The authors did not present any validation of the modelling results with experimental data.

Adjibade et al [80] developed a 0D lumped transient model to represent a commercially available NH_3-H_2O-H_2 diffusion absorption refrigeration system for stationary application. A diffusion absorption refrigeration system works the same way as a conventional NH_3-H_2O absorption system; the only difference is that it does not require a mechanical pump. Mass, species and energy conservation equations with adiabatic boundary conditions were applied between the inlet and outlet of each system component. The thermal capacitance of each element was accounted for in the simulation. Heat transfer coefficients were assumed constants for all components in the simulation, and pressure loss across the heat exchanger was neglected.

Also, the effectiveness for the solution heat exchanger (SHX) and RHX was assumed constant to simplify the modelling. The high and low side pressure was determined via equilibrium assumptions. The refrigerant state at the outlet of evaporator and condenser was assumed saturated. The authors validated the transient response of the simulation with experimental results, and it was determined that the 0D lumped approach reproduced the heat source, evaporation, and condensation temperature with a maximum relative error of 3.8%, 14.5% and 2.9%, respectively.

Castaing-Lasvignottes et al. [81] simulated a commercially available NH_3-H_2O absorption chiller by adopting a 0D lumped modelling approach. Energy, mass, and species conservation equations were applied to each component in the modelling. This study also assumed that the rectifier condensed all water vapour content, and pure ammonia entered the condenser and evaporator. The rectifier model was built with a quasi-static approach, and the pressure drop across the components was neglected to simplify the modelling. The authors did not mention the methodology to calculate the high and low side pressure in the system. Thermodynamic equilibrium was assumed in each component and fluid leaving the component assumed in its saturated phase. The model was validated against experimental results, and it was found that it accurately represented the system transient response.

Kaushik et al. [82] simulated a solar-powered NH_3-H_2O absorption refrigeration system with a 0D lumped transient approach. The system was focused on stationary application. Heat transfer coefficient calculation for each heat exchanger was carried out with a quasi-steady approach. These values were later used in transient modelling. Refrigerant and solution storage was accounted for in the modelling by employing downstream condenser and absorber mass storage tanks in the system. The primary function of the condenser storage tank was to store excess

refrigerant produced under a higher desorber load with a lower evaporator load. On the contrary, a higher evaporator load with a lower desorber load required a high amount of refrigerant, which was drawn from the condenser storage tank to match the load conditions. Thus, the absorber storage tank was filled with an excess solution as a buffer for load changes. Mass storage was only considered in the storage tanks while neglected in the heat exchangers. Mass and energy conservation equations were formulated for each component of the system with adiabatic boundary conditions.

Fu et al. [83] developed an absorption system modelling library with a 1D transient approach to simulate various configurations of absorption chillers (single stage, double stage and triple stage) with NH_3-H_2O and LiBr-H_2O working pairs for stationary application. This developed modelling library was able to characterise absorption system transients from start-up to shutdown phase. Primary heat exchangers of the system, such as absorber, condenser, evaporator, and desorber, were modelled as shell-and-tube heat exchangers with the assumption of two-phase equilibrium and phase change taking place at the shell side. Heat exchangers were divided into several interconnected finite control volumes to consider the spatial variations of the state variables along the flow direction. Pressure dynamics were considered much faster compared to temperature dynamics. Pressure drop in the components was neglected in the 1D transient simulation. The overall heat transfer coefficient was assumed constant for all heat exchangers. The transient model of an exhaust-driven double-effect LiBr-H_2O system was presented in the study without any specific storage mechanism for the excess amount of refrigerant and solution. The developed model was validated with experimental data from the double-effect LiBr-H_2O absorption chiller. Absolute errors for chilled water temperature were within 0.5 K. Hence, the 1D lumped transient model was found to be accurate and reliable.

Viswanathan et al. [84,85] developed a 0D steady state and 1D lumped transient model to simulate a NH_3-H_2O microchannel heat exchanger based absorption refrigeration system developed by Determan and Garimella [45]. The authors presented detailed information including component data. This study is among the few studies in the literature that mentioned all required data and information to build the model. As a first step, a 0D model was developed to estimate mass flow, enthalpy and concentration values at various state points in the system. In addition, a 0D steady state model provided crucial information on heat exchanger performance such as UA values and LMTD values. These values were later used in a 1D transient model. It was mentioned that due to the presence of binary and two-phase mixtures in the NH_3-H_2O absorption system, the 0D lumped transient approach might not be able to predict the system performance with required accuracy. Hence, a 1D transient model was adopted in the study. The discretised model of counter-flow heat exchangers was formulated with an adiabatic boundary assumption. The thermal capacitance of the heat exchanger was taken into account to simulate the transient system response. The storage tanks shared a major part of the fluid inventory in the microchannel heat exchanger-based absorption refrigeration system. Hence mass storage was only considered in solution and refrigerant storage tanks which were modelled with a vapour-liquid equilibrium assumption to determine system pressure. Heat transfer coefficients were assumed constant for each heat exchanger, and pressure drop across the component was neglected to simplify the simulation process.

Martinho a et al. [86] built a 0D lumped transient model to predict the performance of an NH_3-H_2O absorption refrigeration system. Thermal dynamics of the system were derived by applying mass, species and energy conservation equations to each component. The transient model was divided into two parts, namely: NH_3-H_2O binary fluid mixture in the thermal compressor assembly (desorber, absorber, rectifier and solution heat exchanger), and pure NH_3

refrigerant in the condenser, evaporator and expansion valve. Components with only NH_3 refrigerant were solved with conventional ODEs, while components with binary mixtures were solved with non-linear algebraic equations. The NH_3 refrigerant phase at the condenser and evaporator outlet was assumed to be sub-cooled and saturated vapour, respectively, with a constant ammonia mass fraction of 0.998. The desorber, rectifier and absorber were modelled with vapour-liquid equilibrium assumption. Mass storage in the components was neglected. Simulated temperature curves of the system components were compared against experimental values and showed good agreement. A maximum relative error of 2% was found for the desorber temperature profile due to the simple assumption of the liquid vapour equilibrium in the desorber control volume. Hence, it was recommended to model the desorber via a discretised 1D approach to improve the accuracy of the simulation.

Wen et al. [87] developed a simplified 0D lumped transient model to simulate a LiBr-H_2O absorption refrigeration system. Condenser, absorber, evaporator and desorber were built with energy, mass, and species conservation ODEs. The solution heat exchanger, expansion valve and solution pump were modelled with a quasi-static approach. Adiabatic boundary conditions were applied to each component. The thermodynamic properties were assumed homogeneous in each component of the system. Pressure drop across the components and thermal capacitance of heat exchangers were neglected. The constant value of the heat transfer coefficient for different heat exchangers was assumed in the transient simulation. The accuracy of the lumped modelling was proved by comparing transient results with the experimental data. The lumped model successfully reproduced the system performance parameters with a maximum relative error of 2.5%.

A summary and key highlight from the literature studies is presented in Table 2-3.

Table 2-3 : Overview of modelling methodology for absorption refrigeration system.

Approach	Authors	Remarks
0D Lumped	Tiji et al. [78]	• The rectifier model was ignored in the transient modelling. • Constant refrigerant concentration of 0.9996 at desorber outlet. • Refrigerant phase was assumed saturated liquid and vapour at the outlet of the condenser and evaporator, respectively. • System pressures were determined by applying momentum equations.
0D Lumped	Kim and Park [79]	• Heat transfer coefficient was assumed to be constant for each component. • RHX was modelled with quasi-static approach. • Two phase mixture was assumed at thermodynamic equilibrium. • Thermal capacitance of desorber was considered in the modelling, however it was neglected for remaining components. • Frictional pressure loss was assumed in the component.
0D Lumped	Adjibade et al. [80]	• Heat transfer coefficients were assumed for each heat exchanger. • SHX and RHX effectiveness was assumed constant. • The high and low side pressure in the system was determined with equilibrium assumptions. • Maximum relative error between simulation results and experimental data was 15%.
0D Lumped	Castaing-Lasvignottes et al. [81]	• Rectifier was built with quasi-static approach, and it was also assumed that rectifier condensed all water vapour from NH_3-H_2O solution. • Thermodynamic equilibrium was assumed for each component. • The fluid leaving each component was assumed in its saturated state. • Pressure loss was neglected across the components. • Model reproduced comparable results against experimental data.
0D Lumped	Kaushik et al. [82]	• Refrigerant and solution storage tanks were considered to match the load following conditions in the modelling. • Constant flow rate across the expansion valve was assumed.

1D Lumped	Fu et al. [83]	• Absorption system modelling library was developed to analyse absorption chiller with different configurations and working pairs. • Pressure in the system was determined with quasi-static momentum equations. • Pressure dynamics were assumed rapid compared to thermal dynamics. • Pressure drop in the component was neglected. • Two-phase equilibrium was assumed for each component.
0D steady state and 1D lumped transient	Viswanathan et al. [84]	• 0D steady state model was used to provide heat exchanger information and mass flow information to 1D transient model. • Mass storage was considered in storage tanks, while it was neglected in other components. • Adiabatic boundary conditions were applied to heat exchangers with constant heat transfer coefficient value. • Pressure drop across the components was neglected. • High and low side pressures were determined by solving storage tanks model with vapour-liquid equilibrium assumption.
0D Lumped	Martinho a et al. [86]	• Mass accumulation was not considered. • Refrigerant phase was assumed sub-cooled and saturated vapour at condenser and evaporator outlet, respectively. • Condenser and evaporator were modelled with constant ammonia mass fraction of 0.998. • The model reproduced comparable results against experimental data with maximum relative error of 2%. • It was recommended to build discretised 1D transient model to improve the accuracy of the model.
0D Lumped	Wen et al. [87]	• Thermal capacitance and heat loss of the heat exchangers were neglected in the transient simulation. • Constant UA value for the heat exchanger was considered. • SHX, solution pump and expansion valve were modelled with a quasi-static approach. • Model reproduced system performance parameters with a maximum relative error of 2.5% .

2.6.1 Lesson learnt

Most studies reviewed adopted the 0D lumped-capacitance approach to simulate the transient modelling of a VARS. However, due to the presence of binary mixtures, phase change and absorption/desorption processes in the system, a simplified 0D modelling approach might not be able to predict the system transients with great accuracy, especially during system start-up. Therefore, a discretised 1D modelling approach could be more beneficial to deliver essential characteristics of the transient response of the system. As far as system-level analysis is concerned, it is advised to assume a constant heat transfer coefficient value for each heat exchanger to avoid lengthy and complicated calculations, especially for two-phase and binary mixtures. All studies considered adiabatic boundary conditions for heat exchanger modelling. Some studies evaluated the pressure difference across the components with momentum equations, while only few modelled the pressure difference governed by the accumulated solution and refrigerant in the storage tanks. The current study considered a compact microchannel heat exchanger based absorption refrigeration system. In microchannel based absorption systems, the storage tanks share a significant amount of fluid inventory. Therefore, pressures are governed by the vapour-liquid equilibrium conditions in the refrigerant and solution storage tank.

Studies on the transient modelling of absorption systems were mainly focused on stationary applications. Hence transient performance of the absorption system under load following conditions (for automotive transportation) has yet to be demonstrated in detail. To consider absorption refrigeration systems for automotive refrigerated transportation, it is crucial to identify the capability of the VARS to operate in load following conditions, which is something that is missing in the available literature.

2.7 Conclusion and Remarks

High-temperature SOFC systems can generate electric power without PM and NOx emissions. SOFC systems have demonstrated higher efficiency and lower GHG emissions compared to conventional diesel combustion engines. An SOFC integrated, thermally activated absorption refrigeration system for transportation can further increase the overall efficiency with a co-generation concept. Thus, such integration of an SOFC system with a thermally activated refrigeration cycle promises lower environmental impacts and higher efficiency. In addition, the SOFC system produces electricity which can be utilised on-board. Recent developments in the SOFC technology offer high volumetric power density which is one of the requirements of the automotive transportation. Furthermore, the electricity produced by the SOFC could be used not only for auxiliary loads but also in hybrid powertrain concepts, with the heat being used for on-board air conditioning and refrigeration.

Methane fuelled SOFC coupled VARS applications for refrigerated transportation have not been demonstrated or theoretically simulated to date. Therefore, integration of a methane fuelled SOFC system with a VARS for refrigerated automotive transportation is a new concept where a significant amount of information has to be added to prove the feasibility of such a system.

The following points are considered key in investigating the concept of an SOFC integrated VARS for refrigerated automotive transportation in more detail:

- Increased interest in road, maritime, and even airborne logistics in methane fuel (mainly in LNG and CNG) opens up new options and justifies the use of SOFCs in transportation.

- SOFC-integrated thermally activated refrigeration systems appear promising for refrigerated transportation applications by achieving higher efficiency.
- The hybridisation of the SOFC system with an additional electric battery system can satisfy the requirements to cope with load following conditions for automotive transportation.
- Transient and steady state modelling of the combined SOFC integrated absorption refrigeration system requires further attention to evaluate the system performance and ability to deliver optimised performance under various operating conditions.
- There is a considerable potential of SOFC integrated absorption refrigeration systems to decarbonise refrigerated transportation.

Chapter 3: *Research Methodology*

This chapter details the methodology adopted in the current study to achieve the research objectives. Each component used to build the experimental setup of the vapour absorption refrigeration system coupled with simulated SOFC exhaust is discussed. The methodology to assess the experimental prototype performance is also discussed in this chapter. The methodology to calculate the refrigeration load on different types of refrigerated trucks is presented followed by a thermodynamic modelling methodology for the absorption refrigeration and SOFC systems. The detailed methodology to build the mathematical models (transient and steady state) of the SOFC system and absorption refrigeration system is presented in the chapter.

3.1 Experimental Setup

The schematic of the experimental setup of a VARS is shown in Figure 3-1. The primary aim of the experimental investigation was to obtain sub-zero evaporation temperatures needed for refrigerated transportation

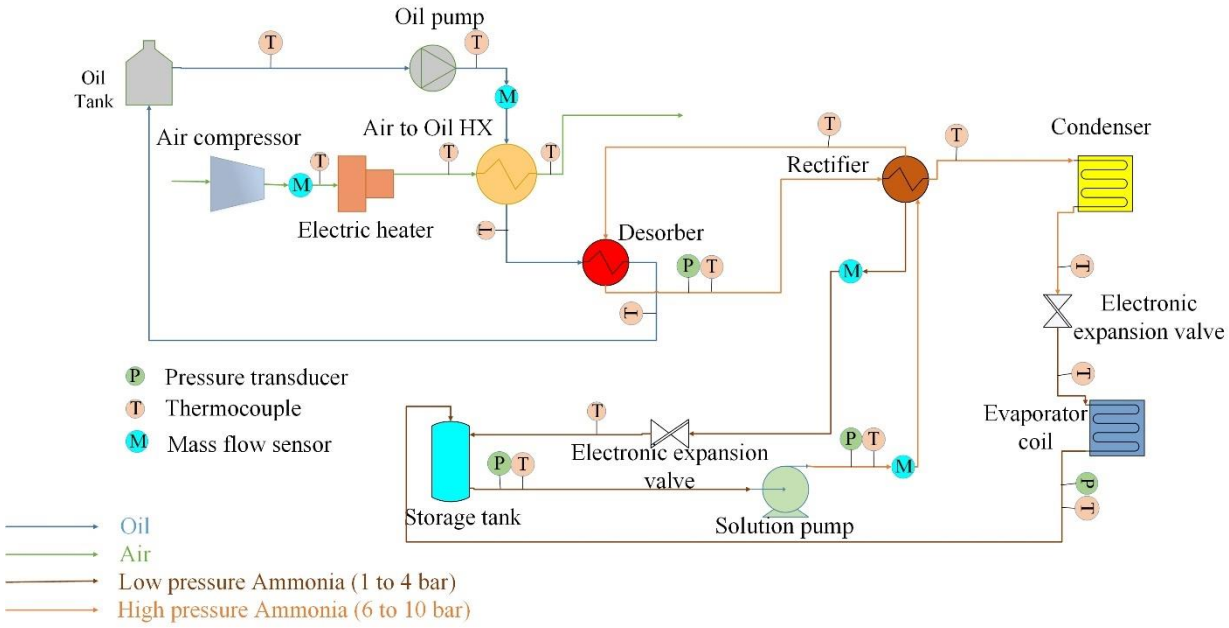

Figure 3-1 : Schematic of the laboratory absorption refrigeration system coupled with simulated SOFC exhaust.

The setup consisted of three fluid loops, with namely: air, heat transfer oil, and aqua-ammonia solution, as shown in Figure 3-1. To simulate high temperature SOFC exhaust, ambient air was heated to the desired temperature using an electric heater. The SOFC system exhaust contains mostly N_2 and O_2 (up to 95 %) and minor amount of H_2O and CO_2 (up to 5%), hence it is fair to treat ambient air as the SOFC system exhaust. The ambient air entered the electric heater via an air compressor where it absorbed the heat from the heating element. The hot air transferred its heat to the thermal oil (Paratherm NF) in an internally finned tube-in-tube heat exchanger.

In this setup, a plate heat exchanger was used as a desorber to achieve the separation of the aqua-ammonia solution.

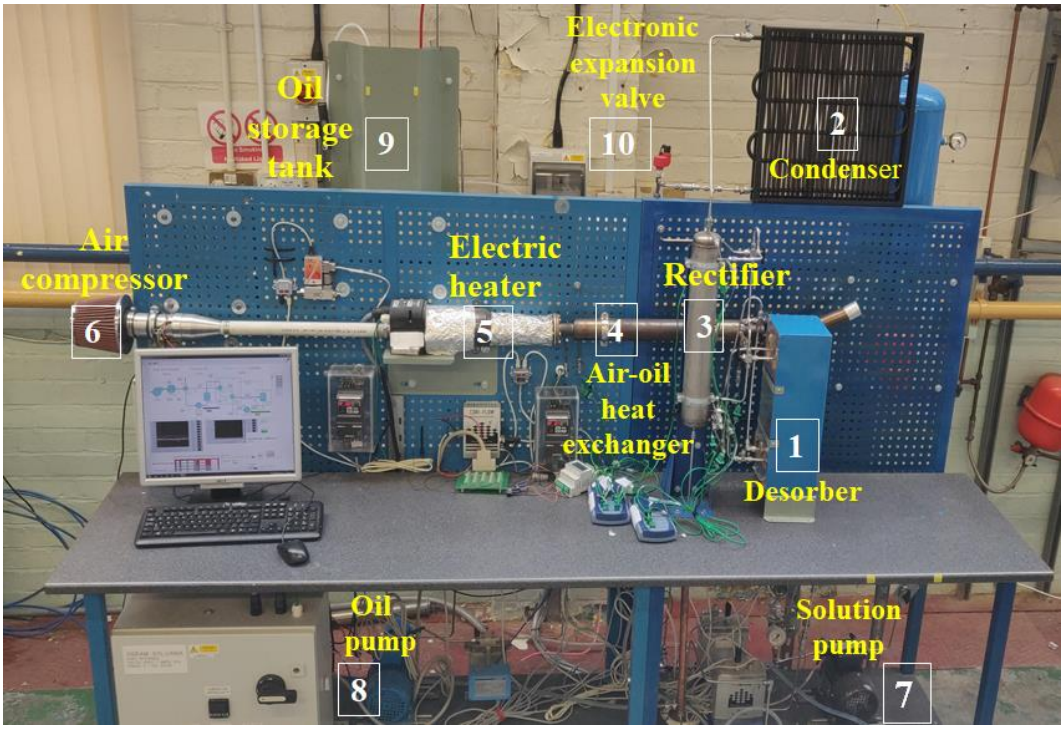

Figure 3-2 : Experimental facility of the simulated SOFC exhaust with VARS.

The solution pump forced the concentrated NH_3-H_2O solution into the desorber via the rectifier where pre-heating of the concentrated NH_3-H_2O solution took place. The pre-heated concentrated NH_3-H_2O solution entered the desorber and absorbed heat from the hot thermal oil. This caused separation of the NH_3 refrigerant vapour from the concentrated ('strong') solution. Due to the high temperature of the desorber (above 100^oC), a small amount of H_2O vapour also evaporated along with the NH_3 vapour and needed to be separated. The H_2O vapour was condensed inside the rectifier by rejecting its heat to the concentrated NH_3-H_2O solution coming from the storage tank through the solution pump. Due to the condensation of water inside the rectifier, only NH_3 refrigerant vapour entered the condenser. High-pressure ammonia vapour rejected heat to the ambient inside the condenser, which converted ammonia vapour to

the liquid phase at the outlet of the condenser. High-pressure liquid ammonia entered the expansion valve where it passed through a small orifice, which caused depressurisation before the ammonia entered the evaporator (Figure 3-3). Low-pressure ammonia evaporated by absorbing heat from the ambient. Ammonia vapour entered the absorber where it mixed with the dilute ('weak') solution coming from the desorber. The dilute solution entered the absorber via an electronic expansion valve where its pressure was reduced. The mixing of refrigerant vapour and dilute solution in the absorber is an exothermic process which releases heat. To maintain a constant absorber temperature and pressure, heat from the exothermic reaction needed to be absorbed by a forced cooling mechanism. However, the absorber in this setup was not integrated with forced cooling, hence heat was rejected from the absorber to ambient only due to natural convection.

Figure 3-3 : Evaporator coil.

NH_3 refrigerant vapour entered the absorber storage tank from the top (Figure 3-4) to avoid immediate mixing of the refrigerant vapour with the solution. If refrigerant vapour were allowed to enter from the bottom, a rapid exothermic reaction could have occurred due to direct mixing of refrigerant vapour with the solution which might have led to a rapid rise in temperature and pressure due to lack of external cooling of the absorber storage tank. If the

lower side pressure increased to higher than 3 bar, the targeted sub-zero evaporation temperature could not be achieved. Therefore, the evaporator outlet pipe was connected to the top of the storage tank intentionally, although this could result in inefficient mixing of the refrigerant vapour with the solution inside the tank and poor system performance. However, this configuration enabled us to run the experiment of achieving the required evaporation temperature, which was the primary objective of this study.

Figure 3-4 : Absorber storage tank.

The experimental facility was charged with 7.5 L NH_3-H_2O solution with ammonia concentration 33 %.

3.1.1 Description of the system component

An electric heater with capacity of 10 kW manufactured by SYLVANIA was connected to a turbo compressor (supplied by Celeroton with rated power of 1 kW and maximum 55 g/s air mass flow rate). The electric heater required a minimum 44 g/s of air flow rate. The heating element temperature increased above its threshold value of 650°C if the air mass flow was kept

below 44 g/s which automatically turned off the electric heater immediately. Therefore, the airflow rate was always kept at its lowest possible value of 44 g/s. Paratherm-NF thermal oil was chosen as a heat transfer fluid to couple the simulated SOFC exhaust with the absorption refrigeration unit. The maximum recommended operating temperature with the Paratherm NF fluid is 332^{o}C [88]. It was found that the counter-flow heat exchanger configuration with lower oil mass flow rate (<5 g/s) and higher air temperature (> 350^{o}C) might deliver an oil outlet temperature higher than its maximum recommended temperature. Hence, to avoid oil vapour pressure inside the air-oil heat exchanger, a parallel flow heat exchanger configuration was chosen for the air-oil heat exchanger despite its drawback of less efficient compared to a counter-flow configuration. The stainless-steel tube-in-tube exchanger was manufactured by EBZ (series: HX-GW-D1.2-01) had fins attached to the inner tube. Oil flowed through the annulus of inner pipe and air flowed through the outer pipe. A positive displacement type gear oil pump (Tuthill GR20) and magnetically coupled drive diaphragm pump (Tuthill TXS2) were utilised to circulate oil and NH_3-H_2O solution through the system, respectively. The oil pump could deliver a maximum flow rate of 14 g/s with a maximum pressure difference of 4 bar while the solution pump can deliver a maximum flow rate of 40 g/s with a maximum pressure difference of 16 bar.

The desorber was a stainless-steel plate heat exchanger manufactured by Alfa Laval (HP-27-20H) with 20 number of plates. The overall dimensions of the desorber plate heat exchanger were 111 mm × 310 mm. A helical coiled tube rectifier was manufactured by EBZ (HX-GW-D-01). Concentrated NH_3-H_2O solution entered the rectifier, and it absorbs heat from the NH_3-H_2O vapour entering from the bottom. A typical U-shaped stainless-steel tube with aluminium fins was used as a condenser. Geometrical details of the condenser are shown in Appendix A. Condenser was cooled by a desk fan (Igenix-DF1210) which had an air flow of 0.33 kg/s with

power consumption of 30 W. Controllable electronic expansion valves manufactured by Carel (E2V05BS000) were integrated to create the pressure difference across the components of the system. A stainless-steel coil was used as an evaporator as shown in Figure 3-3. Heat was added to the evaporator with a desk fan (Igenix-DF9010) blowing air mass flow of 0.18 kg/s. A 15 L stainless steel storage tank was used as an absorber in the experiments as shown in Figure 3-4. This storage tank could resist maximum pressure up to 15 bar. Thick wall of the storage tank makes heat rejection from the tank to ambient difficult which resulted into elevated absorption temperature and pressure.

The geometrical parameters and CAD drawing of the components are mentioned in Appendix A. A summary of all the system components is shown in Table 3-1.

Table 3-1 : Experimental setup component details.

Component	Manufacturer/Model	Capacity/Characteristics
Turbo compressor	Celeroton	1 kW, 55 g/s of maximum air flow rate
Electric heater	SureHeat MAX SYLVANIA	10 kW, Maximum temperature= 650 °C
Oil pump	Positive displacement type gear pump (Tuthill GR20)	0-14 g/s (maximum pressure difference: 4 bar at full load)
Condenser fan	Igenix (DF1210)	Power consumption: 30 W, air flow: 0.33 kg/s
Evaporator fan	Igenix (DF9010).	Power consumption:15 W, air flow: 0.18 kg/s
Solution pump	Magnetically coupled drive diaphragm pump (Tuthill TXS2)	0 to 40 g/s (maximum pressure difference: 16 bar at full load)
Expansion valves	Carel (E2V05BS000)	480 motor steps
Air to Oil HX	EBZ Tube-in-tube heat exchanger (HX-GW-D1.2-01)	-
Desorber	Alfa Laval AlfaNova (Hp 27-20 H)	-
Rectifier	EBZ helical coiled tube heat exchanger (HX-GW-D-01)	-
Condenser	U-shaped tube bundles with aluminium fins	-
Evaporator	Coiled tube	-
Absorber	15 L storage tank	-

To determine the temperature, pressure, and mass flow rate at different state points of the system, a set of type K thermocouples, mass flow meters, and pressure transducers were installed. Two mini CORI-FLOW™ mass flow meters (M15-AGD-55-0-S Digital) were used to measure the mass flow of the concentrated NH_3-H_2O solution and the dilute NH_3-H_2O solution. The oil mass flow was measured with a Rheonik Coriolis mass flow meter. The pressure was measured in the absorber, desorber, and solution pump utilising a RS-PRO (7975015) electronic pressure transducer. Accuracy of these measurement devices is shown in Table 3-2 .

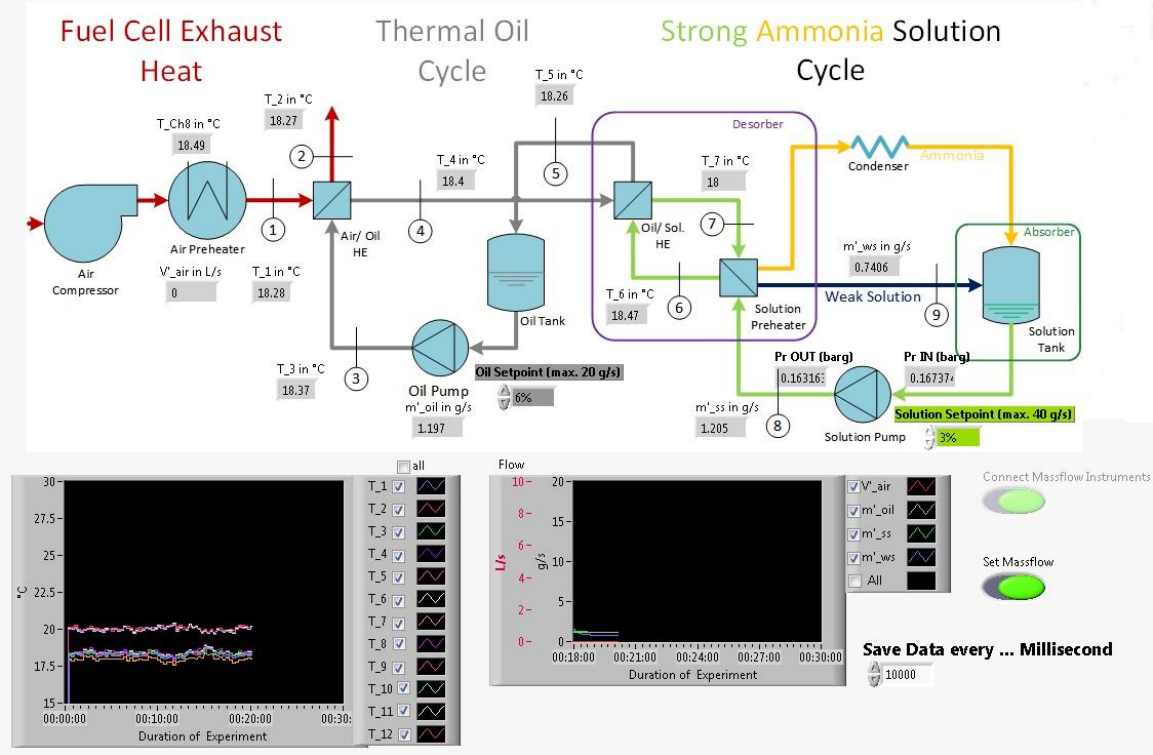

Figure 3-5 : Virtual interface developed in the LabView Software.

The pumps and air compressor were manually controlled by integrating their accompanying software with the LabView software. LabView software enables the operator to develop a virtual interface to control and record experimental data. All signals from various mass flow

meters, thermocouples and pressure transducers were digitally measured by a LabView programmable data acquisition module as shown in Figure 3-5. The sampling frequency was adjusted to 10 Hz and to perform time averaging of the collected data signal. A summary of all the measurement instruments is presented in Table 3-2.

Table 3-2 : Experimental setup component details and measurement instruments specification.

Component	Manufacturer/Model	Capacity/Characteristics
Solution pump	Magnetically coupled drive diaphragm pump (Tuthill TXS2)	0 to 40 g/s (maximum pressure difference: 16 bar at full load)
Mass flow meter	Mini-CORI-FLOW Coriolis (M15-AGD-55-0-S)	0.02 to 45 g/sec, Accuracy: ±0.1 %
Oil mass flow meter	Rheonik Coriolis mass flow meter (RHM03)	0.17 to 20 g/sec, Accuracy :±0.1 %
Pressure transducer	RS-PRO (7975015) Electronic pressure transducer	0 to 25 bar, Accuracy :±0.25%
Thermocouple	Omega® Type-K thermocouple	-200 °C to 1250 °C, Accuracy : ±0.5^{o}C

3.1.2 Component performance analysis

The ammonia concentration in the solution was not measured in the experiments, hence phase quality assumptions were made to determine the ammonia concentration in the solution. The NH_3-H_2O solution was continuously heated along the desorber length, hence two-phase mixture could be assumed along its entire length [77,89,90]. Hence, it was assumed that dilute solution and the ammonia vapour leaving the desorber were in saturated liquid and saturated vapour phase, respectively [77]. With the measured temperature and pressure in experiments

and phase quality assumptions, fluid thermodynamic properties (specific enthalpy and vapour mass fraction) were determined in Engineering Equation Solver (EES). A thermodynamic model was developed in the EES to demonstrate the system performance parameters such as heat load of different components and COP of the system.

3.1.2.1 Oil heat exchanger

In this work, effectiveness (ε) of oil heat exchanger, logarithmic mean temperature difference (ΔT_{lm}), and the overall heat transfer coefficient (U) of the air-oil heat exchanger was computed by eqn.3.1, eqn. 3.6 and eqn.3.7, respectively.

$$\varepsilon = \frac{\text{Actual heat trasfer rate } (\dot{Q})}{\text{Maximum heat transfer } (\dot{Q}_{maximum})} \qquad 3.1$$

The actual heat transfer ($\dot{Q}$) taking place in a heat exchanger can be determined with the help of energy balance of cold and hot fluid as described in eqn.3.2.

$$\dot{Q} = \dot{m}_{cold} c_{p,cold} \left(T_{cold,\,\text{out}} - T_{cold,\,\text{in}}\right) = \dot{m}_{hot} c_{p,hot} \left(T_{h,\,\text{in}} - T_{h,\,\text{out}}\right) \qquad 3.2$$

cold and hot represents cold and hot fluid, respectively.

where,

ṁ	Mass flow of working fluid (kg/s)
c_p	Specific heat of working fluid (Kj/kg K)
T	Outlet temperature of working fluid (ºC)

Maximum possible heat transfer rate depends upon the maximum temperature difference ($T_{maximum}$) in a heat exchanger. The maximum temperature difference is always the difference between inlet temperatures of the hot ($T_{hot,\,in}$) and cold fluid ($T_{cold,\,in}$) which is defined in eqn.3.3.

$$T_{maximum} = T_{hot,\,in} - T_{cold,\,in} \quad (3.3)$$

The fluid with the smaller heat capacity and mass flow will undergo a maximum temperature difference [85]. Hence, $\dot{Q}_{maximum}$ is defined by eqn.3.4.

$$\dot{Q}_{maximum} = (\dot{m}c_p)_{min}(T_{hot,\,in} - T_{cold,\,in}) \quad (3.4)$$

The log mean temperature difference (LMTD) method is one of the widely used method to analyse the heat exchanger performance for steady state conditions [91,92]. The LMTD method predicts heat transfer between hot fluid and cold fluid as shown in eqn.3.5.

$$\dot{Q} = UA\Delta T_{lm} \quad (3.5)$$

where,

A	Surface area of heat exchanger (m^2)
ΔT_{lm}	log mean temperature difference (^oC)

ΔT_{lm} for a parallel flow heat exchanger is expressed as [92,93]

$$\Delta T_{lm} = \frac{(T_{Hot,\,in} - T_{Cold,in}) - (T_{Hot,\,out} - T_{Cold,\,out})}{ln\left[\frac{(T_{Hot,in} - T_{Cold,in})}{(T_{Hot,out} - T_{Cold,out})}\right]} \quad (3.6)$$

$$U = \frac{\dot{Q}}{A\Delta T_{lm}} \quad (3.7)$$

where, A is total heat transfer area (m^2).

The calculation to determine the surface area of air-oil heat exchanger is mentioned in Appendix B.

3.1.2.2 VARS components

To assess the VARS component performance, the mass, species and energy balance equations as shown in eqn.3.8 to eqn. 3.10 were applied between inlet and outlet of each component. Three independent properties were needed to determine the specific enthalpy (h) and other thermodynamic properties of the NH_3-H_2O solution. Temperature (T) and pressure (P) at different state points, concentrated solution mass flow ($\dot{m}_{conc}$) , and dilute solution mass flow ($\dot{m}_{dil}$) was recorded during experiments. The phase quality (q) assumptions were used to get third independent parameter to determine other properties of NH_3-H_2O solution. For saturated vapour and liquid phase, value of phase quality (q) is 1 and 0, respectively. The NH_3 concentration of solution (x) was also used to determine the properties, it represents mass fraction of NH_3 in the NH_3-H_2O solution. Mathematical equations used in modelling to estimate the performance of different VARS components are given in Appendix B.

$$\sum \dot{m}_{in} - \sum \dot{m}_{out} = 0 \qquad 3.8$$

$$\sum \dot{m}_{out}\, h_{out} - \sum \dot{m}_{in} h_{in} = \dot{Q} - \dot{W} \qquad 3.9$$

$$\sum \dot{m}_{in} x_{in} - \sum \dot{m}_{out} x_{out} = 0 \qquad 3.10$$

The COP of the system was defined as the ratio of evaporator heat load ($\dot{Q}_{evp}$) to desorber heat load ($\dot{Q}_{dsrbr}$) which is presented in eqn. 3.11.

$$COP = \frac{\dot{Q}_{evp}}{\dot{Q}_{dsrbr}} \qquad 3.11$$

In the above equation, power required to drive the solution pump was not considered due to its negligible value during experiments.

3.2 Simulation Methodology

In this study, simulation methodology followed a bottom-up approach to match the required refrigeration load demand of different trucks. Hence, end-user demand was identified first, which was followed by the upstream simulation process (VARS and SOFC modelling). The refrigeration demand load was supplied to VARS model to identify VARS performance. The outputs of the VARS model were fed to SOFC model to characterise SOFC system. After formulation all these three models, a combined system performance was assessed to determine performance parameters. This simulation methodology was used to determine the thermodynamic performance, environmental performance and overall performance of the combined system. Figure 3-6 and Figure 3-7 outlines the current methodology to determine the operating envelope for the SOFC system.

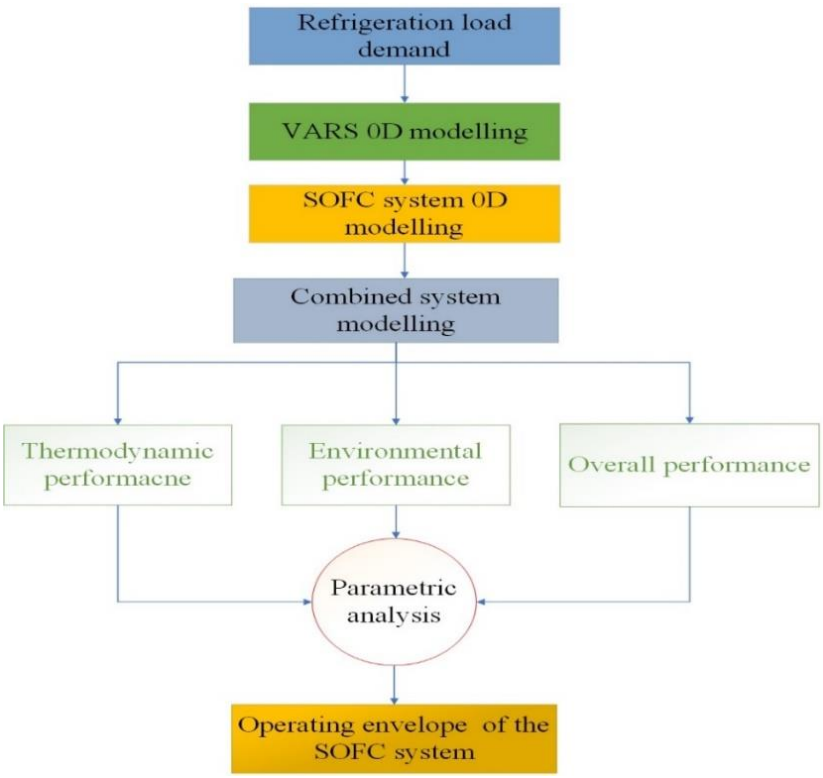

Figure 3-6 : Steady state modelling methodology.

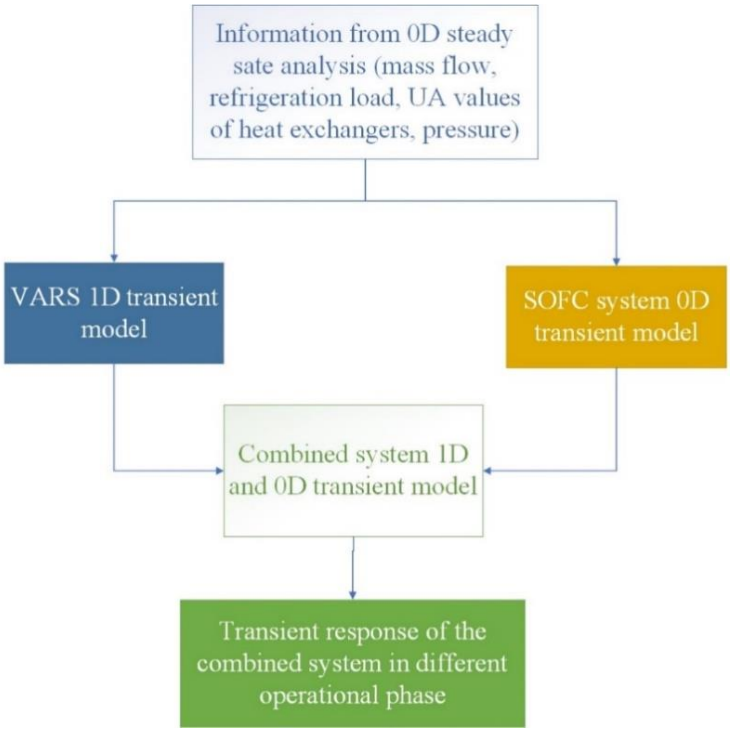

Figure 3-7 : Transient modelling methodology.

3.3 Refrigeration Demand Load Calculation

Refrigeration demand load of the refrigerated vehicles serve crucial input to model the absorption refrigeration system. The SOFC system and absorption refrigeration system operating envelope strongly depends upon the refrigeration load that needs to be satisfied on the refrigerated vehicle. Hence, the first step in the simulation was to compute the refrigeration load requirements. The ASHRAE procedure [94] was strictly followed to determine accurate refrigeration load requirements. The ASHRAE thermal load calculation methodology is mentioned in Appendix C.

This study only considered the frozen transportation application as cooling load for frozen application is always higher compared to chilled transportation. SOFC needs to match the maximum refrigeration demand load. Hence, it was valid to assume frozen transportation

journey only in the study. The setting temperature for frozen transportation was fixed -18ºC [95]. External dimensions needed to determine refrigeration load of the different cabinets are mentioned in Table 3-3[22].

Table 3-3 : External dimensions of different refrigerated cabinet [22].

Type of truck	Length (m)	Height (m)	Width (m)
Large	13.6	2.4	2.6
Medium	9.4	2.4	2.5
Small	2.4	1.57	1.88

3.4 VARS Transient Modelling Methodology

This study considered microchannel heat exchanger based VARS for the simulation. A microchannel heat exchanger with hydraulic coupling fluid demonstrated effective and efficient heat transfer in a compact volume with greater ratio of surface area to volume, and higher heat transfer coefficient [96]. An application of microchannel heat exchanger with hydraulic coupling fluid allows extremely compact components with enhanced thermodynamic performance of the VARS [46,97–100]. Therefore, in this study hydraulic coupling fluid based micro channel heat exchangers are selected to analyse the VARS performance. Condenser and absorber can be coupled to ambient sink (i.e., ambient air HX or radiator) via hydraulic coupling fluid loop. Radiator is one of the existed components of the vehicle architecture (internal combustion engine or electric vehicles). Hence, absorber and condenser microchannel heat exchanger with hydraulic coupling fluid can be coupled to single radiator (or air coupled heat exchanger) to make absorption system greatly compact and efficient. In this work, the SOFC exhaust is coupled with the VARS via a Paratherm NF heat transfer oil circuit. Figure 3-8 shows a schematic of an SOFC exhaust driven VARS.

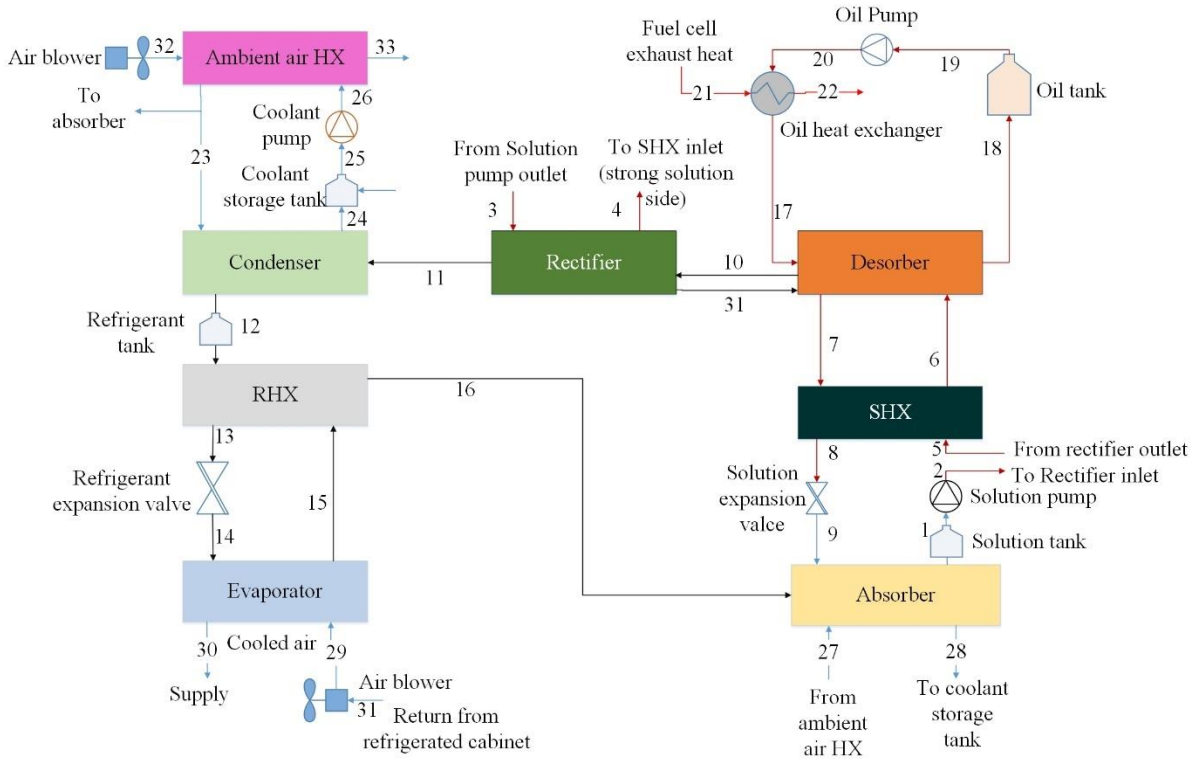

Figure 3-8 : A Schematic diagram of VARS.

The main components of a single stage NH_3-H_2O VARS are desorber, absorber, rectifier, evaporator, condenser, refrigerant heat exchanger (RHX), solution heat exchanger (SHX) and solution pump, as shown in Figure 3-8. The concentrated solution is pumped (2) from the absorber (1) through the SHX (6) to the desorber. Thermal energy is supplied to the desorber (17) to split the NH_3-H_2O binary solution. Ammonia and water vapour enter the rectifier (10) where the ammonia vapour is purified from any traces of water and then enters the condenser (11) where it is liquefied. The condensate is (12) passed through a throttle valve (13) via refrigerant heat exchanger (RHX) to the low-pressure side of the system and in the evaporator (14) absorbs thermal energy from the refrigerated space. The high-temperature and pressurised dilute solution (lower ammonia concentration) flows to the SHX from the desorber (7). SHX facilitates internal heat recovery inside the system by supplying from dilute solution to the strong solution coming from the absorber (8). The low temperature dilute solution enters the

absorber (9) from the SHX where it combines with the ammonia vapour coming from the RHX (16).

This study considered the methodology formulated by Viswanathan [85,89] to build VARS transient 1-D model. There were several assumptions made as follows to build VARS transient model:

1. The heat exchanger performance was assumed adiabatic, heat transfer only takes between working fluids.
2. Changes in potential and kinetic energy were neglected.
3. The pressure drop in the pipelines and components was neglected.
4. The overall heat transfer coefficient remained constant in the heat exchanger.
5. The specific heat of the fluid was assumed constant along the length of the heat exchanger.

It is well known fact that pressure dynamics are rapid compared to that of thermal and mass transfer dynamics. Hence, absorption system components are governed either distinct low side or high-side pressure. Therefore, any change in pressure is immediately communicated to individual heat exchanger. Hence, it is legit to neglect pressure drop between components while carrying out system level analysis, thus avoiding requirement to consider momentum equation in the mathematical modelling. Approximate difference between low side and high side pressure in an absorption system is 12 to 15 bar, hence, frictional drop also been neglected in the mathematical modelling due to its insignificant value. Concentration, pressure, and mass flow rate inside heat exchanger are assumed to be identical (constant) along the fluid flow direction.

3.4.1 VARS heat exchanger modelling

Each heat exchanger was modelled based on discretisation modelling approach, where the heat exchanger was divided into number of interconnected control volume as shown in Figure 3-9. Discretised approach predicts more accurate performance of heat exchanger especially with NH_3-H_2O zeotropic binary mixture [85].

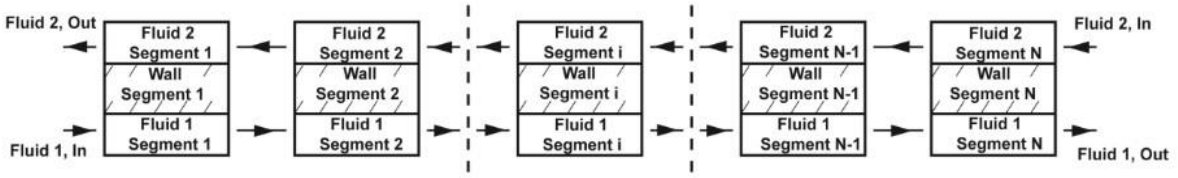

Figure 3-9 : Discretisation of heat exchanger [85].

In this study, each heat exchanger was assumed counter flow, therefore hot and cold fluid entered heat exchanger from opposite direction as shown in Figure 3-9. An individual heat exchanger was divided in three subparts, namely: hot fluid side (hf), cold fluid side (cf), and internal wall (w) between hot fluid and cold fluid. Internal wall was assigned with its thermal capacitance (product of solid mass and heat capacity). The energy conservation equations for hot fluid side, cold fluid side and dividing wall in i^{th} node for a distressed heat exchanger are shown in eqn.3.12 to eqn.3.14.

$$\frac{dU_{hf,i}}{dt} = \dot{m}_{hf}(h_{hf,in} - h_{hf,out}) - \dot{Q}_{hf,i} \quad 3.12$$

$$\frac{dU_{cf,i}}{dt} = \dot{Q}_{cf,i} - \dot{m}_{cf}(h_{cf,out} - h_{cf,in}) \quad 3.13$$

$$(mc_p)_{w,i}\frac{dT_{w,i}}{dt} = \dot{Q}_{hf,i} - \dot{Q}_{cf,i} \quad 3.14$$

where,

U	Specific Internal energy (kJ/kg)
$(mc_p)_w$	Thermal capacitance of wall (kJ/K)
$\dot{Q}$	Heat transfer rate (kW)
$\dot{m}$	Mass flow of fluid (kg/s)
h	Specific enthalpy (kJ/kg)
T	Temperature (K)

Heat transfer rate between hot fluid and wall ($\dot{Q}_{hf,i}$), and wall and cold fluid ($\dot{Q}_{cf,i}$) were determined by eqn.3.15 and eqn.3.16.

$$\dot{Q}_{hf,i} = (UA)_{hf,i}(T_{hf,i} - T_{w,i}) \quad 3.15$$

$$\dot{Q}_{cf,i} = (UA)_{cf,i}(T_{w,i} - T_{cf,i}) \quad 3.16$$

where, A is available heat transfer area on hot fluid and cold fluid side (m^2)

Eqn.3.12 and 3.13 describe the rates of energy stored in hot fluid and cold fluid respectively. Enthalpy values of fluids at inlet ($h_{hf,in}$) and outlet ($h_{hf,out}$) of individual discretised control volume were evaluated using eqn.3.17 and 3.18, respectively [85].

$$h_{hf,in} = h_{hf,i-1} \& \; h_{hf,out} = h_{hf,i} \quad 3.17$$

$$h_{cf,in} = h_{cf,i+1} \; \& \; h_{cf,out} = h_{cf,i} \quad 3.18$$

$\frac{dU_{hf,i}}{dt}$ term in eqn. 3.12 represents the thermal energy stored in the hot fluid. During start-up phase of the VARS, rate of change of energy of hot fluid $(\dot{m}_{hf}(h_{hf,in} - h_{hf,out}))$and the heat transfer from hot fluid to wall ($\dot{Q}_{hf,i}$) are not identical, and this remaining heat transfer difference is the amount of internal energy stored in hot fluid $(\frac{dU_{hf,i}}{dt})$. For cold fluid, $\frac{dU_{cf,i}}{dt}$ term

depicts the amount of internal energy stored when the rate of change of energy of cold fluid ($\dot{m}_{cf}(h_{cf,out} - h_{cf,in})$) and heat transfer rate between wall and cold fluid ($\dot{Q}_{cf,i}$) are not identical during start-up. The difference of heat transfer rate between hot fluid and wall ($\dot{Q}_{hf,i}$), and cold fluid and wall ($\dot{Q}_{cf,i}$) represents the amount of thermal energy stored in the wall ($(mc_p)_{w,i}\frac{dT_{w,i}}{dt}$). Under steady-state conditions of the system, heat transfer across the wall by hot fluid and cold fluid ($\dot{Q}_{hf,i}$and $\dot{Q}_{cf,i}$) are identical, hence amount of internal energy stored in the wall turns into zero.

The relation between internal energy and enthalpy of the fluid is determined by eqn.3.19.

$$U = M(h - Pv) \tag{3.19}$$

where,

M Fluid mass (kg), P Pressure (Pa) and v Specific volume (m^3/kg).

Eqn.3.12 and eqn3.13 can be re-written with the help of eqn.3.19, which are as follows:

$$M_{hf,i}\frac{dh_{hf,i}}{dt} = \dot{m}_{hf}(h_{hf,in} - h_{hf,out}) - \dot{Q}_{hf,i} \tag{3.20}$$

$$M_{cf,i}\frac{dh_{cf,i}}{dt} = \dot{Q}_{cf,i} - \dot{m}_{cf}(h_{cf,out} - h_{cf,in}) \tag{3.21}$$

In this study, pressure loss and volume change of fluid in the component was neglected. Therefore, rate of change of pressure and volume in discretised control volume was always zero, hence it is not mentioned in eqn.3.20 and eqn.3.21.

To solve all above transient equations, several parameters such as heat exchanger wall mass, mass of fluid in discretised control volume, heat transfer coefficient and control volume area were required. Microchannel heat exchangers consist of layer of sheet as shown in Figure 3-10 [77].

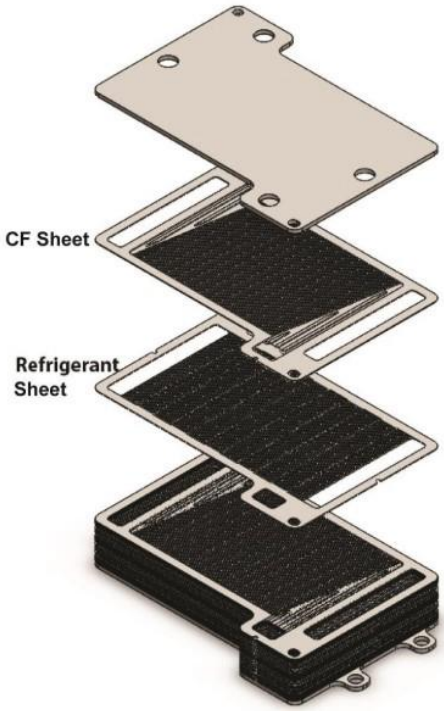

Figure 3-10 : Microchannel heat exchanger assembly [77].

Dilute NH_3-H_2O solution acted as a coupling fluid (CF) for the SHX and liquid refrigerant at higher pressure acted as a coupling fluid for the RHX. Water- propylene glycol mixture acts as a CF for the condenser and absorber. Air is a CF for the evaporator. Paratherm thermal oil is a CF for the desorber.

Important parameters of heat exchanger such as mass of solid wall, heat transfer coefficient, internal fluid volume and thermal conductance were taken from work demonstrated by Goyal [77] is shown Table 3-4.

Table 3-4 : Heat exchanger properties for the VARS [77].

	Parameter	VARS component					
		Evaporator	**Absorber**	**Desorber**	**Condenser**	**SHX**	**RHX**
NH_3-H_2O	Number of sheets	190	80	60	80	80	80
	Fluid volume/sheet (m^3)	2.0E-6	4.4E-6	42.1E-6	2.27E-6	1.5E-6	1.6E-6
	Surface area /sheet (m^2)	0.0072	0.022	0.02	0.0115	0.0074	0.00835
	Heat transfer coefficient (W/m^2 K)	12062	828	5000	3088	4765	265
	Density (kg/m^3)	29	800	800	29	800	29
Coupling fluid (CF)	Fluid volume/sheet (m^3)	2.2E-6	4E-6	7.7E-6	2E-6	1.6E-6	1.4E-6
	Surface area /sheet (m^2)	0.011	0.020	0.032	0.01	0.0084	000074
	Heat transfer coefficient (W/m^2 K)	100	5702	1500	5675	5342	4113
	Density (kg/m^3)	1.225	990	825	990	800	29
Wall	Mass of each sheet (kg)	0.295	0.37	1.16	0.2	0.188	0.188
	Specific heat (kJ/kg K)	0.5	0.5	0.5	0.5	0.5	0.5
	Density (kg/m^3)	8000	8000	8000	8000	8000	8000

In this study, all the heat exchangers were divided into five discretised control volumes. Heat transfer coefficient assumed to be constant for each discretised volume and surface area assumed to be distributed identically between five discretised volumes. A methodology to calculate heat transfer coefficient for NH_3-H_2O solution and coupling fluid can be found in the study carried out by Goyal [77] . Initial amount of stored mass of fluid inside the heat exchanger depends upon the fluid volume of the component and density of fluid, it was determined with eqn.3.22.

$$M_{fluid} = \rho_{fluid} * V_{CV} \qquad 3.22$$

where,

ρ_{fluid} Fluid density (kg/m^3) & V_{CV} Volume of control volume (m^3).

Initial fluid density values are shown Table 3-4. The stored amount of hot fluid and cold fluid inside component was assumed to be uniformly distributed among all the discretised control volumes of the heat exchanger [85]. However, thermal capacitance of fluids and wall was considered while it was neglected for the connecting pipes. Fluid mass storage only considered inside the solution tank and refrigerant tank.

The transient characteristics of electricity driven components such as solution pump and blower were not considered here. In addition, rectifier was also modelled in a steady state condition due to complexity involve to build rectifier transient model [85]. The complexity in the transient rectifier model was presence of the condensation of water droplets, two phase mixture and binary solution. However, as far as system level analysis is concerned, it is fair to assume rectifier modelling as a steady state [85]. Rectifier steady state equations are presented in Table 3-8.

3.4.2 Desorber iterative solver

Desorber was the most complicated component to solve mathematically in the transient model of the VARS. Complexity involved in the desorber can be explained by presence of binary mixture, two-phase mixture, and desorption process. Viswanathan [1] and Venkataraman [4] developed a simplified desorber model for the system level analysis. Hence, a simplified desorber modelling approach was chosen in this study.

Several assumptions were made for the desorber model which are as follows (i) saturated states and phase equilibrium condition were assumed and (ii) thermal capacitance of desorber wall and heated coupled fluid was considered, while it was neglected for NH_3-H_2O solution. In a simplified desorber model, desorber was divided into five discretised control volumes. The

discretised control volume of the desorber is shown Figure 3-11. Energy, mass, and species conservation equations in each discretised volume are presented in Table 3-5.

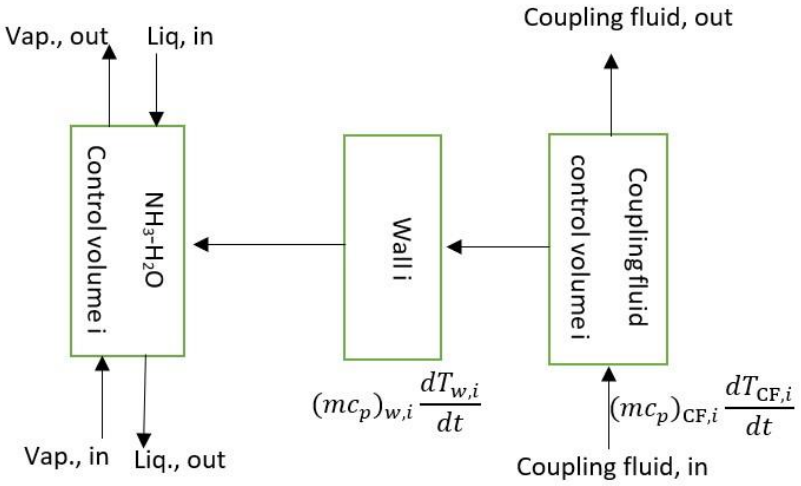

Figure 3-11 : Discretisation of desorber control volume.

Table 3-5 : Equations for transient model of the desorber.

$\dot{m}_{liquid,i} + \dot{m}_{vapour,i} = \dot{m}_{liquid,i+1} + \dot{m}_{vapour,i-1}$
$\dot{m}_{liquid,i}x_{liquid,i} + \dot{m}_{vapour,i}x_{vapour,i} = \dot{m}_{liquid,i+1}x_{liquid,i+1} + \dot{m}_{vapour,i-1}x_{vapour,i-1}$
$\dot{m}_{liquid,i}h_{liquid,i} + \dot{m}_{vapour,i}h_{vapour,i} = \dot{m}_{liquid,i+1}h_{liquid,i+1} + \dot{m}_{vapour,i-1}h_{vapour,i-1}$
$(mc_p)_{CF,i}\frac{dT_{CF,i}}{dt} = \dot{m}_{CF}c_{p,CF}(T_{CF,i-1} - T_{CF,i}) - (UA)_{CF,i}(T_{CF,i} - T_{w,i})$
$(mc_p)_{w,i}\frac{dT_{w,i}}{dt} = (UA)_{CF,i}(T_{CF,i} - T_{w,i}) - (UA)_{liquid,i}(T_{w,i} - T_{liquid,i})$

A further detailed explanation on the desorber iterative solver is mentioned in Appendix D.

3.4.3 Storage tank modelling

The primary function of the storage tanks in the VARS is to maintain fluid inventory that serve as a buffer during transient phase of the system. For transient simulation, storage tanks can also

be treated as a component that governs the pressure of the system [77,85,101]. There are several assumptions were made to model the storage tanks which were as follows:

- Fluid phase at the outlet of the storage tanks was always saturated liquid.
- Vapour and liquid phases were always in thermodynamic equilibrium.
- The fluid inside the storage tank was well mixed.
- The high side and low side pressure of the system were governed by the refrigerant tank and the solution tank, respectively.
- Heat transfer between storage tank and ambient was neglected.

Ammonia concentration, specific internal energy and specific volume of the solution were used in the transient modelling to compute the temperature and pressure of fluids. Mass, concentration, and energy conservation equations as shown in Table 3-6 were applied to storage tanks determine the accumulated mass (m), ammonia concentration (x), and specific internal energy of the fluids (U) inside the storage tank [85].

Table 3-6 : Equations for transient model of storage tanks.

$\frac{dm}{dt} = \dot{m}_{in} - \dot{m}_{out}$
$\frac{d(mx)}{dt} = \dot{m}_{in}x_{in} - \dot{m}_{out}x_{out}$
$\frac{dU}{dt} = \dot{m}_{in}h_{in} - \dot{m}_{out}h_{out}$

Once above three differential equations were resolved for both tanks, high side and low side pressure were determined from NH_3-H_2O property data using three independent parameters, concentration (x), specific volume (v) and specific internal energy (U). The specific volume of the fluid was determined by diving tank volume to accumulated mass in the tank. The equations

to determine pressure and temperature of fluid in the storage tanks are shown in Appendix D. Solution and refrigerant tank properties are shown in Table 3-7.

Table 3-7 : Solution and refrigerant tank properties.

Parameters	**Value**	**Reference**
Solution tank volume (m^3)	0.005	[85]
Refrigerant tank volume (m^3)	0.005	
Mass of solution in solution tank (kg)	1.25	
Mass of solution in refrigerant tank (kg)	1.25	
Initial ammonia concentration in refrigerant tank	0.61	
Initial ammonia concentration in solution tank	0.61	

3.4.4 Expansion valve modelling

Refrigerant mass flow through the expansion valve ($\dot{m}_{refrigerant,valve}$) was computed using a coefficient (C_{valve}) of valve and pressure difference across the expansion valve using eqn.3.23

$$\dot{m}_{refrigerant,valve} = C_{valve} \cdot \sqrt{P_{high} - P_{low}} \quad 3.23$$

The steady state pressure values and mass flow of refrigerant from the steady state were used to determine C_{valve}. The C_{valve} was determined to be 4.2E-6 kg/s $Pa^{0.5}$ for the transient analysis. The expansion valve that connects absorber and SHX was considered as a simple flow valve. It only reduced the pressure without affecting the mass flow of the fluid [85,90].

The radiator (ambient air heat exchanger) is one of the existing components of the vehicle architecture, hence this would not add any additional component on-board. Therefore, this study did not consider transient of the ambient air heat exchanger which is shown in Figure 3-8. The required air flow to radiator/ ambient air HX was determined with the steady state analysis and supplied to the transient model.

3.5 Transient Modelling of Refrigerated Cabinet

To develop a generic transient model to predict the transient performance of the refrigerated cabinet, a zero-dimensional lumped model approach was adopted here. Thermal transient of the refrigerated cabinet was determined by using eqn.3.24.

$$(mc_p)_{RC}\frac{dT_{RC}}{dt} = \dot{Q}_{loss} - \dot{Q}_{evaporator} \qquad 3.24$$

where,

$(mc_p)_{RC}$ Thermal capacitance of the refrigerated cabinet (kJ/K).

T_{RC} Temperature of refrigerated cabinet (K).

$\dot{Q}_{evaporator}$ Heat load of evaporator (kW).

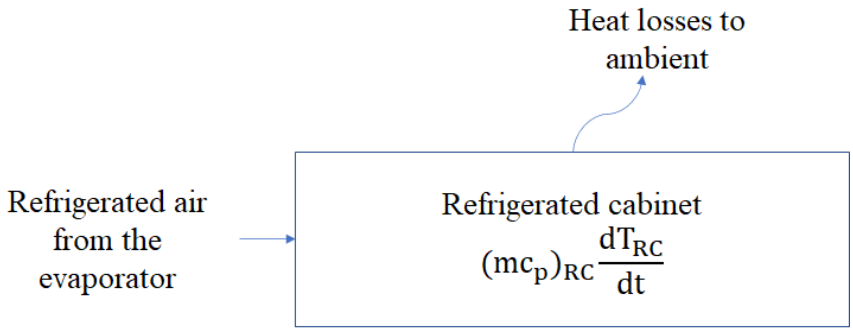

Figure 3-12 : A schematic to predict heat losses in refrigerated cabinet.

Here, $\dot{Q}_{loss}$ is the heat loss from the refrigerated cabinet, which is nothing but refrigeration demand load of the cabinet. It was not easy to determine thermal capacitance ($(mc_p)_{RC}$) of the refrigerated cabinet as it is made from different materials such as fibreglass, polyurethane foam, and wooden and metal localised reinforcement [102]. Artuso et al. [102] carried out detailed transient analysis of refrigerated cabinet with dimensions of 2×3×2 m (H×L×W). Authors have mentioned detailed procedure to determine the thermal capacitance of the refrigerated cabinet.

In this study, thermal capacitance value of the refrigerated cabinet of 632.3 kJ/K was taken from study carried out by Artuso et al. [102].

3.6 VARS Steady-state Methodology

Thermodynamic steady state modelling is required to determine the various performance parameters such as heat exchanger UA values, mass and energy flows at different state point, and COP. Therefore, this section of the chapter represents the steady state analysis methodology of the VARS. In steady-state analysis, mass and energy conservation equations were applied between inlet and outlet of each heat exchanger as shown in eqn.3.8 to eqn. 3.10, respectively. The steady state mass and energy conservation equation for the different components is mentioned in the Table 3-8. The state points in Table 3-8 are according to Figure 3-8 Refrigerant vapour and solution state at desorber and rectifier outlet was assumed saturated in steady state analysis. Also, refrigerant phase at the outlet of condenser and evaporator was assumed saturated liquid and vapour, respectively. The refrigerant and solution storage tanks were neglected in the steady state analysis.

. Table 3-8 : Equations used in steady-state thermodynamic modelling of VARS.

Absorber	$\dot{m}_1 = \dot{m}_{16} + \dot{m}_9$ $\dot{m}_1 x_1 = \dot{m}_9 x_9 + \dot{m}_{16}\, x_{16}$ $\dot{m}_{27} = \dot{m}_{28}$ $\dot{Q}_{absorber} = \dot{m}_1 h_1 - \dot{m}_{16} h_{16} - \dot{m}_9\, h_9$ $\dot{Q}_{absorber} = \dot{m}_{23} c_{p,CF,absorber}(T_{28} - T_{27})$
Desorber	$\dot{m}_6 + \dot{m}_{31} = \dot{m}_{10} + \dot{m}_7$ $\dot{m}_6 x_6 + \dot{m}_{31} x_{31} = \dot{m}_{10} x_{10} + \dot{m}_7\, x_7$ $\dot{Q}_{desorber} = \dot{m}_7 h_7 + \dot{m}_{10} h_{10} - \dot{m}_6 h_6 - \dot{m}_{31}\, h_{31}$ $\dot{m}_{17} = \dot{m}_{18}$ $\dot{Q}_{desorber} = \dot{m}_{17} c_{p,CF,desorber}(T_{17} - T_{18})$

Rectifier	$\dot{m}_{10} = \dot{m}_{11} + \dot{m}_{31}$ $\dot{m}_{10}x_{10} = \dot{m}_{11}x_{11} + \dot{m}_{3l}\,x_{31}$ $\dot{Q}_{rectifier} = \dot{m}_{10}h_{10} - \dot{m}_{11}h_{11} - \dot{m}_{3l}\,h_{31}$ $\dot{m}_3 = \dot{m}_4$ $\dot{Q}_{rectifier} = \dot{m}_3(h_4 - h_3)$
Condenser	$\dot{m}_{11} = \dot{m}_{12}$ $\dot{Q}_{condenser} = \dot{m}_{11}(h_{11} - h_{12})$ $\dot{m}_{23} = \dot{m}_{24}$ $\dot{Q}_{condenser} = \dot{m}_{23}c_{p,CF,condenser}(T_{24} - T_{23})$
RHX	$\dot{m}_{12} = \dot{m}_{13}$ $\dot{Q}_{RHX} = \dot{m}_{12}(h_{12} - h_{13})$ $\dot{m}_{15} = \dot{m}_{16}$ $\dot{Q}_{RHX} = \dot{m}_{15}(h_{16} - h_{15})$
Evaporator	$\dot{m}_{14} = \dot{m}_{15}$ $\dot{Q}_{evaporator} = \dot{m}_{14}(h_{15} - h_{14})$ $\dot{m}_{29} = \dot{m}_{30}$ $\dot{Q}_{evaporator} = \dot{m}_{29}c_{p,CF,evaporator}(T_{29} - T_{30})$
SHX	$\dot{m}_5 = \dot{m}_6$ $\dot{Q}_{SHX} = \dot{m}_{12}(h_5 - h_6)$ $\dot{m}_7 = \dot{m}_8$ $\dot{Q}_{SHX} = \dot{m}_{15}(h_7 - h_8)]$
Solution pump (sp)	$P_{sp} = \frac{\dot{m}_2 v_2\,\Delta P_{sp}}{\eta_{sp}}$ $\dot{m}_1 = \dot{m}_2$
Refrigerant expansion valve (REXP)	$\dot{m}_{13} = \dot{m}_{14}$ $h_{13} = h_{14}$
Solution expansion valve (SEXP)	$\dot{m}_8 = \dot{m}_9$ $h_8 = h_9$
Ambient air HX (ahx)	$\dot{m}_{26} = \dot{m}_{23}$ $\dot{Q}_{ahx} = \dot{m}_{26}c_{p,26}(T_{26} - T_{23})$ $\dot{m}_{32} = \dot{m}_{33}$ $\dot{Q}_{ahx} = \dot{m}_{32}c_{p,32}(T_{33} - T_{32})$
Coolant pump	$P_{cp} = \frac{\dot{m}_{26}v_{26}\,\Delta P_{cp}}{\eta_{cp}}$ $\dot{m}_{25} = \dot{m}_{26}$
Ambient air HX blower (ahxb)	$P_{ahxb} = \frac{\dot{m}_{32}v_{32}\,\Delta P_{ahxb}}{\eta_{ahxb}}$ $\dot{m}_{32} = \dot{m}_{33}$
Evaporator air blower (eab)	$P_{eab} = \frac{\dot{m}_{31}v_{31}\,\Delta P_{eab}}{\eta_{eab}}$ $\dot{m}_{31} = \dot{m}_{29}$

where P Electric power needed to operate a component (kW)

Efficiency and pressure drop for the VARS components are shown in Table 3-9.

Table 3-9 : Efficiency and pressure drop for the VARS components.

Parameter	Value	Reference
Coolant pump efficiency (%)	70	[97]
Blower efficiency (%)	70	[103]
Pressure drop for ambient air HX blower (ΔP_{ahxb}) (kPa)	0.5	[104]
Pressure drop for coolant pump (ΔP_{cp}) (kPa)	5	Design parameter
Pressure drop for evaporator blower (ΔP_{eab}) (kPa)	0.5	[104]

There are two mostly used method to predict the heat exchanger performance, namely: Log Mean Temperature Difference method (LMTD) and effectiveness approach [91] [105]. The effectiveness approach is only valid for the heat exchanger with the single phase as it considers heat capacity rates ($\dot{m}c_p$) of both hot and cold fluid. Heat capacity does not remain constant when fluid phase change takes place inside the heat exchanger. Therefore, heat exchangers (desorber, absorber, condenser and evaporator) with the phase change were solved by LMTD method and heat exchangers (SHX, RHX, and ambient air HX) with single phase were solved by the effectiveness approach [92]. The effectiveness approach is already mentioned in section 3.1.2.1 (eqn.3.1 to eqn.3.4), hence it is not mentioned here. The closest approach temperature (CTA) is one of the crucial input parameters in the LMTD method to determine UA values for heat exchanger. The CTA is defined as the minimum temperature difference between hot fluid and cold fluid at the inlet or outlet, as relevant [46]. The CTA values for the different component of the VARS for the modelling were adopted from the study carried out by Staedter [106] which is shown in Table 5-2. The LMTD (ΔT_{lm}) for the counter-flow heat exchanger is determined using eqn.3.25. The CTA value determined heat load ($\dot{Q}$) and ΔT_{lm} value for individual heat exchanger. Once both these values are determined, UA value was found with eqn.*3.5*. to determine Once the required UA is determined, required surface area (A) was

determined by having known values of heat transfer coefficient (U) as mentioned Table 3-4. The surface area per sheet mentioned in Table 3-4 and total surface area required led to number of sheets required.

$$\Delta T_{lm} = \frac{\left(T_{Hot,\,out} - T_{Cold,in}\right) - \left(T_{Hot,\,in} - T_{Cold,\,out}\right)}{\ln\left[\frac{\left(T_{Hot,out} - T_{Cold,in}\right)}{\left(T_{Hot,in} - T_{Cold,out}\right)}\right]} \quad 3.25$$

The COP of the VARS is the ratio of obtained refrigeration effect in the evaporator to the heat supplied to the desorber and work required to drive the solution pump. eqn. 3.26 represents the COP of the absorption refrigeration system.

$$COP = \frac{\dot{Q}_{evaporator}}{\dot{Q}_{desorber} + P_{sp}} \quad 3.26$$

3.7 SOFC System Modelling

3.7.1 SOFC stack modelling

The electrochemical reactions taking place at anode and cathode are shown in eqn.3.27 and eqn.3.28, respectively [107].

$$H_2 \rightarrow 2H^+ + 2e^- \quad 3.27$$

$$\frac{1}{2}O_2 + 2e^- \rightarrow O^{-2} \quad 3.28$$

Produced oxide ions (O^{-2}) are diffused to the anode from the cathode through the dense electrolyte layer and react with hydrogen ions (H^+) which produces water at the anode interface. The overall electrochemical reaction is shown in eqn.3.29.

$$H_2 + \frac{1}{2}O_2 \rightarrow H_2O \qquad \Delta H^0_{OX}\text{=-241.8 kJ/mol} \tag{3.29}$$

Oxidation of carbon monoxide (CO) at the anode is possible as shown in eqn.3.30 when the SOFC is fuelled with hydrocarbon fuels. However, it is found that electrochemical oxidation of CO is two to five times slower compared to the electrochemical oxidation of H_2 [10] . It facilitates the dominant pathway to rapid WGS reaction to consume carbon monoxide. Thus, the electrochemical oxidation of CO was not considered in this study.

$$CO + O^{2-} \rightarrow CO_2 + 2e^- \tag{3.30}$$

The maximum electrical work generated by the SOFC is determined by computing the change in the Gibbs free energy of the electrochemical reaction (ΔG^0_{OX}) at standard state pressure (1 atmospheric) shown in eqn.3.29. The change in Gibbs free energy of eqn.3.29 is determined by eqn.3.31.

$$\Delta G^0_{OX} = \left(G^0_{H_2O}\right) - \left(G^0_{H_2} + \frac{1}{2}G^0_{O_2}\right) \tag{3.31}$$

where, $G^0$is the standard molar Gibbs free energy (J/mole) which was determined by using eqn.3.32.

$$G^0 = h - Ts \tag{3.32}$$

where,

h Molar specific enthalpy (J/mole),
s Molar specific entropy (J/mole K) and
T Absolute operating temperature (K).

The reversible open circuit voltage (E_0) of the SOFC was determined by computing change in Gibbs free energy (ΔG^0_{OX}) of eqn.3.29 as shown in eqn.3.33 [108]. This is the maximum possible cell voltage without any irreversible losses.

$$E_0 = \frac{-\Delta G^0_{OX}}{n.F} \quad 3.33$$

where,

n Number of electrons transferred in electrochemical reaction (n=2 for eqn.3.29).

F Faraday constant (96485C.mol^{-1}).

V_{Nernst} is the maximum theoretical voltage that can be obtained by fuel cell operation which is determined by eqn.3.34 [70]. It considers a change in Gibbs free energy of the electrochemical reaction, operating temperature, and pressure.

$$V_{Nernst} = E_0 - \frac{R \cdot T}{n \cdot F} \cdot \ln\left(\frac{p_{H_2O}}{p_{H_2} \cdot p_{O_2}^{1/2}}\right) \quad 3.34$$

where,

R Universal gas constant (8.314 J/mole K),

p_{H_2O}, p_{H_2}, and p_{O_2} Partial pressure (bar) of gas species.

The actual SOFC operating voltage is always lower due to irreversibilities and losses that occur during the electrochemical reaction. The actual SOFC operating voltage (V_{cell}) can be determined using eqn.3.35 [109] .

$$V_{cell} = V_{Nernst} - V_{act} - V_{conc} - V_{ohm} \quad 3.35$$

where,

V_{act} Activation loss (V)

V_{conc} Concentration loss (V)

V_{ohm} Ohmic loss (V)

The activation loss (V_{act}) is the summation of anode and cathode activation over potential. Activation polarisation relates to voltage over-potential needed to overcome the activation energy at the catalytic interface. [110]. The activation loss is dominant at lower current density. However, due to the high SOFC operating temperature, the activation loss magnitude is significantly lower compared to concentration and ohmic loss [111]. The concentration loss (V_{conc}) occurs preliminary due to the change in concentration of the reactants during the electrochemical reaction. At a higher fuel utilisation, the concentration loss increases significantly. The Ohmic loss (V_{ohm}) is primarily attributed to resistance to the flow of ions and electrons through the electrolyte, interconnectors, anode and cathode [111].

Mathematical modelling of the operating voltage losses requires anode, cathode and electrolyte material details. In addition, it is also essential to feed various parameters of the cell and material properties such as transport resistance, total electrical resistance, anode, and cathode exchange current density to the simulation tool [112]. All these input parameters vary significantly regarding the type of SOFC assumed in the simulation. In order to build a generic and versatile SOFC system model, it is required to build a model with minimal inputs. The area-specific resistance (ASR) is a standard measuring tool to determine electrochemical system performance. The ASR approach does not need geometrical parameters and material properties [70,113]; hence it is often used for the system-level analysis rather than detailed electrochemical analysis of the fuel cell systems. A typical I-V curve illustrated by Noponen et al [114] (Figure 3-13 (a)) and Lim et al [115] for SOFC operating with natural gas is shown in Figure 3-13 (b). It was observed that the substantial part of the I-V curve is a linear portion which represents the dominancy of the ohmic resistance.

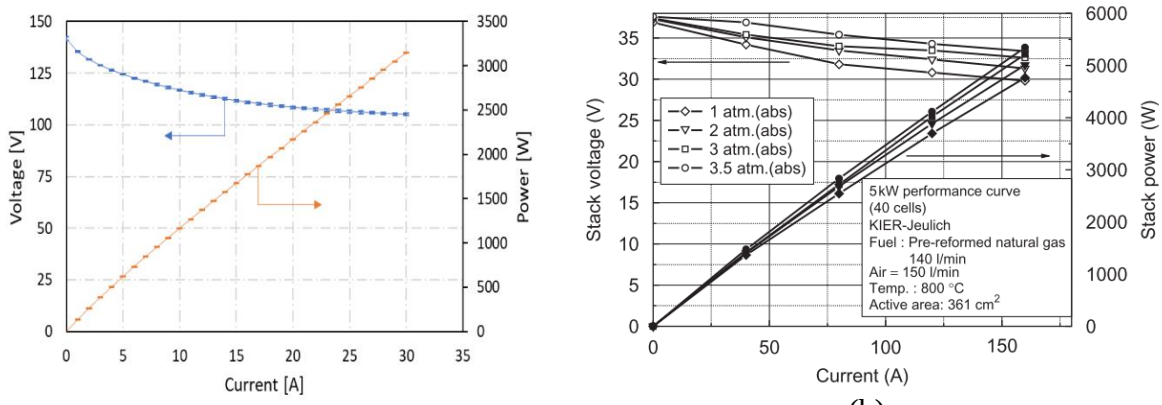

Figure 3-13 : A typical J-V curve for SOFC stack operating with natural gas.

Few literatures also defined ASR as an internal resistance, which can be determined by eqn.3.36 [116,117]. It represents all voltage losses (ohmic, activation and concentration losses) that occurred at the specific operating point and conditions [117]. However, to maintain consistency, internal resistance was defined as an ASR in this study, as shown in eqn.3.36.

$$ASR = \frac{V_{OCV} - V}{j} \qquad 3.36$$

where,

V_{OCV} Open circuit voltage (V) (voltage when no current is being drawn from the cell/stack)

V Operating voltage (V)

j Operating current density (A/cm^2).

There were number of ASR values reported in the literature for SOFC stack which is shown in Table 3-10. The ASR value used in this study is mentioned in sub-section of 5.3.2.2. Cell ASR values are not reported here as Stack ASR values are always higher compared to scaled-up cell ASR values due to additional losses that occur due to interconnects, current collectors, and other components in the current flow path, which are not considered for computing cell ASR values.

Table 3-10 : Different ASR values reported in literature studies.

Stack operating temperature (°C)	**ASR value (ohm/cm^2)**	**Reference**
636	0.8	[114]
800	0.29	[116]
800	0.38	[115]
830	0.5	[118]
850	0.98	[119]
850	0.78	[120]
850	1.19	[121]
860	0.65	[122]

Most literature [68,70,116,123,124] define ASR as a function of temperature. This is due to the remarkable changes in the characteristics of the SOFCs with temperature. Therefore, the ASR is usually implemented as a function of the temperature. The ASR can be linear, exponential or any user-defined function of the temperature. However, eqn.3.37 is widely used to describe the ASR as a function of temperature [68,116].

$$\mathrm{ASR}(\mathrm{T_{stack}}) = \mathrm{ASR_0} \exp\left[\frac{\mathrm{E_A}}{\mathrm{R}}\left(\frac{1}{\mathrm{T_{stack}}} - \frac{1}{\mathrm{T_0}}\right)\right] \quad 3.37$$

$\mathrm{E_A}$ is Activation energy of the electrochemical reaction (0.65 eV) [68], $\mathrm{T_0}$ is Reference temperature (K), $\mathrm{ASR_0}$ is Stack ASR at $\mathrm{T_0}$ reference temperature. $\mathrm{T_{stack}}$ is an average stack temperature (K).

The available cell voltage ($\mathrm{V_{cell}}$) is given by eqn.3.38 [68,116].

$$\mathrm{V_{cell}} = \mathrm{V_{Nernst}} - \mathrm{ASR} * \mathrm{j} \quad 3.38$$

Only three parameters (V_{Nernst}, ASR, and j) are needed to calculate cell voltage using eqn.3.38. Hence, the ASR approach reduces the complexity involved in an SOFC operating voltage. However, the ASR approach is only valid for 80 to 85 % fuel utilisation. This is due to the increased value of the concentration losses with higher fuel utilisation which the ASR approach cannot represent [125]. Therefore, the maximum fuel utilisation was restricted to 80 % in this study.

The next important step in the modelling was to determine the reaction rate of different chemical reactions taking place inside an SOFC. This study considers, SOFC operation with direct internal reforming concept. Methane and steam react in the presence of a nickel catalyst to produce a hydrogen-rich gas mixture as shown in Figure 3-14.

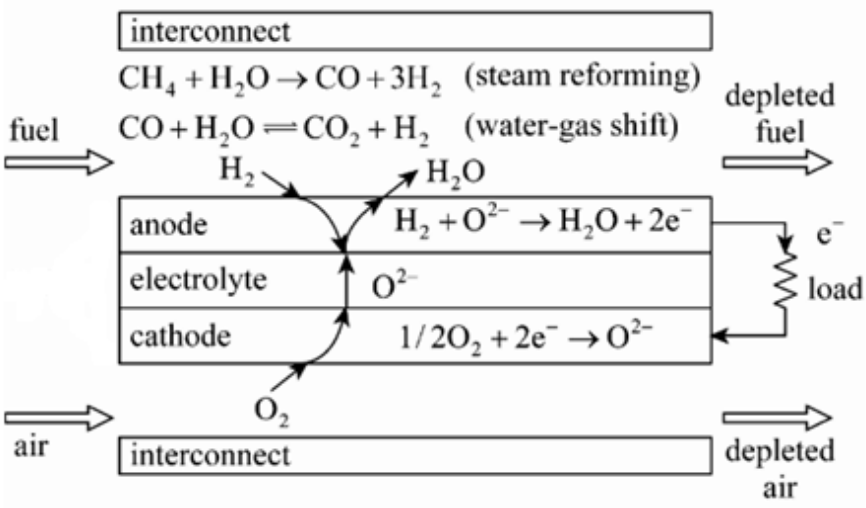

Figure 3-14 : Schematic diagram of SOFC with DIR[73].

The SMR chemical reaction is shown in eqn.3.39. CO is a by-product of SMR which catalytically converts to CO_2 in presence of steam and generates an additional amount of H_2, as shown in eqn.3.40. SMR is an endothermic reaction, and WGS is an exothermic reaction.

The standard enthalpies of formation of both these reactions are shown in eqn.3.39 and 3.40, respectively.

$CH_4 + H_2O \leftrightarrow CO + 3H_2$ (steam methane reforming) $\Delta H^0_{SMR} = 206.1$kJ/mol 3.39

$CO + H_2O \leftrightarrow CO_2 + H_2$ (water gas shift reaction) $\Delta H^0_{WGS} = -41.1$ kJ/mol 3.40

$H_2 + \frac{1}{2}O_2 \leftrightarrow H_2O$ (electrochemical hydrogen oxidation) $\Delta H^0_{OX} = -241.8$ kJ/mol 3.41

The gas concentration in the anode section changes due to simultaneously occurring chemical reactions of SMR, WGS and H_2 oxidation [126]. However, the gas composition of the air in the cathode section only changes due to electrochemical H_2 oxidation as shown in eqn.3.41. It was necessary to determine the reaction rate of SMR, WGS and H_2 oxidation to compute gas composition at the outlet of anode and cathode sections of an SOFC. The reaction rate of the electrochemical H_2 oxidation ($\dot{r}_{ox}$) was determined using eqn.3.42 [127].

$$\dot{r}_{ox} = \frac{I}{2F} \quad 3.42$$

where I Operating current (A)

The most frequent equation used to determine SMR reaction rate ($\dot{r}_{SMR}$) is shown in eqn.3.43 [10,12,128,129].

$$\dot{r}_{SMR} = k_0 p_{CH_4} \exp\left(\frac{-E_A}{RT}\right) A \quad 3.43$$

where,

k_0 Pre-exponential factor (4274 mol/s-m^2 bar).

p_{CH_4} Partial pressure of methane (bar).

A Reforming reaction surface area (m^2).

E_A Activation energy of the SMR (82 kJ/mol)

The above equation only applies to specific nickel-cermet anode material; hence it was not a preferred option for the generic SOFC model. In addition, the 0-D modelling approach cannot accurately predict the CH_4 partial pressure, which may lead to a higher degree of error in the final modelling results. Several works of literature assumed complete conversion of the methane at the anode section of the stack [70,130] while literature sources considered equilibrium conditions for the SMR reaction [109,111,113,127,131–135] to build a 0-D SOFC mathematical model. The SMR reaction rate dramatically relies upon the operating temperature. In this study, the temperature is one of the varying input parameters for the parametric study. Complete conversion of methane may not be a legit assumption under different operating conditions for the parametric analysis. Therefore, the SMR reaction rate is determined with the help of an equilibrium assumption. The WGS reaction is rapid along the anode channel length due to the enhanced activity of the catalyst material at high SOFC operating temperature. Therefore, most literatures [109,111,113,127,131–135] considered equilibrium conditions to determine the WGS reaction rate($\dot{r}_{WGS}$). The equilibrium constant for the WGS and SMR reactions were determined using equations highlighted in Table 3-11.

Table 3-11 : SMR and WGS equilibrium constant equations.

Equations	**Abbreviations**	
$k_{WGS} = \frac{\dot{n}_{CO_2,out,SOFC}\dot{n}_{H_2,out,SOFC}}{\dot{n}_{CO,out,SOFC}\dot{n}_{H_2O,out,SOFC}}$	k_{SMR}	SMR equilibrium constant
$k_{SMR} = \frac{\dot{n}_{co,out,SOFC}\dot{n}^3_{H_2,out,SOFC}}{\dot{n}_{CH_4,out,SOFC}\dot{n}_{H_2O,out,SOFC}}$	k_{WGS}	WGS equilibrium constant
$\ln(k_{WGS}) = \frac{-\Delta G^0_{WGS}}{RT_s}$	ΔG^0_{WGS}	Change in Gibbs free energy of WGS reaction (J/mol)
$\ln(k_{SMR}) = \frac{-\Delta G^0_{SMR}}{RT_{s,}}$	ΔG^0_{SMR}	Change in Gibbs free energy of SMR reaction (J/mol)
	T_s	Stack temperature (K)

The calculations of the molar flow of different gas species at the outlet of an SOFC anode and cathode channels are presented in Table 3-12.

Table 3-12 : Equations to determine molar flow at SOFC outlet.

$\dot{n}_{CH_4 out,SOFC} = \dot{n}_{CH_4 in,SOFC} - \dot{r}_{SMR}$
$\dot{n}_{H_2 Oout,SOFC} = \dot{n}_{H_2 Oin,SOFC} - \dot{r}_{SMR} - \dot{r}_{WGS} + \dot{r}_{ox}$
$\dot{n}_{COout,SOFC} = \dot{n}_{COin} + \dot{r}_{SMR} - \dot{r}_{WGS}$
$\dot{n}_{CO_2 out,SOFC} = \dot{n}_{CO_2 in,SOFC} + \dot{r}_{WGS}$
$\dot{n}_{H_2 out,SOFC} = \dot{n}_{H_2 in,SOFC} + 3\dot{r}_{SMR} + \dot{r}_{WGS} - \dot{r}_{ox}$
$\dot{n}_{N_2 out,SOFC} = \dot{n}_{N_2 in,SOFC}$
$\dot{n}_{O_2 out,SOFC} = \dot{n}_{O_2 in,SOFC} - \frac{\dot{r}_{ox}}{2}$

3.7.2 SOFC stack thermal dynamics

Several assumptions were made in the current study to formulate the SOFC stack/system model as follows:

1. V_{Nernst} is determined by the average partial pressure of gas species (average partial pressure between SOFC inlet and outlet section) and SOFC stack outlet temperature [70].
2. All gases are considered ideal gas mixtures due to lower pressure operation (close to 1 bar) [124].
3. The specific heat of the gases in the fuel cell channel is assumed negligible compared to specific heat of the SOFC components [76].
4. Uniform temperature and current density distribution along all stack directions.
5. Distribution of the gases was assumed uniform in the stack and among the channels in each cell.
6. Radiation heat transfer was neglected.
7. The transient analysis only considered the thermal dynamics, mass dynamics were not considered as they are rapid.

8. This analysis did not consider the transient characteristics of the work-driven components (blowers, pumps).
9. Different sub-components of the stack (anode, electrolyte, cathode and interconnector) possess the same temperature at any instance.
10. Gas crossover between anode and cathode was neglected.
11. Fluid and solid temperatures are identical at the outlet a component.
12. Outlet fluid temperature was considered as the state variable of thermal transient
13. Gas species were considered in chemical equilibrium at the outlet of each system component

Energy conservation equation between SOFC inlet and outlet can be applied by eqn.3.44.

$$\left(mc_p\right)_s \frac{dT_s}{dt} = \sum \dot{n}_i^{in} \int_{T_{ref}}^{T_{in}} C_{p,i}(T)dT - \sum \dot{n}_i^{out} \int_{T_{ref}}^{T_s} C_{p,i}(T)dT - P_{SOFC} - \dot{Q}_{SOFC} - \dot{Q}_{loss} \qquad 3.44$$

$$i = [CH_4, H_2, H_2O, CO_2, CO, O_2, N_2]$$

where,

$C_{p,i}$	Specific heat of the gas species (J/mol K)
$\dot{n}$	Molar flow (mol/s)
T_{in}	Inlet temperature of fluid stream (K)
T_{ref}	Reference temperature (298 K)
$(mc_p)_s$	Thermal capacitance of the stack (J/K)
P_{SOFC}	Electrical power produced by SOFC (W)
$\dot{Q}_{SOFC}$	Heat generated in the SOFC (W)
$\dot{Q}_{loss}$	Heat loss to ambient (W)

In this study, the mass of the SOFC stack and the surface area are taken from the commercially available SOFC stack [4]. The commercially available 3 kW SOFC stack weighs around 30 kg

with dimensions of 190 (W)×230 (L)×280 (H) [4]. The mass and surface area of the stack in the analysis was linearly scaled up according to stack power capacity. The specific heat of the SOFC stack was taken as 500 J/kg K [136].

Exothermic electrochemical and WGS reactions generates excess heat inside the SOFC stack. The endothermic SMR reaction utilises heat produced within the stack, and the remaining heat is absorbed by the gas species flowing inside the SOFC stack. Net generated heat from the electrochemical reaction was defined by eqn.3.45. Values of $\Delta H_{oxidation}$ and ΔH_{WGS} are negative in eqn.3.45.

$$\dot{Q}_{SOFC} = -\dot{r}_{ox}\Delta H_{oxidation} - \dot{r}_{SMR}\Delta H_{SMR} - \dot{r}_{WGS}\Delta H_{WGS} \quad 3.45$$

Electric power generated by SOFC stack is determined by eqn.3.46.

$$P_{electric} = IV_{cell}N_{cell} \quad 3.46$$

where, N_{cell} Number of cells in stack.

Heat losses from the stack to environment was computed using eqn.3.47. Figure 3-15 depicts the temperature profile along the SOFC stack and insulation case during. Usually, it is assumed that the insulation's inner temperature is approximately similar to the stack temperature to make mathematical calculation simple[137]. Conduction heat transfer from the insulation case to outer air is not usually considered due it its negligible value [138,139].

$$\dot{Q}_{loss} = \frac{T_s - T_0}{R_{total}} \quad 3.47$$

where,
T_0 Ambient temperature, and & R_{total} Heat resistance (K/W).

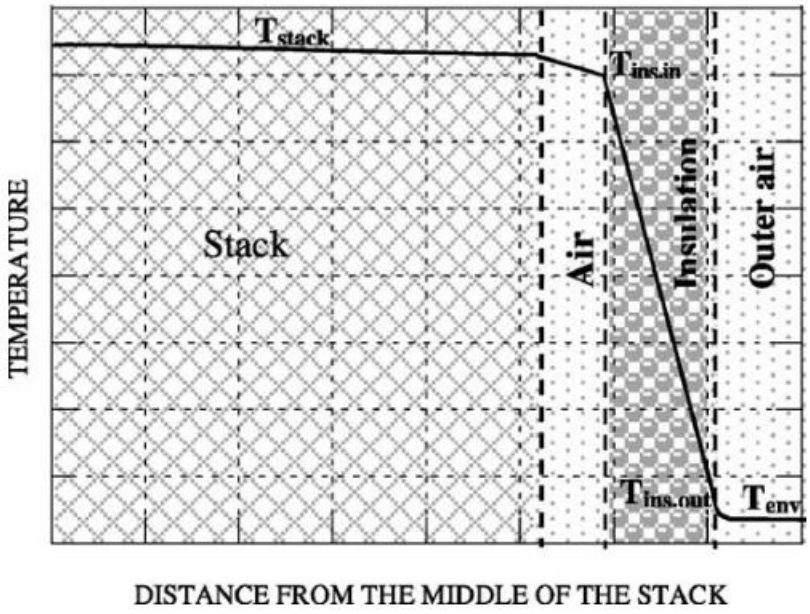

Figure 3-15 : Temperature profile during cool down [138].

Heat losses from stack to ambient encounter two heat resistance: conduction resistance through the insulation case ($R_{insl,wall}$) and convection resistance outside ambient air (R_{conv}). Equations to determine heat loss from the stack is mentioned in Table 3-13.

Table 3-13 : Equations to determine heat loss from the SOFC stack.

Equations	Abbreviations	
$R_{total} = R_{conv} + R_{insl,wall}$	k_{ins}	Insulation thermal conductivity (W/m K)
$R_{conv} = \frac{1}{h_{conv} A_{surf}}$	t_{insl}	Insulation thickness (m)
$R_{insl,wall} = \frac{1}{\frac{k_{ins}}{t_{insl}} A_{surf}}$	A_{surf}	Surface area (m^2)
	h_{conv}	Heat transfer coefficient of outer air (W/m^2 K).

Heat losses from the SOFC stack to the insulation case (outer surface) dramatically rely upon the insulation thermal conductivity and thickness of the insulation material. The ratio of insulation thermal conductivity to thickness is also defined as thermal conductance

(c_{insl}) which was taken as the input parameter for the parametric study. This study is focused on automotive transportation, where fast heat-up is one of the requirements, lower heat loss from SOFC stack makes heat-up of the system faster. Therefore, heat losses should be minimised, which can be achieved with a low value of c_{insl}. In this study, the value is chosen as 0.2 W/m^2 K [139].

The surface area of the burner, CPOX reformer, and heat exchangers was required to estimate the heat loss from the different SOFC system components. The surface area greatly relies on the component dimensions, and there is a lack of data available in the literature for the BoP component dimensions. Therefore, a generic approach was adopted in the study to determine heat loss form BoP components. Cirici [140] determined heat loss from different BoP components as shown in Table 3-14 for the natural gas fuelled 12.5 kW of SOFC system. The heat loss was scaled linearly with reference to the SOFC system power capacity. All hot components of the SOFC system are well insulated, hence heat loss does not vary significantly. Therefore, it was fair to predict the heat loss with linear corelation to system power capacity. This simplified approach was the best choice to develop a generic SOFC system model for a system level analysis.

Table 3-14 : Heat loss in BoP components determined by Cirici [140].

BoP component	Heat loss (W)
Air heat exchanger	134
Fuel heat exchanger	91
Burner	386
Reformer	55

The fuel utilisation (U_F) is a key input parameter to simulate the SOFC system. In this study, the fuel utilisation of the SOFC was defined as shown in eqn.3.48 [10,141].

$$U_F = \frac{\text{moles of fuel reacted}}{\text{moles of fuel supplied}} = \frac{\dot{r}_{ox}}{(4\dot{n}_{CH_4} + \dot{n}_{CO} + \dot{n}_{H_2})_{stack,inlet}} \quad 3.48$$

It is common practice with SOFC operation to feed excess air to the SOFC to absorb heat released by the exothermic reaction. The excess air ratio (λ_{O_2}) determines the amount of excess air supplied to the SOFC, which was calculated by eqn.3.49.

$$\lambda_{O_2} = \frac{\text{Oxyegn moles supplied with air}}{\text{Oxygen moles needed for electrochemical reaction}} = \frac{(\dot{n}_{O_2})_{stack,inlet}}{0.5\dot{r}_{ox}} \quad 3.49$$

Excess air ratio greatly relies upon allowable temperature gain across the SOFC stack. The typical allowable temperature gain across the SOFC stack (dT_{stack}) ranges from 100°C to 150°C. The higher the excess air ratio, the lower the temperature gain across the SOFC stack. SOFC operating point with higher excess air ratio also increases blower power, eventually reducing the SOFC system efficiency.

3.8 SOFC System - BoP Component Modelling

Anode off-gas recycling (AOGR) is most adopted SOFC system layouts [135], as shown in Figure 3-16. The main components of SOFC system layouts are: SOFC stack, air heat exchanger, fuel heat exchanger, air blower, recirculation blower, and oil heat exchanger (for waste heat recovery) to drive the VARS. Methane fuel and air were preheated in the fuel and air heat exchangers via heat extracted from the afterburner exhaust gases. This hot fuel was supplied to the anode and preheated air was supplied to the cathode. A DC current was generated by the electrochemical reaction between air and fuel. The unreacted fuel leaving the anode and the excess air exiting at the cathode are directed towards the afterburner, where

complete combustion takes place, and the exhaust is used to preheat the inlet fuel and air of the SOFC. The AOGR SOFC system recovers super-heated steam from the recirculated anode-off gas mixture. Heshmat and Cordova [142] developed an ultra-high temperature recirculation lower (up to 700°C) for SOFC systems. Therefore, in this study an ultra-high temperature recirculation blower was considered to recirculate the anode off-gas mixture.

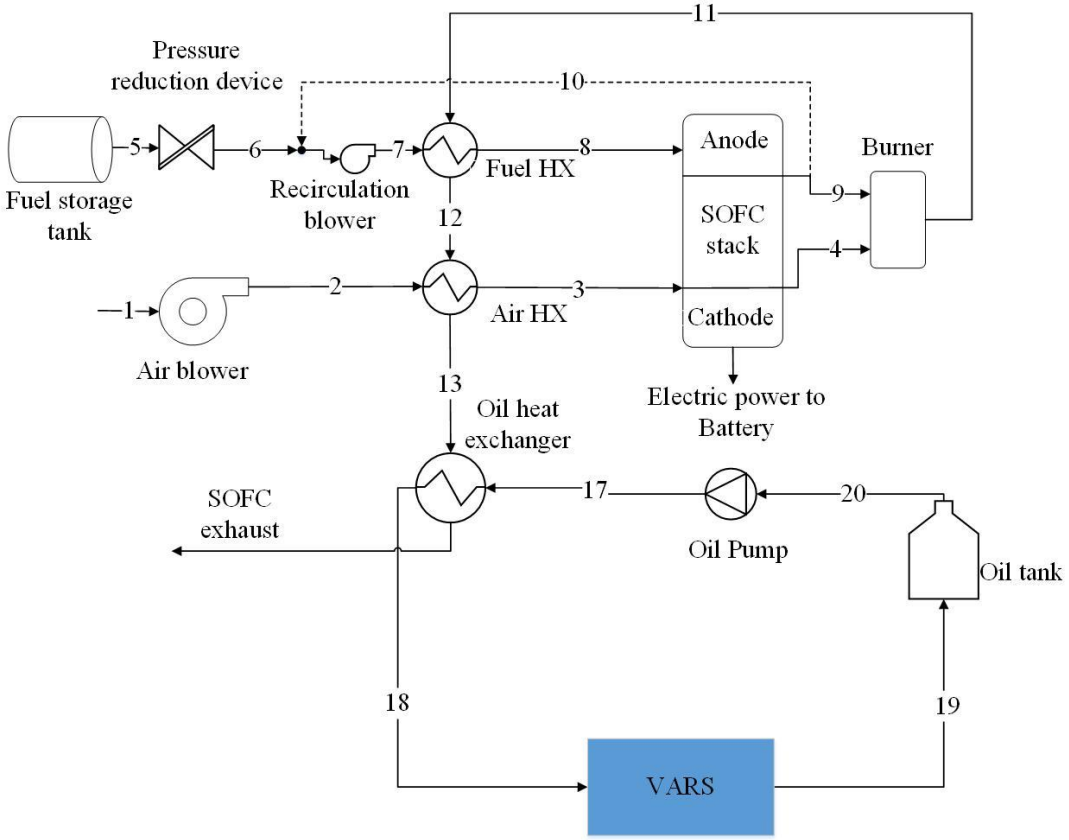

Figure 3-16 : SOFC system with AOGR layout.

The recirculation ratio (RR) was the most important parameters for SOFC AOGR layout. The recirculation ratio is the ratio of molar flow recirculated anode-off gas ($\dot{n}_{recirculated}$) to molar flow of total anode-off gas ($\dot{n}_{anode\ off-gas}$) which is defined by eqn.3.50.

$$RR = \frac{\dot{n}_{recirculated}}{\dot{n}_{anode\ off-gas}} \qquad 3.50$$

The AOGR layout demonstrated several advantages as follows:

1. AOGR provides H_2 fuel at the SOFC anode inlet, which is advantageous, especially with DIR. It generates a uniform current density distribution and minimises the temperature gradient magnitude [141]. In addition, the presence of recirculated H_2 and CO_2 also reduces the risk of carbon formation with DIR SOFC concept [141].
2. Braun [10] concluded that the AOGR system layout with DIR lowered air requirements for SOFC system (up to 7 %). It also reduces the parasitic losses from the SOFC system which improved overall efficiency of the system.

3.8.1 CPOX reformer

The hydrocarbon fuelled SOFC system requires steam for the SMR and WGS reaction. As far as nominal operation is concerned, anode off-gas recirculation provides enough steam for SMR and WGS reactions. However, fresh steam requires during the start-up phase of the SOFC system. It is not feasible to equip SOFC systems with continuous fresh steam supply mechanisms for automotive transportation. As far as the automotive application is concerned, a CPOX reformer is often equipped in the SOFC system to make the SOFC star-up phase water neutral [74,143]. As mentioned in the literature review chapter that the CPOX reformer requires only oxygen and methane to produce a syngas mixture. Therefore, CPOX looks attractive option for SOFC automotive applications. CPOX reformer needs to operate until enough steam is available in the recirculate off-gas to initiate SMR and WGS reaction inside the SOFC stack. Once enough steam would available, the CPOX reformer can be deactivated, and the SOFC stack can operate with DIR. The CPOX reformer is not depicted in Figure 3-16 as CPOX reformer was not activated during nominal operation of the system. More details on CPOX reformer operation are presented in the transient analysis chapter (Chapter 6:).

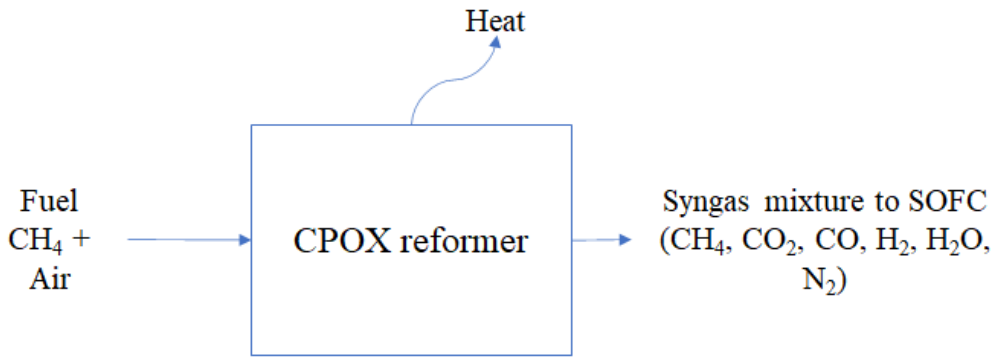

Figure 3-17 : Schematic diagram of CPOX reformer.

A mathematical model was built based on a similar approach as demonstrated by Pukrushpan et al.[144] and Zhu et al. [145]. Various chemical reactions occur inside the CPOX reformer, depending on several input parameters. The essential reactions are highlighted in Table 3-15 with their standard enthalpy of formation values. There are mainly four reactions taking place inside the CPOX reformer, namely (i) partial oxidation of methane (POX) (ii) total oxidation of methane (TOX) (iii) hydrogen oxidation (HOX) and (iv) carbon monoxide oxidation (COX).

Table 3-15 : CPOX reactions [146].

Reaction name	Reaction equation	Enthalpy of reaction
POX	$CH_4 + 0.5O_2 \rightarrow CO + 2H_2$	$\Delta H^0_{POX} = -36$ kJ/ mol
TOX	$CH_4 + 2O_2 \rightarrow CO_2 + 2H_2O$	$\Delta H^0_{TOX} = -802.6$ kJ/mol
HOX	$2H_2 + O_2 \rightarrow 2H_2O$	$\Delta H^0_{HOX} = -483.6$ kJ/mol
COX	$2CO + O_2 \rightarrow 2CO_2$	$\Delta H^0_{COX} = -566$ kJ/mol

The reaction rate of all these different chemical reactions depends upon the CPOX reformer temperature and oxygen-to-carbon ratio (λ_{O2C}) in fuel feed stream. The λ_{O2C} ratio defines the molar ratio of oxygen to CH_4 entering the CPOX reformer. λ_{O2C} was defined using eqn.3.51.

$$\lambda_{O2C} = \frac{\dot{n}_{O_2,CPOX.in}}{\dot{n}_{CH_4,CPOX.in}} \quad 3.51$$

Table 3-16 : CPOX reaction equilibrium constant equations.

$k_{POX} = \frac{\dot{n}_{CO,CPOX.out}\dot{n}_{H_2O,CPOX.out}^{2}}{\dot{n}_{CH_4,CPOX.out}\dot{n}_{O_2,CPOX.out}^{0.5}}$
$k_{TOX} = \frac{\dot{n}_{CO_2CPOX.out}\dot{n}_{H_2O,CPOX.out}^{2}}{\dot{n}_{CH_4,CPOX.out}\dot{n}_{O_2,CPOX.out}^{2}}$
$k_{HOX} = \frac{\dot{n}_{H_2O,CPOX.out}^{2}}{\dot{n}_{O_2,CPOX.out}\dot{n}_{H_2,CPOX.out}^{2}}$
$k_{COX} = \frac{\dot{n}_{CO_2CPOX.out}^{2}}{\dot{n}_{O_2,CPOX.out}\dot{n}_{CO,CPOX.out}^{2}}$
$\ln(k_{POX}) = \frac{-\Delta G^0_{POX}}{RT_{CPOX,ref}}$
$\ln(k_{TOX}) = \frac{-\Delta G^0_{TOX}}{RT_{CPOX,ref,}}$
$\ln(k_{HOX}) = \frac{-\Delta G^0_{HOX}}{RT_{CPOX,ref}}$
$\ln(k_{COX}) = \frac{-\Delta G^0_{COX}}{RT_{CPOX,ref}}$

Most literature studies considered equilibrium conditions to compute the reaction rate of CPOX reactions [144–147]. Therefore, in this study, equilibrium conditions were assumed for all four chemical reactions highlighted in Table 3-15. The equilibrium constant for all four chemical reactions was computed by using equations displayed in Table 3-16.

Molar flow of different gas species leaving the CPOX reformer is presented in Table 3-17.

Table 3-17 : Equations to determine molar flow rate at CPOX reformer outlet.

$\dot{n}_{CH_4,CPOX.out} = \dot{n}_{CH_4,CPOX.in} - \dot{r}_{POX} - \dot{r}_{TOX}$
$\dot{n}_{CO,CPOX.out} = \dot{r}_{POX} - 2\dot{r}_{COX}$
$\dot{n}_{H_2,CPOX.out} = 2\dot{r}_{POX} - 2\dot{r}_{HOX}$
$\dot{n}_{H_2O,CPOX.out} = 2\dot{r}_{TOX} + 2\dot{r}_{HOX}$
$\dot{n}_{CO_2CPOX.out} = \dot{r}_{TOX} + 2\dot{r}_{COX}$
$\dot{n}_{O_2,CPOX.out} = \dot{n}_{O_2,CPOX.in} - 0.5\dot{r}_{POX} - 2\dot{r}_{TOX} - \dot{r}_{HOX} - \dot{r}_{COX}$
$\dot{n}_{N_2,CPOX.out} = \dot{n}_{O_2,CPOX.in}\frac{79}{21}$

Energy conservation equation between CPOX reformer inlet and outlet was applied using eqn.3.52

$$(mc_p)_{CPOX,ref}\frac{dT_{CPOX,ref}}{dt} = \sum \dot{n}_i^{in}\int_{T_{ref}}^{T_{in}} C_{p,i}(T)dT - \sum \dot{n}_i^{out} \times \int_{T_{ref}}^{T_{CPOX,ref}} C_{p,i}(T)dT - \dot{Q}_{CPOX,ref} - \dot{Q}_{loss} \quad 3.52$$

$$i = [CH_4, H_2, H_2O, CO_2, CO, O_2, N_2]$$

where,

$(mc_p)_{CPOX,ref}$ Thermal capacitance of CPOX reformer bed

Heat released by exothermic chemical reactions inside CPOX reformer ($\dot{Q}_{CPOX,ref}$) was determined using eqn.3.53.

$$\dot{Q}_{CPOX,ref} = -\dot{r}_{POX}\Delta H_{POX} - \dot{r}_{COX}\Delta H_{COX} - \dot{r}_{HOX}\Delta H_{HOX} - \dot{r}_{TOX}\Delta H_{TOX} \quad 3.53$$

Holtappels et. al. [148] demonstrated CPOX reformer with weight of 20 kg for the 50 kW of SOFC system The mass of the CPOX reformer was scaled up linearly according to the nominal power of the SOFC system considered in this study. The specific heat of CPOX reformer is taken as 500 J/kG K [136].

3.8.2 Heat exchangers

A zero heat capacity approach was adopted for transient analysis of the heat exchanger [149]. In this approach, the thermal capacitance of the solid heat exchanger is added to the hot fluid side. It was assumed that the change in hot and cold fluid temperature was liner along the heat

exchanger [150]. The energy conservation equations for the hot and cold fluid side are presented in eqn.3.54 and eqn.3.55, respectively [70]

$$\left((mc_p)_{HE} + (mc_p)_{hf}\right) \cdot \frac{dT_{hf,\,out}}{dt} = \dot{m}_{hf} c_{p,hf} (T_{hf,\,in} - T_{hf,\,out}) - \dot{Q} - \dot{Q}_{loss} \quad 3.54$$

$$\left((mc_p)_{cf}\right) \cdot \frac{dT_{cf,\,out}}{dt} = \dot{m}_{cf} c_{p,cf} (T_{cf,\,out} - T_{cf,\,in}) - \dot{Q} - \dot{Q}_{loss} \quad 3.55$$

hf, cf, and HE represents hot fluid, cold fluid, and heat exchanger, respectively.

where,

$(mc_p)_{HE}$	Thermal capacitance of the heat exchanger solid wall (J/K)
$(mc_p)_{hf}$ & $(mc_p)_{cf}$	Thermal capacitance of hot and cold fluid, respectively (J/K)

In this study, the same effectiveness approach was adopted for the counter-flow heat exchanger as mentioned in section 3.1.2.1 (eqn.3.1to eqn.3.4). The effectiveness of the air heat exchanger, fuel heat exchanger and waste heat recovery exchanger (oil heat exchanger) were assumed constant (80 %) for design and off-design system operation [10,16,70]. The weight of air and fuel heat exchangers scaled based on an existing 6.29 kW_{el} capacity SOFC system developed by Whyatt and Chick at the Pacific Northwest National Laboratory as shown in Table *3-19* [151]. The reference value of the oil heat exchanger was taken from the oil heat exchanger specification mentioned in Appendix A. Heat exchangers was made from steel, therefore the specific heat for heat exchanger material was considered 500 J/kg K.

3.8.3 Afterburner

An afterburner generally used to combust unreacted fuel from the anode and convert this to thermal energy. Residual combustible gases from the SOFC anode such as CH_4, H_2 and CO chemically react with O_2 coming from the SOFC cathode in the burner. The afterburner

converts toxic CO into CO_2, reducing the SOFC system's environmental impact when fuelled by hydrocarbons [148,152].

$$CH_4 + 2O_2 \leftrightarrow CO_2 + 2H_2O \quad \Delta H^0_{CH_4-oxidation} = -890.2 \text{ kJ/mol} \quad 3.56$$

$$H_2 + \frac{1}{2}O_2 \leftrightarrow H_2O \quad \Delta H^0_{H_2-oxidation} = -241.8 \text{ kJ/mol} \quad 3.57$$

$$CO + \frac{1}{2}O_2 \leftrightarrow CO_2 \quad \Delta H^0_{CO-oxidation} = -280.8 \text{ kJ/mol} \quad 3.58$$

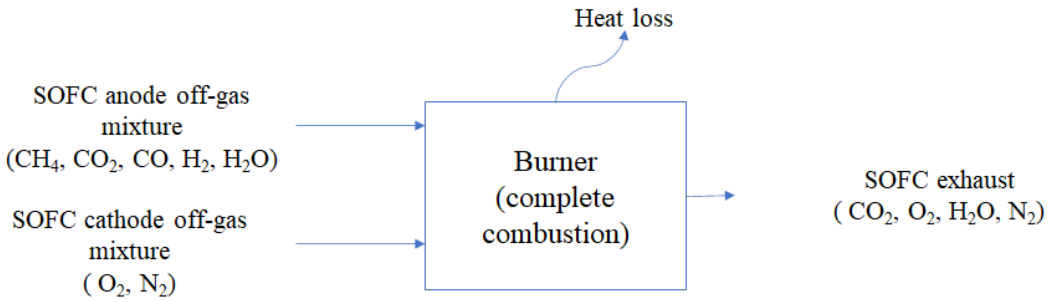

Figure 3-18 : Schematic diagram of burner.

Various exothermic chemical reactions taking place inside the afterburner with their standard value of enthalpy of formation are shown in eqn.3.56 to eqn.3.58. It was assumed that the combustion in the burner is complete and isobaric, implying complete oxidation of residual hydrogen, inlet fuel (methane), and carbon monoxide [153]. It was assumed that no NOx generation take place in the burner. The molar flow rate of gas species at the outlet of afterburner is shown in Table 3-18.

Table 3-18 : Molar flow rate of gas species at afterburner outlet.

$\dot{n}_{H_2O,AB,\text{ out}} = \dot{n}_{H_2O,AB,\text{ in}} + \dot{n}_{H_2,AB,\text{ in}} + 2\dot{n}_{CH_4,AB,\text{ in}}$
$\dot{n}_{CO_2,AB,\text{ out}} = \dot{n}_{CO_2,AB,\text{ in}} + \dot{n}_{CO,AB,\text{ in}} + \dot{n}_{CH_4,AB,\text{ in}}$
$\dot{n}_{O_2,AB,\text{ out}} = \dot{n}_{O_2,AB,\text{ in}} - 0.5\dot{n}_{CO,AB,\text{ in}} - 2\dot{n}_{CH_4,AB,\text{ in}} - 0.5\dot{n}_{H_2,AB,\text{ in}}$
$\dot{n}_{N_2,AB,\text{ out}} = \dot{n}_{N_2,AB,\text{ in}}$

AB stands for afterburner.

Afterburner outlet temperature was determined by applying the energy conservation equation mentioned in eqn.3.59.

$$(mc_p)_{AB}\frac{dT_{AB}}{dt} = \sum \dot{n}_i^{in}\int_{T_{ref}}^{T_{in}} C_{p,i}(T)dT - \sum \dot{n}_i^{out}\int_{T_{ref}}^{T_{AB}} C_{p,i}(T)dT - \dot{Q}_{loss} - \dot{Q}_{AB,ref} \quad 3.59$$

$$i = [CH_4, H_2, H_2O, CO_2, CO, O_2, N_2]$$

$(mc_p)_{AB}$ Thermal capacitance of the burner.

T_{AB} Afterburner temperature.

Heat released by exothermic chemical reactions in burner reformer ($\dot{Q}_{AB}$) was determined using eqn.3.60.

$$\dot{Q}_{AB} = -\dot{n}_{CH_4,AB,\,in}\,\Delta H^0_{CH_4-oxidation} - \dot{n}_{H_2,AB,\,in}\,\Delta H^0_{H_2-oxidation} - \dot{n}_{CO,AB,\,in}\,\Delta H^0_{CO-oxidation} \quad 3.60$$

Holtappels et. al. [148] predicted burner weight of 15 kg for the 50 kW of SOFC system. The weight the burner in the analysis was linearly scaled up according to system power capacity. The specific heat of the burner was assumed to be 765 J/kg K [136].

Table 3-19 : Base value for weight of BoP components.

Element	Base weight (kg)	Scaling	Reference
Air heat exchanger	7.912	Air flow ratio	[151]
Fuel heat preheater	3.33	Fuel flow ratio	[151]
Oil heat exchanger	7	Oil flow ratio	Experimental facility
CPOX reformer	20	System power	[148]
Burner	15	System power	[148]

3.8.4 Air blower and recirculation blower

Electric power consumption (in W) of the air blower and recirculation blower computed via generic equation shown in eqn.3.61.

It required the pressure difference ($\Delta P -$ kPa), volume flow of the fluid ($\dot{V} - m^3/s$) and the isentropic efficiency (η_s) of the component.

$$P = \frac{\dot{V} \cdot \Delta P}{\eta_s} \qquad 3.61$$

In this study, isentropic efficiency of blowers was assumed 70 % [10]. The primary function of the blower was to raise the fluid pressure to overcome the pressure losses in the SOFC system. The value for the pressure drops on the air and fuel side was chosen from several literature references [10,113]. The efficiency of the blower significantly varied under off-design operating conditions. Therefore, a performance map of the blower as shown in Figure 3-19 under various operating conditions can assist in accurately computing SOFC system efficiency[10].

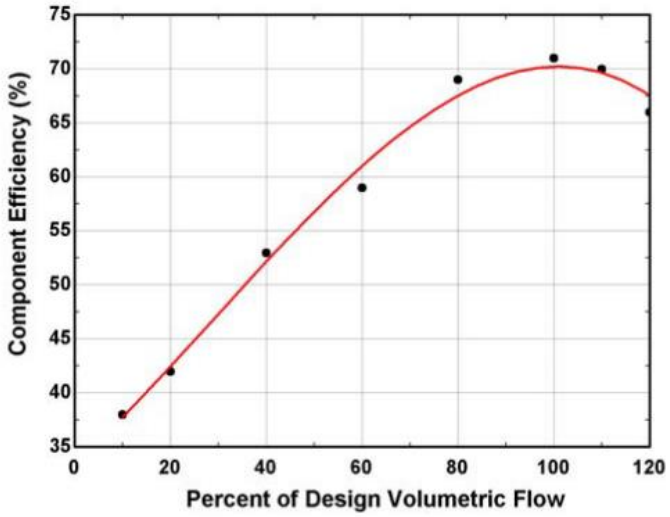

Figure 3-19 : Blower efficiency map[10].

The pressure drop in various SOFC system components for the nominal design operating point were adopted from the study conducted by Little [154] and Braun [10]. These values are

presented in Table 3-20. Component pressure drop values are an approximate estimate; precise pressure drops values estimations require several parameters such as geometrical design, gas velocity, flow rate, etc., which was not the primary focus of this study. A simplified approach was adopted in this study to predict the pressure losses for a generic SOFC system model. The system component pressure drop is proportional to the volumetric fluid flow. The system component pressure drop at different operating points (different volumetric fluid flow) was determined using eqn.3.62 [10] .

$$\Delta P_{component} = \Delta P_{component,design} \cdot \left(\frac{\dot{V}_{gas}}{\dot{V}_{design}}\right)^{\frac{3}{2}} \quad 3.62$$

where,

$\Delta P_{component}$ Component pressure drop (mbar)

$\Delta P_{component,design}$ Component pressure drop at nominal operation (mbar) (Table 3-20).

$\dot{V}_{gas}$ Fluid flow (m^3/s) at off-design conditions

$\dot{V}_{design}$ Fluid flow (m^3/s) at nominal operation point.

It should be noted that the nominal operating point of the system was decided after the detailed system simulation. The nominal operation point represents the value of $\dot{V}_{design}$ for fuel and air flow. Once these values were determined, eqn.3.62 was used to determine the component pressure drop at off-design conditions.

Table 3-20 : SOFC system component pressure drop values[10,154].

Component	Pressure drop (mbar)
Air heat exchanger (hot fluid and cold fluid side)	100
Afterburner	20
Fuel electrode-Stack	20
Air electrode-Stack	30
Fuel heat exchanger (hot fluid and cold fluid side)	50
Piping	5

The steady state equations for the SOFC stack and its BoP components are shown in Table *3-21*.

Table 3-21 : Steady state equations for SOFC system.

Mass conservation	$\sum \dot{m}_{out} = \sum \dot{m}_{in}$
Heat exchanger	$(\dot{m}h)_{hf,in} + (\dot{m}h)_{cf,in} - (\dot{m}h)_{hf,out} - (\dot{m}h)_{cf,out} - \dot{Q}_{loss} = 0$ $\dot{Q}_{hf} = (\dot{m}h)_{hf,in} - (\dot{m}h)_{hf,out}\text{-}\dot{Q}_{loss}$ $\dot{Q}_{cf} = (\dot{m}h)_{cf,in} - (\dot{m}h)_{cf,out}\text{-}\dot{Q}_{loss}$
Afterburner	$\sum (\dot{n}h)_{AB,in} - \sum (\dot{n}h)_{AB,out} - \dot{Q}_{AB} - \dot{Q}_{loss} = 0$
SOFC stack	$\sum (\dot{n}h)_{SOFC,in} - \sum (\dot{n}h)_{SOFC,out} - P_{electric} - \dot{Q}_{SOFC} - \dot{Q}_{loss} = 0$

3.9 System Performance Parameters

Electric power generated by SOFC is also utilised by the BoP components of the SOFC system and VARS auxiliary components. Hence, net electric power ($P_{electric,net}$) from the SOFC system that can be utilised further was determined by using eqn.3.63.

$$P_{electric,net} = P_{electric} - (P_{ab} + P_{sp} + P_{op} + P_{cp} + P_{eab} + P_{rb} + P_{ahxb}) \quad 3.63$$

ab, rb, and op stands for air blower (SOFC system), recirculation blower and oil pump, respectively.

The net electric power density (in W/cm^2) was computed by eqn.3.64.

$$Dens_{elec,net} = \frac{P_{electric,net}}{A_{stack}} \quad 3.64$$

where A_{stack} is active area of stack (cm^2)

Active area of stack is the produce of number of cells (A_{cell}) and area of each cell (N_{cell}) calculated using eqn.3.65.

$$A_{stack} = N_{cell}A_{cell} \quad 3.65$$

The refrigeration power density ($Dens_{ref}$ in W/cm^2) is calculated using eqn.3.66.

$$Dens_{ref} = \frac{\dot{Q}_{evaporator}}{A_{stack}} \quad 3.66$$

The net power density ($Dens_{net}$ in W/cm^2) includes both net electric power density and refrigeration power density and it was computed using eqn.3.67.

$$Dens_{net} = Dens_{elec,net} + Dens_{ref} \quad 3.67$$

The SOFC system efficiency and combined efficiency of the SOFC-VARS system were defined by eqn.3.68 and eqn.3.69, respectively.

$$\eta_{SOFC,system} = \frac{P_{electric,net}}{\dot{Q}_{in}} \quad 3.68$$

$$\eta_{cogeneration} = \frac{P_{electric,net} + \dot{Q}_{evaporator}}{\dot{Q}_{in}} \quad 3.69$$

The energy supplied to the SOFC system can be expressed by eqn.3.70.

$$\dot{Q}_{in} = \dot{n}_{CH_4,in} LHV_{CH_4} \quad 3.70$$

where,

$\dot{n}_{CH_{4,in}}$ Inlet molar flow of methane (mol/s).

LHV_{CH_4} Lower heating value of methane (802.3 kJ/mol).

CO_2 emissions ($kgCO_2/kWh$) from the system are determined using eqn.3.71

$$\text{Emissions} = \frac{\dot{m}_{CO_{2,,SOFC}}}{P_{electric,net} + \dot{Q}_{evaporator}} * 3600 \quad 3.71$$

where, $\dot{m}_{CO_{2,,SOFC}}$ Total mass flow of the CO_2 in the SOFC system exhaust.

The net electrical power to refrigeration power ratio ($Ratio_{EtoR}$) of the combined system was computed using eqn.3.72.

$$Ratio_{EtoR} = \frac{P_{electric,net}}{\dot{Q}_{evaporator}} \quad 3.72$$

Chapter 4: *Experimental Research - Absorption Refrigeration System*

This chapter evaluates the performance of the absorption refrigeration setup. The vapour absorption refrigeration system was powered by the simulated SOFC exhaust via heated oil at the approximate temperature of 180°C to generate sub-zero temperatures in the evaporator. The limitations with the setup are explicitly discussed in this chapter and several recommendations have been made to get the optimised performance from the setup.

4.1 Experimental Procedure

Before supplying heat to the VARS, it was necessary to make sure that all fluids were circulated in the system. The turbo compressor, oil pump and solution pump were turned on successively. Once the mass flow of different fluid streams, and system temperature and pressure were displayed accurately by the LabView virtual interface, the electric heater was activated. The set point temperature in the heater was gradually increased. Steps involved in the start-up process of the experimental facility were as follows:

1. Turn on the required AC and DC power supply to the experimental facility.
2. Connect temperature thermocouples, pressure sensors and mass flow meters to LabVIEW software via the data acquisition module for data logging.
3. Turn on the turbo air compressor, and ramp the turbo compressor rpm at the rate of 10000 rpm/min (recommended by the manufacturer) to its desired value or145000 rpm to get the air flow rate of 44 g/s.
4. Turn on the oil pump and solution pump. The mass flow of oil and aqua-ammonia solution pump was increased in steps of 0.1 g/s to reach the desired mass flow of 12 g/s and 1.2 g/s of oil and NH_3-H_2O solution, respectively.
5. The electric heater was turned on and the set point temperature of the heater was increased by 25^{o}C/min.

The scope of the experiments did not include optimisation of the system performance (such as refrigeration capacity and COP) and perturbation studies. In addition, several components, such as the absorber, condenser, and evaporator were not specifically designed to achieve the best performance, as the experimental setup was rather intended as a proof of concept. The focus

was entirely on achieving sub-zero temperatures and not on the efficiency of the setup. In addition, the primary focus of this study was on the detailed simulation of the SOFC-integrated VARS. Hence, experiments showing the effect of varying input parameters on the protype performance were not included here to focus more on the system simulation results presented in upcoming chapters.

A high degree of fluctuations was observed in the oil pump operation when the pump operated at the maximum flow rate of 15 g/s. This high degree of fluctuations could have led to inaccurate prediction of the system performance. Hence, it was decided to operate oil pump at 12 g/s of oil where the pump demonstrated stable operation. During experiments, it was observed that the NH_3-H_2O solution temperature in the desorber must be above 110°C to achieve the sub-zero evaporation temperature. Hence, several experiments were carried out to determine the NH_3-H_2O flow to the desorber that could achieve temperature higher than 110°C with a pre-fixed 12 g/s of oil mass flow. It was found that the required temperature could only be achieved if NH_3-H_2O mass flow value set to $\leq$ 1.2 g/s. Hence, experimental facility was operated at the maximum feasible 1.2 g/s of NH_3-H_2O solution mass flow, despite the capability of the solution pump to deliver maximum of 40 g/s.

The refrigerant expansion valve and solution expansion valve opening kept constant during the experiments. Several experiments were carried out to determine the possible combination of the refrigerant and solution expansion valve opening to achieve targeted sub-zero evaporation temperature. The system performance variation with refrigerant and solution expansion valves openings were not mentioned here with details, as it did not fit in the scope of the current study. The refrigerant expansion valve and solution expansion valve were kept 12.5 % and 27 % open, respectively. The recorded room temperature during experiment was approximately 23°C.

The oil heat exchanger and VARS transient model were also validated with experimental data in this section.

4.2 Air-Oil Heat Exchanger Performance

The data shown in Figure 4-1 depicts the temperature profile of air and oil in the air-oil heat exchanger. Air flow of 44g/s was heated to 350°C to simulate an SOFC exhaust. This replicated approximately 17 kW of SOFC stack exhaust.

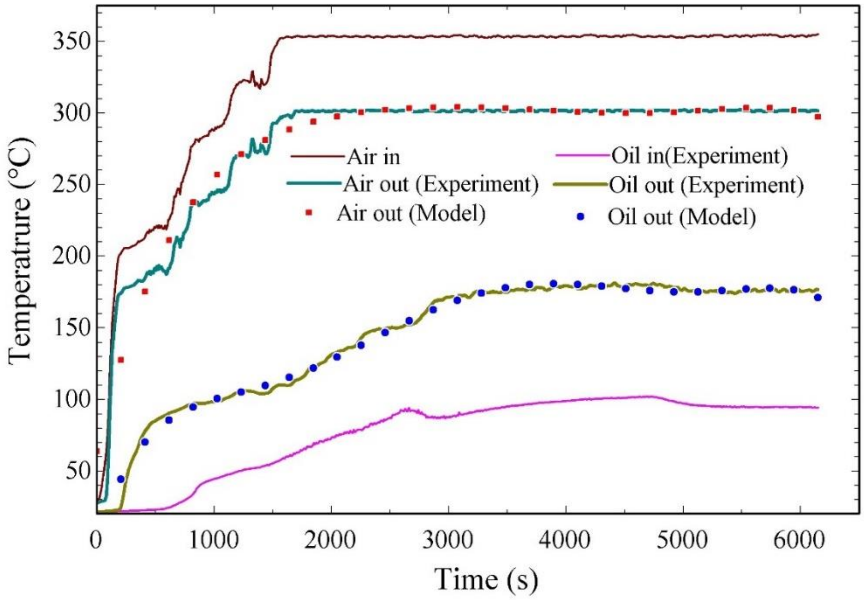

Figure 4-1 : Temperature evolution of the working fluids in the air-oil heat exchanger.

A slight noise can be observed in the heated air inlet temperature profile which was caused by intermittency of the electric heater. It also caused the slight disturbances in the oil and air outlet temperature. Disturbances in the oil inlet temperature were less compared to the oil outlet temperature. It was due to thermal stratification effect in the oil storage tank which smoothen the oil inlet temperature profile. It can be seen from Figure 4-1 that the heated air achieved stable 350°C temperature after 1600 s. Steady state air outlet temperature was recorded around

300°C. Oil inlet and outlet achieved the steady state temperature close to 100°C and 178°C after approximately 3000 s. Hence, oil mass flow of12 g/s gained approximately 78°C in the air-oil heat exchanger. The oil HX model was also validate as highlighted in Figure 4-1. Inlet temperatures and mass flows were inputs for the oil HX transient model. It was found that the model could not replicate the initial transient behaviour (up to 500 s) accurately, however model reproduced comparable transient evolution of temperatures after 500 s.

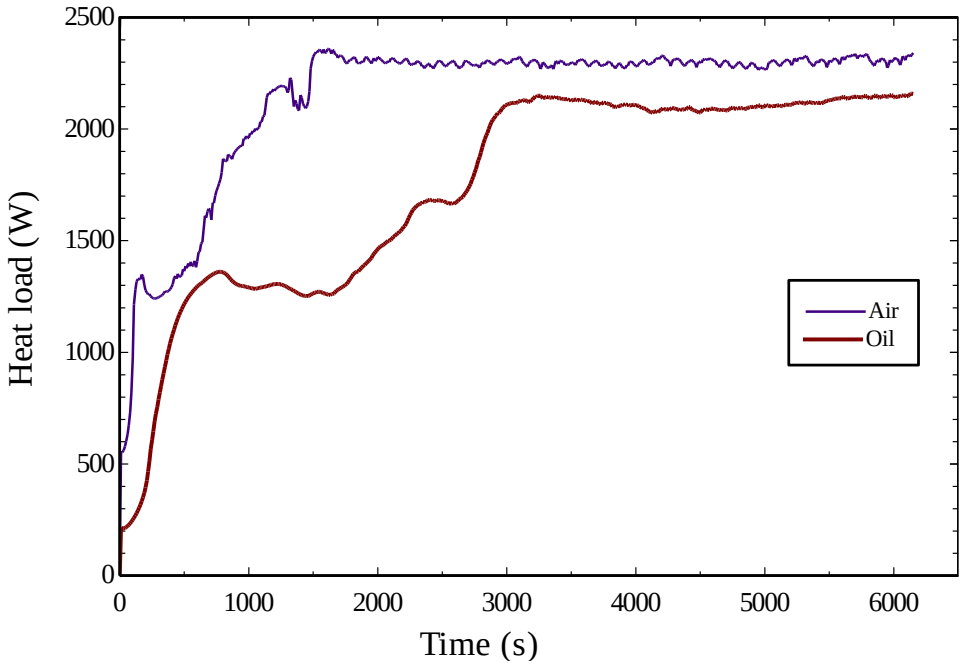

Figure 4-2 : Heat load profile of air and oil in the air-oil heat exchanger.

The heat duty profile of air and oil in the air-oil heat exchanger is shown in Figure 4-2. Air and oil mass were kept constant during experiment; hence, the heat load followed the temperature profile characteristics as shown in Figure 4-1. The steady state heat duty load on air side was determined approximately 2310 W after 2000 s and oil gained steady state heat load of 2170 W after 4000 s. Hence, heat loss from the heat exchanger was determined approximately 140 W.

The steady state performance parameters of the air-oil HX are shown in Table 4-1. It was found that the heat exchanger showed effectiveness of 0.36 under steady state conditions. Overall heat transfer coefficient and LMTD of the heat exchanger were found to be 70 W/m^2 °C and 184°C, respectively. The steady state difference between the air and oil outlet temperature was 125°C which was significantly high, and in response to that effectiveness of the air-oil heat exchanger also reduced significantly to 0.36. This was not a great characteristic for efficient heat exchangers. However, it was completely due to the requirement of high amount of air flow rate (44 g/s) needed by the electric heater as explained in Section 3.1.1.

Table 4-1 : Steady state performance parameters of the air-oil heat exchanger.

Performance parameters	**Value**
Air flow (g/s)	44
Oil flow (g/s)	12
Air inlet temperature (°C)	350
Air outlet temperature (°C)	300
Oil inlet temperature (°C)	100
Oil outlet temperature (°C)	178
Air heat load (W)	2310
Oil heat load (W)	2170
Heat losses (W)	140
Maximum possible heat transfer (W)	6027
Effectiveness	0.36
Overall heat transfer coefficient (W/m^2 °C)	70
LMTD (°C)	184

4.3 VARS -Laboratory Setup Performance

This section discusses the setup performance with the VARS transient model validation. The VARS transient methodology required storage tank details to estimate the high and low side

pressure (section 3.4.3). However, the setup was not equipped with the refrigerant and solution storage tank. Hence, it was not possible to predict the pressure evolution in the protype with the current VARS transient model. Hence, it was decided to feed the high and low side pressure values from the experiment to the model for the validation. In addition, the oil inlet temperature to the desorber and geometrical parameters of the system components (mentioned in Appendix A) were fed to the VARS transient model.

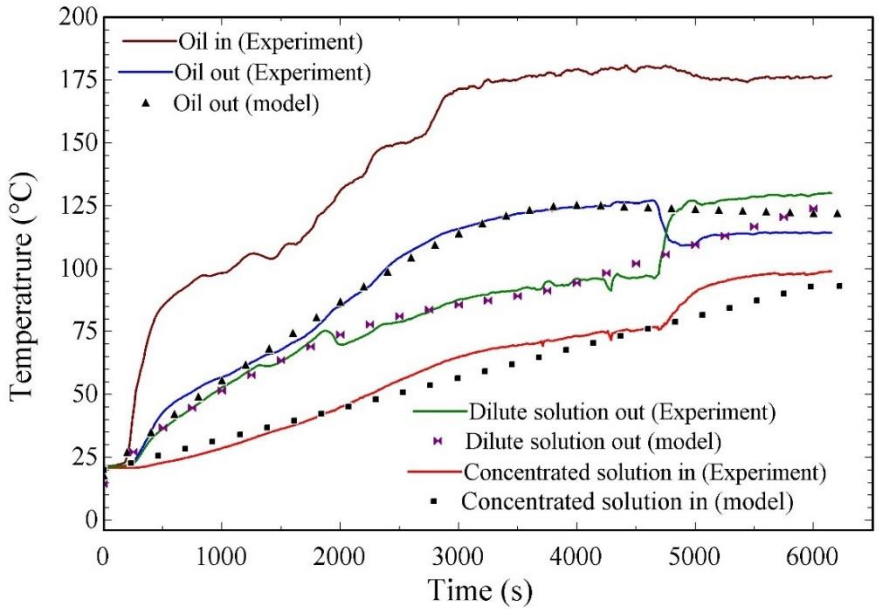

Figure 4-3 : Temperature evolution of the working fluids in the desorber.

The temperature evolution of the working fluids in the desorber is shown Figure 4-3. From t=0 s to t=4700 s, the temperature of dilute NH_3-H_2O solution increased gradually by absorbing heat from the oil, however, after 4700 s solution temperature increased rapidly. The concentrated NH_3-H_2O solution was heated by the thermal oil which boiled the NH_3 refrigerant and a partial amount of water from the solution. The boiling of the NH_3 refrigerant increased its volume, however the cavity volume of the desorber remained the same. As a result, the pressure inside the system increased. Refrigerant vapour formed inside the desorber could not

immediately move to the remaining components, as NH_3 vapour entered storage tank from the top which resulted into inefficient mixing of the NH_3 vapour and solution in the storage tank. The refrigerant vapour that could not move further, receives more heat in the desorber from the thermal oil which increased its temperature even higher, and it converted into superheated vapour. This resulted in reduced oil outlet temperature after 4700 s as shown in Figure 4-3. Therefore, system temperature and pressure increased rapidly which are legible in the Figure 4-3 and Figure 4-5 after 4700 s. The concentrated and dilute solution achieved the steady state temperature of 100°C and 130°C respectively, after 5500 s. The steady state temperature of thermal oil leaving the desorber was recorded approximately 115°C. Hence, temperature difference between oil inlet temperature and dilute solution outlet temperature (closest temperature approach) was observed around 45°C. The closest temperature approach for an efficient desorber performance should be around 25°C [46]. Hence, the desorber closest temperature approach derived for the experimental setup was a bit higher. Oil entered the storage tank at 115°C from the desorber and it entered the air-oil heat exchanger at the temperature of 100°C. It showed that the there was a temperature drop of 15°C in the oil recirculation path, this was due to the lack of insulation in the thermal oil recirculation path.

As far as model validation is concerned, model reproduced the comparable results, However, model was not able to reproduce results with good accuracy after 4000 s due to pressure fluctuations in the system. It was not possible to predict the mixing phenomena of NH_3 refrigerant vapour and liquid solution in the absorber storage tank, which affected modelling validation up to a great extent. Concentrated solution entered the desorber from the rectifier, and the rectifier model was built with the steady-state assumptions, Hence, model reproduced

concentrate solution inlet temperature linearly without any transient effects which can be seen in Figure 4-3.

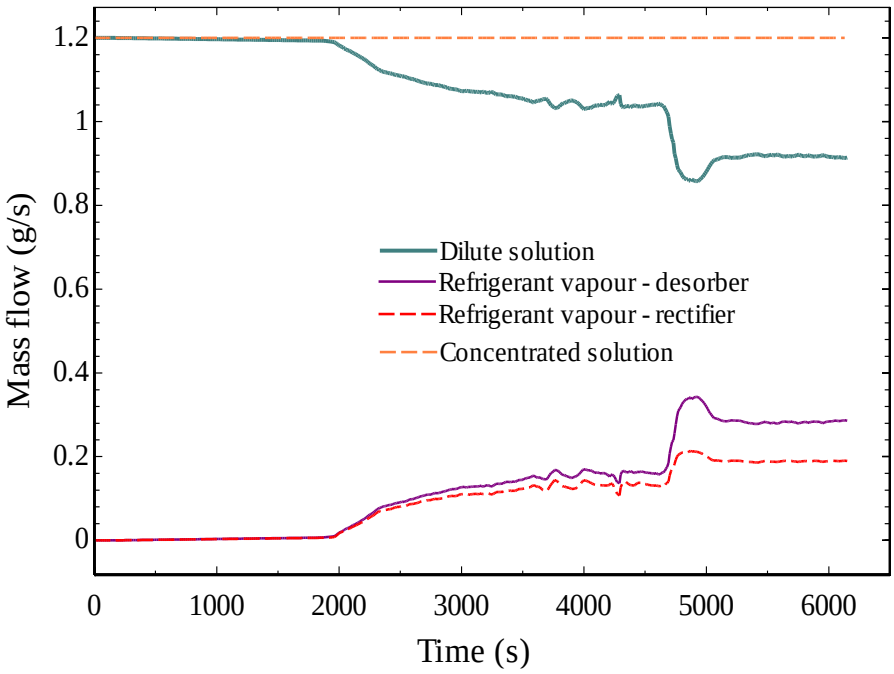

Figure 4-4 : Variation of mass flow in the system.

The variation of the mass flow in the system is shown in Figure 4-4. Up to 2000 s, vapour generation in the desorber was not significant due to lower desorber temperature. The solution pump delivered a constant 1.2. g/s mass flow of concentrated solution. Heat addition in the desorber by thermal oil resulted in separation of the refrigerant vapour from the concentrated solution which increased the vapour mass flow. The vapour mass flow increased gradually from 0 g/s to 0.15 g/s between 2000 s and 4700 s. After 4700 s, the rapid rise in vapour mass flow was observed due to the increased dilute solution temperature from 100°C to 130°C as shown in the Figure 4-3. It was obvious that the dilute solution flow rate decreased with vapour generation in the desorber, hence, variations in dilute solution flow rate depicted exact opposite trend of the vapour mass flow. The steady state value of the vapour leaving the desorber and dilute solution mass flow was 0.3 g/s and 0.9 g/s, respectively. Due to high temperature in the

desorber, water has been evaporated along with the NH_3 refrigerant vapour which needed to be removed before it enters condenser. The removal of water vapour was accomplished in the rectifier. The H_2O vapour condensed in the rectifier by rejecting its heat to concentrated solution coming from the solution pump. The variation of the refrigerant vapour leaving the rectifier is also shown in Figure 4-4. The steady state value of the NH_3 refrigerant vapour mass flow leaving the rectifier was approximately 0.2 g/s.

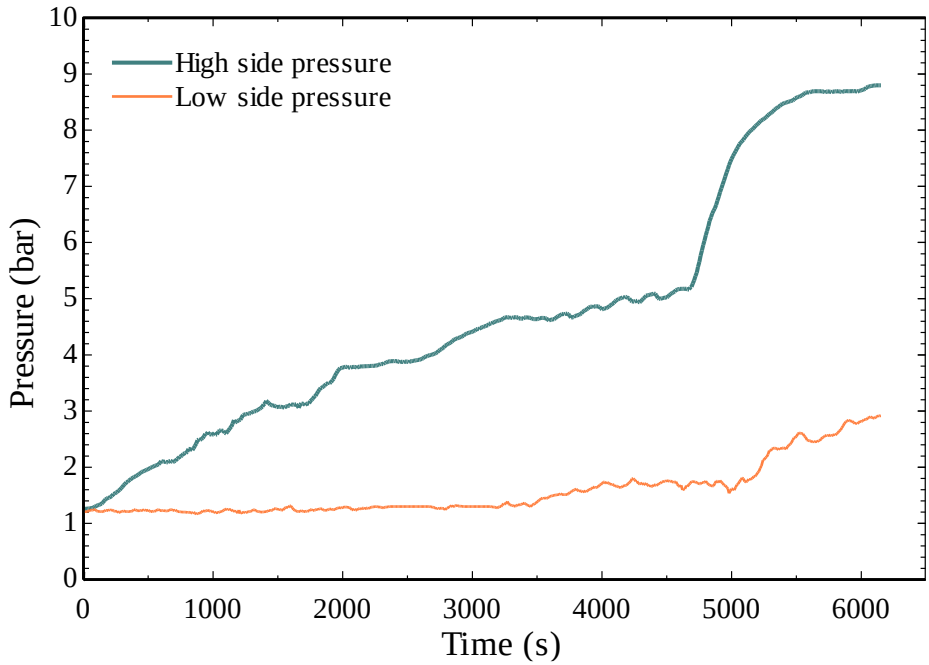

Figure 4-5 : Evolution of high and low side pressure in the system.

The high and low side pressure evolution during experiment is shown in Figure 4-5. These values represent gauge pressure. The system pressure profile depended upon the temperature evolution and vapour generation in the desorber. The high and low side pressure increased from 1.5 bar to 8.8 bar, and 1 bar to 2.9 bar, respectively form 0 s to 6000 s. Vapour generation in the desorber increased the high side pressure. On the other side, low side pressure was predominantly governed by the absorber tank. Low side pressure depicted negligible variation for initial 3500 s due to the inefficient mixing refrigerant vapour and low absorber temperature

shown in Figure 4-6. Low side pressure increased gradually from 1.4 bar to 1.8 bar between 3500 s and 5000 s and then showed quickly escalating behaviour. From 5000 s to 6200 s, the lower side pressure rose rapidly from 1.8 bar to 2.9 bar. High amount of vapour entered absorber tank after 5000 s, which also released greater amount of exothermic heat form the mixing of refrigerant vapour with solution in the absorber tank. As discussed in the previous section, absorber tank was not externally cooled, hence heat could not be absorbed from the absorber effectively, which increased low side pressure and absorber temperature as shown in Figure 4-6.

As shown in the Figure 4-6, absorber temperature increased gradually with high amount of vapour entering the absorber tank. The maximum error observed in the absorber temperature validation was 8°C. The maximum recommended operating temperature with solution pump was 55°C as described by its manufacturer. Hence, if the absorber temperature increased beyond 55°C, the experimental facility needed to be shutdown to avoid any damage to the equipment.

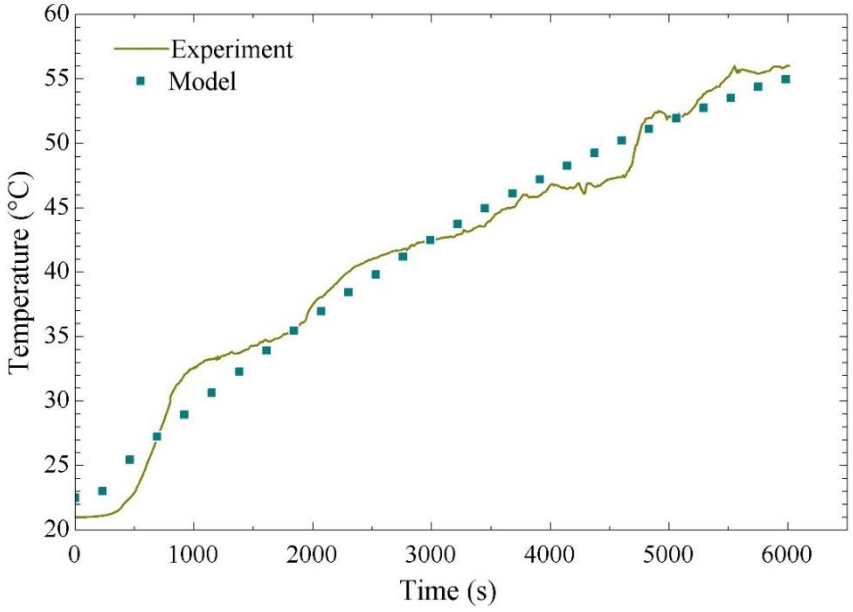

Figure 4-6 : Temperature evolution of NH_3-H_2O solution in the absorber.

The ammonia concentration variation in the system is shown in Figure 4-7. At low desorber temperature, ammonia concentration in the vapour leaving the desorber was found as high as 0.99. This was due to fact that a low amount of water vapour was evaporated. However, with increase in desorber temperature, more water vapour was formed which resulted in a lower ammonia concentration as shown in Figure 4-7. The steady state value of the ammonia concentration in the vapour leaving the desorber was computed as 0.74. The primary reason responsible for this low ammonia concentration was low value of the high-side pressure (< 9 bar). The saturation temperature of water increased at high pressure, hence, if desorber pressure was kept at a high pressure (>14 bar), a lower amount of water vapour would have been evaporated. However, the rectifier improved ammonia concentration from 0.74 to 0.975 under steady state conditions. It was observed that the ammonia concentration decreased from 0.99 to 0.975 in the vapour leaving the rectifier from 2000 s to 5500 s as shown in the Figure 4-7. This was due to the higher amount of water vapour entered the rectifier with increased desorber temperature, and the rectifier could not remove all the water vapour which reduced ammonia concentration. The ammonia concentration in the dilute solution decreased with time evolution, this was due to evaporation of refrigerant vapour from the concentrated solution. Under steady state conditions, the ammonia concentration in dilute solution was determined 0.17. The initial concentration of ammonia in the absorber tank was 33 %, this setup was not equipped with refrigerant storage tank to store the inventory of the refrigerant. Hence, the ammonia concentration in the absorber tank should remain constant at 0.33 value, however it was observed that the ammonia concentration in the absorber was reducing up to 5000 s, and after 5000 s it showed escalating behaviour. Ammonia entered storage tank from the top which resulted into inefficient mixing which reduced the ammonia concentration in the tank. It can be predicted thar the after 5000 s, the top part of the tank was completely occupied with the NH_3 vapour and in started mixing with the solution in the tank effectively, which increased

ammonia concentration in the tank rapidly as highlighted in Figure 4-7. It also caused rapid rise in low side pressure as shown in Figure 4-5.

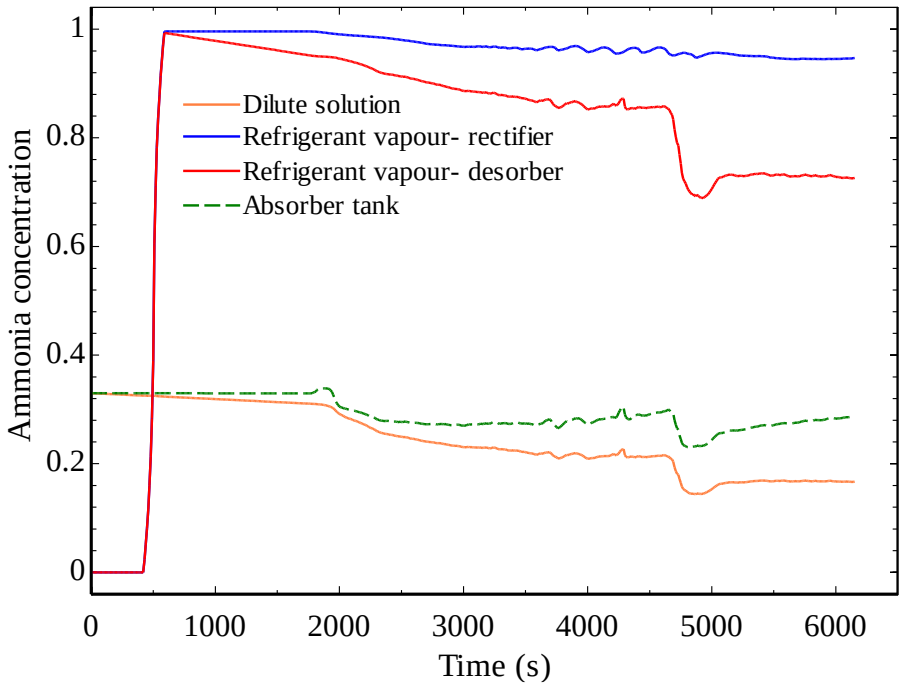

Figure 4-7 : Variation of ammonia concentration in the system.

Figure 4-8 depicts the temperature profile of the NH_3 vapour in the condenser. Under steady state conditions, the refrigerant vapour temperature at condenser inlet was recorded 91°C. The NH_3 refrigerant achieved 27°C of steady state temperature at the condenser outlet. Condenser outlet temperature gradually increased up to 5000 s and then started decreasing over time due to increase high side pressure as shown in Figure 4-5. Due to small temperature difference between refrigerant vapour and ambient temperature during system start-up, inefficient heat transfer in the condenser took place which resulted into higher condenser temperature. This can also be explained by computing vapour mass fraction of the NH_3 refrigerant at the condenser outlet. In Figure 4-9 the variation of vapour mass fraction at the condenser outlet is presented. As shown, NH_3 phase at the outlet condenser was always two-phase mixture with steady state value of vapour mass fraction 0.52. Oscillations were observed in the condenser

outlet temperature between 3000 s and 4500 s. This was due to variations noticed in the refrigerant mass flow as shown in Figure 4-4..

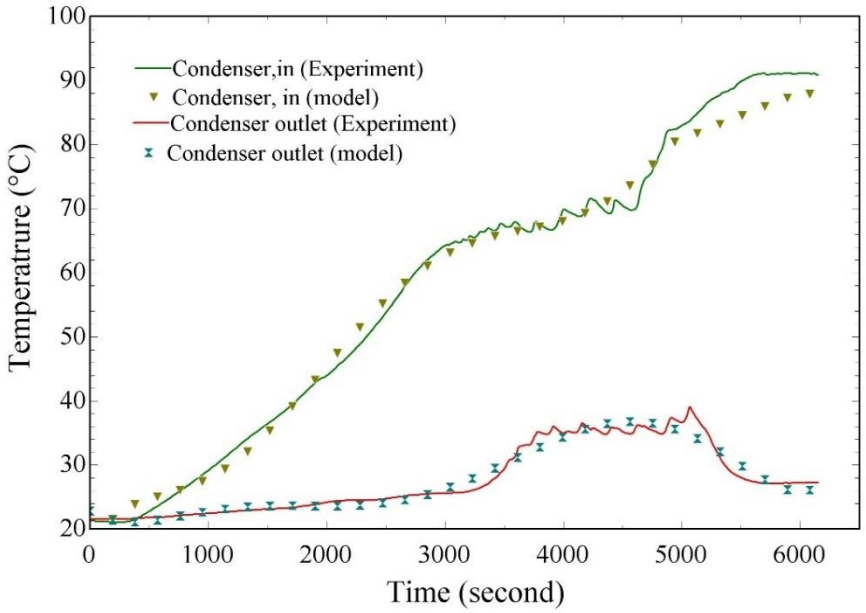

Figure 4-8 : Temperature evolution of the working fluid in the condenser.

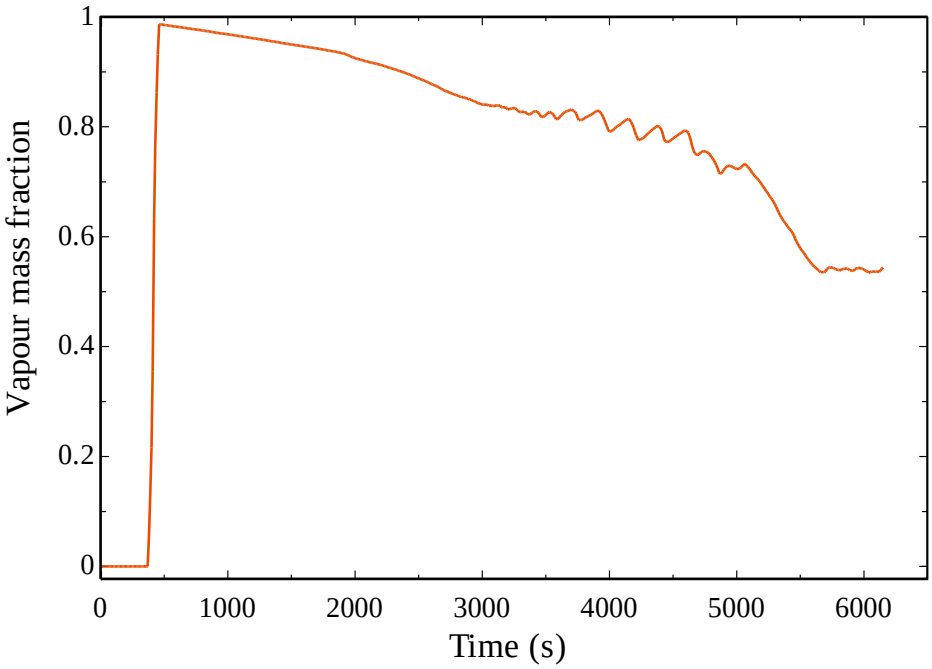

Figure 4-9 : Variation of vapour mass fraction at condenser outlet.

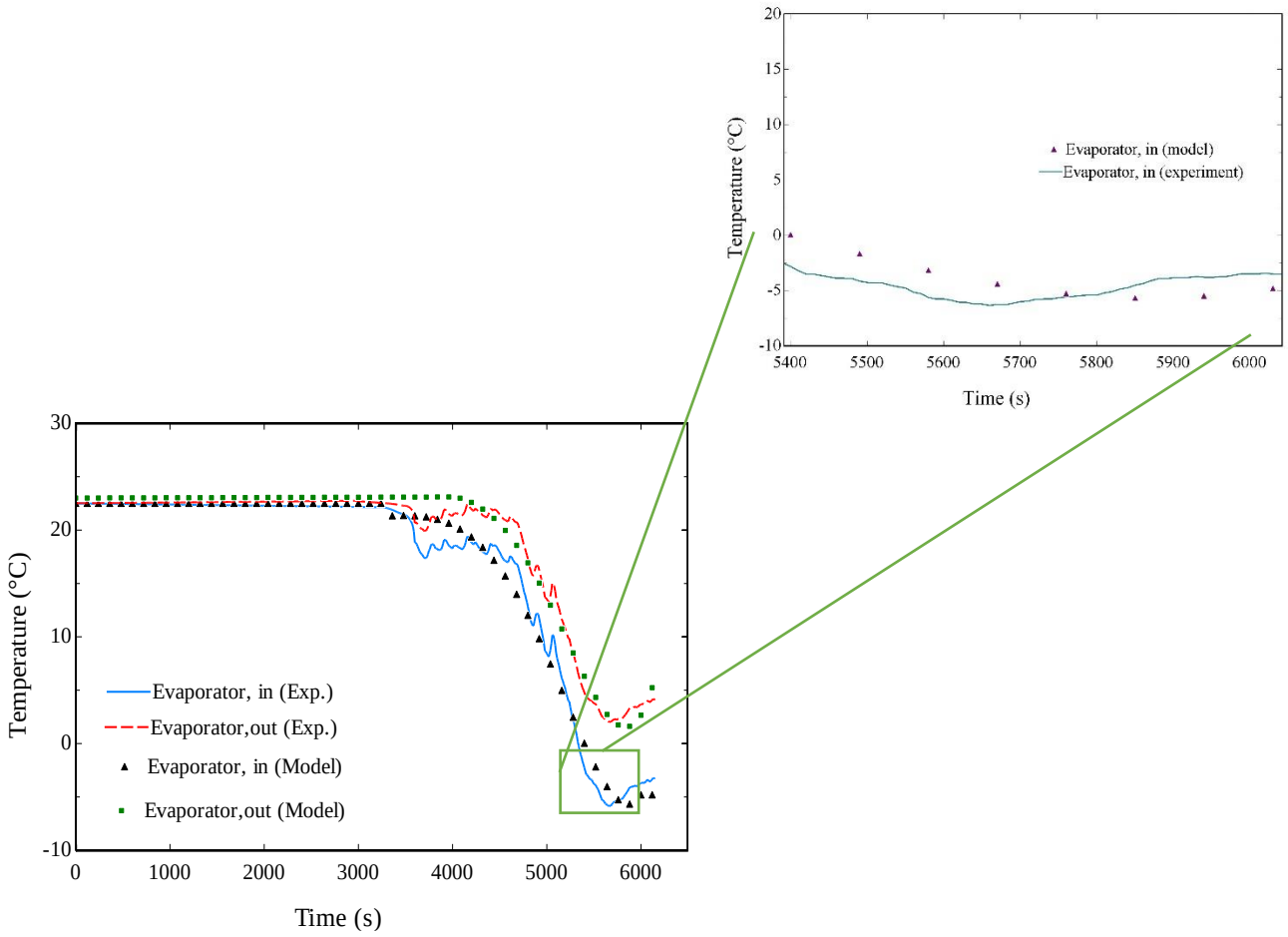

Figure 4-10 : Temperature evolution of the NH_3 refrigerant in the evaporator.

Figure 4-10 illustrates temperature evolution in the evaporator. The evaporator temperature in the system decreased with reduced vapour mass fraction of NH_3 refrigerant at the outlet of condenser. Fluctuations in the refrigeration temperature were observed between 3000 s and 4500 s, due to refrigerant mass flow variation as shown in Figure 4-4. The experimental facility started producing sub-zero temperature after 5200 s. The system was able to maintain temperature below -4°C for continuous 600 s (10 minutes) between 5400 s and 6000s. The system managed to achieve a refrigeration temperature as low as -8°C. To maintain the constant sub-zero evaporator temperature over a longer period, it was required to keep the low side pressure below 2.5 bar by controlling the absorber temperature. However, with this experimental facility, due to lack of external cooling in the absorber it was no possible to

maintain low side pressure below 2.5 bar gauge pressure. Hence, evaporator temperature increased with low side pressure after 6000s.

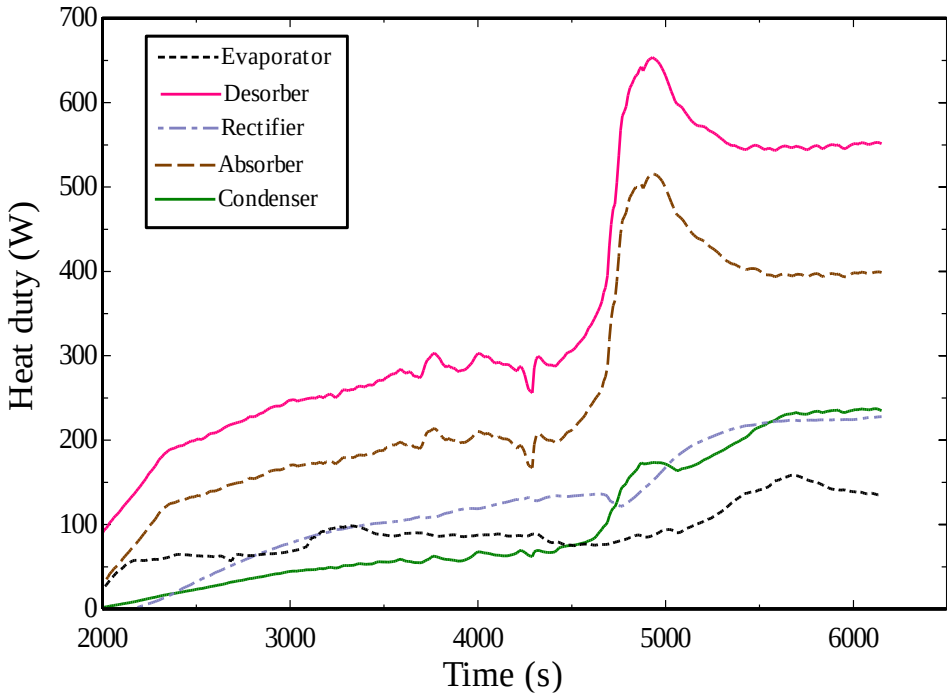

Figure 4-11 : Variation of heat load of experimental setup components.

Heat load variations of different system components are shown in the Figure 4-12. The steady state heat load of desorber, absorber, rectifier, condenser, and evaporator determined were 550 W, 405 W, 210 W, 260 W, and 133W, respectively. Noticeable heat transfer in the system was observed after 2000 s, hence variations of heat load after 2000 s are only depicted in Figure 4-12. A sudden spike was observed in the desorber heat load after 4500 s which was due to the temperature variations in the desorber as shown in the Figure 4-3. The sudden change in the desorber heat load also affected the heat load of remaining components after 4500 s. Due to a small temperature difference between ambient and NH_3 refrigerant in condenser and evaporator during the system start-up, heat load of both these components was low initially. The evaporator heat load increased between 5000 s and 5700 s, it started decreasing after 5700

s. This variation can be explained by evaporator temperature variation as show in Figure 4-10. The evaporator temperature started increasing after 5700 s, which reduced temperature difference in the evaporator resulting into poor heat transfer.

The heat duty of the components could be increased by operating desorber at higher temperature which would have been improved the system performance. However, it should be briefly noted that the system could not operate above 135°C of dilute solution temperature. The desorber temperature at too high temperature caused significant amount of water vapour generation. The rectifier was not able to condense all the water vapour with a such scenario. If the water vapour concentration was too high (> 3% to 5%) in the refrigerant vapour leaving the rectifier, water accumulated in the condenser and evaporator, which might flood the system and could damage the electronic expansion valves. Therefore, desorber was operated at the maximum possible temperature which could deliver sub-zero temperatures.

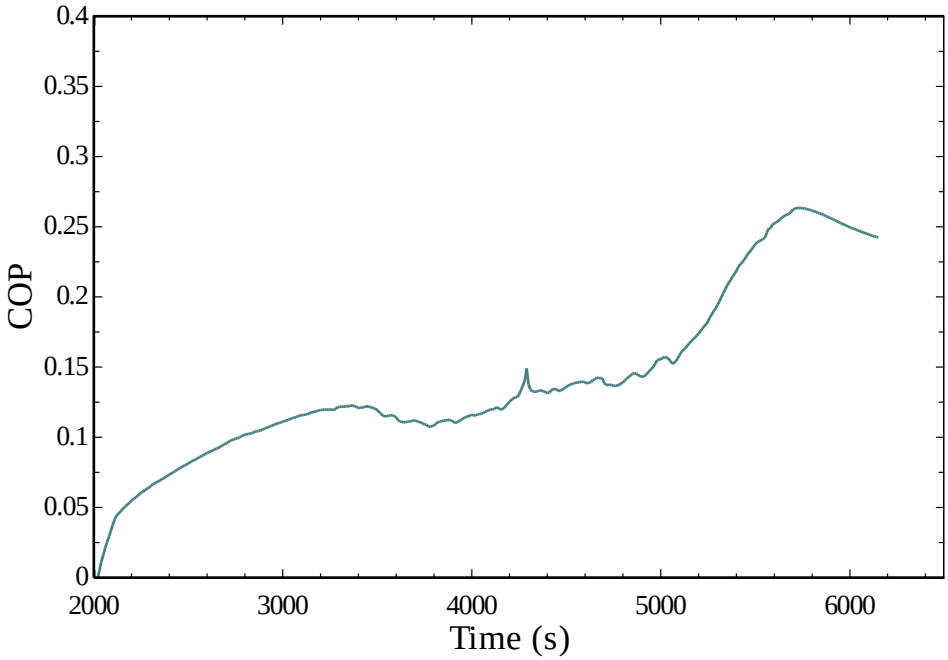

Figure 4-12 : COP variation of experimental setup.

Transient variation of system COP is presented in Figure 4-12. The system COP depends upon the evaporator and desorber heat load (eqn.3.11). Due to a low value of the evaporator heat load during system start-up, COP value was also found to be low. The system depicted peak COP value of 0.25. The COP was significantly lower compared to COP values found in literature (0.5 to 0.6) [13,155,156]. It implied that the system would require several modifications to deliver efficient performance.

4.4 Recommended Modifications

The one of the major problems associated with the experimental facility was the oversized solution pump. During the experiments, the solution pump operated at only three percentage of its full load capacity (maximum flow rate: 40 g/s, delivered: 1.2 g/s), hence it could not establish required pressure drop across the components. The high side pressure in the NH_3-H_2O VARS usually ranges anywhere from 14 to 18 bar. Operation of the NH_3-H_2O absorption refrigeration at increased high side pressure also reduces water vapour generation along with the NH_3 refrigerant. This is due to the increased value of saturation temperature of water at higher pressure. This allows to achieve high ammonia concentration in the stream leaving the desorber and rectifier. Usually, ammonia mass concentration in the stream leaving the rectifier should be close to 1 (at least above 0.99), however, during the experiment it was computed only as 0.975. In addition, the vapour mass fraction at the outlet of the condenser was also found to be higher (0.52 as described in the above section). Usually, phase quality at the outlet of condenser should be saturated liquid (vapour mass fraction is zero). The vapour mass fraction also reduces with high side pressure, hence a VARS should operate at high side pressure to achieve efficient performance. Due to all these issues, system delivered maximum COP of 0.25. In particular, the following components of the experimental setup require modifications as follows:

- Inefficient performance of the oil-heat exchanger was only due to the poor component selection. If the existing 10 kW heater could be replaced with small capacity of 2 kW which can operate with a lower air mass flow (8 to 10 g/s, simulated exhaust of 2.5 kW of SOFC stack), effectiveness of the air-oil heat exchanger can be as high as 0.8.
- The system can be more efficient if the solution pump can generate an adequate pressure lift to raise the higher side pressure up to 15 bar. Hence, system should be equipped with smaller solution pump which can deliver required solution flow (close to 1.2 to 1.5 g/s) at full load.
- The absorber heat exchanger absorber should incorporate a forced cooling mechanism/design. Forced cooling/convection absorber design removes heat effectively and efficiently and helps to restrict the absorber temperature to maintain the low side pressure below 2.5 bar to achieve required evaporator temperature.
- For improved internal heat recovery in the system, it is recommended to equip system with the solution heat exchanger between desorber and absorber. It can reduce external heat input to the desorber which will be resulted into improved COP of the system.

To simulate the possible effect of modifications as mentioned above upon the system performance, a simple comparison between current system performance and system performance after modification is presented in the Table 4-2. The modified values of high side and low side pressure, and the absorber temperature were selected as 15 bar, 2 bar and 42°C, respectively. As shown in Table 4-2, COP of the setup can be improved to 0.51 which would be very close to what has been achieved for the efficient VARS in the literature studies.

Table 4-2 : Comparison between system performance parameters of the current setup and an improved experimental setup.

Performance Parameters	Current system	Modified system
Air flow rate (g/s)	44	8
Simulated exhaust SOFC stack capacity (kW)	17	2.5
Air-oil heat exchanger effectiveness	0.34	0.79
Absolute high side pressure (bar)	9.8	15
Absolute low side pressure (bar)	3.5	2
Evaporator temperature (°C)	-7.5	-19
Absorber temperature (°C)	50	42
Ammonia concentration leaving desorber	0.74	0.9
Ammonia concentration leaving rectifier	0.98	0.9998
Vapour mass fraction at the condenser outlet	0.52	0.015
Desorber heat load (W)	550	1200
Rectifier heat load (W)	210	320
Condenser heat load (W)	260	635
Evaporator heat load (W)	150	620
SHX heat load (W)	-	570
Absorber heat load (W)	400	1180
COP	0.25	0.51

4.5 Conclusions

Experimental research was carried with the VARS setup integrated with the simulated SOFC exhaust. The proposed primary objective of integration of the SOFC exhaust to VARS via thermal oil circuit has been met and the setup achieved sub-zero temperatures. The system delivered refrigeration temperature down to -8°C. Overall, the experimental setup demonstrated unsatisfactory thermodynamic operation with the maximum COP of 0.25. It was determined that the low value of high side pressure (less than 9 bar) and higher absorber temperature (more than 50°C) resulted in a poor thermodynamic performance of the system. Several recommendations were made to improve the performance of the setup. With modifications in the absorber design and solution pump flow capacity, system could achieve

improved thermodynamic performance. It was found that the proportional improvement to the setup could demonstrate a comparative COP value of 0.51.

This research study was focused on automotive transportation applications, where the efficiency of the system is one of the most important criteria to check its feasibility. Hence, feasibility analysis of the VARS should be performed by evaluating the most efficient system available in the literature or commercial market. As discussed above, the setup did not deliver the efficient performance. To characterise the system transient performance, several system input parameters are needed such as geometrical parameters of the heat exchangers, components volume, and thermal mass. If all these input parameters were selected based on the setup, then the assessment would underestimate the potential of the VARS. Hence, for the steady state and transient models presented in upcoming chapters, system input parameters were selected from the efficient and compact microchannel heat exchanger based absorption refrigeration technology demonstrated by Garimella et al [157], Goyal [77] and Staedter and Garimella [46].

Chapter 5: *Steady State Analysis of the Combined System*

In this chapter, steady state thermodynamic modelling results of the SOFC and VARS system are presented. The results are assessed and analysed to characterise the SOFC system for different types of trucks and applications. The combined system performance is evaluated under different operating conditions. Based on modelling results, the most preferred operating envelope of the SOFC system is evaluated to drive absorption refrigeration system.

Note: Certain sections of this chapter were published in Applied Thermal Engineering 179 (2020): 115597 [158].

5.1 Refrigeration Load of Different Trucks

The variation of refrigeration load of different types of refrigerated trucks (large, medium, and small) with ambient temperature for frozen transportation is shown in Figure 5-1. The cooling load requirements for large and medium trucks varied from 3 kW to 5 kW, and 1.9 kW to 3.2, kW respectively. Increase in ambient temperature caused greater temperature difference between refrigerated space and ambient temperature which also increased the heat penetration from ambient to refrigerated cabinet.

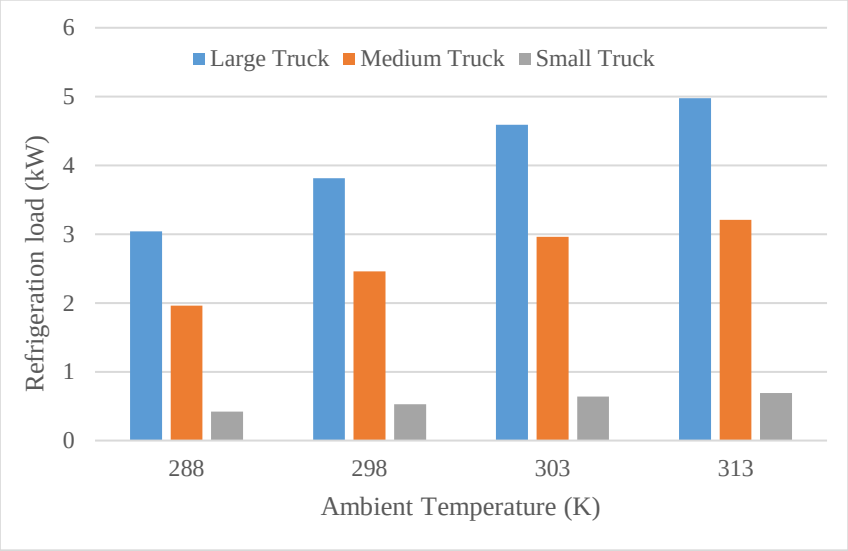

Figure 5-1 : Variation of refrigeration load with ambient temperature for different types of trucks.

According to ASHRAE guideline, the calculated cooling load for refrigerated transportation should be increased by 20 % of a safety factor to match possible disparity between system design criteria and actual operation [94]. Therefore, the maximum refrigeration load has been recalculated and highlighted in Table 5-1.

Table 5-1 : Cooling load of different trucks for frozen transportation.

Type of truck	Cooling load (kW)	ASHRAE safety factor	Final refrigeration load (kW)
Small	2.4	20	2.8
Medium	3.2	20	3.9
Large	5	20	6

5.1.1 Effect of door opening

The door opening activity during journey increases refrigeration load demand dramatically due to large amount of infiltration load from the ambient air. Therefore, it was required to derive the effect of door opening on the final cooling load. In this study, the focus was on development of SOFC system to power VARS for the maximum demand load. It is obvious that the large truck demand load is always high compared to small and medium trucks. Hence, this section only discusses effect of door opening for large truck. Effect of door opening for small truck is shown in Appendix C.

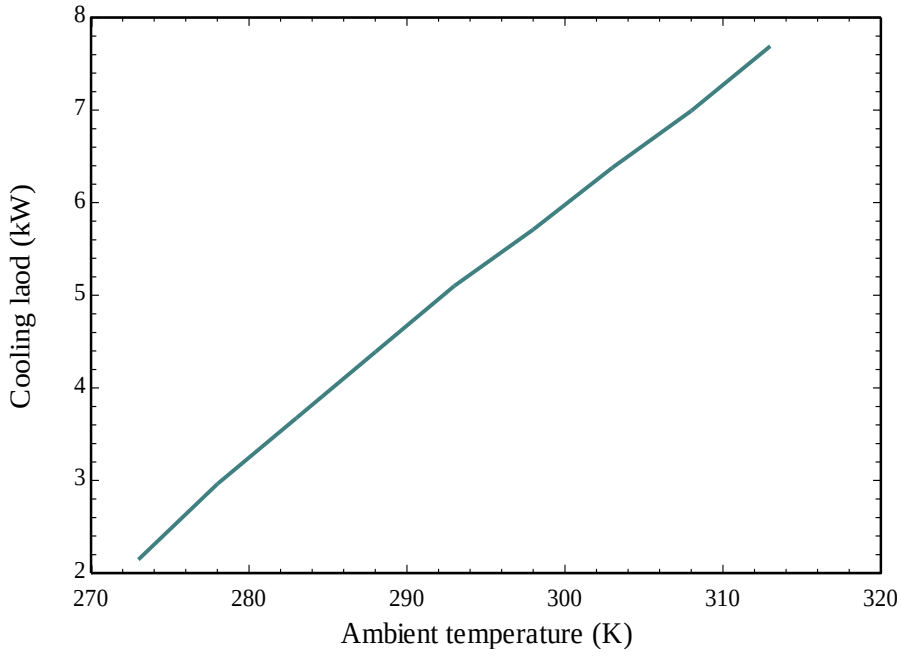

Figure 5-2 : Effect of door opening on refrigeration load for large trucks.

Large trucks normally used for end-to-end point delivery, hence door opening activity does not take often. However, it was still important to show the effect of door opening. Therefore, it was assumed that the door was kept open for three minutes in an hour. The variation of refrigeration load with three-minute door opening is shown in Figure 5-2. It was observed that the peak refrigeration load can as be high as 7.7 kW at ambient temperature of 313 K.

The nominal and peak load at the maximum ambient temperature of 313 K for large trucks are 6 kW and 7.7 kW, respectively. These are crucial information to model the VARS which is highlighted in the next section.

5.2 Steady-State Results of VARS

A steady state 0D thermodynamic model as mentioned in Table 3-8 was built in Engineering Equation Solver (EES) to predict the absorption system performance parameters. The inputs for the model are outlined in Table 5-2.

5.2.1 Model validation

For validation of the steady state absorption system modelling, results obtained from the model were compared with experimental and modelling study carried out by Staedter and Garimella [46] as shown in Table 5-3 and Table 5-4. Most state-point temperatures obtained from the thermodynamic modelling are in close agreement with experimental results. Hence, steady state VARS model found reliable with adopted assumptions in this study.

Table 5-2 : VARS thermodynamic model inputs.

Input parameters	Value	Reference
Ambient temperature (ºC)	40	[106]
Condenser closest temperature approach (ºC)	3ºC	
Absorber closest temperature approach (ºC)	3ºC	
Evaporator closest temperature approach (ºC)	3ºC	
Desorber closest temperature approach (ºC)	25ºC	
SHX effectiveness	0.8	
RHX effectiveness	0.8	
Ammonia refrigerant concentration	0.9985	
Ambient air HX effectiveness	0.75	[104]
Evaporator coupling fluid inlet temperature	-16ºC	Design parameter
Evaporator coupling fluid outlet temperature	-18ºC	
Desorber coupling fluid inlet temperature	220ºC	

Table 5-3 : Model validation with work conducted by Staedter and Garimella [46].

Performance parameters	**Present study**	**Staedter and Garimella** [46]
Higher side pressure (kPa)	2003	1956
Lower side pressure (kPa)	447	496
Refrigerant temperature at evaporator inlet (ºC)	4.8	4.5
Refrigerant temperature at evaporator outlet (ºC)	7.14	7.2
Thermal oil temperature at desorber inlet (ºC)	183	183
Dilute solution temperature at desorber outlet (ºC)	156	155
Refrigerant temperature at condenser inlet (ºC)	59.4	59.3
Refrigerant temperature at condenser out (ºC)	49	47
Coupling fluid temperature at condenser outlet (ºC)	51.3	48.9
Concentrated solution temperature at absorber outlet (ºC)	42.5	43
Coupling fluid temperature at absorber outlet (ºC)	51.03	55.6
Concentrated (strong) solution temperature at SHX inlet (ºC)	70.5	63
Concentrated (strong) solution temperature at SHX outlet (ºC)	118.2	103
Weak (dilute) solution temperature at SHX outlet (ºC)	71.8	79

Table 5-4 : Comparison of performance parameters with study carried out by Staedter and Garimella [46].

Performance parameters	**Present study**	**Staedter and Garimella** [46]	**Difference (%)**
Evaporator heat load (kW)	7.03	7.03	-
Condenser heat load (kW)	6.7	6.5	-2.9
Desorber heat load (kW)	11.2	11.1	-0.8
Absorber heat load (kW)	11.4	11.2	-1.6
SHX heat load (kW)	5	5.6	8.9
RHX heat load (kW)	0.69	0.7	1.4
Rectifier heat load (kW)	1.73	1.6	8.1
COP	0.632	0.63	0.8
$(UA)_{Evaporator}$ (kW/K)	1.7	1.6	-5
$(UA)_{Condenser}$ (kW/K)	1.1	1.08	-2
$(UA)_{Desorber}$ (kW/K)	0.29	0.29	-
$(UA)_{Absorber}$ (kW/K)	1.07	1.3	5.6
$(UA)_{SHX}$ (kW/K)	0.196	0.18	8.1
$(UA)_{RHX}$ (kW/K)	0.068	0.063	7.9
$(UA)_{Rectifier}$ (kW/K)	0.055	0.05	10

Heat load and UA value of each component and COP of the system for the nominal operation of VARS at 6 kW is shown in Table 5-5. UA values and mass flow values are crucial parameters to build transient model of the absorption refrigeration system. COP of the system was determined approximately 0.5.

The few important performance parameters for the VARS are shown in Table 5-5.

Table 5-5 : Thermodynamic performance parameters of VARS at 6 kW of nominal load.

Performance parameters	**Value**
Evaporator heat load (kW)	6
Condenser heat load (kW)	6.7
Desorber heat load (kW)	12.2
Absorber heat load (kW)	11.4
SHX heat load (kW)	4.9
RHX heat load (kW)	1.2
Rectifier heat load (kW)	2
Solution pump work (W)	35
Coolant pump work (W)	30
Oil pump work (W)	40
Evaporator air blower work (W)	100
Ambient air HX blower work (W)	80
COP	0.5
$(UA)_{Evaporator}$ (kW/K)	1.56
$(UA)_{Condenser}$ (kW/K)	0.84
$(UA)_{Desorber}$ (kW/K)	0.312
$(UA)_{Absorber}$ (kW/K)	1.26
$(UA)_{SHX}$ (kW/K)	0.18
$(UA)_{RHX}$ (kW/K)	0.0576
$(UA)_{Rectifier}$ (kW/K)	0.0384
Concentrated solution mass flow rate (kg/s)	0.185
Diluted mass flow rate (kg/s)	0.013
Refrigerant mass flow rate (kg/s)	0.0054
Desorber coupling flow rate (kg/s)	0.185
Air flow to evaporator (kg/s)	1
Coolant flow to condenser/absorber (kg/s)	0.2
Air flow rate to ambient air HX (kg/s)	0.8
Higher side pressure (kPa)	1780
Lower side pressure (kPa)	177

Current research study is focused on the application of absorption refrigeration system for refrigerated transportation. It is expected that the VARS would encounter load following conditions. To maintain the refrigerated cabinet temperature, it is required to satisfy transient load following conditions. The operating parameters should be varied according to load

following conditions; hence it is crucial to carry out the sensitivity analysis to depict the effect of input parameters upon the performance. A detailed sensitivity analysis of the vapour absorption refrigeration system is presented in the next session.

5.2.2 Sensitivity analysis of VARS

VARS is a heat driven system; hence, it is required to identify sensitivity of the system performance to the desorber hot coupling fluid temperature and mass flow. In addition, NH_3-H_2O solution flow affects system component heat load dramatically. Truck refrigeration units (TRUs) encounters various ambient conditions, it is well known fact that the refrigeration system performance depends upon the ambient conditions to a great extent. With keeping all these points in considerations, a parametric analysis was carried out to depict the sensitivity of the system performance to the operating parameters. It should be noted that all other operating parameters kept constant to depict system performance sensitivity to particular operating parameter.

5.2.2.1 Effect of desorber coupling fluid mass flow

The variation of component heat load and COP with the desorber coupling fluid mass flow is depicted in Figure 5-3. The heat energy supplied to the desorber greatly relied on the desorber coupling fluid mass flow. It is obvious that the heat load of the desorber increases with the mass flow which followed by increased heat load in the remaining components. It was interesting to note that the over a wide variation of a mass flow (0.16 kg/s to 0.22 kg/s), only a marginal variation in heat load of the components and COP (0.515 to 0.51) was observed. It is well known fact that the heat transfer coefficient is a weak function of the mass flow for single phase flow [159], hence heat load of the desorber did not change remarkably. Therefore,

system performance parameters were found insensitive to the desorber coupling fluid mass flow variation.

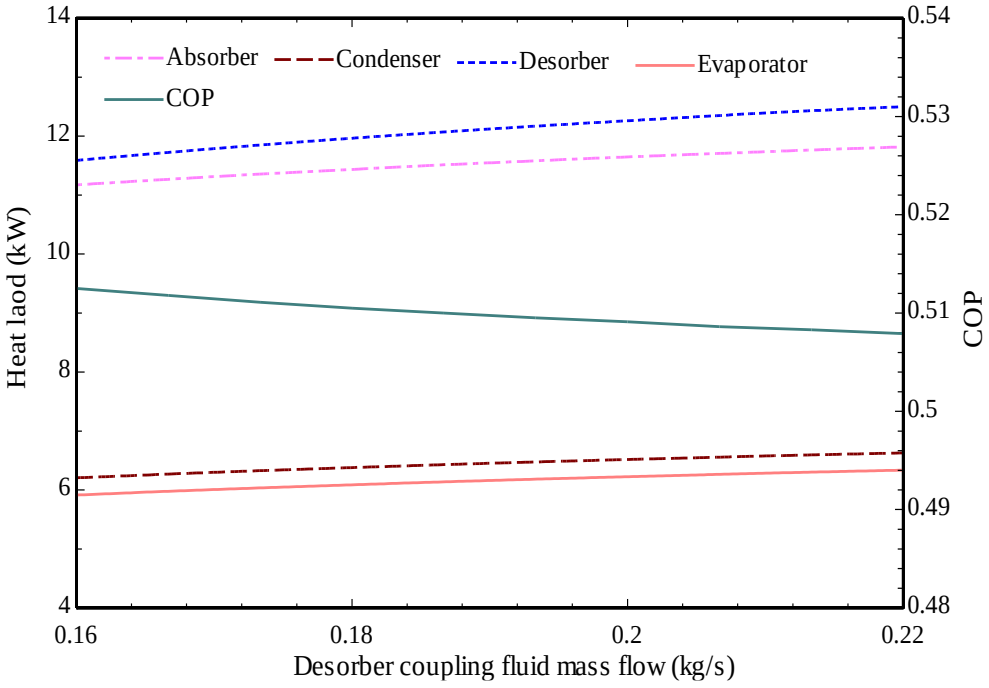

Figure 5-3 : Effect of desorber coupling fluid mass flow on component heat load and COP.

5.2.2.2 Effect of desorber coupling fluid temperature

As shown in Figure 5-4, heat load of all the components increased with the desorber coupling fluid temperature. With increase in heat source temperature from 473 K to 495 K, the desorber heat load increased from 10.9 kW to 12.3 kW. Heat supplied at elevated temperature also generated more amount of refrigerant vapour inside the desorber which also increased the heat load of the evaporator (5.3 kW to 6 kW), condenser (5.8 kW to 6.7 kW) and absorber (9.5 kW to 11.7 kW). However, change in the evaporator heat load was not that significant compared to that of the desorber heat load. Therefore, the system COP degrades from 0.516 to approximately 0.5. The System COP was higher at lower coupling fluid temperature, however system delivered higher cooling capacity at higher temperature. The system delivered 13 %

more cooling capacity (5.3 kW to 6 kW) with marginal 2.2 % of reduction in COP (0.516 to 0.505) when desorber CF temperature increased from 473 K to 495 K. This result is remarkably interesting for the selection of the heat source temperature to drive refrigeration system to match the trade-off between cooling capacity and thermodynamic performance. The higher desorber coupling fluid temperature helped to achieve higher refrigeration load.

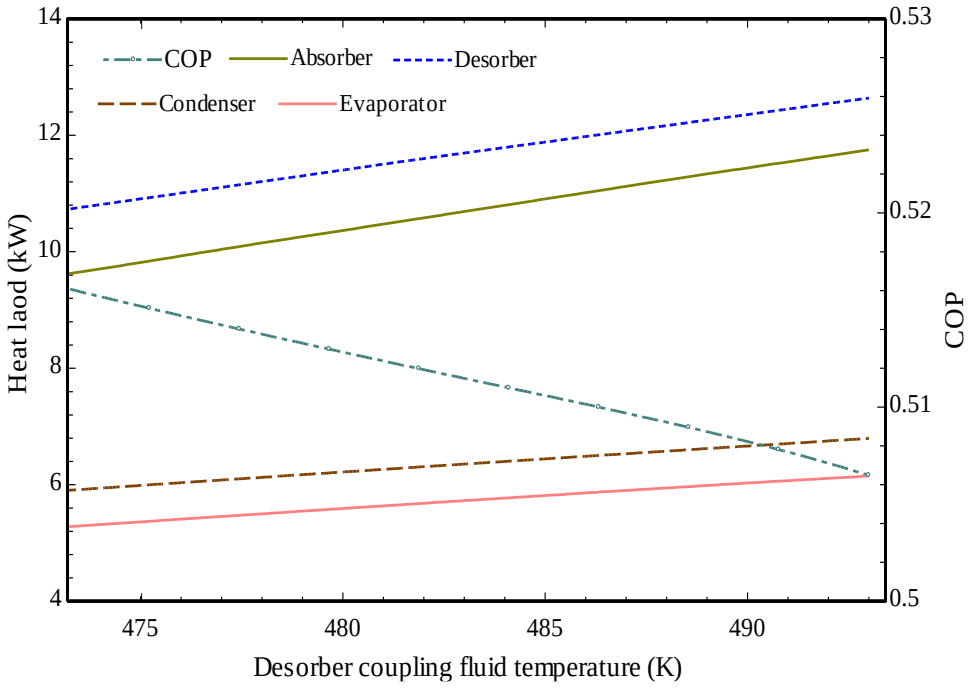

Figure 5-4 : Effect of desorber coupling fluid temperature on component heat load and COP.

5.2.2.3 Effect of NH_3-H_2O solution mass flow

Figure 5-5 shows the effect of solution mass flow on component heat load and COP of the system. Component heat load increased with solution mass flow which was expected. However, negligible variation observed in the COP behaviour, and it remained almost constant which is in match with the results published by Goyal [77] and Vinodh [85]. It was observed that with increase of solution flow from 0.018 kg/s to 0.025 kg/s, evaporator load approximately increased from 5.9 kW to 7.7 kW.

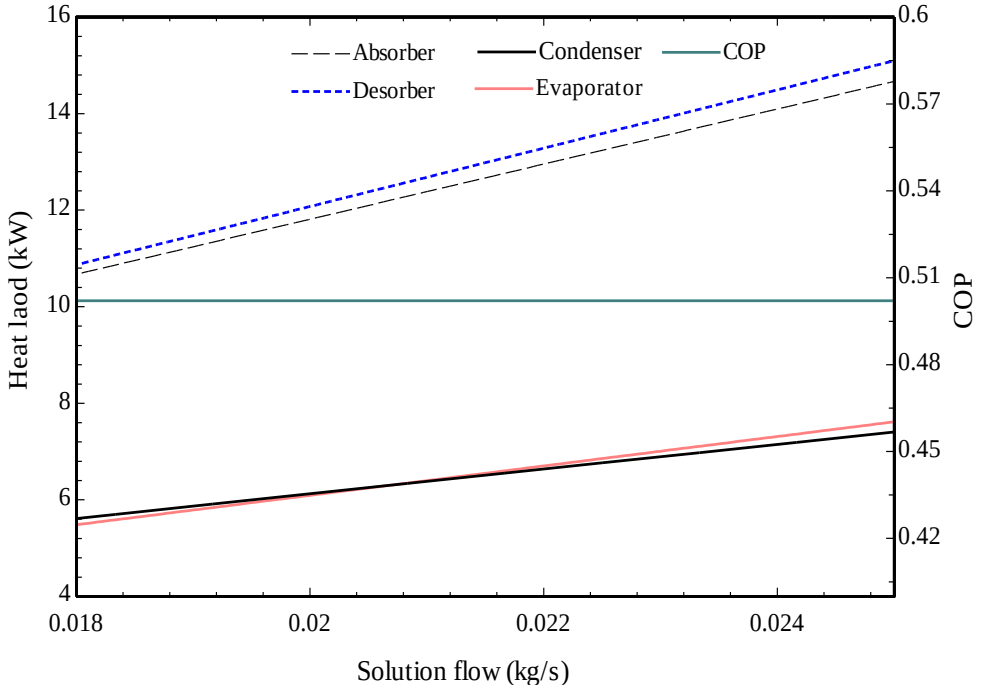

Figure 5-5 : Effect of solution mas flow on component heat load and COP.

5.2.2.4 Effect of ambient temperature

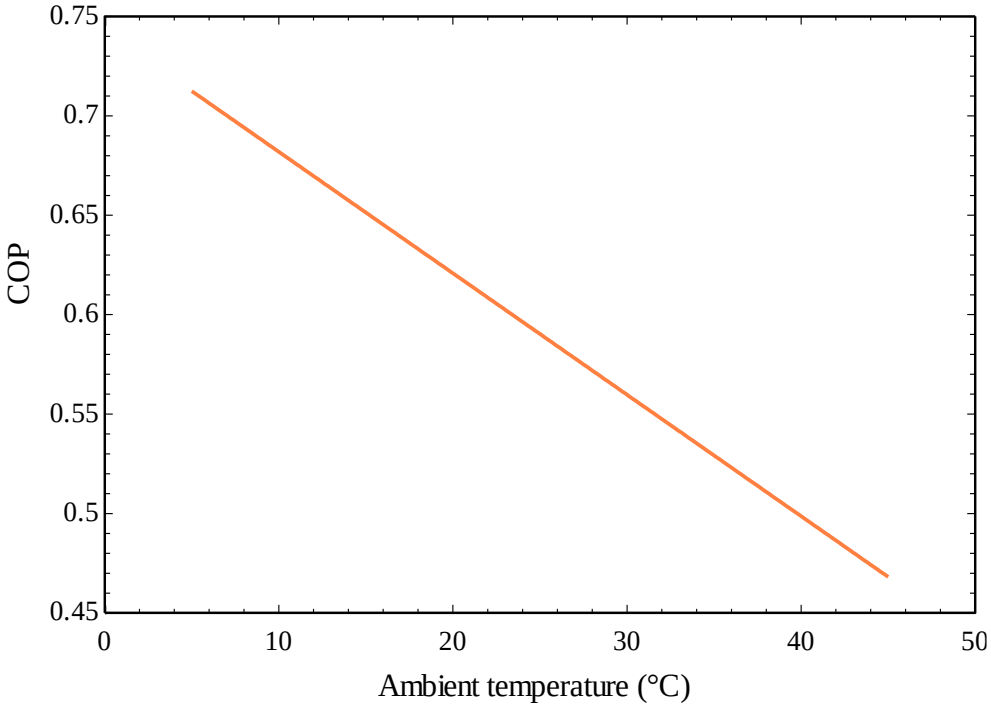

Figure 5-6 : Effect of ambient temperature on COP.

Ambient temperature is one of the crucial parameters which affects the VARS performance significantly. Higher ambient temperature resulted into higher condensation temperature and pressure in the system. Due to increased ambient, higher amount of heat needed to be delivered to desorber to obtain same cooling capacity from the system. As the ambient temperature changed from 5 ºC to 45 ºC, the system COP significantly reduced from 0.72 to 0.48 as shown in Figure 5-6.

A summary of the sensitivity of the system performance parameters is shown in Table 5-6.

Table 5-6 : System steady state response to change in operating parameters.

Operating parameters	**Variation**	**Desorber heat load**	**Evaporator heat load**	**COP**
		(kW)	(kW)	
Desorber coupling fluid mass flow	0.16-0.22 kg/s	11.5-12.5	5.9-6.3	0.515-0.5
Desorber coupling fluid temperature	473-495 K	10.7-12.6	5.2-6.02	0.51-0.5
Solution mass flow	0.018-0.025 kg/s	8.4-10.7	4.4-5.6	~0.52
Ambient temperature	5ºC - 45ºC	8.33- 12.7	~6	0.72-0.48

As mentioned above, the peak cooling load can as be high as 7.7 kW. It is obvious that operating parameters needs to change to get higher cooling load form the VARS. Table 5-7 outlines the operating parameters to achieve peak load of 7.7 kW from VARS. The steady state results at nominal load and peak load are utilised later in the transient analysis which is explained in upcoming chapter of the thesis.

Table 5-7 : VARS operating and performance parameters at 7.7 kW of peak load.

Parameters	Value
Concentrated solution mass flow rate (kg/s)	0.0246
Diluted mass flow rate (kg/s)	0.0165
Refrigerant mass flow rate (kg/s)	0.069
Evaporator heat load (kW)	7.7
Condenser heat load (kW)	7.9
Desorber heat load (kW)	16.2
Absorber heat load (kW)	15.2
SHX heat load (kW)	6.8
RHX heat load (kW)	1.4
Rectifier heat load (kW)	2.9
COP	0.47
Desorber coupling fluid temperature (K)	493
Higher side pressure (kPa)	1800
Lower side pressure (kPa)	180
Air flow to evaporator (kg/s)	1.15
Desorber coupling flow rate (kg/s)	0.25
Coolant flow to condenser/absorber (kg/s)	0.25
Air flow rate to ambient air HX (kg/s)	0.92
Solution pump work (W)	51
Coolant pump work (W)	40
Oil pump work (W)	58
Evaporator air blower work (W)	115
Ambient air HX blower work (W)	93

A detailed sensitivity analysis of the absorption refrigeration system was carried out to evaluate the effect of change in operating parameters on the system performance characteristics. It was concluded that the refrigeration system COP changed significantly when system encountered variations in ambient temperature. The refrigeration capacity increased approximately 13% with 2 % of reduced COP when desorber hot coupling fluid temperature was increase by 20 K (473 K to 493 K). Hence, it was decided to operate VARS at the maximum desorber coupling fluid temperature of 493 K. This temperature is one of the most crucial parameters to characterise the SOFC system to power VARS. The COP found insensitive to solution and

desorber hot coupling fluid mass flow. However, component heat load found strong function of solution mass flow in the system. The desorber coupling fluid temperature, mass flow and heat energy needed to operate refrigeration system served as primary inputs to determine operating envelope design of the SOFC system. These thermodynamic results build the foundation for the SOFC system steady state and transient analysis. The next step in the simulation was to characterise the performance of the SOFC system to power the VARS.

5.3 Steady state Results of SOFC system

The most important step before assessing the system performance was to validate the SOFC stack model. The following sub-section represents the model validation of the developed model.

5.3.1 Model validation

The modelling results were compared with the experiments conducted by Noponen et al.[114] and Lawrence [119]. The primary objective for validating the modelling results with two experimental studies is to prove the versatility of the SOFC generic model. Noponen et al. [114] conducted experiments characterising SOFC I-V and I-P curves with pre-reformed natural gas. Table 5-8 outlines the inlet conditions fed to the SOFC model for the validation. The ASR value of the I-V curve (Figure 3-13(a)) depicted by Noponen et al [114] was determined by using eqn.3.36. The model reproduced comparable I-V curve characteristics with a maximum 4.8 % absolute error. In addition, the I-P curve was validated, as shown in Figure 5-8. It shows the acceptable degree of agreement between experimental and modelling results.

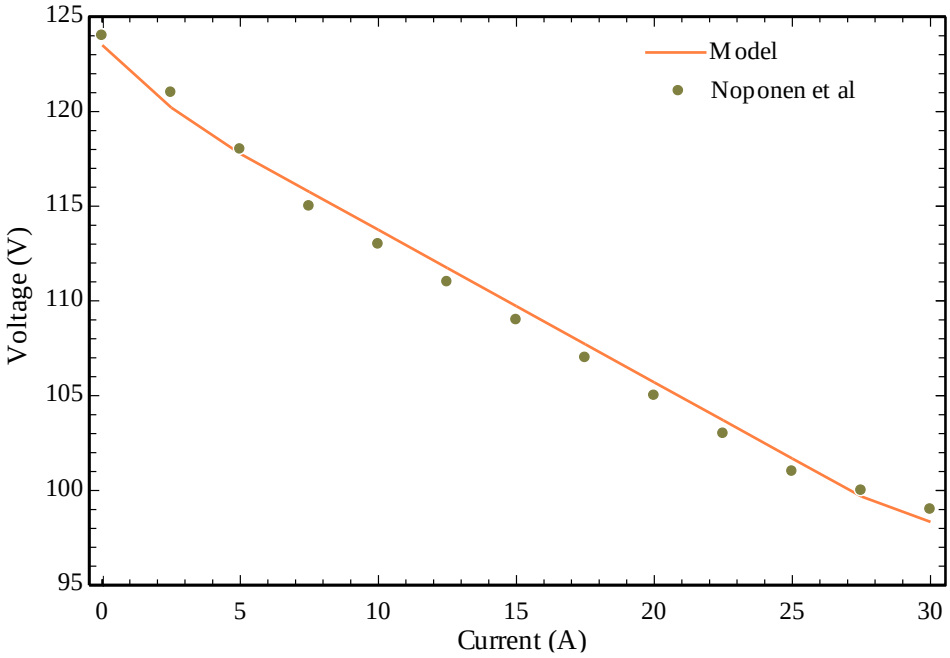

Figure 5-7 : I-V curve validation with Noponen et al [114].

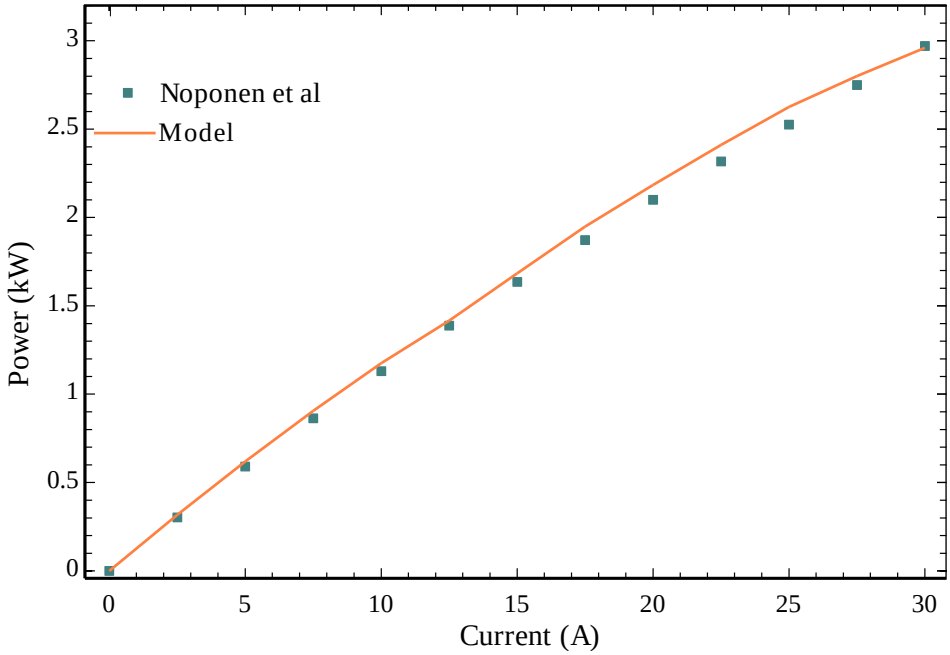

Figure 5-8 : I-P curve validation with Noponen et al [114].

Table 5-8 : Input parameters for the model validation with Noponen et al [114].

Input parameters	Value
Inlet temperature of air and fuel	590°C
CH_4 flow rate	33 Nl/min
H_2O flow rate	72.6 Nl/min
Air flow rate	327 Nl/min
CH_4 (vol %)	7%
H_2O (vol %)	26%
CO (vol %)	7%
H_2 (vol %)	52 %
CO_2 (vol %)	8 %

Table 5-9 : Input parameters for the model validation with Lawrence [119].

Input parameters	SMR	CPOX
Air inlet temperature	650°C	650°C
Reformer equilibrium temperature	657°C	657°C
Solid temperature	850°C	850°C
CH_4 (vol %)	8%	-
H_2O (vol %)	24%	5%
CO (vol %)	6%	15%
H_2 (vol %)	53 %	31 %
CO_2 (vol %)	9%	2%
N_2 (vol %)	-	46%
Fuel utilisation	0.74	0.74

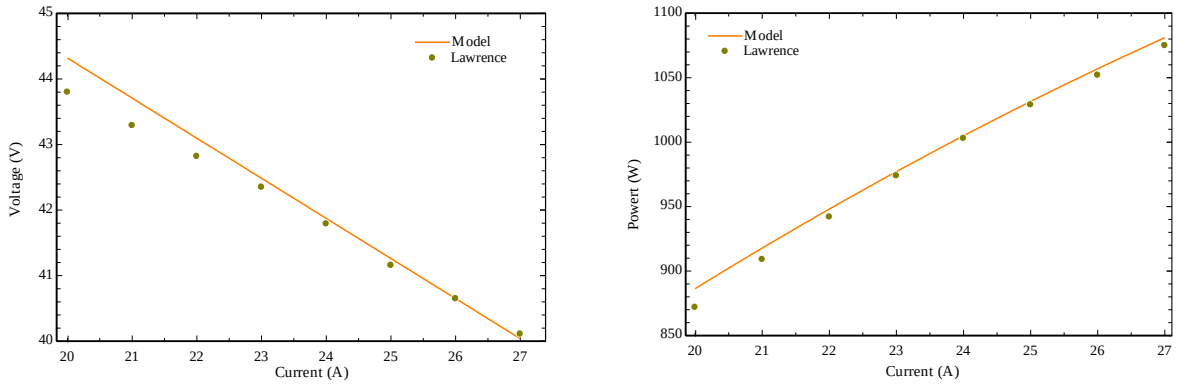

(a) I-V curve (b) I-P curve

Figure 5-9 : Model validation with Lawrence [119]- SMR reformate.

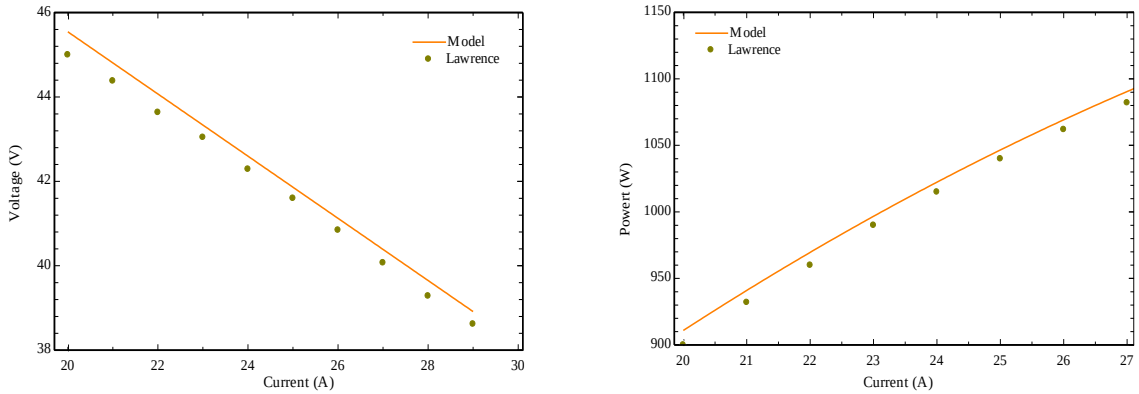

(a) I-V curve (b) I-P curve

Figure 5-10 : Model validation with Lawrence [119] - CPOX reformate

Lawrence [119] performed experimental I-V characteristics of a SOFC stack with SMR and CPOX reformate. The validation of the modelling results with this literature source is shown in Figure 5-9 and Figure 5-10 respectively. The model overestimated the stack voltage for SMR and CPOX reformate due to a simplified simulation approach, which is understandable. However, the model predicted comparable results with experimental results with a maximum of 5.9 % and 5.6 % error with I-V and I-P curves, respectively. In both these studies, no details were provided for the system components such as reformer, heat exchangers and burner. Hence, it was not possible to validate the BoP component modelling.

Several modelling assumptions were responsible for the disparity in the modelling results and experimental data. One of the dominant sources of error could be the chemical equilibrium assumption to calculate SMR reaction kinetics. Biert [12,160] concluded that the chemical equilibrium assumption of SMR reaction led to an overestimated conversion of methane, the reaction rate of SMR is always restricted by thermodynamics kinetics. Overestimated methane conversion leads to higher cell/stack voltage in the simulation compared to the experimental data. Another error source is the lumped solid temperature approach to determine stack temperature. The model did not consider heat transfer due to conduction and radiation modes.

However, the stack model with ASR approach reproduced comparable results with experimental data published by Noponen et al [114] and Lawrence [119]. The ASR approach model appeared to be sufficiently reliable to continue further SOFC system simulation.

5.3.2 Parametric analysis of the SOFC system

In this study, several operating parameter constraints such as minimum inlet temperatures to SOFC and temperature gain across the SOFC stack are adopted from commercially available SOFC stack that might be suitable to automotive application [114,161]. This study also restricts the maximum afterburner temperature to 1223 K (due to material constraints) [113].

If SOFC system operates with low excess air ratio, it also increases burner temperature tremendously high (>950°C), hence this study restricts minimum value of excess air ratio to two. The SC ratio is defined by eqn.5.1. It is the ratio of molar flow of H2O to the number of C atoms in the combustible gases at stack inlet [162]. If value of the SC ratio is too low, it may lead towards carbon formation inside an SOFC stack [163,164]. Too high SC ratio value reduces reactant partial pressure which eventually reduces the stack voltage, power, and efficiency. Hence, SC ratio value needs to be chosen carefully.

$$\text{SC ratio} = \frac{\dot{n}_{H_2O,stack,inlet}}{\dot{n}_{CH_4,stack,inlet} + \dot{n}_{co,stack,inlet}} \quad 5.1$$

The various adopted operating constraints for the modelling in this study are mentioned in Table 5-10.

Table 5-10 : Operating constraints for the SOFC system.

Operating parameter	Value	Reference
Minimum air and fuel inlet temperature (K)	853	[114,161]
Minimum air and fuel inlet temperature (K)	893	[114,161]
Maximum stack temperature (K)	993	[114,161]
Maximum temperature difference across stack (dT_{stack}) (K)	100	[114,161]
Maximum afterburner temperature (K)	1223	[113]
Minimum excess air ratio	2	[113]

The refrigeration demand load values were known from the previous section, operating envelope of the SOFC system needs to be developed such a way that it can satisfy the refrigeration demand load. However, before characterising the SOFC system to operate the VARS, it was necessary to carry out a parametric analysis to get optimised performance from the SOFC system. A detailed steady state model of the SOFC system (as mentioned in Table *3-21*) was developed in the EES to carry out the simulation.

5.3.2.1 Effect of SOFC and VARS efficiency on the combined system efficiency

It is important to decide the sensitivity of the combined system efficiency, whether the system efficiency is more sensitive to the SOFC system efficiency or the VARS efficiency. A contour is depicted as shown in Figure 5-11 to represent the combined system efficiency. It was observed that the combined efficiency of the system is sensitive to SOFC system efficiency compared to VARS COP values. If the VARS COP improved from 0.3 to 0.7 under the same SOFC efficiency of 45 %, combined efficiency of the system only improved from 48% to 56 %. However, if the SOFC efficiency increased from 35% to 65% under the same VARS COP value of 0.4, combined efficiency increased from 44% to 70%. In addition, the VARS is a heat driven system which suffers from low COP values, it is challenging to optimise the VARS

performance. Hence, it is fair to focus on optimisation of the SOFC system performance. Hence, this section focused on the SOFC system performance and its optimisation.

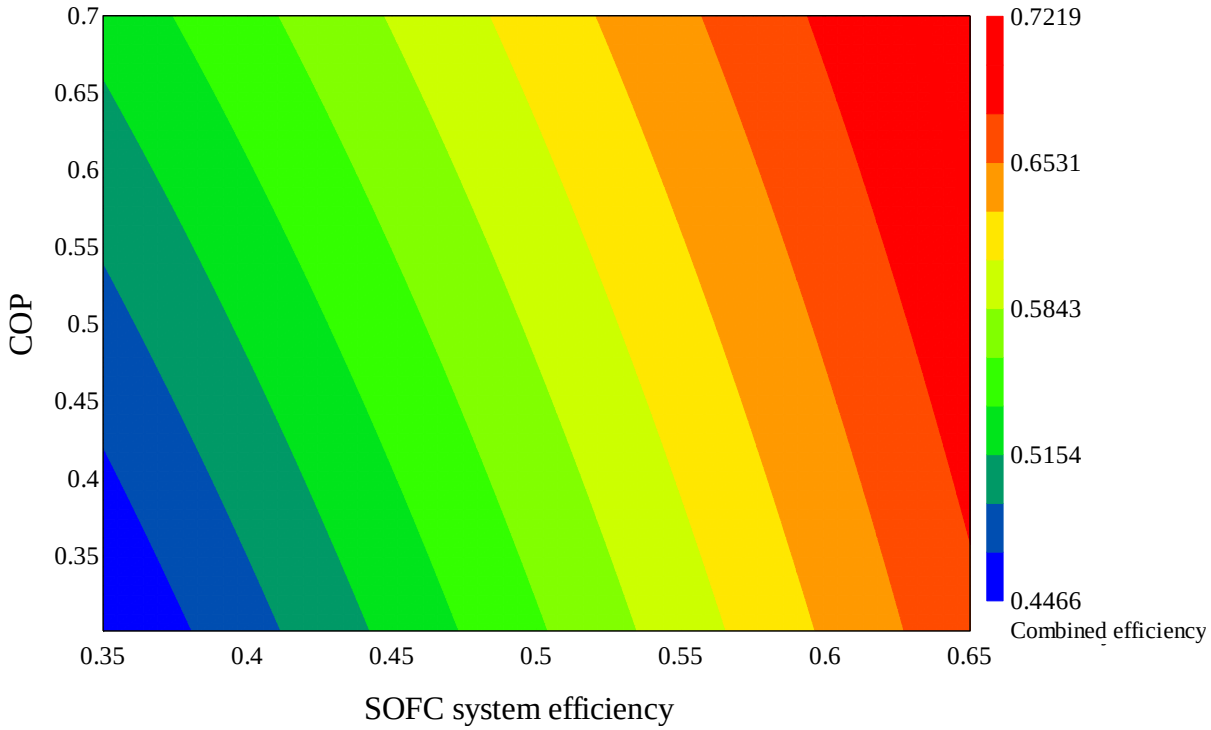

Figure 5-11 : Contour of the combined system efficiency.

5.3.2.2 Effect of ASR

The ASR is one of the most crucial input parameters which affects the SOFC system performance significantly. A high value of ASR represents high voltage losses. However, high losses generate an elevated amount of heat from the SOFC system that might be beneficial to the heat driven VARS. Figure 5-12 highlights the effect of varying ASR on key performance parameters. The electrical power density ($Dens_{elec,net}$) reduced from 0.43 W/cm^2 to 0.21 W/cm^2 (approximately 51 %) under increased ASR value from 0.4 ohm/cm^2 to 0.9 ohm.cm^2. However, the refrigeration power density ($Dens_{ref}$) increased approximately 54 %, from 0.11 W/cm^2 to 0.17 W/cm^2. The combined efficiency of the system was reduced from 69 % to 49

%. This was due to the reduced SOFC system electrical efficiency, from 54 % to 27 %. The electrical efficiency loss was so high that even increased refrigeration power could not compensate for it. Thus, the SOFC stack with high ASR cannot deliver efficient performance. Research and development activities focus on developing a robust SOFC stack for mobile applications that can operate at 650 to 700°C with 0.5 Ohm/cm^2 of ASR [165]. Hence, this study considered reference ASR value (ASR_0) of 0.5 Ohm/cm^2 at reference temperature (T_0) of 700°C.

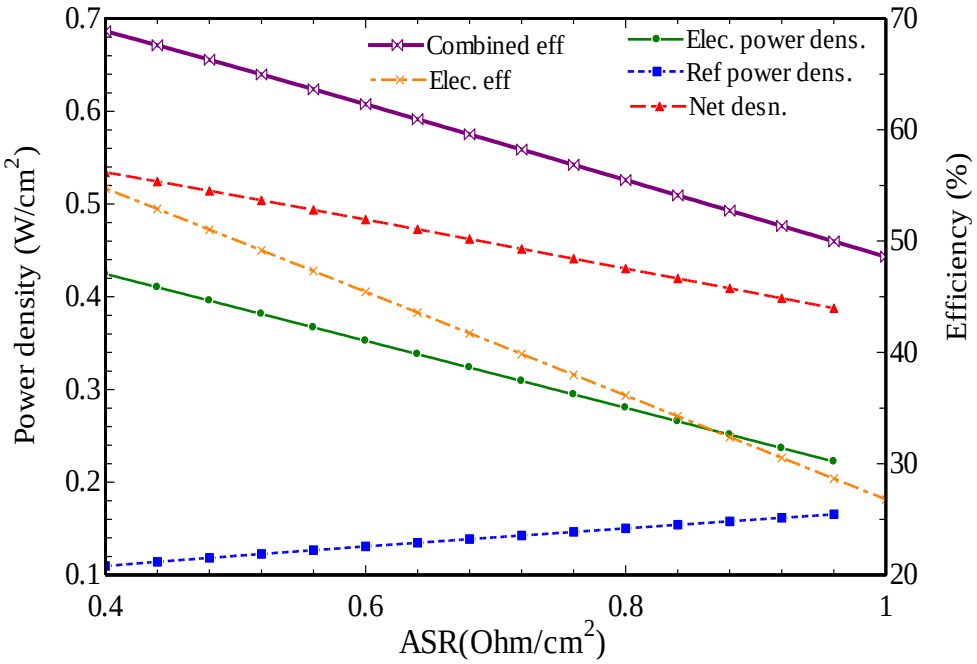

Figure 5-12 : Effect of ASR on system performance parameters (Stack inlet temperatures=893 K, U_F=0.7, J=0.6 A/cm^2, dT_{stack}=100 K).

5.3.2.3 Effect of stack inlet temperatures

The influence of varying anode and cathode inlet temperature upon combined system performance is illustrated in Figure 5-13 and Figure 5-14, respectively. The input conditions for fuel utilisation and current density were same as mentioned in Figure 5-12. The $Dens_{elec,net}$

increased approximately 25 %, from 0.32 W/cm^2 to 0.4 W/cm^2 when the anode inlet temperature changed from 853 K to 893 K, as shown in Figure 5-13. The chemical reaction (electrochemical, SMR and WGS) kinetics improved with temperature, and the ASR decreased at elevated temperature (eqn.3.37), resulting in improved electrical performance of the system. However, the refrigeration power density decreased roughly 15 %, from 0.13 W/cm^2 to 0.11 W/cm^2. It was due to more heat being utilised to pre-heat the anode stream at higher temperature which reduced net available heat to the VARS. The combined efficiency increased from 59 % to 68 %. Thus, a higher anode inlet temperature was found to be advantageous for effective and efficient SOFC combined system performance.

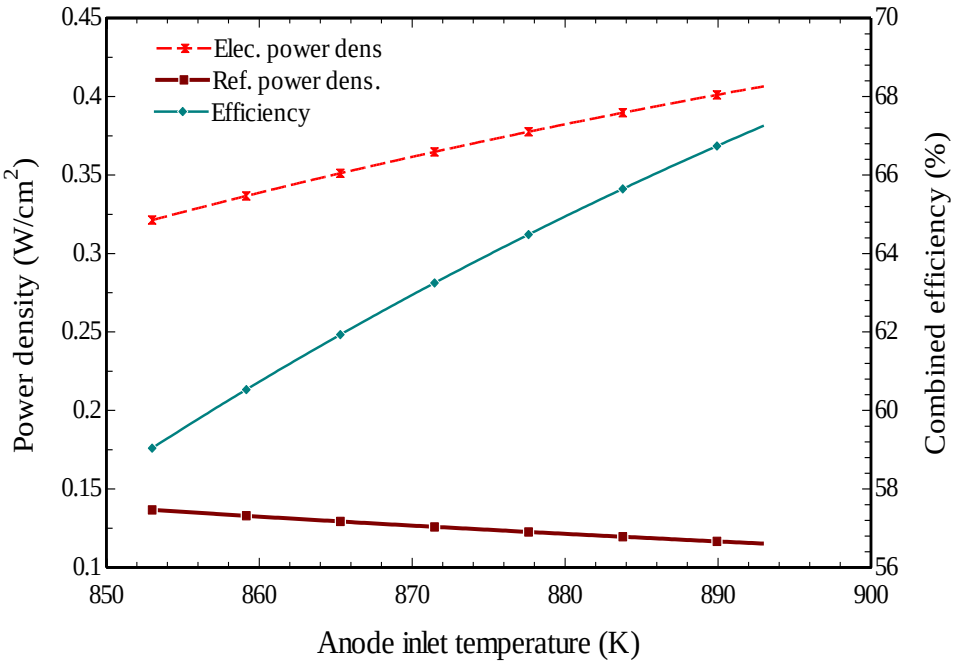

Figure 5-13 : Influence of anode temperatures upon system performance.

Figure 5-14 shows the influence of cathode inlet temperature upon the system performance. The higher mass flow of air was required at higher cathode inlet temperature to keep the same temperature gain over the stack. Therefore, the blower required greater power, reducing

combined system efficiency and electrical power density from 69 % to 67 % and 0.42 W/cm^2 to 0.4 W/cm^2, as shown in Figure 5-14. The higher cathode inlet temperature also produces heat at higher temperature in the burner. Thus, the refrigeration power density increased from 0.10 W/cm^2 to 12 W/cm^2. Interestingly, electrical density and combined efficiency marginally decreased by 4 % and 2 %, respectively; however, refrigeration density was improved by 20 %. Therefore, it is beneficial to operate the combined system with a higher cathode inlet temperature to counterbalance the electrical and thermal performance of the SOFC system, especially when refrigeration power density improves significantly. Therefore, in the further simulation SOFC system would be operated with maximum possible inlet temperature which is 893 K as mentioned in Table 5-10.

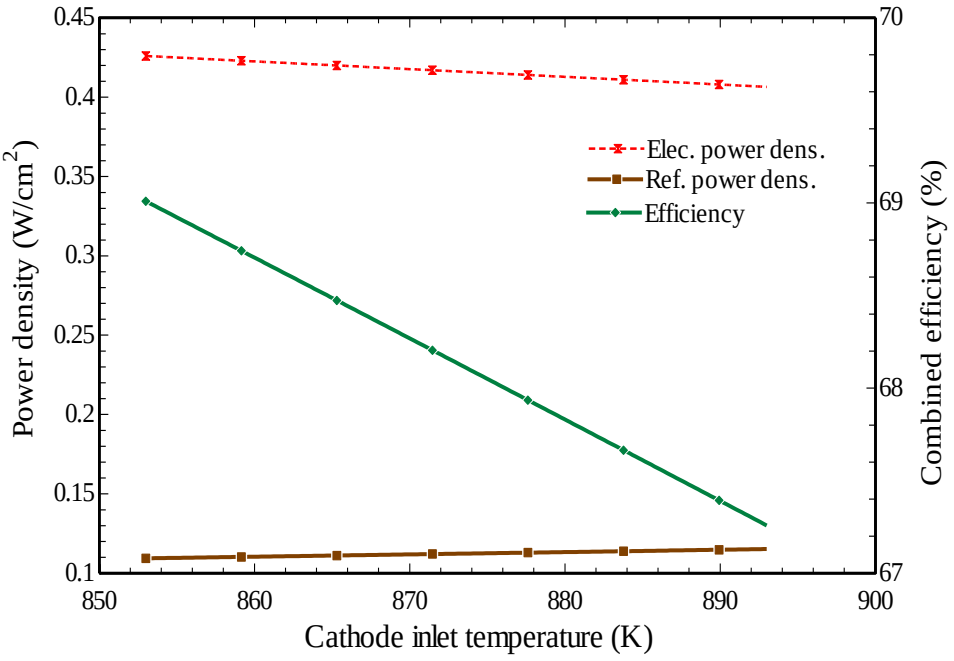

Figure 5-14 : Influence of cathode temperatures upon system performance.

5.3.2.4 Effect of recirculation ratio

The effect of recirculation ratio on the combined system performance is outlined in Figure 5-15. It was observed that the net power density ($Dens_{net}$) and combined efficiency of the system reduced from 0.53 W/cm^2 to 0.507 W/cm^2 and 65 % to 62.7 %, respectively when the recirculation ratio varied from 0.6 to 0.81. The higher recirculation rate introduced high amount of steam to inlet of the stack, which dilutes the H_2 concentration and its partial pressure. It reduced the system power and efficiency. In addition, with higher recirculation rate, the burner received reduced flow of combustible gases from SOFC stack which eventually reduce the available heat from the SOFC system. Hence, SOFC system at higher recirculation rate is neither preferred from the SOFC operation nor for the VARS performance. Hence, in this study recirculation rate was decided such a way that, it can provide SC ratio value of 2.2 at the stack inlet to avoid any possibility of the carbon formation.

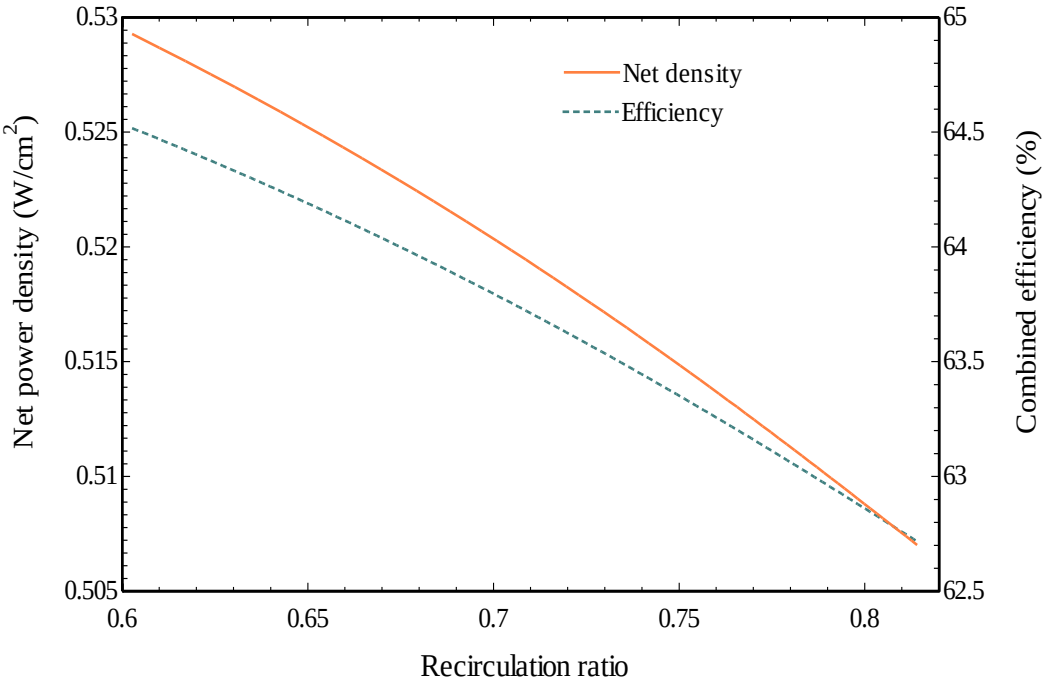

Figure 5-15 : Effect of recirculation rate on the SOFC system performance.

5.4 Thermal Integration of SOFC System with VARS

If the thermal integration of the SOFC system with the VARS is not carried out efficiently, it would reduce the combined system efficiency. In a conventional SOFC system layout (Figure 3-16), the available exhaust heat from the SOFC is utilised for preheating the inlet gases, with the remaining heat directed towards the VARS via heat recovery exchanger. It is usual to extract heat from SOFC exhaust temperature up to 50 to 60°C with the combined heating and power cogeneration systems [19,60,166]. However, SOFC exhaust temperature greatly relies upon the thermal oil circuit temperatures in the current system. As mentioned in Table 5-2 that the VARS needs heat source temperature of 220°C (493 K). Temperatures of thermal oil circuit with VARS heat source temperature of 220°C (493 K) is shown in Figure 5-16.

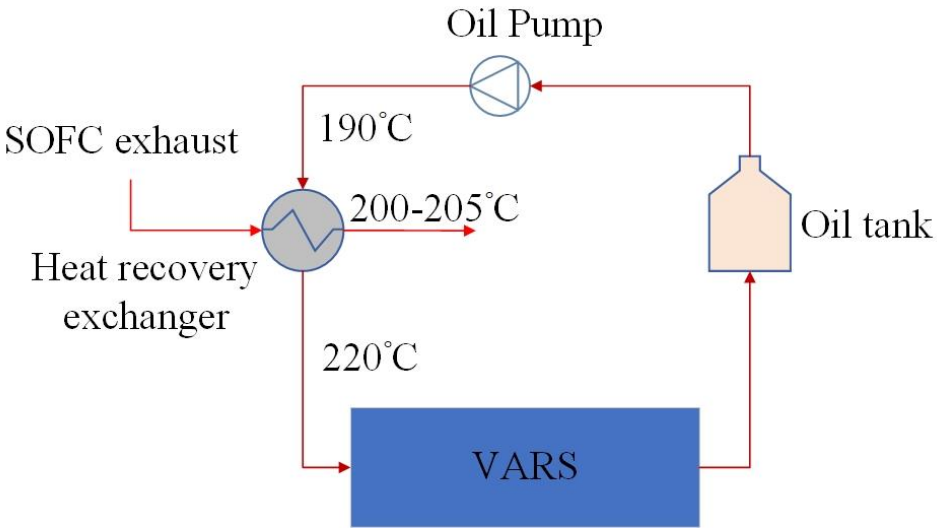

Figure 5-16 : Working temperatures of thermal oil circuit.

With given thermal oil temperature range, SOFC exhaust outlet temperature was determined in the range of 200-205°C by assuming approximate CTA value of 10-15°C (Figure 5-16). Therefore, it was not feasible to extract maximum possible amount of heat from the SOFC

exhaust with a conventional layout. It represented an opportunity to develop modified SOFC system layout which can extract the maximum amount of heat from the SOFC exhaust for such systems. Therefore, a modified SOFC system layout was investigated, as shown in Figure 5-17. A modified SOFC system layout was equipped with two air heat exchangers. The primary reason was to utilise the available heat from the SOFC exhaust leaving the waste heat recovery exchanger. The SOFC exhaust leaving the oil exchanger enters the first air HX and preheats air before entering the second air heat exchanger. Due to preheating of the air, less heat was needed to heat-up the air up to SOFC operating temperature in the second air heat exchanger. Hence, a modified layout improved the internal heat recovery in the SOFC system heat exchanger network.

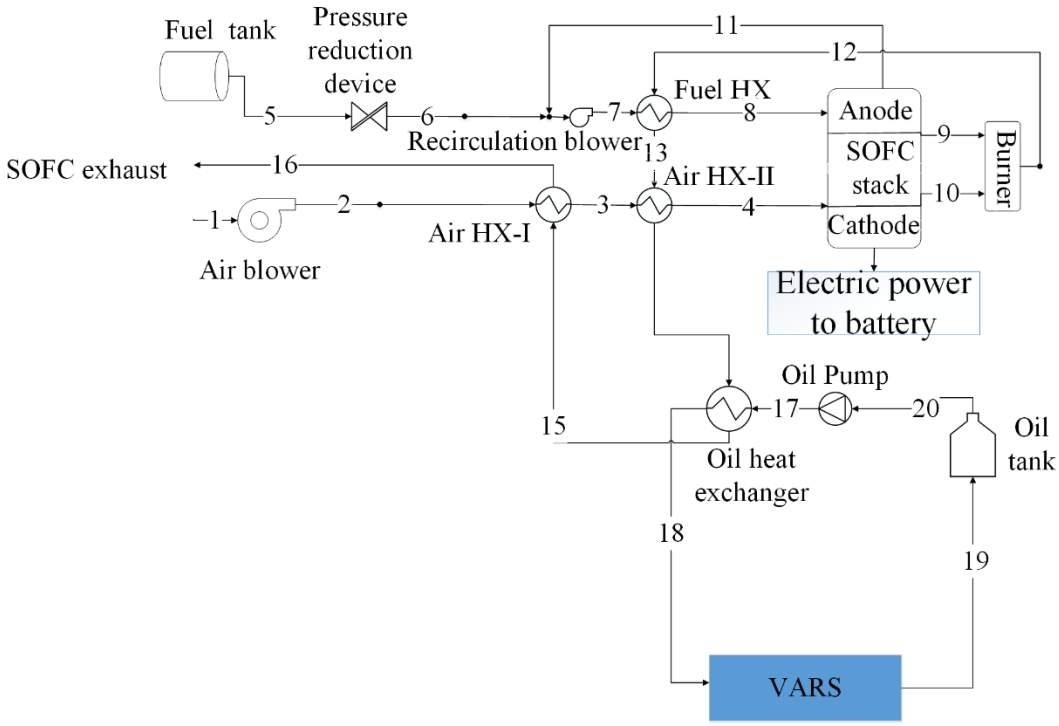

Figure 5-17 : A modified layout of SOFC system integrated with VARS.

The improved performance of the modified SOFC system layout can be explained in Figure 5-18. Figure 5-18 shows air path and oil path working temperatures comparison between

conventional and modified layouts. A higher amount of oil flow (4.5E-3 g/s/cm^2 area of stack) could be heated up with the modified layout compared to the conventional layout (1.5E-3 g/s/cm^2 are of stack). It should be noted that temperature crosses of hot and cold fluid are not considered in this comparison study between two layouts. The higher amount of heated oil flow resulted into greater amount of refrigeration load from the VARS. In this comparison analysis, the CTA for heat recovery exchanger was assumed 15°C for both layouts. It also fixed the SOFC exhaust temperature at the oil heat exchanger outlet (205°C) for both layouts. Due to preheating of air in the modified layout, SOFC exhaust entered oil heat exchanger at higher temperature of 335 °C in the modified layout compared to the conventional layout (250°C). Therefore, the higher temperature gradient was available in the oil heat exchanger with the modified layout, resulting in improved heat transfer and able to heat high amount of oil flow which also delivered high amount of heat to VARS.

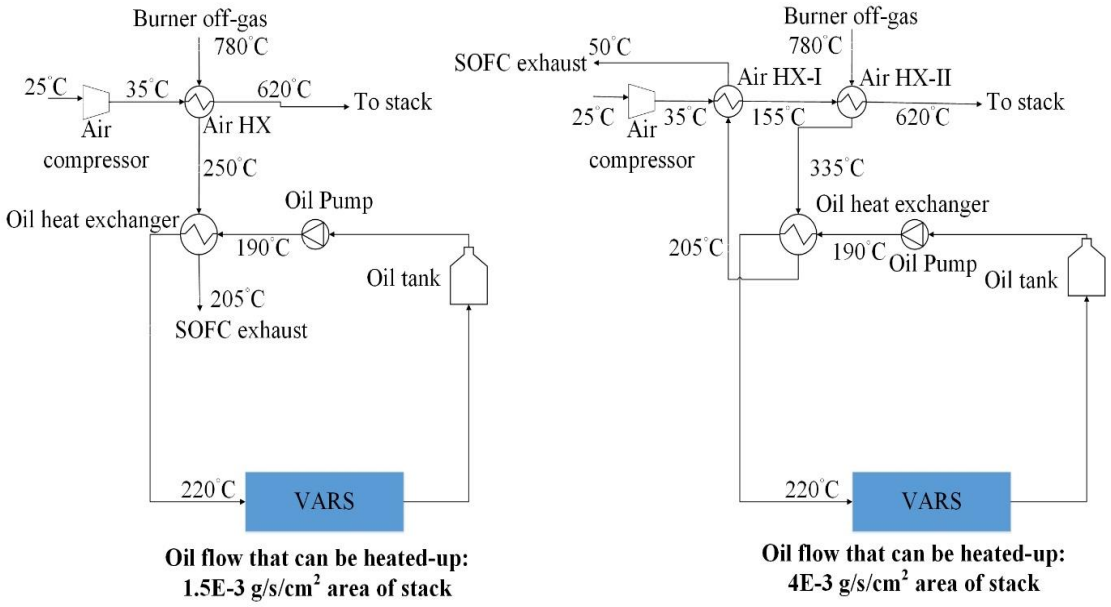

(a) conventional layout (b) modified layout

Figure 5-18 : Working temperatures of air path and thermal oil circuit in conventional layout and modified layout.

Figure 5-19 compares the performance of these layouts under varying current density at a constant 0.7 fuel utilisation and 893 K stack inlet temperatures. At lower current density (0.2-0.3 A/cm^2), the modified layout showed marginally improved performance; however, at mid and higher current density (above 0.3 A/cm^2), a significant difference in the performance was observed between both these layouts. It was also understandable as the SOFC stack produced a significant amount of heat at higher current density, at high current density stack was fed with higher amount of air to keep its temperature constant (993 K). It also increased recovered heat from the SOFC exhaust via afterburner. At the highest current density (0.85 A/cm^2), refrigeration power density ($Dens_{ref}$) and combined efficiency of the system with a modified layout were approximately 240 % and 15 % higher than the conventional layout.

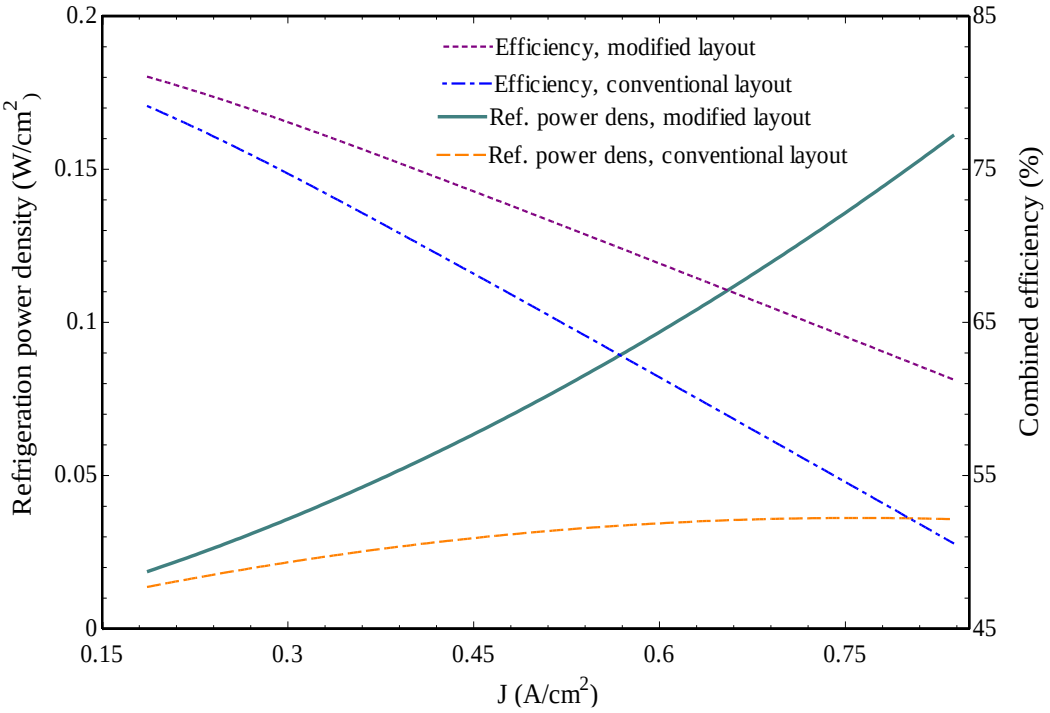

Figure 5-19 : Performance comparison between conventional and modified layout.

Hence, it was proved that the modified layout performed efficiently compared to conventional layout for combined cooling and power application. A modified layout was considered in this

study as shown in Figure *5-20* to determine optimised operating conditions for the SOFC system to power a VARS for different types of trucks and applications.

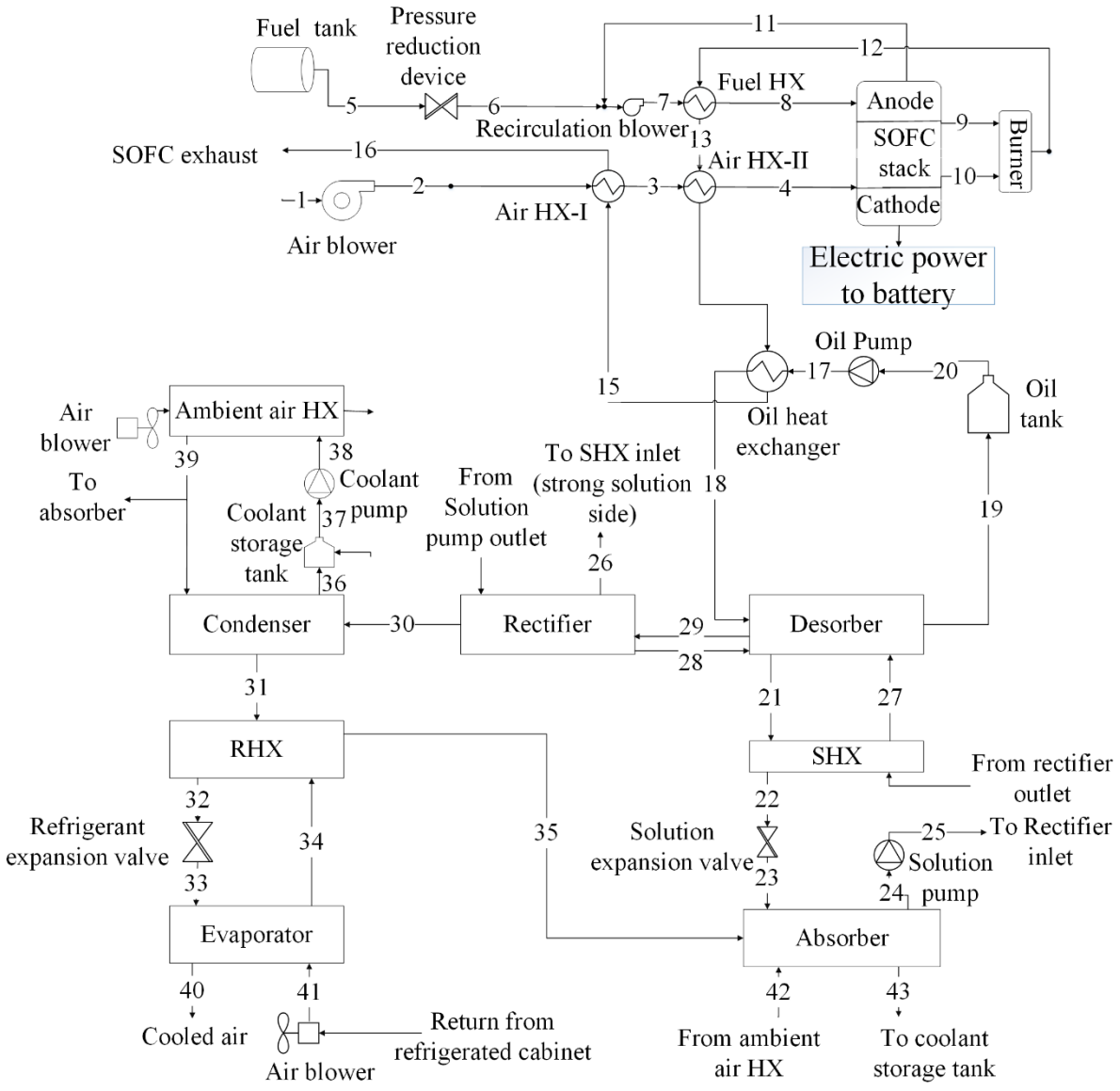

Figure 5-20 : SOFC integrated VARS combined system layout for the steady state analysis.

5.5 Operating Envelope of SOFC System

It was essential to characterise SOFC current density-voltage and current density- power density curves to carry out further process of the simulation. The effect of current density upon

the cell voltage (V_{cell}) and power density are illustrated in Figure 5-21 and Figure 5-22 for the three different values of fuel utilisation (0.7, 0.75 and 0.8).

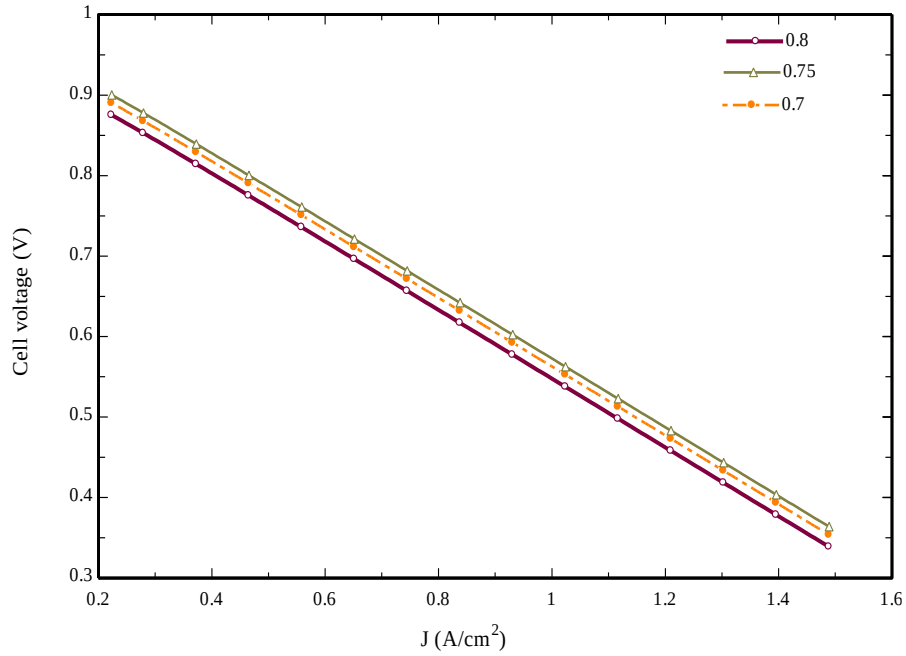

Figure 5-21 : SOFC current density-voltage curve.

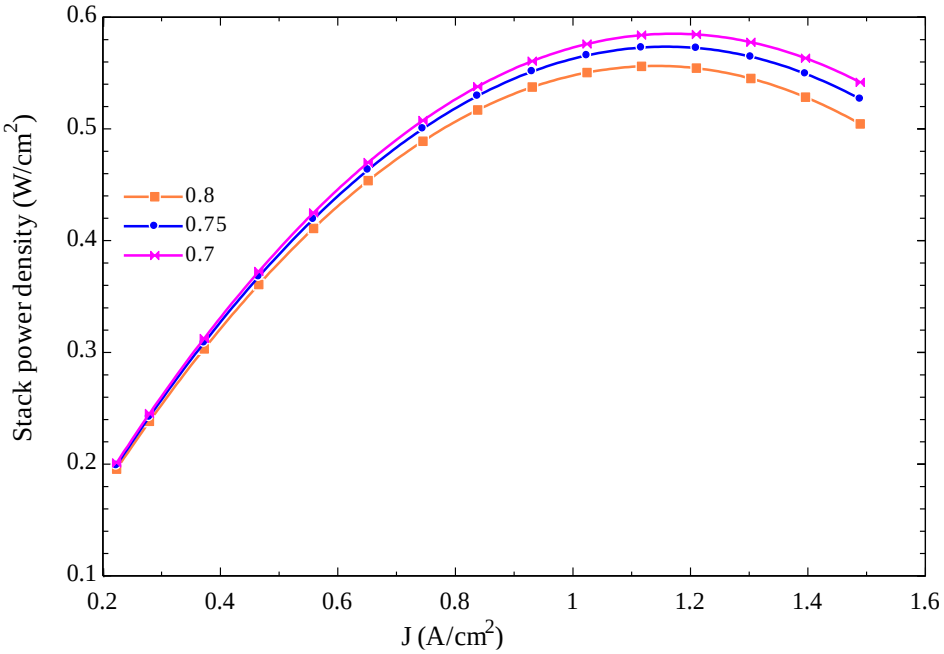

Figure 5-22 : SOFC current density-power density curve.

As current density increases, voltage losses increased (eqn.3.38), which reduced cell voltage. Higher fuel utilisation led to a decrease in partial pressure of the fuel towards the fuel channel exit, which caused the further reduction of cell voltage, as shown in Figure 5-21. Stack power density increased up to 1.1 A/cm^2 current density, and it reached its maximum value of 0.58 W/cm^2 as shown in Figure 5-22.

SOFC facilitates an opportunity to generate efficient electric power production on-board. There are interesting options available to utilise the electric power produced by SOFC on-bord. One promising way to utilise electrical power generated by SOFC is to store it in a battery to satisfy either auxiliary power or range extender for electrified trucks. In future, SOFC could also act as a prime mover to provide tractive force. Thus, the SOFC system with VARS can be integrated on trucks with three different configurations as follows:

1. Auxiliary power unit (APU): to satisfy auxiliary/hotel loads of the vehicle.
2. Range extender: to increase the range of the electric vehicles/electrified powertrain.
3. Prime mover: SOFC to provide tractive force to the vehicle.

The maximum possible auxiliary power requirements and refrigeration load of a different trucks are shown in Table 5-11 [167].

Table 5-11 : Maximum auxiliary power and refrigeration load requirements of different trucks.

Type of truck	**Maximum Auxiliary power requirement (kW)**	**Maximum refrigeration load (kW)**	**Power to refrigeration ratio**
Small	5	2.8	1.8
Medium	5	3.9	1.3
Large	15	6	2.5

The operating envelope of SOFC for all these three configurations could be different when satisfying the electrical power requirements according to targeted applications. Therefore, the next important step in the simulation process is to determine preferred operating conditions of the SOFC system to power VARS for different types of trucks.

In the next step of simulation, the fuel utilisation and current densities were selected as varying input parameters. Here, SOFC system characteristics were determined for large trucks first. Once determined, the scale of the SOFC stack was changed by varying the number of cells in the stack to meet the refrigeration load for a medium refrigerated truck and small refrigerated trucks.

5.5.1 SOFC APU application - large trucks

Contour plots were used to understand SOFC-VARS combined system behaviour in achieving 6 kW of refrigeration power. The power density is one of the critical factors in evaluating the feasibility of the SOFC system for automotive transportation; power density also significantly relies on the active area of the stack. Therefore, the first contour plot shows the results for a variation of active stack area (A_{stack}) under different operating conditions as shown in Figure 5-23. At low fuel utilisation, more unreacted fuel was available at the inlet of afterburner, releasing more heat. Hence, the required amount of heat to operate the VARS could be obtained with a lower A_{stack}, as shown in Figure 5-23. As current density increases, the inlet fuel flow rate to the system also increases which results in more fuel combusted in the afterburner and consequently the release of more heat. Therefore, if the SOFC stack operated at higher current density, the A_{stack} to achieve the required refrigeration load would be lower. It was found that the SOFC stack requires as high as 25.1 m^2 active area if the SOFC was to be operated at 0.2 A/cm^2 current density and 0.8 fuel utilisation to satisfy 6 kW refrigeration load. However, it

can be as low as 1.3 m^2 if SOFC stack is operated at 1.5 A/cm^2 current density and 0.7 fuel utilisation.

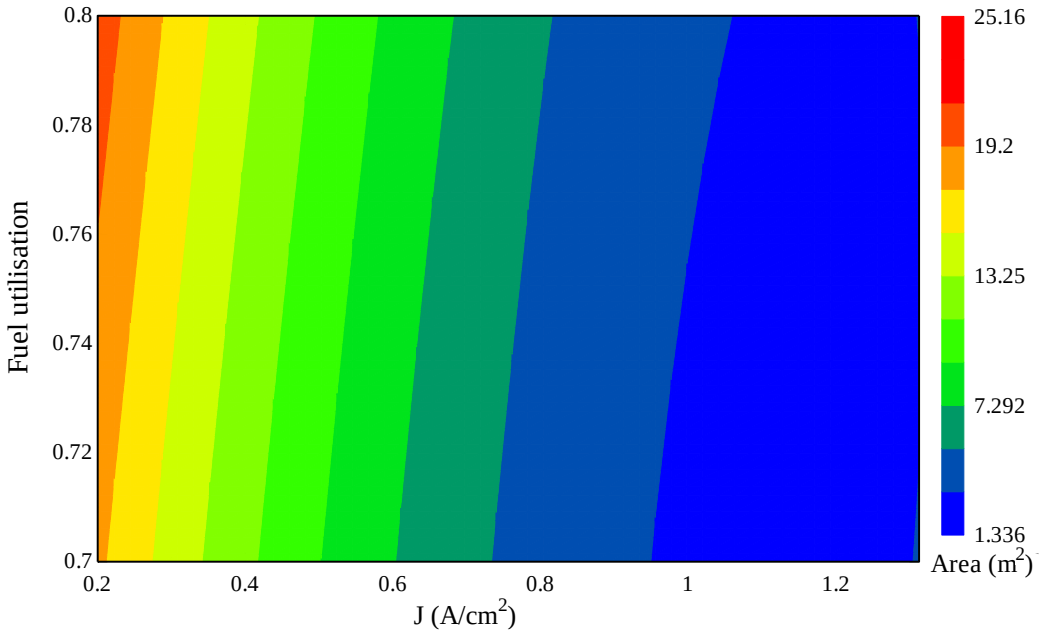

Figure 5-23 : Contour plot of stack active area requirements for 6 kW refrigeration power output.

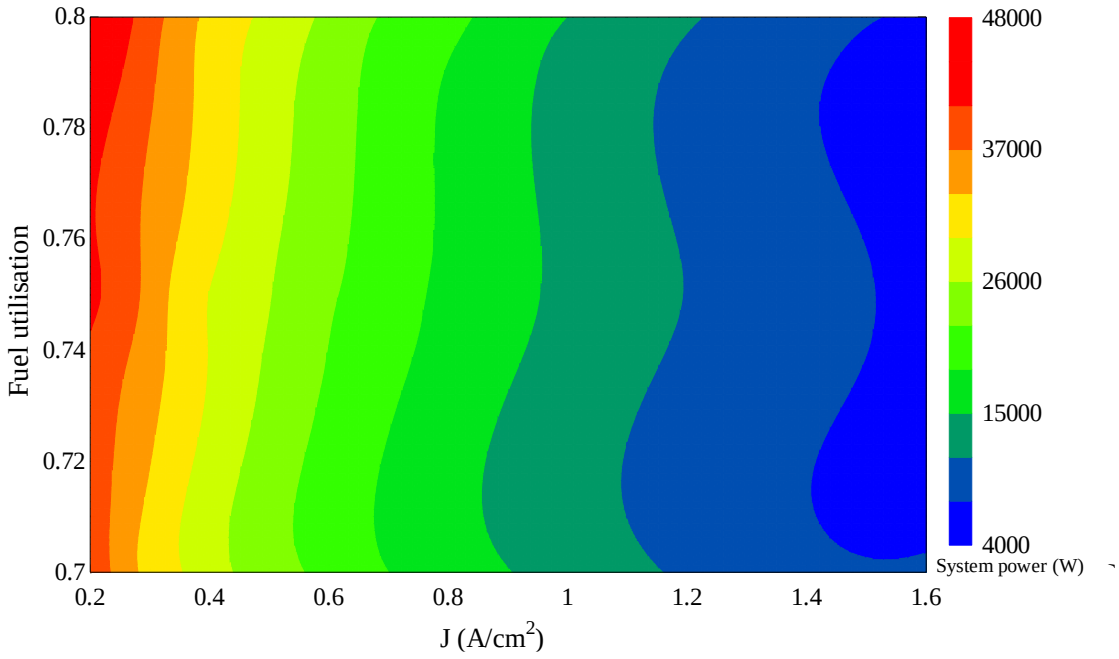

Figure 5-24 : Contour plot of SOFC system power for 6 kW refrigeration power output.

Figure 5-24 illustrates net electrical power ($P_{electric,net}$) (eqn.3.63) produced by the SOFC to achieve a 6-kW refrigeration load at different operating points. This refrigeration load can be satisfied with $P_{electric,net}$ ranging from 48 kW to 4 kW. From Figure 5-23, at higher values of current density, it follows that the required active area in the SOFC stack was reduced. A reduced stack area also contributed to reducing the $P_{electric,net}$ from the SOFC stack as the available electric power is proportional to the active stack area. In addition, a higher current density (>1.1 A/cm^2) also power density, as shown in Figure 5-22, resulting in reduced $P_{electric,net}$ at higher current density.

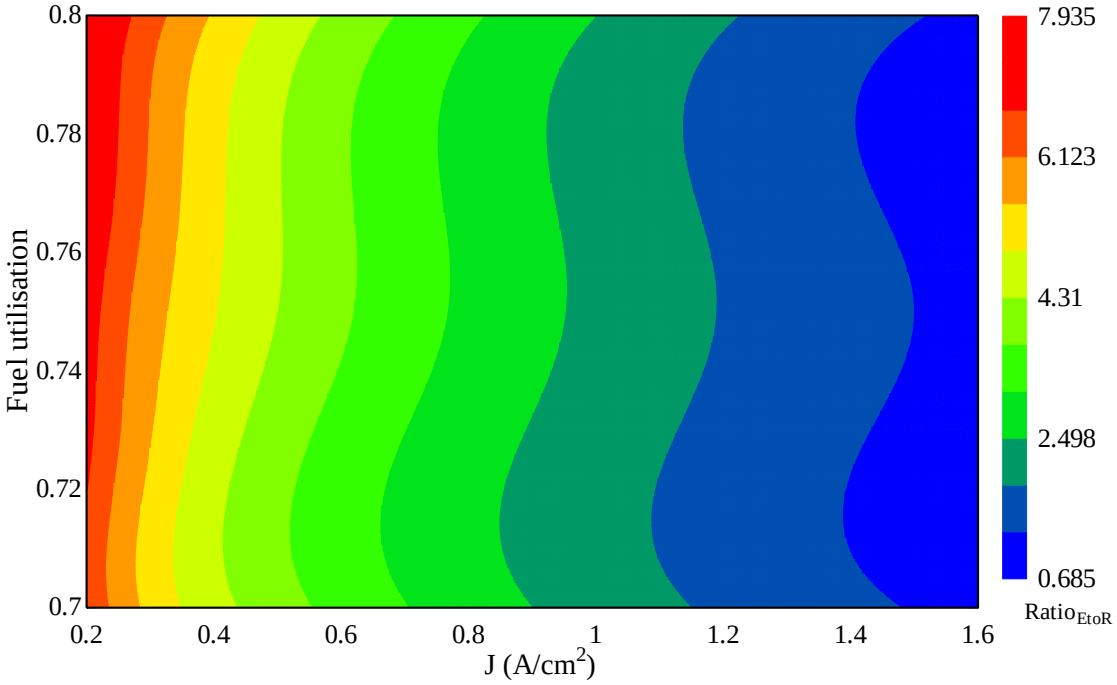

Figure 5-25 : Contour plot of system electrical power to refrigeration power ratio.

The contour map for the electrical power to-refrigeration power ratio ($Ratio_{EtoR}$) is illustrated in Figure 5-25. In this analysis, the refrigeration capacity was kept constant at 6 kW, thus $Ratio_{EtoR}$ (eqn.3.72) was also proportional to electric power. Therefore, the $Ratio_{EtoR}$ followed the same trend as $P_{electric,net}$, as shown in Figure 5-25. For large trucks, SOFC system needs

to operate at a 2.5 $\text{Ratio}_{\text{EtoR}}$ (Table 5-11). The SOFC stack needs to be operated near 0.7 to 0.9 A/cm^2 current density and preferably lower fuel utilisation in the range of 0.7 to 0.75 to achieve a $\text{Ratio}_{\text{EtoR}}$ of 2.5.

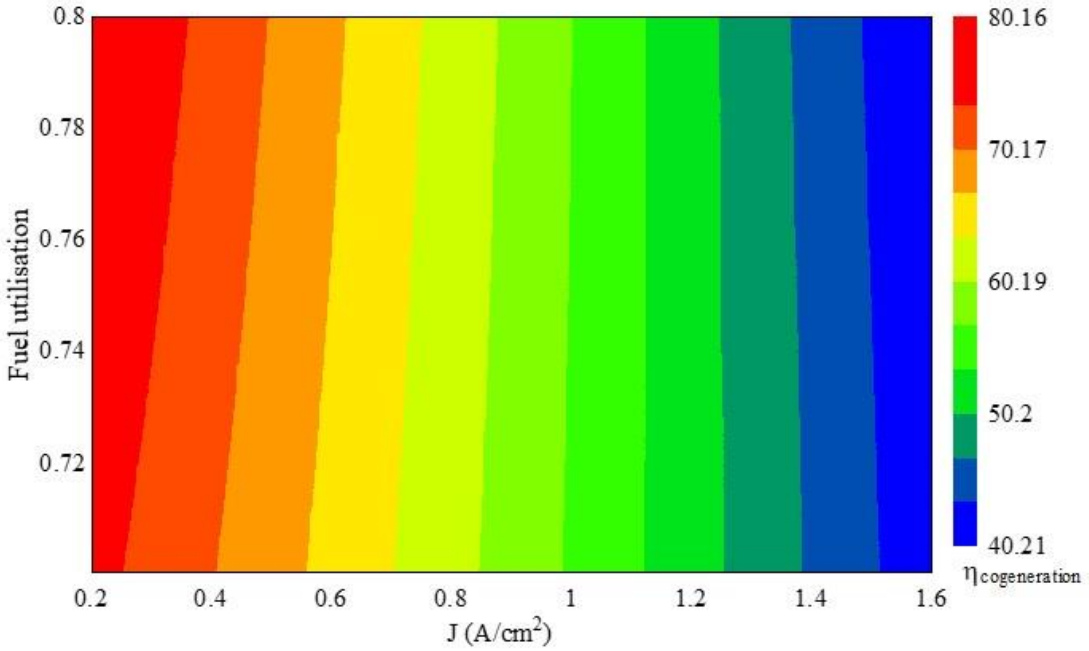

Figure 5-26 : Contour of combined efficiency.

The primary objective of integrating a VARS with an SOFC is to enhance overall system efficiency ($\eta_{\text{cogeneration}}$) of the system. Therefore, SOFC-VARS $\eta_{\text{cogeneration}}$ should be high enough to justify the integration of the SOFC with VARS. The contour plot of $\eta_{\text{cogeneration}}$ is shown in Figure 5-26. Figure 5-26 shows the combined efficiency decreased from 80% to 40% as the value of current density increased from 0.2 to 1.5 A/cm^2. It was observed that at low fuel utilisation, the combined system showed enhanced performance. This can be understood by observing Figure 5-21, since a higher cell voltage is achieved at low fuel utilisation, and system generated high thermal power at low fuel utilisation which was advantageous to drive VARS. It can be seen from Figure 5-26 that the system needs to be operated below 0.5 A/cm^2 current density to achieve higher combined efficiency (> 70 %). However, it was not possible to

achieve required $Ratio_{EtoR}$ for large truck it SOFC system operated below 0.5 A/cm^2 current density as shown in Figure 5-25. Therefore, the system must compromise its efficiency to match SOFC APU electrical and refrigeration power requirements.

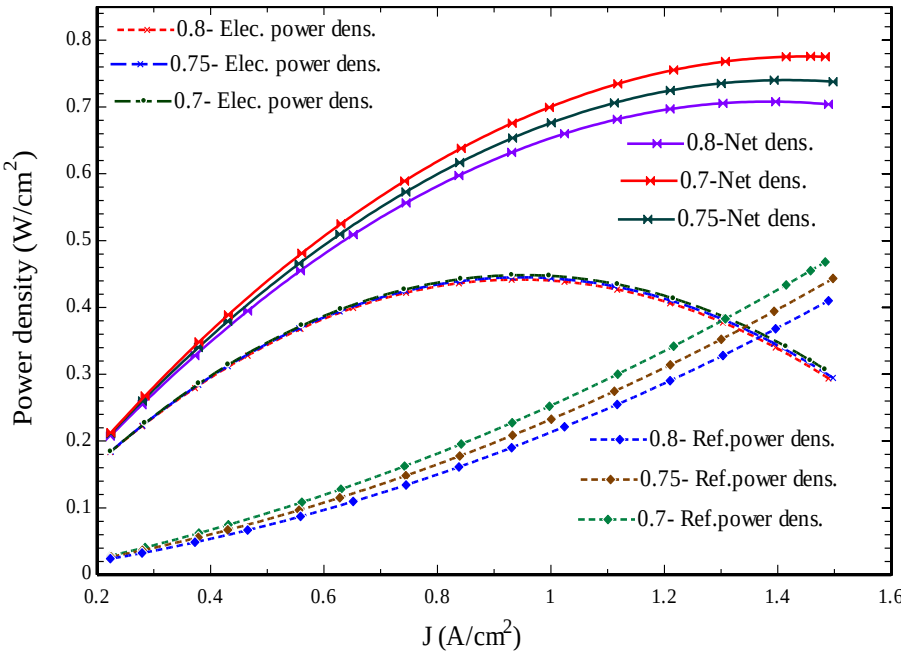

Figure 5-27 : Variation of power density at different fuel utilisation and current density.

Figure 5-27 shows the influence of current density and fuel utilisation on power density values of the system. Net electrical power density ($Dens_{elec,net}$) (eqn.3.64) increased up to 0.9 A/cm^2 current density, and further increment in current density reduced $Dens_{elec,net}$. The highest achievable system $Dens_{elec,net}$ was 0.45 W/cm^2 at 0.9 A/cm^2 current density and 0.7 fuel utilisation. At higher current density, voltage losses increased further (higher heat generation), and the required mass flow of air increased to keep stack temperature constant which increased the system's parasitic losses and reduced $Dens_{elec,net}$. However, net power density ($Dens_{net}$) (eqn.3.67) continued rising, as system generated more heat at high current density which increased refrigeration power density ($Dens_{ref}$) (eqn.3.66). $Dens_{net}$ increased remarkably up to 1.2 A/cm^2 of current density. It was observed that $Dens_{net}$ only increased by 1.6 % if the

current density increased from 1.2 A/cm^2 to 1.4 A/cm^2. However, system efficiency reduced from 50 % to 41 %, as shown in Figure 5-26 if the current. Therefore, the less efficient performance of the system could not be compensated by the increased power density if the system was operated above 1.2 A/cm^2 of current density.

$\eta_{cogeneration}$ and $Dens_{net}$ trend was the most interesting result to investigate in detail. Figure 5-26 shows that the system demonstrated high efficiency (70 % to 80 %) at low current density values. However, at a lower current density (0.2-0.4 A/cm^2), net electrical density between 0.2 and 0.25 W/cm^2, as shown in Figure 5-27 . Operating the SOFC system at such a low power density range for automotive transportation is not recommended. It is recommended to operate SOFC system at high power density (above 0.35 to 0.4 W/cm^2) [148,168]. To achieve high power density, it was proposed to operate an SOFC system around 0.6 to 0.9 A/cm^2 current density and 0.7 to 0.75 fuel utilisation. $\eta_{cogeneration}$ was not at its peak with such high current density values as shown in Figure 5-26. The high value of current density delivered enhanced power density of the SOFC system; however, it also reduced the system efficiency.

Decarbonisation of refrigerated transportation is also one of the motivations for conducting this research study. The SOFC system fuelled with hydrocarbon also emits CO_2 emissions. The operating envelope affects the carbon footprint of the system significantly. The contour plot of CO_2 emissions from the system is depicted in Figure 5-28. $Emissions$ (eqn.3.71) increased with the current density, this was due to the increased fuel consumption by SOFC stack, and more fuel being combusted in the afterburner. $Emissions$ from the system increased at low fuel utilisation, where a higher amount of unreacted fuel from the stack entered and combusted in the afterburner, enhancing emissions from the system. However, system emission was more sensitive to current density than the fuel utilisation, as shown in Figure 5-28. It was observed

that the least possible and highest Emissions from the system were 0.25 $kgCO_2/kWh$ and 0.5 $kgCO_2/kWh$, respectively. The system operation at a low current density and high fuel utilisation is advisable to make it environmentally friendly.

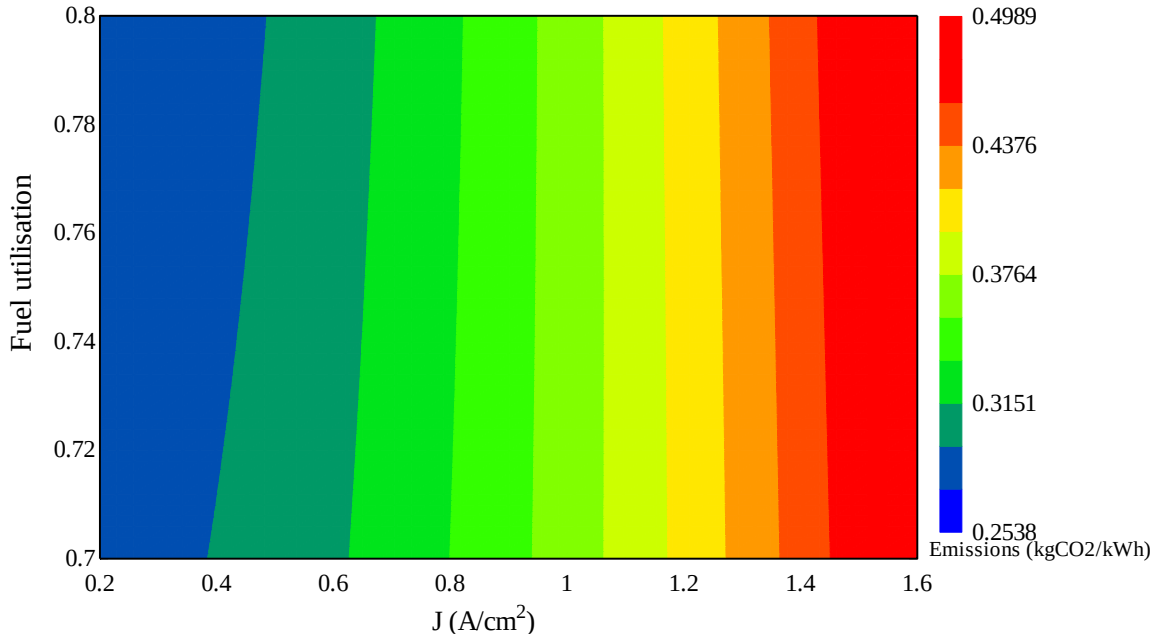

Figure 5-28 : Contour of system CO_2 emissions.

Table 5-12 shows favourable operating conditions for the most important performance parameters.

Table 5-12 : Favourable operating conditions for difference performance parameters.

Performance parameter	Min/Max	Operating conditions	
		Fuel utilisation	Current density
Emissions ($kgCO_2/kWh$)	Minimum	High	Low
$\eta_{cogeneration}$	Maximum	Low	Low
$Dens_{net}$ (W/cm^2)	Maximum	Low	High

To determine the optimum operating conditions corresponding to the three selected objective functions, a benefit function was built, and the value of the benefit function was determined at

different operating conditions. A preferred set of operating conditions was selected based on the maximum value achieved from the benefit function. Operating conditions determined at maximum benefit do not necessarily represent an optimised thermodynamic performance. Instead, the benefit function created a balance across all the selected objective functions.

$$\text{benefit function} = f\left(\eta_{\text{cogeneration}}, \text{Emissions}, \text{Dens}_{\text{net}}\right) \quad 5.2$$

$$\text{benefit function} = \frac{\eta_{\text{cogeneration}} * \text{Dens}_{\text{net}}}{\text{Emissions}} \quad 5.3$$

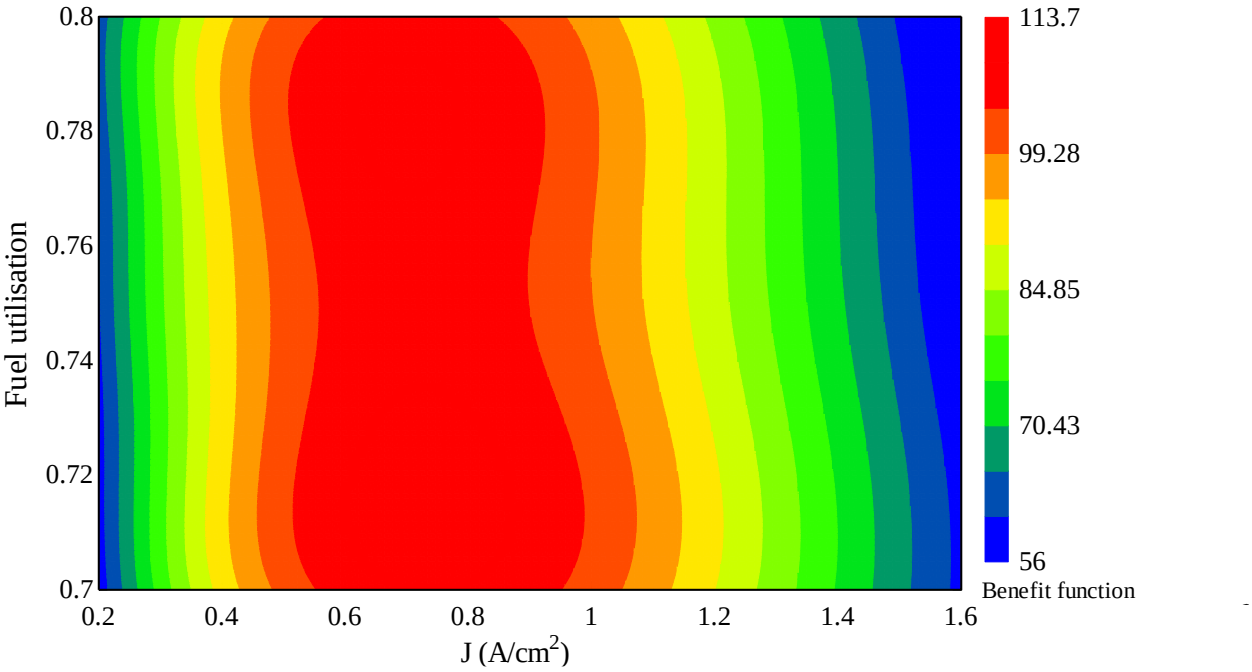

Figure 5-29 : Contour plot of benefit function.

Benefit function variation under different operating conditions is shown in Figure 5-29. It was found that the maximum value of benefit function occurred when system operation was between 0.6 A/cm^2 and 0.9 A/cm^2 current density and 0.7 and 0.75 fuel utilisation. System operation at lower current density and high fuel utilisation optimised energetic performance, cannot justify efficient thermal performance to power the VARS. In addition, these conditions

are not favourable operating conditions for SOFC for automotive transportation, where high power density is one of the requirements (above 0.35 to 0.4 W/cm^2) [148,168].

5.5.2 SOFC APU application - small and medium trucks

One of the driving factors in deciding the operating envelope for SOFC-powered VARS for APU applications was its $\text{Ratio}_{\text{EtoR}}$. As mentioned in Table 5-11, $\text{Ratio}_{\text{EtoR}}$ for medium and small trucks was even lower, 1.3 and 1.8, respectively. The same simulation methodology was used for small and medium trucks to determine the operating envelope for SOFC APU applications. Hence, it is not mentioned here to keep section short. The important findings are presented in the next sub-section.

5.5.3 Important findings – SOFC APU application

It was observed that the benefit function favoured SOFC operating envelope with high current density (> 0.7 A/cm^2) and a low fuel utilisation ($\leq$0.75) as shown in Table 5-13.

The SOFC-powered VARS combined system showed its best performance for large truck applications where higher efficiency above 60 % was feasible to achieve. The worst case was for medium trucks where the system only achieved the highest 50 % efficiency. SOFC systems focused APU for automotive transportation already demonstrated 50 % net electrical efficiency [169]. Hence, SOFC system should not operate below 50% of efficiency to power VARS (thermal power dominant performance). Therefore, the VARS should only be integrated when system efficiency can be enhanced significantly. The maximum combined efficiency of the system for small and medium trucks were found 54.6 % and 50 %, respectively.

Table 5-13 : SOFC system performance parameters at different operating conditions for different trucks.

j (A/cm^2)	**U_F**	**Benefit function**	**$\eta_{cogeneration}$ (%)**	**$Dens_{net}$ (W/cm^2)**	**Emissions (kg/kWh)**	**$Dens_{elec,net}$ (W/cm^2)**	**$P_{electric,net}$ (kW)**	**$\dot{Q}_{evaporator}$ (kW)**	**A_{stack} (m^2)**	**$Ratio_{EtoR}$**
Large trucks										
0.85	0.75	110	60	0.61	0.33	0.44	14.9	6	3.4	2.5
0.72	0.7	114	62	0.59	0.32	0.42	15.1	6	3.6	2.5
Medium trucks										
1.15	0.7	93	50	0.73	0.39	0.43	5.1	3.9	1.3	1.3
1.25	0.7	88	48.3	0.75	0.41	0.41	5	3.9	1.15	1.3
1.2	0.75	85	48.5	0.72	0.408	0.41	5.1	3.9	1.2	1.3
1.2	0.8	81	48.4	0.69	0.41	0.40	5.2	3.9	1.4	1.3
Small trucks										
1	0.7	106	54.6	0.7	0.36	0.45	5.1	2.8	1.2	1.8
0.96	0.75	101	54.6	0.67	0.36	0.44	5.2	2.8	1.3	1.9
1.28	0.75	95	51.3	0.706	0.38	0.43	4.9	2.8	1.0	1.8
1.15	0.8	89	51.2	0.68	0.39	0.42	4.8	2.8	1.1	1.7

SOFC system needs to operate at current density closer to/higher than 1 A/cm^2 for small and medium refrigerated trucks to match the $\mathrm{Ratio}_{\mathrm{EtoR}}$ demand. Therefore, employing SOFC-powered VARS for small and medium trucks does not enhance combined system efficiency significantly. However, the large truck system's efficiency improves remarkably. Thus, developing such a system for large truck is more advantageous compared to small and medium trucks. As far as SOFC APU applications for large trucks is concerned, the SOFC needs to be operated somewhere around 0.7 to 0.8 A/cm^2 of current density and 0.7 to 0.75 fuel utilisation to fulfil $\mathrm{Ratio}_{\mathrm{EtoR}}$.

5.5.4 A hybrid VARS powered by SOFC and burner

The SOFC system needs to develop as an APU to power a VARS for small and medium trucks, a hybrid VARS powered by SOFC exhaust and an additional heat source could be a novel solution, better configuration to the vehicle needs. In this configuration, the SOFC exhaust only delivers a partial amount of the refrigeration load demand, and an additional heat source supplies the remaining refrigeration load. The SOFC system is always equipped with a burner as an additional heat source. Therefore, it is possible to burn additional fuel in the burner to satisfy refrigeration load demand. A schematic of hybrid VARS powered by SOFC, and burner is shown in Figure 5-30. In this configuration, the SOFC system can be operated to satisfy electrical power requirements, and refrigeration load can be matched by both SOFC and burner. However, it is essential to determine possible efficiency enhancement with this hybrid configuration. SOFC system achieved 50 % and 54.6 % combined efficiency for a medium and small truck to match the required $\mathrm{Ratio}_{\mathrm{EtoR}}$ as mentioned in above section. Therefore, a hybrid system must deliver higher efficiency than what has been achieved already. If the hybrid system does not enhance system efficiency considerably, then it is not worth exploring a hybrid VARS

for small and medium truck APU applications. A simple analysis was carried out to find the potential of a hybrid VARS.

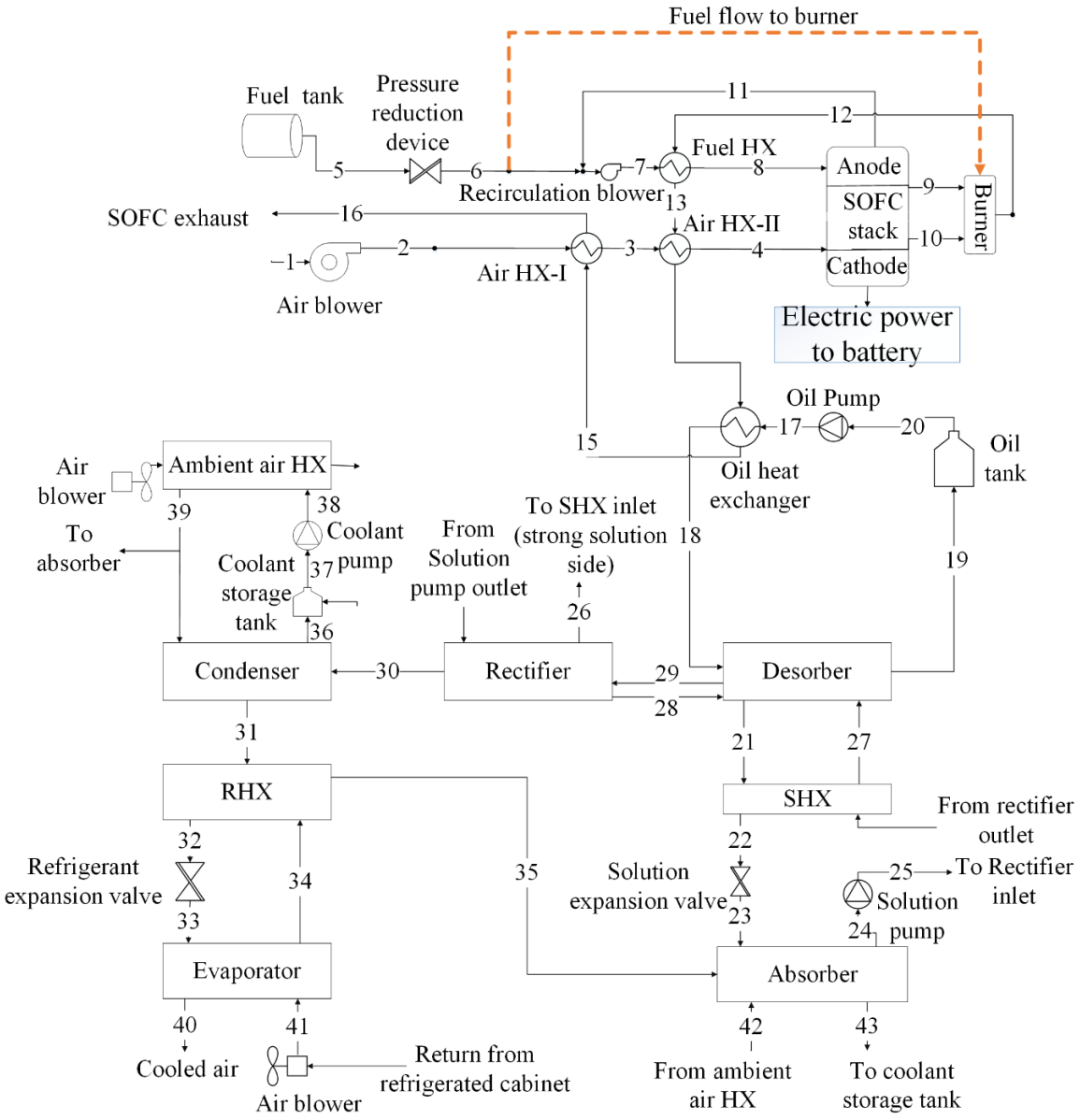

Figure 5-30 : A schematic of hybrid VARS powered by SOFC and burner.

A hybrid system possesses only a small change during operation compared to SOFC system layout depicted Figure 5-20. The fuel split to burner is always activated during nominal operation of the system with such a hybrid system. Fuel split to burner is highlighted in Figure

5-30. Apart from this small change, remaining system works same as explained in the previous section. There is a no change in the components and sub-systems in the hybrid system compared to SOFC-VARS combined system.

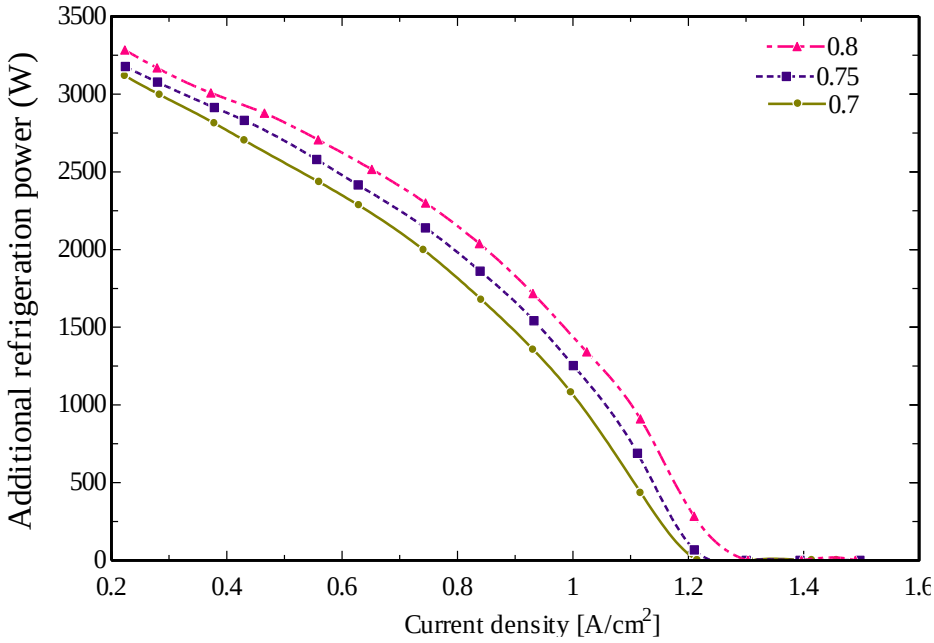

Figure 5-31 : Additional refrigeration power needed for 5 kW SOFC APU- medium truck.

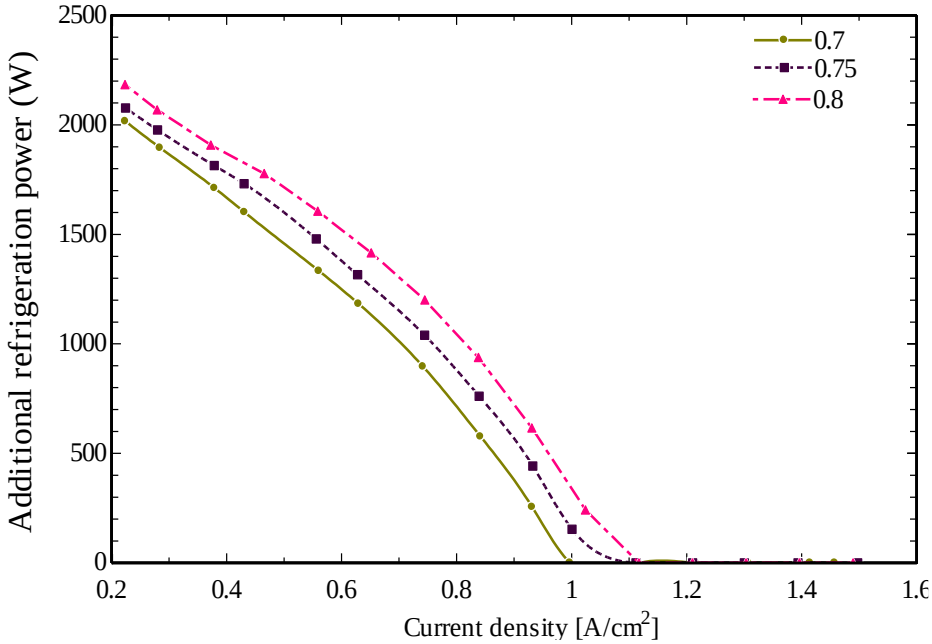

Figure 5-32 : Additional refrigeration power needed for 5 kW SOFC APU- small truck.

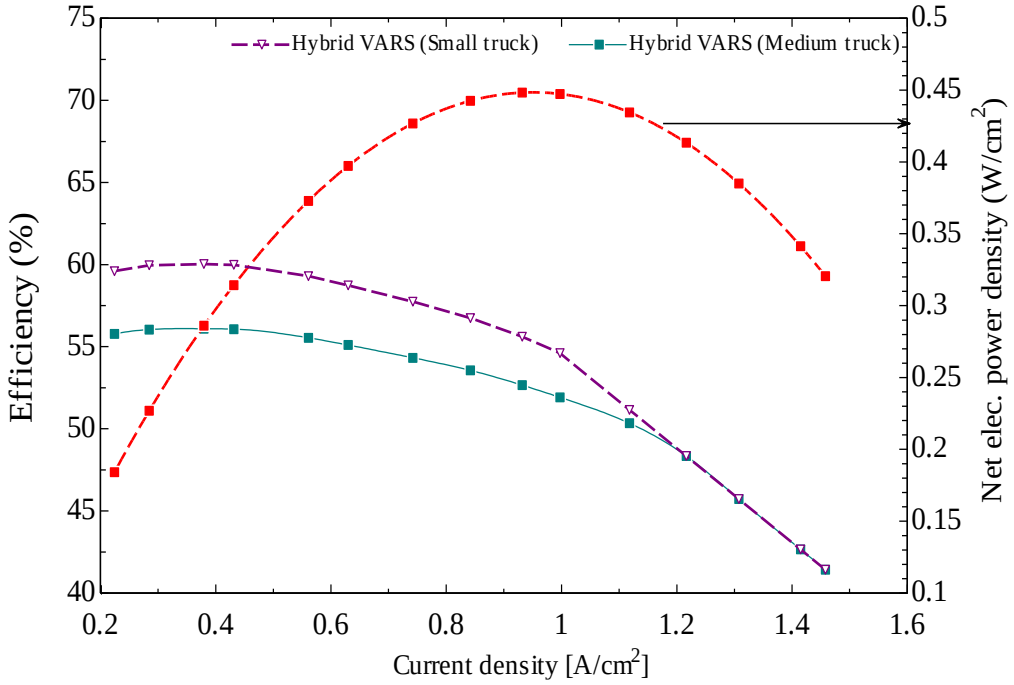

Figure 5-33 : Efficiency and power density curve of a hybrid VARS for medium and small truck.

A maximum auxiliary power requirement for both small and medium trucks, was 5 kW (Table 5-11). Therefore, a parametric analysis was carried out for a 5 kW SOFC system. The system was subjected to different current density and fuel utilisation to identify the additional amount of refrigeration load that needs to be satisfied by the burner. This is shown in Figure 5-31 and Figure 5-32 for medium and small trucks, respectively. The required refrigeration load demand for medium and small truck was 3900 W and 2800 W, respectively (Table 5-11). It was observed that the additional amount of refrigeration power needed to be fulfilled decreased with increase in current density as shown in Figure 5-31 and Figure 5-32, which was as expected. $Dens_{elec,net}$ and $\eta_{cogeneration}$ graphs are plotted at a constant fuel utilisation of 0.7 as shown in Figure 5-33. If the SOFC system would be operated at 0.38 W/cm^2 of $Dens_{elec,net}$ (in match with automotive transportation requirements) at 0.7 fuel utilisation and 0.56 A/cm^2 of current density, a hybrid system could achieve efficiency as high as 56% and 60 % for medium and small trucks, respectively. It highlights the possible improvement of the overall

efficiency of hybrid VARS systems compared to SOFC exhaust-driven VARS. SOFC exhaust fulfilled only 1450 W of refrigeration power with this operating envelope for medium and small trucks. Hence remaining 2450 W and 1350 W of refrigeration power for medium and small trucks needed to be obtained by supplying additional heat to VARS by the burner. It was also observed that at higher current density (>1.1 A/cm^2), truck size did not influence efficiency up to a great extent, it was due to enough amount of heat available from SOFC system exhaust to satisfy the maximum refrigeration load demand of 3900 W.

Table 5-14 : Comparison between SOFC-VARS and hybrid VARS for medium and small trucks.

Performance parameters	**Medium truck**		**Small truck**	
	SOFC-VARS	**Hybrid VARS**	**SOFC-VARS**	**Hybrid VARS**
j (A/cm^2)	1.1	0.56	1	0.56
U_F	0.7	0.7	0.7	0.7
$\eta_{cogeneration}$ (%)	50	56	54.6	60
$Dens_{elec,net}$ (W/cm^2)	0.43	0.38	0.45	0.38
Emissions (kg/kWh)	0.39	0.36	0.36	0.33
$P_{electric,net}$ (kW)	5.1	5	5.1	5
$Ratio_{EtoR}$	1.3	3.4	1.8	3.4
A_{stack} (m^2)	1.3	1.4	1.2	1.4
Ref. power from SOFC exhaust (kW)	3.9	1.45	2.8	1.45
Ref. power from burner exhaust (kW)	-	2.45	-	1.35
Additional heat generation in burner (kW)	-	6.4	-	3.5
Additional fuel to burner (g/s)	-	0.13	-	0.07

Table 5-14 outlines a comparison between SOFC-driven VARS and hybrid VARS. A hybrid VARS showed approximately 6 % and 5 % higher $\eta_{cogeneration}$ compared to SOFC driven VARS for medium and small trucks, respectively, as shown in Table 5-14. In addition, a hybrid

VARS emitted approximately 8 % reduced GHG emissions compared to SOFC-driven VARS even though additional fuel to burner was supplied. This was due to overall reduced fuel demand (fuel to SOFC stack and fuel to burner) with hybrid VARS compared to SOFC driven VARS. As explained above, SOFC-driven VARS should not be the preferred choice for medium and small trucks APU application due to the low $\mathrm{Ratio_{EtoR}}$ requirement. A Hybrid VARS delivered enhanced energetic performance (efficiency) and environmental performance (GHG emissions) compared the SOFC-driven VARS. Therefore, a hybrid VARS was found preferred option for medium and small truck SOFC APU applications. It should also be noted that hybrid VARS is still far more efficient (by 25 % to 30 %) compared to diesel driven conventional TRUs, which are only 30 % efficient.

5.5.5 SOFC- range extender application

Udomsilp et al [41] demonstrated that the required SOFC system power output should be higher than 15 kW for range extender application focused on long-distance driving. Hence, SOFC as a range extender for large trucks found to be most preferred application to power VARS. There is a no strict $\mathrm{Ratio_{EtoR}}$ requirement for a range extender application. This provides degree of freedom to choose the optimised operating envelope to power VARS. There are number of operating conditions feasible for SOFC range extender application to power VARS to obtain 6 kW of refrigeration power as shown in Table 5-15. Therefore, SOFC operating envelop can be chosen to achieve $\eta_{\mathrm{cogeneration}}$ and the required $\mathrm{Dens_{elec,net}}$. As shown in Table 5-15, SOFC integrated VARS for rage extender application can deliver as high as 68 % $\eta_{\mathrm{cogeneration}}$ with 0.37 W/cm^2 of $\mathrm{Dens_{elec,net}}$ (comparable to automotive transportation requirements). The SOFC system depicted a maximum 0.44 W/cm^2 of $\mathrm{Dens_{elec,net}}$ with 60 % $\eta_{\mathrm{cogeneration}}$ if the operating envelope is chosen to deliver the highest

$Dens_{elec,net}$. As far as most efficient operating envelope is concerned, the SOFC system should operate at 0.55 A/cm^2 of current density and 0.75 of fuel utilisation to achieve 68 % $\eta_{cogeneration}$ and 0.37 W/cm^2 of $Dens_{elec,net}$ and 0.47 W/cm^2 of $Dens_{net}$.

Table 5-15 : SOFC system performance parameters for range extender application-large trucks.

j (A/cm^2)	**U_F**	**Benefit function**	**$\eta_{cogeneration}$ (%)**	**$Dens_{net}$ (W/cm^2)**	**Emissions (kg/kWh)**	**$Dens_{elec,net}$ (W/cm^2)**	**$P_{electric,net}$ (kW)**	**A_{stack} (m^2)**
0.63	0.7	112	65	0.52	0.30	0.4	18.6	4.7
0.84	0.75	110	60	0.61	0.33	0.44	14.8	3.4
0.74	0.7	114	62	0.59	0.32	0.42	15.6	3.6
0.62	0.75	112	66	0.51	0.30	0.39	20.6	5.2
0.56	0.7	109	67	0.49	0.30	0.37	21	5.6
0.65	0.8	112	66	0.51	0.30	0.4	22	5.4
0.55	0.75	110	68	0.47	0.29	0.37	22.6	6.1

5.5.6 SOFC-prime mover application

The SOFC needs to generate power in the range of 120 kW to 250 kW to act as a prime mover for different types of trucks [9]. With this high electrical power generation, the SOFC generates sufficient thermal power to obtain refrigeration power demand. Therefore, to power a VARS for the SOFC prime mover application, the operating envelope should be selected to optimise $\eta_{cogeneration}$ with acceptable value of $Dens_{elec,net}$ for automotive transportation application. Therefore, the SOFC operating envelope preferred for the range extender application As mentioned in the above section can be adopted for the prime mover application as well.

5.6 Environmental Impacts of Different Technologies

A brief comparison analysis was carried out in this section to compare the environmental impacts of the SOFC integrated VARS with conventional diesel driven VCRS and recently

emerged cryogenic systems using Liquid Nitrogen (LN_2) and Liquid Carbon dioxide (LCO_2) for refrigerated transportation. The working principle of cryogenic transportation systems is presented in Appendix E.

Rai and Tassou [3,170] presented detailed methodology to compare the environmental impacts for 18 and 38 tonne refrigerated trucks for different types of food products with different refrigerated transportation technologies. In this study, the same methodology was adopted to estimate the emissions from the SOFC-VARS system relative to the functional unit of kg of food product - km of distance travelled (gCO2e/kg-km).

The following assumptions were made in the current analysis:

- Two types of trucks, an 18-tonne medium size, and a 38 tonne refrigerated trucks were considered.
- 10 % of the refrigerant content was assumed to be lost per year through leaks [171].
- The required temperature for frozen product transportation was set to -18°C.
- The food products considered in this study are shown in Table 5-16. It was assumed that all the products were pre-frozen at the required temperature before loading into the refrigerated compartment,
- The number of pallets (N_{pallet}) in the 18 and 38 tonne trucks were taken as 6 and 17, respectively, with standard stamped Euro pallets with dimensions 1.2 m × 0.8 m [3].
- A 10-hour delivery journey with door opening occurring every other hour was assumed as the transport profile.

Table 5-16 : Food products considered to compare GHG emissions

Food product	Total weight in Euro pallet (kg)
Frozen chips	640
Frozen peas	576

Total GHG emissions from the vehicle (GHG_{total}) can be expressed as the total of operational GHG emissions ($GHG_{operation}$) and emissions related to fuel production ($GHG_{production}$), this can be determined by eqn.5.4.

$$GHG_{total} = GHG_{operation} + GHG_{production} \quad 5.4$$

Further, $GHG_{operation}$ is the sum of the emissions generated to run the energy generation system (prime mover) that powers the refrigeration system ($GHG_{indirect}$) and refrigerant leakages (GHG_{direct}) from refrigeration system:

$$GHG_{operation} = GHG_{direct} + GHG_{indirect} \quad 5.5$$

The magnitude of the GHG_{direct} emissions measured in units of CO_{2eq} depends on the GWP value and leaked mass of the refrigerant ($M_{ref,leaked}$). As mentioned earlier, in this study the functional unit is kg of food product-km distance travelled and the GHG emissions were calculated as mass of CO_{2eq} per functional unit. Hence, GHG_{direct} are therefore determined as:

$$GHG_{direct} = \frac{M_{ref,leaked} GWP_{factor}}{N_{pallet} M_{pallet} D_{HGV}} \quad 5.6$$

Where N_{pallet},M_{pallet} and D_{HGV} are the number of pallets, mass of pallet and distance travelled by the vehicle, respectively. GWP_{factor} is GWP of the refrigerant used in the system.

$GHG_{indirect}$ emissions relate to emissions generated due to combustion/reaction of fuel in the energy generation system to power the refrigeration system. It can be expressed as:

$$GHG_{indirect} = \frac{M_{fuel} E_{fuel}}{N_{pallet} M_{pallet} D_{HGV}} \quad 5.7$$

where M_{fuel} and E_{fuel} are the total amount of combusted fuel (in kg) and the emission factor of the particular fuel employed (in $kgCO_{2eq}\,l^{-1}$), respectively.

$GHG_{production}$ greatly relies upon the emissions generated from the production of fuel to run the prime mover ($GHG_{fuel,prod.}$) and production of refrigerant ($GHG_{refrigerant,prod.}$). $GHG_{production}$ can be expressed as:

$$GHG_{production} = GHG_{fuel,prod.} + GHG_{refrigerant,prod.} \quad 5.8$$

where $GHG_{fuel,prod.}$ and $GHG_{ref,prod.}$ were determined as follows:

$$GHG_{fuel,prod.} = \frac{M_{fuel} * EP_{fuel}}{N_{pallet} M_{pallet} D_{HGV}} \quad 5.9$$

$$GHG_{ref,prod.} = \frac{M_{ref,} * EP_{ref}}{N_{pallet} M_{pallet} D_{HGV}} \quad 5.10$$

where EP_{fuel} and EP_{ref} are the production related emission factor of the particular fuel and refrigerant, respectively, in $kgCO_{2eq}\,kg^{-1}$.

5.6.1 Diesel driven conventional VCRS

Once the refrigeration load ($\dot{Q}_{refrigeration}$ in kWh) was determined, the required mass of diesel (M_{diesel}) to drive the refrigeration system was determined, taking the lower heating value of diesel (ε_{diesel}) as 11.8 kWh/kg [172]. Auxiliary diesel engines employed on trucks to drive the VCRS display only 20 to 25 % efficiency [173]. Out of the useful power produced by the engine, one-third is used to drive auxiliary devices and only two thirds are used to drive the compressor, contributing to cooling effect of 1.68 kWh/kg diesel which is comparable to 1.6 kWh/kg diesel illustrated by [3].

The required amount of diesel to deliver the refrigeration duty can be calculated from:

$$M_{diesel} = \frac{\dot{Q}_{refrigeration}}{\varepsilon_{diesel}} \quad 5.11$$

For diesel, the emission factor (E_{fuel}) and the production emission factor (EP_{fuel}) are considered as 2.6 kg CO_{2eq}/litter and 0.9 kgCO_{2eq}/litter, respectively [174]. R452A was assumed as the refrigerant in use in VCRS. The production emission factor (EP_{ref}) for R452A was taken as 0.214 kgCO_{2eq} /kg of refrigerant [3] and the GWP_{factor} as 2,141 [175]

5.6.2 Cryogenic transportation

The required properties such as specific heat (c_p), specific latent heat of vaporisation (L_v) and saturation temperature (T_{sat}) of the cryogenic fluids were determined from the EES library. The LN_2 and LCO_2 pressure in the vehicle tank was assumed to be 3 bar and 8.6 bar, respectively [176]. The required mass of LN_2 and LCO_2 to satisfy the journey cooling load were determined from:

$$\dot{Q}_{refrigeration} = M_{LN_2}\left(L_{v_{LN_2}} + c_{p_{LN_2}}(T_{refrigeration} - T_{sat_{LN_2}})\right) \quad 5.12$$

$$\dot{Q}_{refrigeration} = M_{LCO_2}\left(L_{v_{LCO_2}} + c_{p_{CO_2}}(T_{refrigeration} - T_{sat_{CO_2}})\right) \quad 5.13$$

The production emission factors (EP_{ref}) for LN_2 and LCO_2 were taken as 0.254 kgCO_2/kgLN_2 and 0.305 kgCO_2/kgCO_2, respectively [3]. The GWP_{factor} for LN_2 and LCO_2 was taken as zero and one, respectively.

5.6.3 SOFC-VARS combined system

The production related emission factor for methane (EP_{fuel}) was taken as 0.69 kgCO_2-eq/kg CH_4 [177] and for NH_3 (EP_{ref}) 0.840 kg CO_2-eq/kg NH_3 [178], respectively. The GWP_{factor} for ammonia was considered zero [179]. Figure 5-34 depicts the approach to determine total GHG emissions from the different refrigerated transportation technologies.

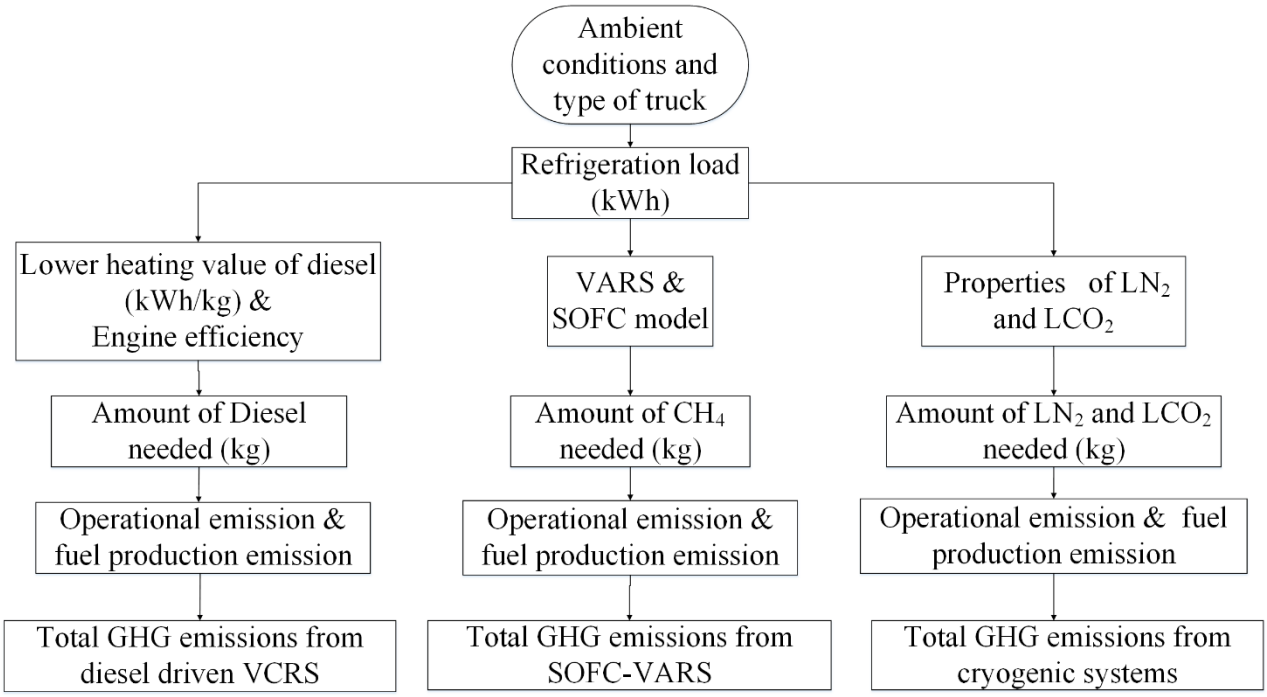

Figure 5-34 : Methodology for determining the GHG emissions from different transportation refrigeration technologies.

5.6.4 Average refrigeration load demand over a year

The average monthly temperature to calculate refrigeration demand load over a year is taken from the study caried out by Rai and Tassou [3]. The refrigeration load demand over a year is shown in Figure 5-35.

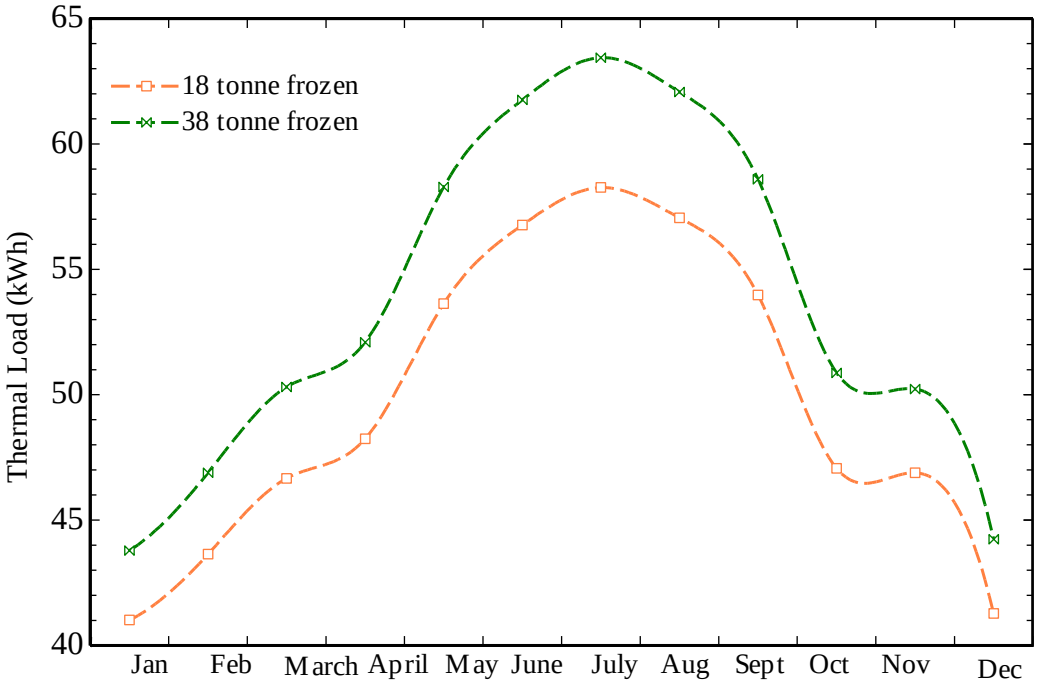

Figure 5-35 : Average monthly refrigeration load of 18 and 38 tonnes trucks in the average UK climate for a daily cycle of 10 hours.

5.6.5 Amount of fuel needed for different technologies

The VARS and VCRS technologies require heat and electricity to run the refrigeration systems, whereas the cryogenic systems 'merely' work with an inert gas, though liquified. It was therefore hardly possible to compare these technologies on the merits of fuel or energy consumption unless the full life cycle was taken into account. As the analysis presented here concentrated on GHG emissions, comparison of technologies accomplished based on the amount of 'driving substances' the vehicle is required to carry, which would also reflect in the volume of tanks required, an aspect that is, though, not discussed here. This will be methane for the VARS, diesel for the VCRS and the respective cryogenic gases for the LCO_2/LN_2 systems. Amounts will be converted via the fuel use of the SOFC and the main diesel engine, respectively, for the fuel driven systems.

Table 5-17 : Amount of CH_4, diesel, LCO_2, LN_2 and required for 10 hours of journeys in UK climate.

Fuel		**18 Tonne**	**38 Tonne**
CH4 (kg)	average	26.2	28.3
	min.	23.4	24.3
	max.	30.1	31.9
Diesel (kg)	average	31.2	33.9
	min.	25.6	27.7
	max.	36.8	40.3
LCO2 (kg)	average	504.5	544.1
	min.	417.2	446.2
	max.	592.3	644.1
LN2 (kg)	average	539.5	583.1
	min.	446.2	477.2
	max.	634.5	691.3

Table 5-17 shows the average and peak amounts of CH_4, diesel, LCO_2, and LN_2 required for 10-hours of product transportation over a year as depicted in Figure 5-35. It was found that the CH_4 fuelled SOFC-VARS showed least fuel demand followed by conventional VCRS, and LCO_2 and LN_2 cryogenic transportation. Cryogenic transportation refrigerant flow varied between 41 kg/h and 69 kg/h. Fuel intensity (fuel used per hour) of conventional VCRS varied between 2.5 kg/h and 4 kg/h, while it varied between 2.6 and 3.1 kg/h for SOFC-VARS combined system, which was approximately 21% lower compared to diesel engine driven VCRS. The SOFC-VARS required approximately 95% less fuel for driving substances compared to LCO_2 and LN_2 cryogenic transportation.

5.6.6 Total GHG emissions

The GHG impact of the distribution of frozen food products with conventional auxiliary diesel engine powered VCRS, cryogenic transportation using LCO_2 and LN_2 and SOFC-VARS were determined. It was obvious that the greater refrigeration load during summer season required more fuel to match the refrigeration load demand, which followed by higher GHG_{total} emissions compared to the winter season. It can be seen from Figure 5-36 to Figure 5-39 that the conventional VCRS emitted the highest amount of GHG emissions for all considered cases, followed by the LCO_2 and LN_2 cryogenic systems, and finally the SOFC-VARS combined system. GHG_{total}emissions per kg per km from the 38-tonne truck was less compared to GHG_{total} emissions from the 18-tonne truck for all the considered food products. This was due to the higher amount of transported food (M_{food}) with the 38 tonne-truck which did not translate into the respective increase in cooling load, making the larger vehicle more efficient.

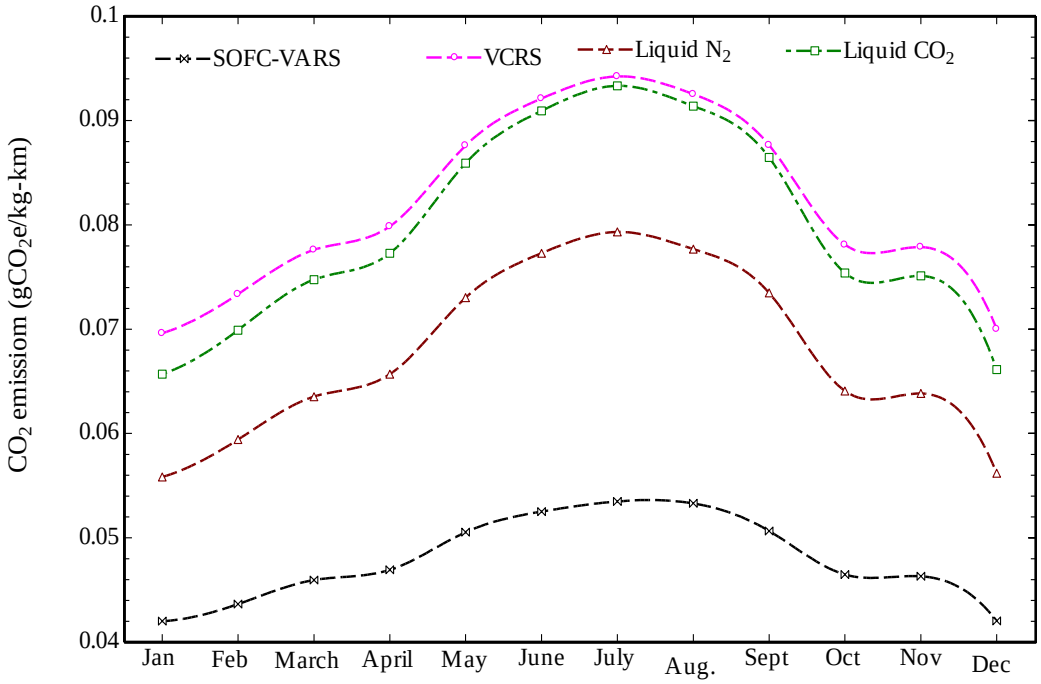

Figure 5-36 : Emissions from an 18-tonne truck over a year- frozen chips.

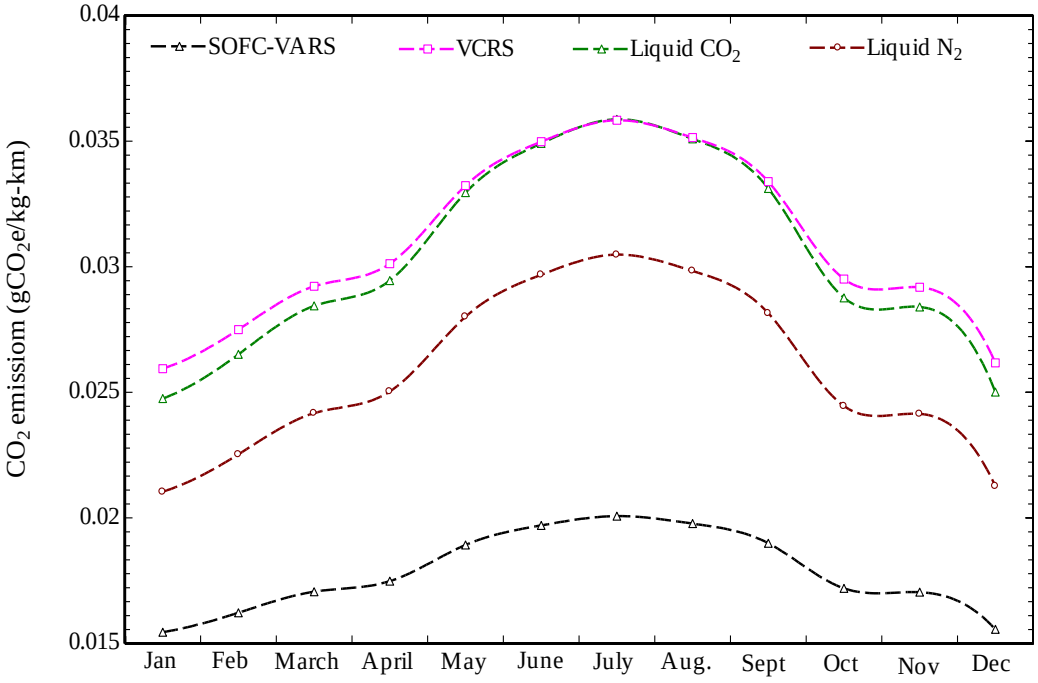

Figure 5-37 : Emissions from a 38-tonne truck over a year- frozen chips.

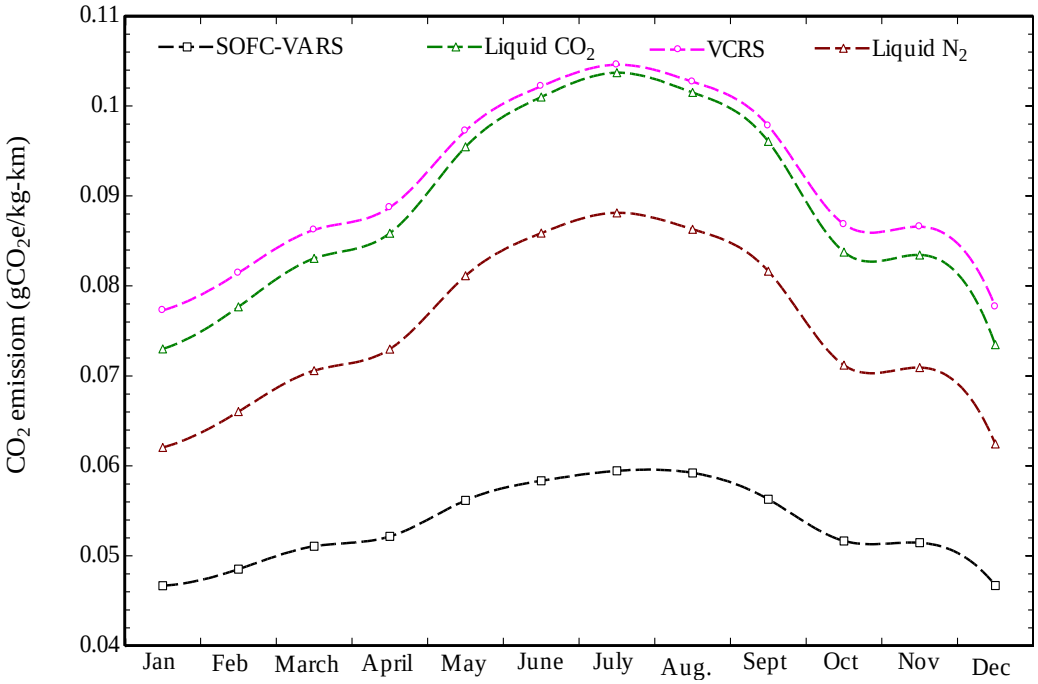

Figure 5-38 : Emissions from an 18-tonne truck over a year - frozen peas.

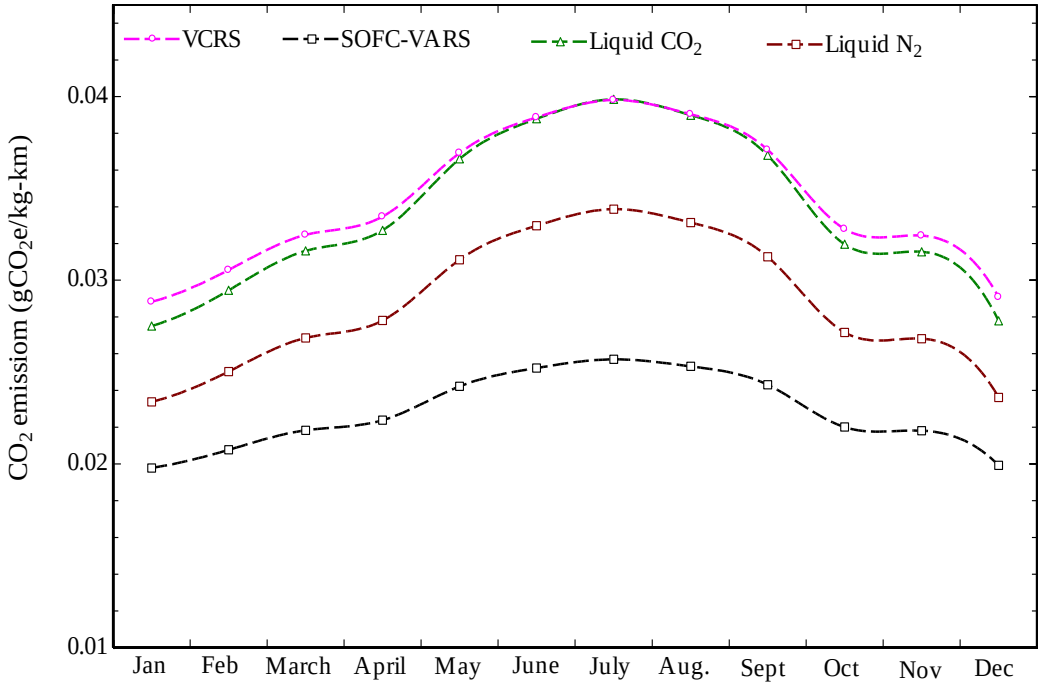

Figure 5-39 : Emissions from a 38-tonne truck over a year - frozen peas.

Table 5-18 shows the average and peak amounts GHG emissions from all considered technologies over a year for 10-hours of product transportation.

Table 5-18 : Total GHG emissions for a 10-hour journey in average UK climate.

Food products	**System**	**Total GHG emission (gCO_2e/kg-km)- 18 tonne**			**Total GHG emission (gCO_2e/kg-km)- 38 tonne**		
		average	**min.**	**max.**	**average**	**min.**	**max.**
Frozen Chips	SOFC-VARS	0.047	0.042	0.053	0.017	0.015	0.020
	VCRS	0.082	0.07	0.094	0.031	0.026	0.036
	LCO_2	0.079	0.066	0.093	0.030	0.025	0.036
	LN_2	0.067	0.056	0.079	0.026	0.021	0.03
Frozen Peas	SOFC-VARS	0.053	0.046	0.06	0.022	0.019	0.025
	VCRS	0.091	0.077	0.105	0.034	0.029	0.04
	LCO_2	0.088	0.073	0.104	0.034	0.028	0.04
	LN_2	0.075	0.062	0.088	0.029	0.023	0.034

For all considered food products distribution journeys, GHG_{total} emissions from the SOFC-VARS were approximately 25%-45% lower compared to diesel driven VCRS and cryogenic transportation.

5.7 Conclusions

A comprehensive steady-state analysis of the SOFC integrated VARS was carried out in this chapter. The SOFC and VARS modelling results were compared with the experimental studies available in the literature, both models showed satisfactory accuracy. The operating envelope of the combined system operating envelope should be selected to optimise SOFC performance, combined efficiency found to be more sensitive to SOFC system efficiency compared to the VARS COP. It was also found that the SOFC operating envelope needed to be changed for different applications. As far as APU application is concerned, $Ratio_{EtoR}$ requirement affected the SOFC operating envelope significantly. The SOFC APU application with large trucks to power VARS achieved great efficiency (≥60%) However, for medium and small trucks, it did not achieve high efficiency (≤55%). SOFC as a range extender for large trucks to power VARS shows highest efficiency of 68 % to cater 6 kW of refrigeration load.

The main takeaways of this chapter are as follows:

1. The VARS performance was found sensitive to desorber heat source temperature, and solution mass flow. The refrigeration capacity of VARS increased approximately 13% when desorber heat source increased from 473 K to 493 K. Hence, it was decided to operate VARS with 493 K of desorber coupling fluid temperature. In addition, refrigeration load was increased from 6 kW to 7.7 kW when solution mass flow was increased from 0.018 kg/s to 0.025 kg/s.

2. The SOFC system should operate with minimum possible recirculation ratio. The higher recirculation introduced great amount of steam at stack inlet which reduced the system performance. Also, a smaller amount of combustible gases entered burner with high recirculation ratio, which was not advantageous to drive VARS as system generated less heat.
3. It was found that the $\mathrm{Dens_{elec,net}}$ and $\eta_{\mathrm{cogeneration}}$ increased by 25 % and 8%, respectively when the anode inlet temperature increased from 853 K to 893 K. The change in cathode inlet temperature from 853 K to 893 K reduced $\eta_{\mathrm{cogeneration}}$ (up to 2 %). However, it increased the $\mathrm{Dens_{ref}}$ significantly (up to 20 %). Therefore, SOFC system operation with highest possible inlet should be preferred.
4. An SOFC system should be operated at low fuel utilisation (≤0.75). The operation of SOFC system at low fuel utilisation improved both electrical and thermal performance of the combined system.
5. A modified SOFC system layout was investigated for the SOFC system to power VARS. The heat exchanger network of the SOFC system played remarkable role in optimising the system efficiency. The SOFC system with modified layout showed significant improvement with approximately 10 % to 15% enhanced $\eta_{\mathrm{cogeneration}}$ compared to conventional layout. It also increased $\mathrm{Dens_{ref}}$ by approximately 150 % to 240 % at high current density compared to conventional SOFC system layout.
6. For small and medium trucks SOFC APU application, a hybrid VARS powered by SOFC exhaust and burner proved to be preferred option compared to SOFC-driven VARS. The hybrid VARS achieved approximately 5 % higher efficiency with 8 % reduced CO_2 emissions compared to SOFC-driven VARS.
7. The SOFC range extender (for large trucks) and SOFC prime mover application to power VARS for refrigerated transportation were the most efficient configurations.

These SOFC configurations generate enough heat to power VARS without compromising the electrical efficiency of the SOFC system. These configurations have excellent combined efficiency of up to 68 %.

8. The SOFC-VARS emitted approximately 25% to 45% reduced emissions over a year compared to cryogenic transportation systems and conventional diesel driven TRUs. Therefore, SOFC-VARS presented a great potential to decarbonise the refrigerated transportation.

The above steady state modelling results provide crucial information to build transient model of the combined system. Several parameters such as current density, fuel utilization, inlet temperature, and mass flow were used in the transient model which is presented in the next chapter of this thesis.

Chapter 6: *Transient Analysis of the Combined System*

A detailed transient analysis of the SOFC powered VARS combined system is presented in this chapter. The transient response of the combined system is determined for the different operational phases. The transient response of the system helps to evaluate the feasibility of the system to satisfy the end requirements in different operational phases. The system response to load following conditions is also outlined in this chapter.

Note: Certain sections of this chapter were published in 14th European SOFC and SOE Forum, October 2020, Lucerne, European Fuel Cell Forum [180].

6.1 Different Operation Phases of the System

The six operational phases of the SOFC system are considered in this chapter as shown in Figure 6-1. The characteristic of each operational phase is as follows:

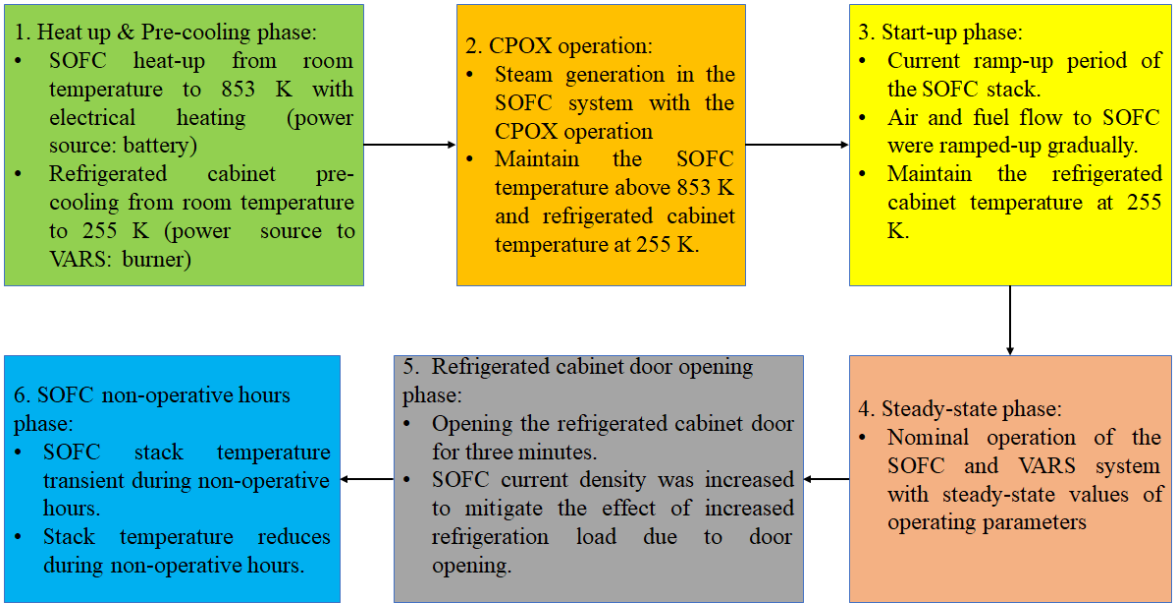

Figure 6-1 : Different operational phase of the SOFC system.

1. Heat-up & Pre-cooling phase: In the first step, SOFC needs to heat-up to its activation temperature from room temperature. In addition, refrigerated transportation requires pre-cooling of the refrigerated cabinet before a journey. In this study, SOFC system was equipped with a burner which can provide heat to the VRAS. Hence, SOFC heat-up and cabinet pre-cooling phase can take place simultaneously.

2. CPOX operation: SOFC system needs steam before entering its active operation. In this study, CPOX reformer was used to generate initial amount of steam needed for the SOFC system.

3. Start-up phase: During the start-up of the SOFC, the current is ramped-up gradually to reach its nominal value. During start-up, it is not recommended to step up the current; it is due to the possibility of rapid temperature rise (and also temperature ramp) if the current is stepped-up. The Start-up phase bridges the heat-up phase and nominal operation load point.

4. Steady state phase: The steady state phase represented the nominal operation point for the SOFC stack which was derived in the previous chapter.

5. Refrigerated cabinet door opening phase: The SOFC stack operating condition needs to change according to the refrigeration demand. Refrigeration demand always increases due to cabinet door opening. Therefore, a door opening for three minutes in an hour was considered to investigate the system thermal transient during door opening. SOFC current needed to be increased to generate more thermal power to mitigate increased refrigeration load.

6. SOFC non-operative hours phase: SOFC stack temperature reduces during a non-operative period of the vehicle due to heat losses from stack to ambient. Hence, it is necessary to require determining the SOFC stack temperate drop-in non-operative hours. The SOFC system may encounter occurrence of a non-operative period often for automotive transportation.

It was found that the SOFC system layout needed to be updated compared to what has been shown in Figure 5-20 (system layout for steady state analysis) to make the system operation feasible in all different operating phases. For transient analysis investigation, several mass flow splits and CPOX reformer were added in the SOFC system which are highlighted with doted lines in Figure 6-2. Storage tanks were considered for VARS transient analysis which was

neglected for steady state analysis. These splits were activated according to different operational phase. It should be noted that the current study did not consider control valves to regulate the flow splits because control methodology was not within scope of the current study.

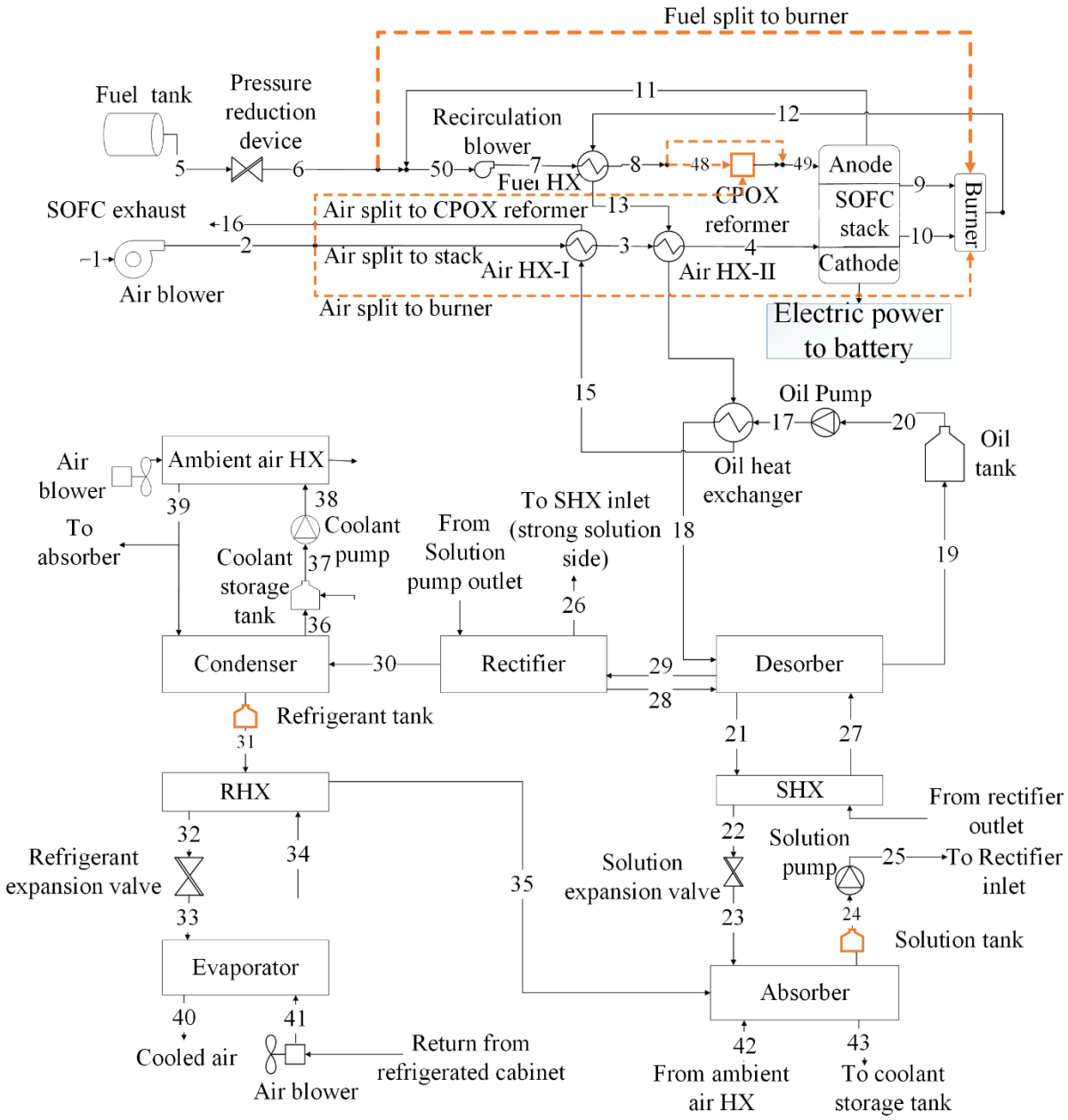

Figure 6-2 : SOFC integrated VARS combined system layout for transient analysis.

Table 6-1 represents activation of air, fuel, and exhaust mass flow splits in different operational phase of the system.

Table 6-1 : Mass flow split activation during different operational phase of the system.

Phases	Mass flow split activation
Heat-up & Pre-cooling phase	1. Air and fuel flow split to burner were activated to deliver heat generated by burner to power VARS. 2. All remaining flow splits were deactivated in this phase.
CPOX operation	1. Air and fuel split to the CPOX reformer were activated to generate steam. 2. Air split to the SOFC stack was also activated. 3. Burner exhaust split to fuel heat exchanger was activated to pre-heat feed stream entering CPOX reformer. 4. Fuel flow split to burner and burner exhaust split to oil heat exchanger were activated as CPOX operation phase did not produce sufficient heat to power the VARS. VARS was powered by SOFC exhaust and burner.
Start-up phase	1. Fuel and Air split to stack were activated to start the stack operation. 2. Burner exhaust split to fuel HX was activated to pre-heat feed stream entering stack. 3. Fuel split to burner and burner exhaust split to the oil heat exchanger were also activated as SOFC start-up phase did not produce sufficient heat to run VARS. VARS was powered by SOFC exhaust and burner.
Steady-state phase/ Refrigerated cabinet door opening phase	1. Fuel and Air split to stack were activated 2. Burner exhaust split to fuel HX was activated to pre-heat feed stream and to power VARS via oil heat exchanger. The VARS was completely powered by SOFC exhaust, burner power was no longer needed. 3. All other splits were no longer activated in this phase

Graphical representation of activated flow path in different phases is shown in Figure 6-3 to Figure 6-6.

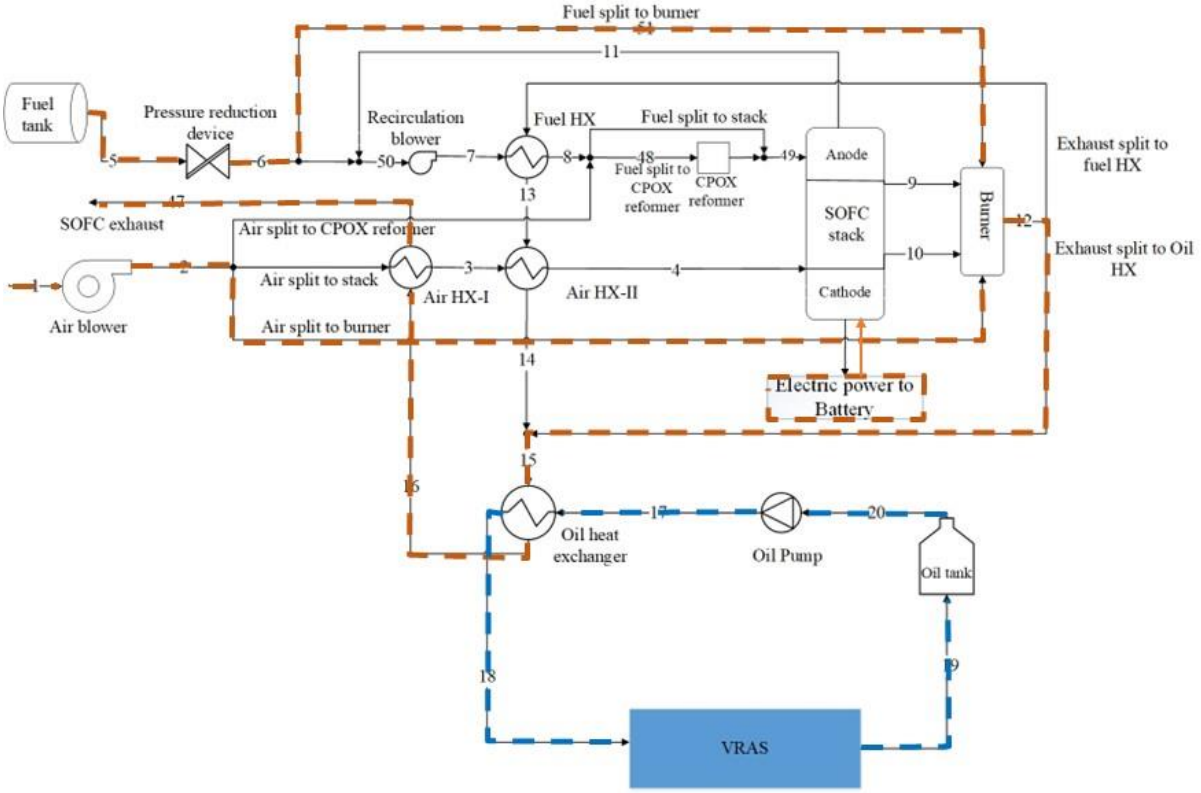

Figure 6-3 : Activated mass flow split in heat-up and pre-cooling phase.

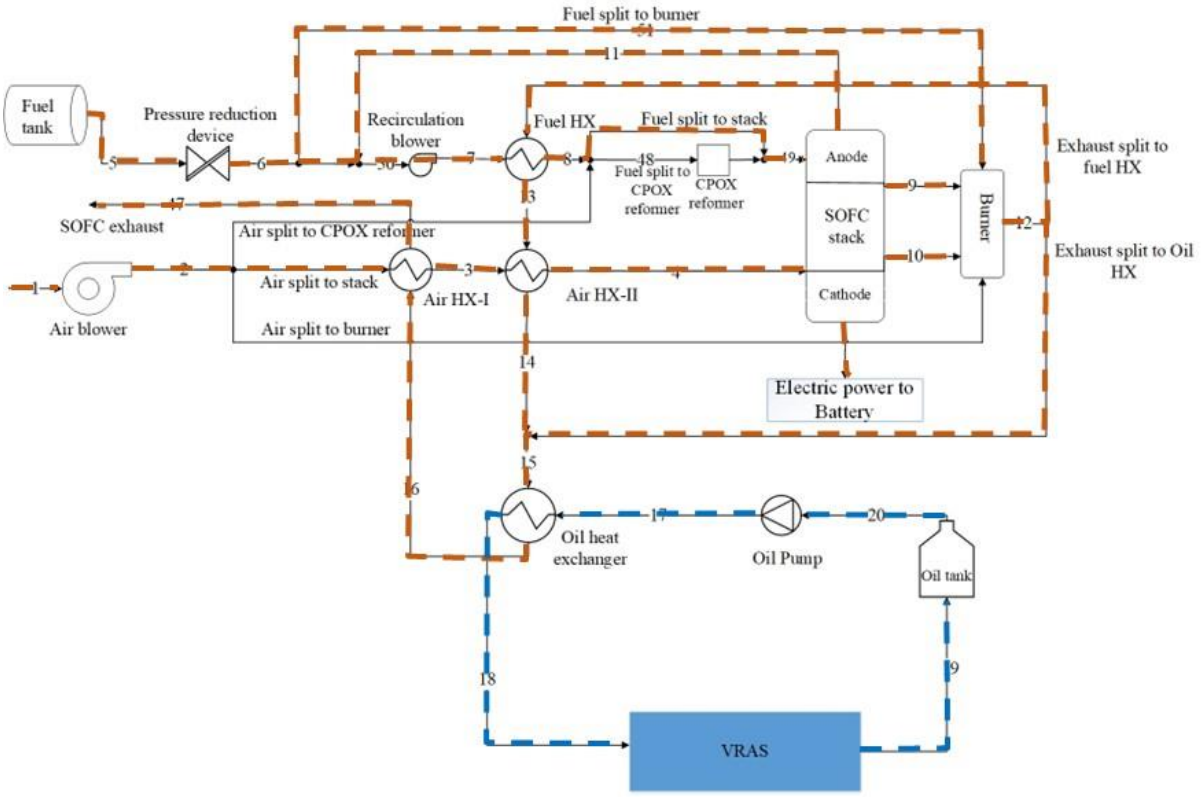

Figure 6-4 : Activated mass flow split in CPOX operation phase.

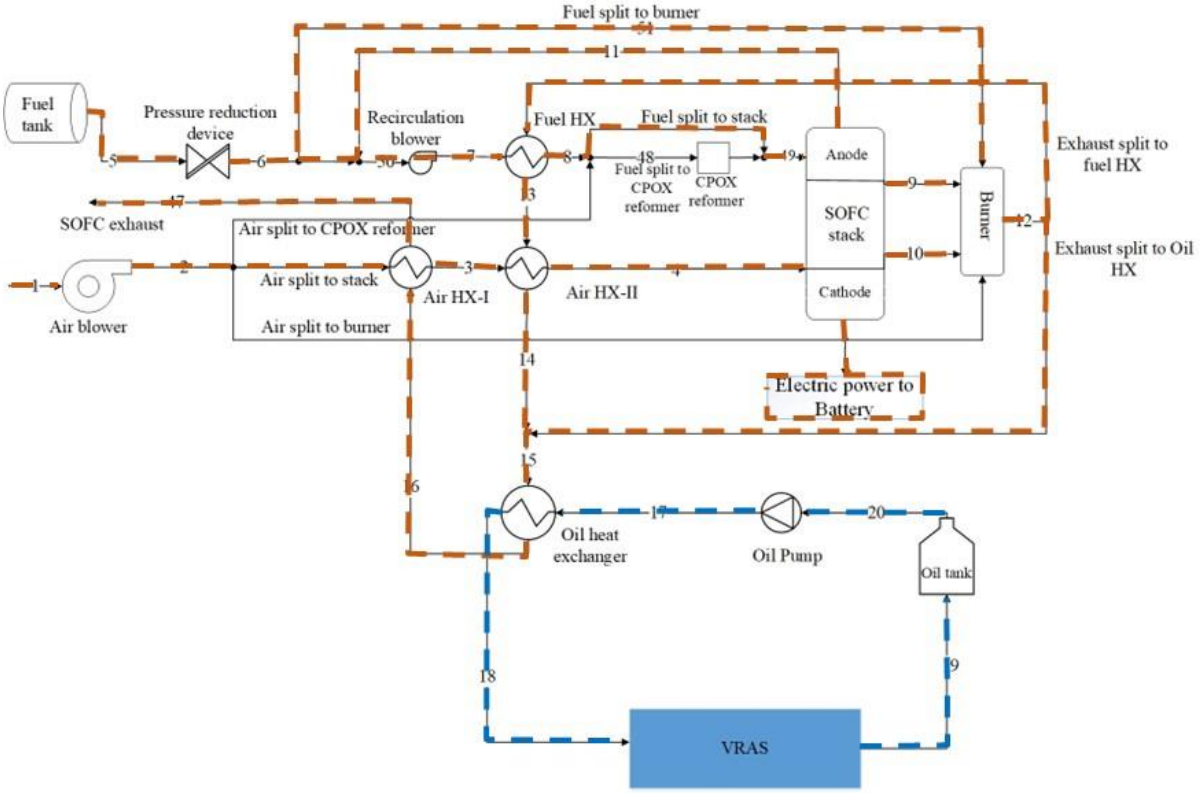

Figure 6-5 : Activated mass flow split in start-up phase.

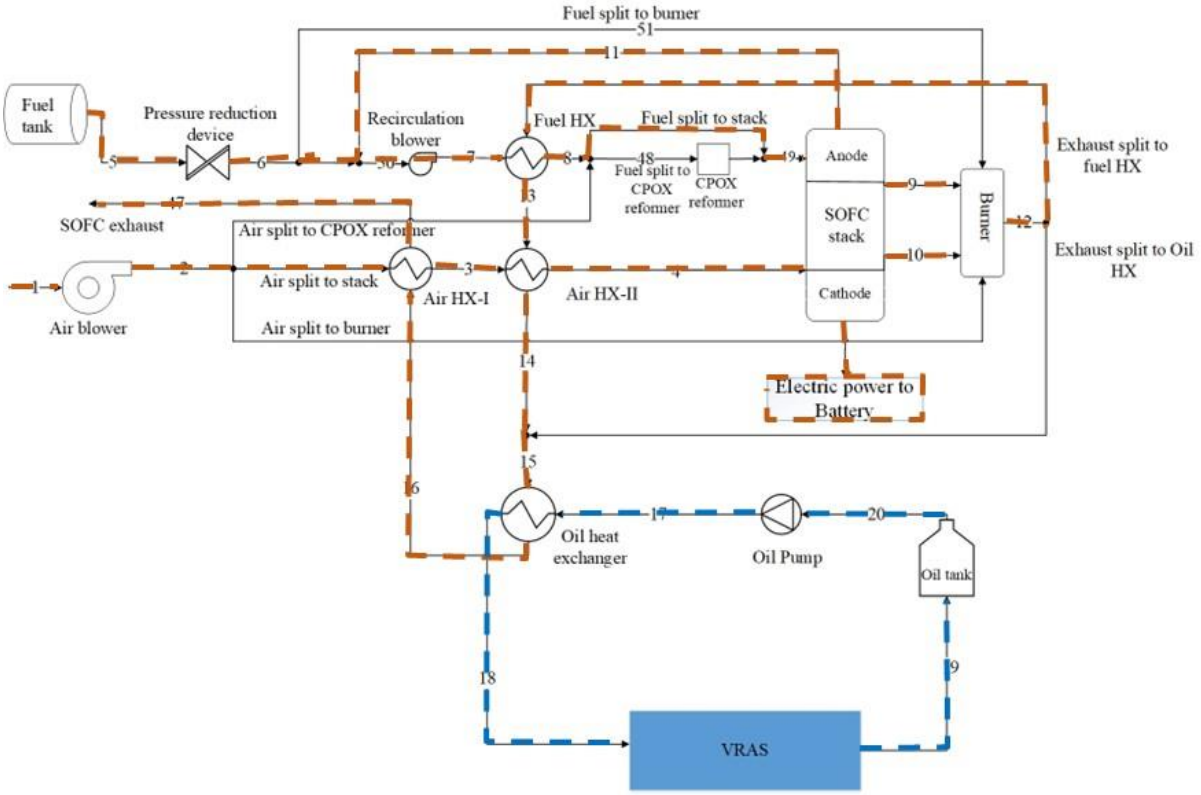

Figure 6-6 : Activated mass flow split in steady-state phase/ Refrigerated cabinet door opening phase.

As mentioned in the previous chapter (section 5.5.5), an SOFC as a range extender was the best possible configuration to integrate with VARS. It was derived that the SOFC system with 22.6 kW of power could operate 6 kW of VARS at nominal operation. Hence, transient characteristics are evaluated for a 22.6 kW SOFC system (25 kW SOFC stack) and its BoP components. The transient model of both systems was developed in MatLab/Simulink software. In the transient simulation, NH_3-H_2O properties were taken from the study carried out by Goyal [181], and gas properties for the SOFC system modelling were adopted from the EES software.

It was extremely challenging to validate SOFC system transient model due to lack of data available in the literature. In addition, literatures focused on SOFC system transient response do not contain all the required information needed to validate the system transient model. Therefore, the current study did not include validation of the SOFC system transient response. Nevertheless, steady state I-V curve has been validated in section.5.3.1. The VARS transient model was validated with results obtained from the experimental set-up as mentioned in Chapter 4:.

6.2 Heat-up & Pre-cooling Phase Transient

6.2.1 SOFC heat-up transient

The heat-up phase of the SOFC stack is one of the most challenging aspects of the SOFC systems, especially for automotive applications. Rapid heat-up of the SOFC stack is the primary requirement for automotive transportation. However, the rapid heat-up of the SOFC accelerates the thermal gradient and stresses inside the SOFC stack, affecting the SOFC system's durability and resilience. Khanafer et al. [182] conducted a comprehensive thermo-

mechanical and CFD analysis of different heat-up procedures for SOFC automotive applications. The authors considered three different heat-up ramps: exponential, parabolic and linear strategies, shown by curves A, B and C, respectively in Figure 6-7. Curve A represents the exponential relationship between time and heat-up speed, where heat-up speed gradually decreases over time. The ramp reaches a maximum value and then decreases, as depicted by curve B in Figure 6-7. Curve C is characterised by constant heat-up speed. It was observed that constant heat-up speed should be the least preferred option. It was found that the heat-up strategy with a curve A led towards more uniform temperature distribution. Uniform temperature distribution over a stack eliminates thermal stress in the SOFC stack. Curve A characterises an initial heat-up rate as high as 20.4 °C/min to a final least value of 1.3 °C/min. Authors recommended developing an SOFC heat-up strategy that can replicate curve A characteristics.

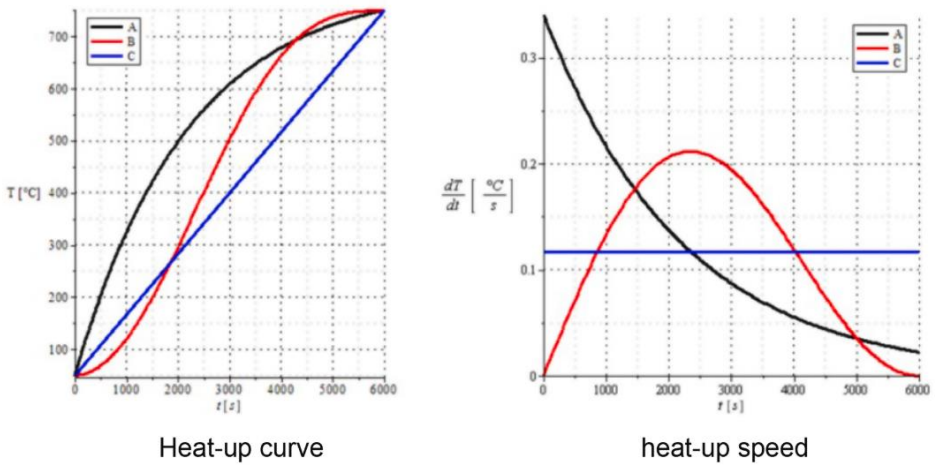

Figure 6-7 : Heat-up strategy proposed out by Khanafer et al. [182].

Bossel [183] demonstrated SOFC modules with heating element integrated into the bipolar plate, as shown in Figure 6-8. This configuration should be the preferred option for SOFC system focused on automotive applications. Integrated heating element facilitates SOFC stack

with rapid heat-up compared to conventional heat-up strategy. Conventional heat-up strategies use external start-up heater power or burner to warm up the air/gas mixture. The cathode hot air passes through SOFC channels and heats up the SOFC stack. Heat loss in the conventional heat-up process was high compared to heat-up with an integrated heating element configuration. The author concluded that 100 Wh electric energy from battery was needed to heat an SOFC stack with 16 cells (stack nominal power 200 W) to 600°C.

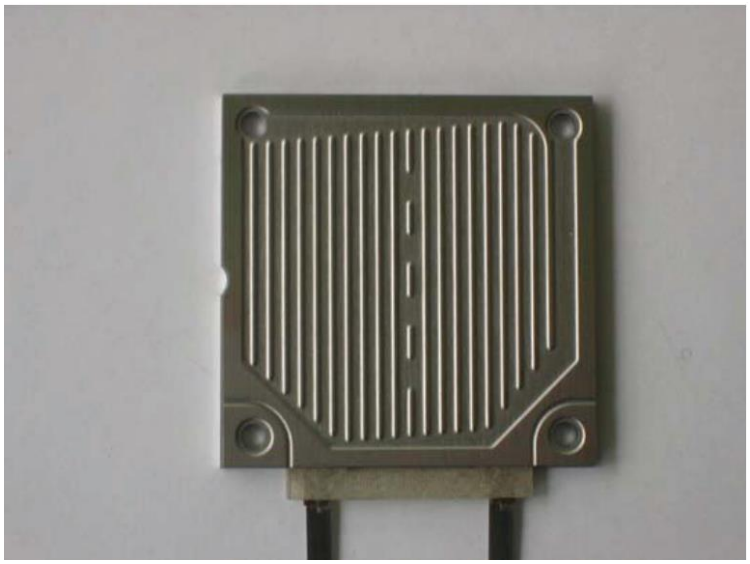

Figure 6-8 : Electrical heating element integrated SOFC bipolar plate [183].

The automotive powertrain is always equipped with a battery. Hence, electric power to the heating element can be supplied from the battery during SOFC heat-up. The battery can be recharged later during SOFC system operation. SOFC heat-up with an integrated heating element looks promising, especially for automotive transportation. Therefore, in this study, it was assumed that the SOFC stack is equipped with the heating element.

Electrical power supplied to the heating element ($P_{electric}$) was determined by using eqn.6.1. With available stack ramp ($\frac{dT_s}{dt}$), the thermal capacitance of the stack ($(mc_p)_s$) and heat losses ($\dot{Q}_{loss}$) by using eqn.6.1.

$$P_{electric} = (mc_p)_s \frac{dT_s}{dt} - \dot{Q}_{loss} \qquad 6.1$$

This study determined electric power consumption for three different heat-up strategies, as shown in Figure 6-7. It was assumed that the required amount of electrical energy to heat-up the SOFC stack was powered by on-board battery. Three different heat-up strategies were explained in the previous section are adopted here; therefore, they are only mentioned briefly here as follows:

(i) Strategy A: Temperature ramp is an exponential function with respect to time,

(ii) Strategy B: Temperature ramp increased with time up to a particular value, and then it starts reducing with time,

(iii) Strategy C: Constant temperature ramp.

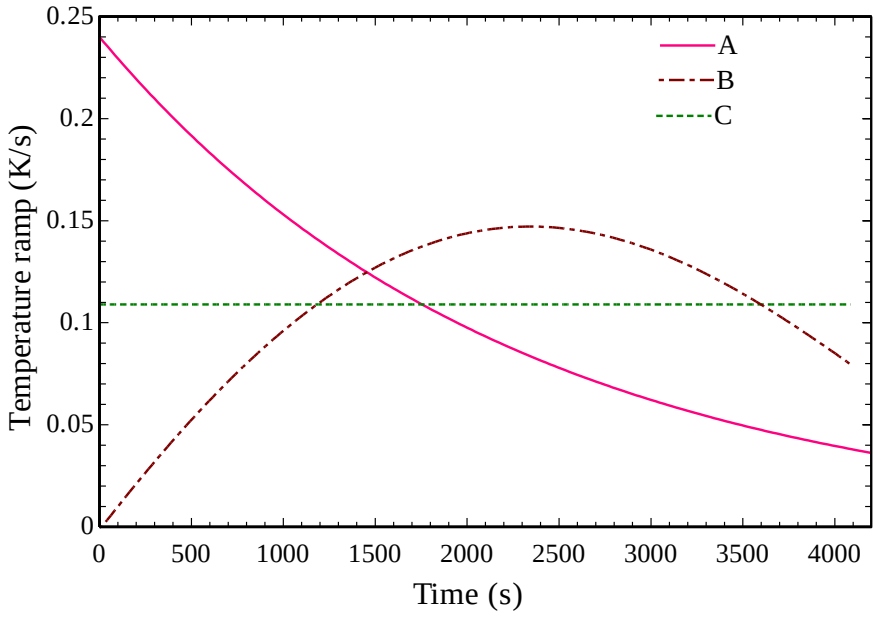

Figure 6-9 : Time function of temperature ramp (heat-up speed).

Electric power to the heating element needs to be adjusted to match the required heat-up speed according to eqn. 6.1. The time function of electrical power to the heating element is shown in Figure 6-10. The strategy A and B require 28 kW and 18 kW maximum electric power, respectively. The minimum electric power requirement for strategies A and B was roughly 4.5 kW and 9 kW, respectively. Strategy C required a constant 13 kW electric power. Commercially available SOFC stack can sustain a temperature ramp rate up to 15 K/min (0.25 K/s). Therefore, the rate of change of electrical power was selected so that the maximum temperature ramp during heat-up should not cross the limit of 15 K/min (0.25 K/s). The initial temperature of the stack was assumed to be standard atmospheric temperature (25°C). Heat-up strategy A resulted in a rapid temperature rise of the stack with strategy A compared to B and C, which can be seen in Figure 6-11. The SOFC heat-up phase tool approximately 4100 s (1 hour 10 minutes) to achieve a minimum SOFC temperature to start its operation, as shown in Figure 6-11. Heat-up of the SOFC from colder temperatures might take longer, but this is not the primary focus of this study.

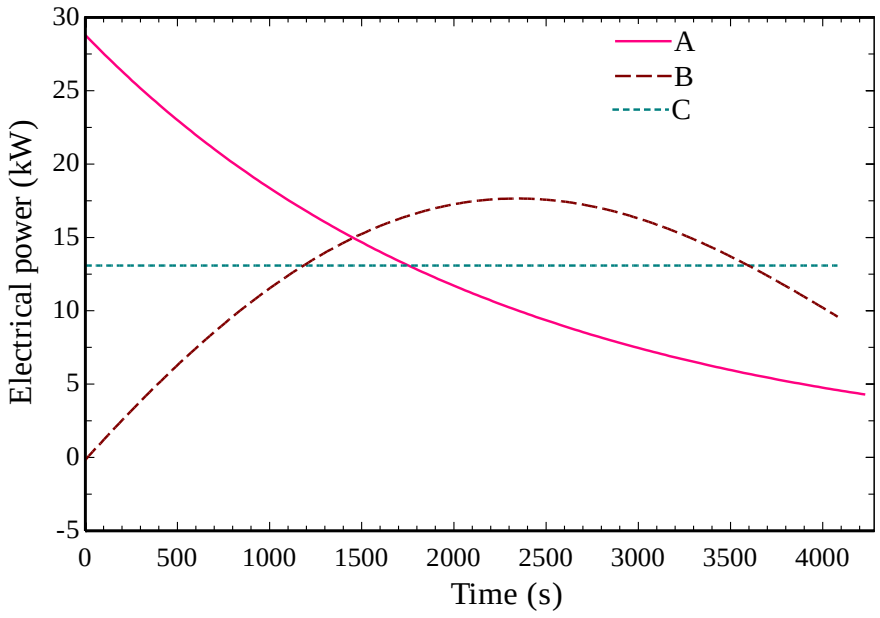

Figure 6-10 : Time function of electrical power of heating element.

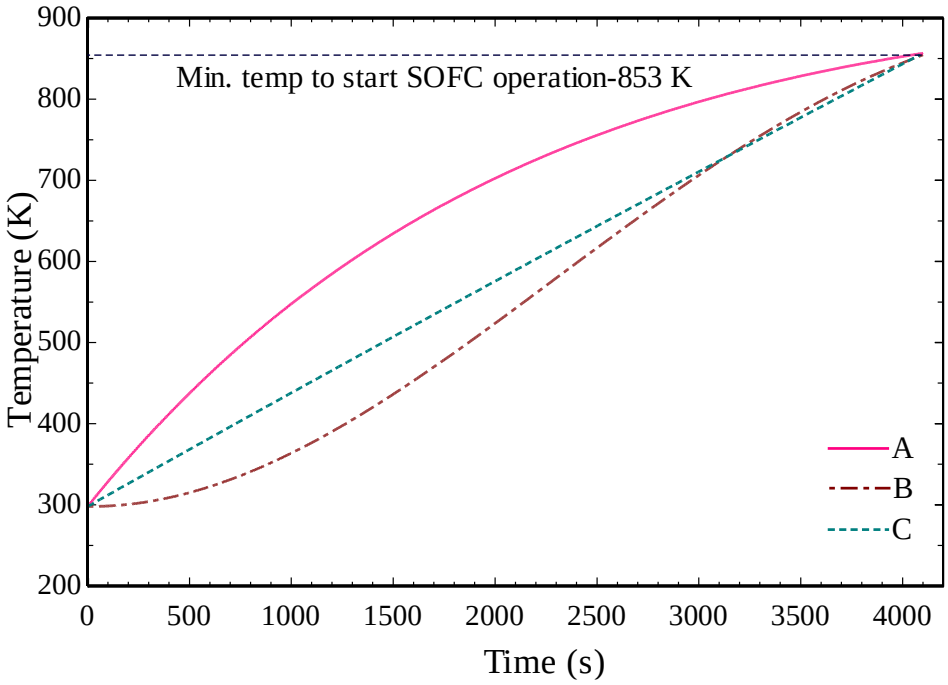

Figure 6-11 : Temperature transient during heat-up phase.

The heat-up transient analysis also helped to determine the power needed from the battery, which also decided the battery size. Table 6-2 outlines the battery capacity needed for all the heat-up strategies. It is determined that strategy A required the largest capacity battery with 15.1 kWh capacity, followed by strategy C (14.7 kWh) and strategy B (14.2 kWh). Strategy A required higher electrical power during the initial heat-up phase, resulting in the highest electrical consumption. It was found that all three considered heat strategy required approximately same energy input to heat-up the SOFC stack, required energy difference between different strategies was negligible.

Table 6-2 : Battery capacity for different heat-up strategies.

Heat-up strategy	**Battery size (kWh)**
A	15.1
B	14.2
C	14.7

Khanafer et al. [182] concluded that the heat-up of the SOFC with exponential characteristics was most beneficial for the SOFC stack. Therefore, strategy A should be recommended to heat the SOFC. The following equation eqn.6.2 describes the time function of the temperature ramp-up.

$$\frac{dT_{stack}}{dt} = 0.24 * \mathbf{exp}(-0.00045 * time) \quad 6.2$$

It should be briefly noted here that this analysis only considered the heat-up of the SOFC stack. However, a few BoP components, such as the heat exchangers and CPOX reformer also needed to heat up along with the stack. The CPOX reformer must be heated-up to its activation temperature. Heat-up of the heat exchangers and the stack should be heated-up to avoid any large temperature gradient between the components. The SOFC system is equipped with a burner. A small amount of CH_4 should supply to the burner, and hot exhaust from the burner can be used to preheat the SOFC system heat exchangers. Transient characteristics of pre-heating BoP components did not contribute significantly to the primary motive of this transient research study; hence it was not considered in the current analysis.

6.2.2 VARS pre-cooling phase transient

Once the heat-up transient was evaluated, the next step was to perform the transient analysis of pre-cooling phase of the refrigerated cabinet. The nominal load of the refrigeration system in this analysis was determined 6 kW (section.5.1). It was observed that the pre-cooling phase took less time if refrigeration system was operated at peak load than its nominal load. The concentrated solution flow and other input parameters for VARS to operate at its nominal load and peak load were taken from Table 5-5 and TableTable *5-7*, respectively. These inputs from the steady-state model were fed to the transient model. The comparison of time taken to

accomplish the pre-cooling phase is shown in Figure 6-12. The variation of refrigerated cabinet temperature was determined using eqn.3.24. It was observed that the pre-cooling phase takes approximately 4150 s and 6500 s if VARS is operated at 7.7 kW (peak load) and 6 kW (nominal load), respectively. Therefore, the VARS could be operated at its peak load during pre-cooling phase. One of the advantages of operating VARS at its peak load during pre-cooling phase was the similarity of the pre-cooling phase duration with SOFC heat-up time. The refrigerated cabinet achieved the required temperature of 255 K within 4150 s which was very close to SOFC heat-up duration, which last long, approximately 4100 s, as shown in Figure 6-11. The prolonged heat-up period is one of the significant constraints of SOFC for automotive application. However, with refrigerated transportation, a journey cannot begin without pre-cooling the refrigerated cabinet. If SOFC can achieve the heat-up phase whilst at the same time running the pre-cooling of the refrigerated cabinet, then the long SOFC heat-up period is no additional burden.

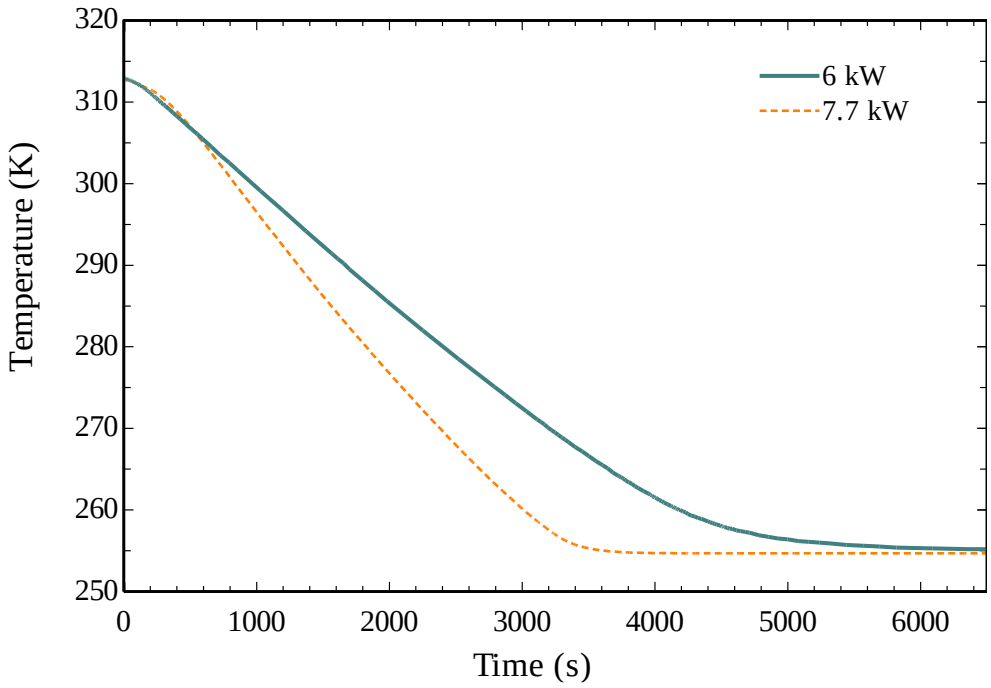

Figure 6-12 : Comparison of pre-cooling phase duration.

Refrigerated cabinet temperature variation entirely depends upon the VARS transient. Therefore, a detailed transient of each VARS component is presented below.

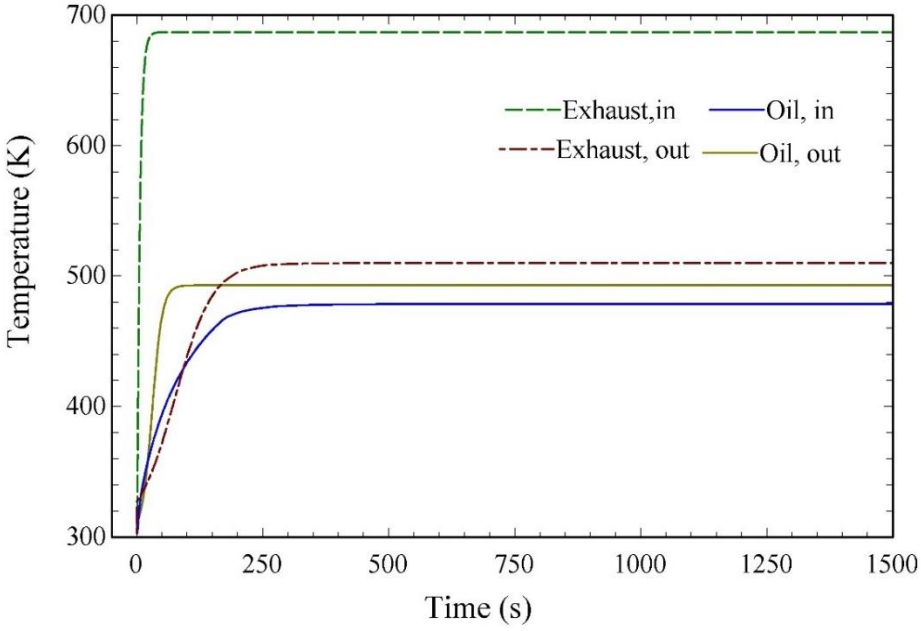

Figure 6-13 : Transient of Oil HX during pre-cooling period.

The Oil HX temperature variation during the pre-cooling phase is shown in Figure 6-13. The rapid increase in the exhaust inlet temperature (T_{12} in Figure 6-2) is understandable due to burner operation. A steady state hot exhaust inlet temperature (T_{12}) of 680 K was achieved within (~ 40 s). As explained in section 3.8.2 that, the thermal mass of the heat exchanger is added to the hot fluid side; hence, hot exhaust outlet temperature showed a slower thermal response compared to a cold fluid oil. Exhaust outlet temperature (T_{16}) attains its steady state value of 510 K after 600 s. Oil was heated up to its steady state temperature (T_{18}) of 493 K within approximately 400s. Oil and exhaust displayed a smooth temperature profile due to burner operation with constant CH_4 and air flow rate (constant power). CH_4 mass flow and air mass flow during this phase is illustrated in Figure 6-28 and Figure 6-29 respectively.

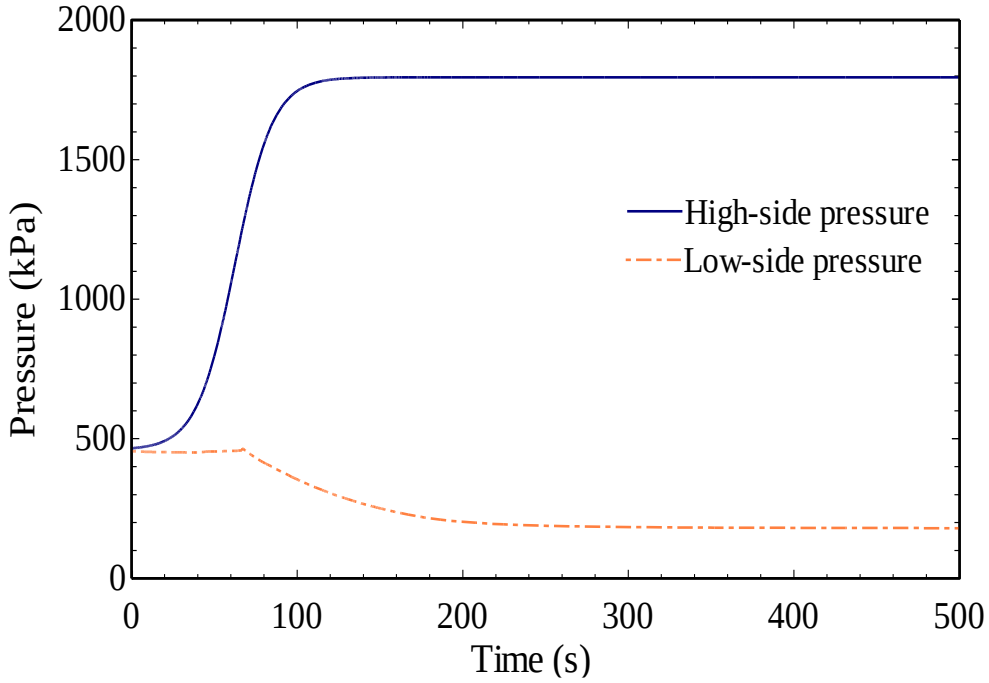

Figure 6-14 : Pressure transient of refrigeration system during pre-cooling period.

High and low side pressure transient during the pre-cooling period of the absorption refrigeration system is shown in Figure 6-14. The high side pressure encountered a rapid increase from 490 kPa to 1800 kPa from 0 s to 400 s. The rapid rise in high side pressure was expected due to a rapid rise in oil temperature from 303 K to 450 K within the initial 300 s, as shown in Figure 6-13. Heat transfer in desorber evaporated a higher amount of refrigerant vapour (NH_3) from the NH_3-H_2O concentrated solution. An increased amount of refrigerant vapour could not condense entirely in the condenser due to poor heat transfer during the initial phase of system operation. It was due to the low-temperature difference between coupling fluid and refrigerant vapour in the condenser, as shown in FigureFigure *6-15*. Hence, the refrigerant vapour as a two phases mixture enters refrigerant tank which eventually increased the high side pressure, as shown in Figure 6-14. After 250 s, the high side pressure displayed slight variation. It can be explained by presenting a variation of vapour quality at the condenser outlet. The variation of refrigerant vapour quality at the condenser outlet is shown in Figure 6-16. It shows that refrigerant vapour quality at the condenser outlet reduces from 1 to 0 within 200 s. Hence,

the high side pressure showed a slight variation after 200 s once the condenser condensed incoming refrigerant vapour completely (vapour quality zero).

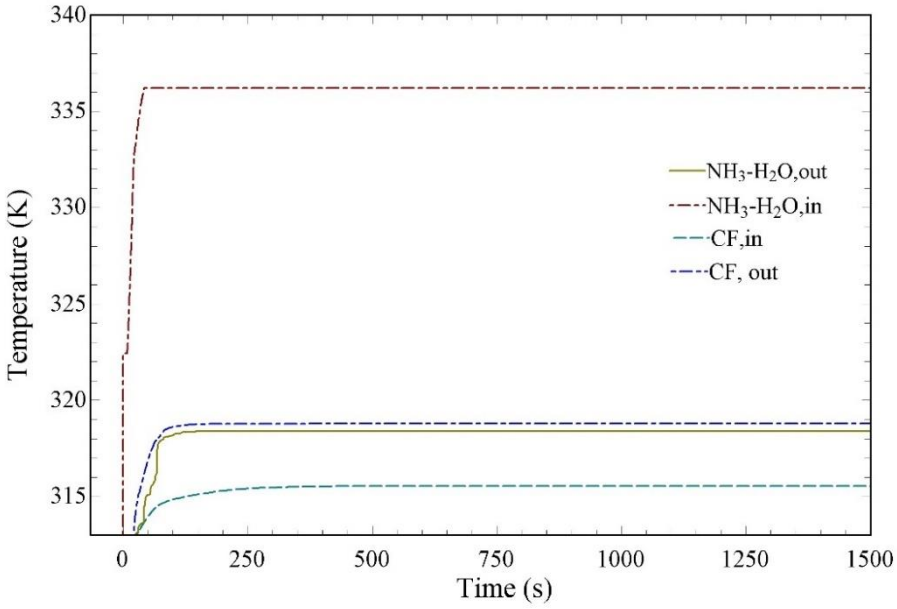

Figure 6-15 : Condenser temperature transient during pre-cooling period.

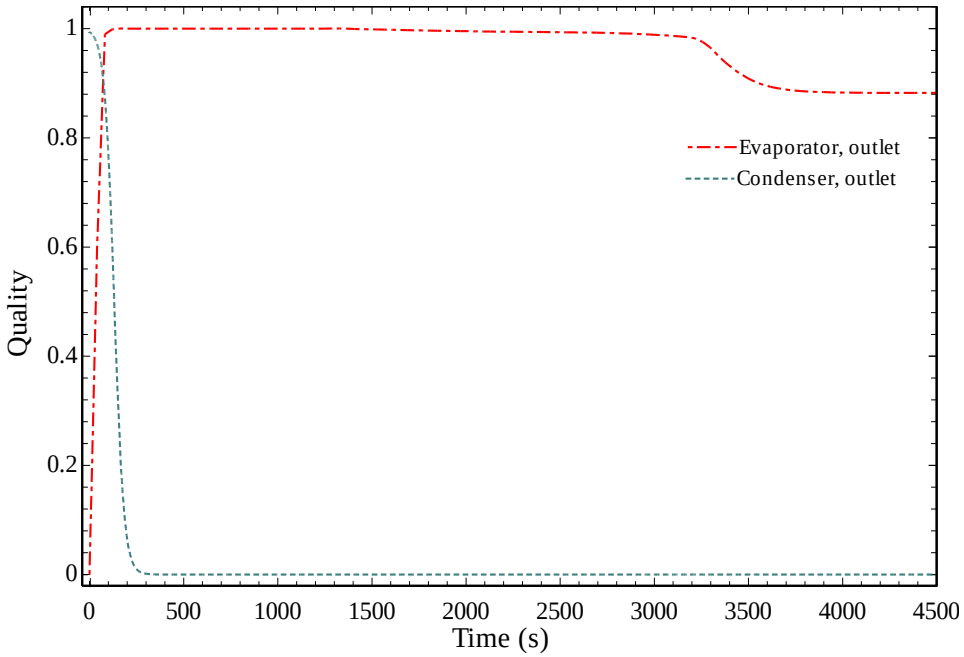

Figure 6-16 : Refrigerant vapour quality variation at condenser and evaporator outlet during pre-cooling period.

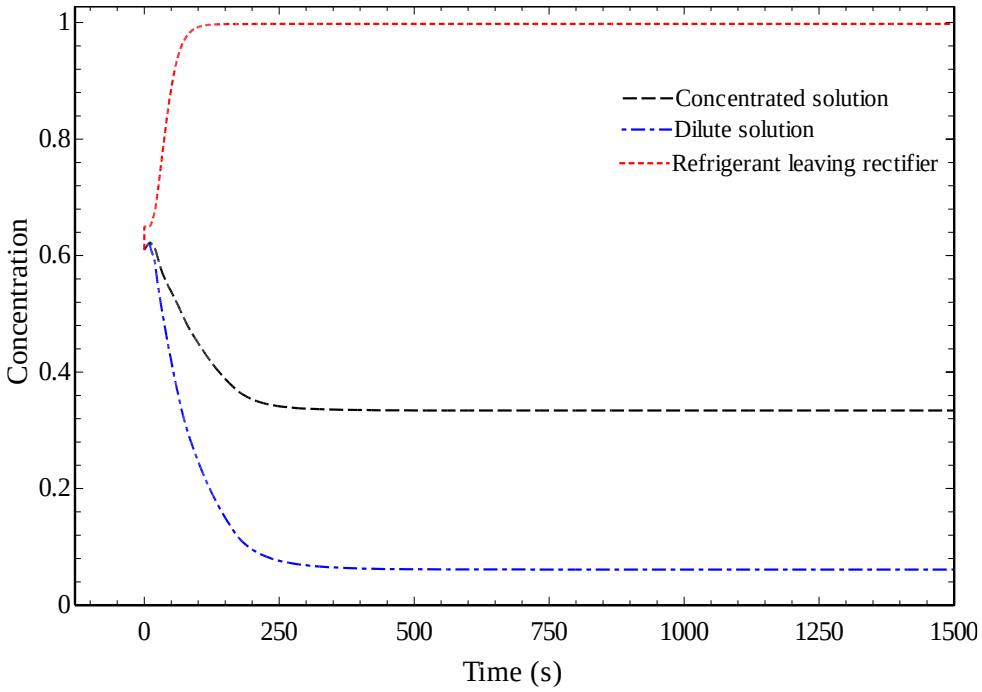

Figure 6-17 : Ammonia concentration variation in the absorption refrigeration system during pre-cooling period.

The low side pressure reduced from 485 kPa to 180 kPa from 0 s to 480 s. The low side pressure decreased mainly due to reduced ammonia concentration of the concentrated solution in the storage tank with the time evolution of the system operation. The variation of ammonia concentration in dilute solution, concentrated solution, and refrigerant vapour is shown in Figure 6-17. The ammonia concentration of concentrated solution in the solution tank decreased from its initial value of 0.61 to 0.33 from 0 s to 400 s. The concentrated solution was drawn from the solution tank during system operation by the pump; the refrigerant evaporated in the desorber, and it accumulated in the refrigerant tank. During system start-up, less amount of refrigerant flow passed through the refrigerant valve due to lower pressure difference (difference between high and low pressure), hence less amount of refrigerant entered the solution tank. It reduced ammonia concentration in the solution tank. Hence, it was evident that the pressure of the storage tank reduced with the depletion of ammonia concentration. It

was found that the high side pressure transient was faster compared to the low-pressure transients. This observation agreed with the study carried out by Viswanathan [85]. It was mainly due to the rapid refrigerant vapour generation in the desorber by heated oil, as shown in Figure 6-19.

Figure 6-18 depicts variations of concentrated solution flow rate, dilute solution flow rate and refrigerant vapour flow. The system was operated with a constant concentrated solution flow of 0.024 kg/s. The refrigerant vapour flow increased from 0 kg/s to 0.0068 kg/s from 0 s to 450 s. With time evolution of the system, heat transfer increased in the desorber, which evaporated a higher amount of refrigerant and reduced the dilute solution flow as shown in Figure 6-19. The dilute solution flow decreased from 0.024 kg/s to 0.165 kg/s from 0 s to 450 s. The dilute solution flow is equal to the concentrated solution flow rate during an initial period (up to 10-15 s) as there was no refrigerant vapour generation in the desorber. The refrigerant flow across the valve depends on the evolution of the system's high and low side pressure. The refrigerant flow rate across the valve increased from 0 kg/s to 0.0067 kg/s from 0 s to 480 s. The low side pressure achieved a steady-state value at 480 s. therefore refrigerant flow rate across the valve also followed the same trend. The refrigerant flow across the valve increased up to 200 s (from 0 kg/s to 0.0059 kg/s) due to change of high side pressure during this time window. These mass flows value is very close to its steady state value mentioned in Table 5-7.

The refrigerant concentration in the refrigerant tank increased from 0.61 to 0.997 from 0 s to 475 s due as shown in Figure 6-17. The refrigerant vapour generated in the desorber accumulated in the refrigerant tank, which eventually increased the ammonia concentration of in the refrigerant tanks. The increased ammonia concentration of refrigerant vapour was

compensated by a reduced ammonia concentration of a dilute solution. Dilute solution reduces from 0.61 to 0.09 from 0 s to 475 s, as shown in Figure 6-17.

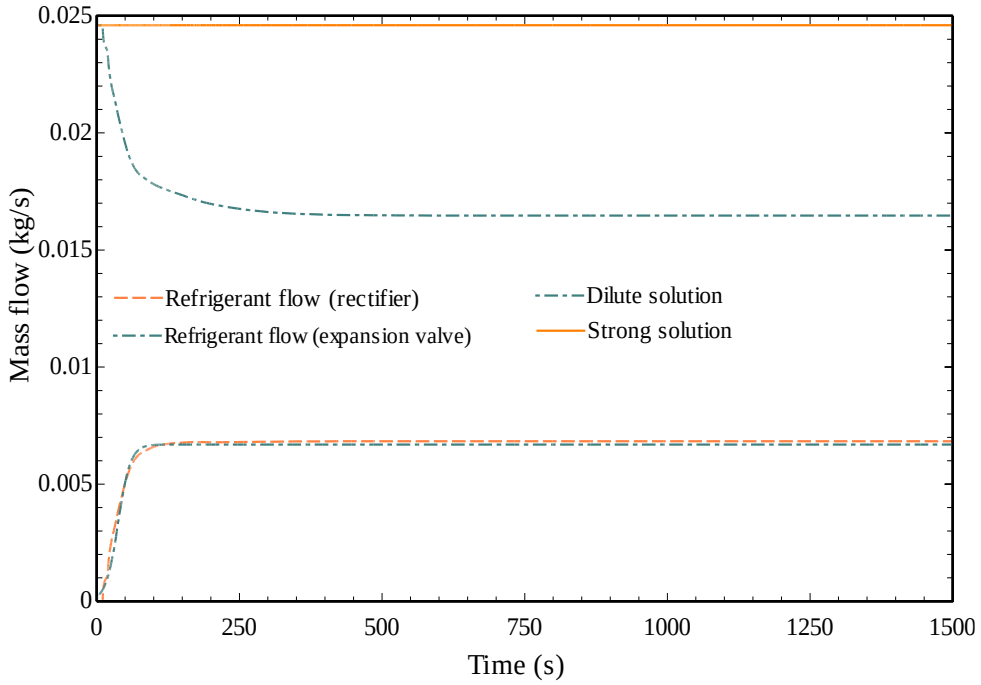

Figure 6-18 : Variation of mass flow rate during pre-cooling period.

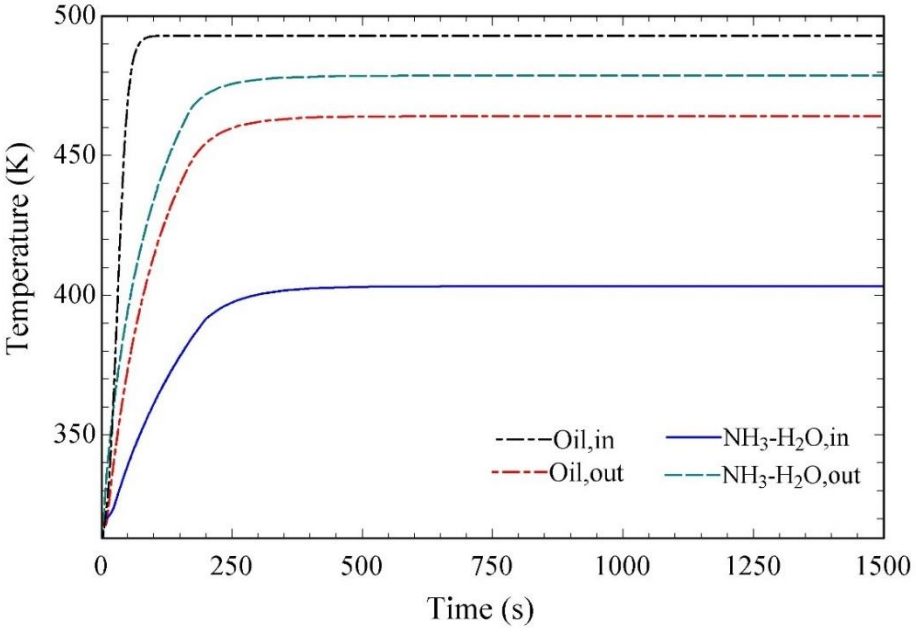

Figure 6-19 : Temperature variation in desorber during pre-cooling phase.

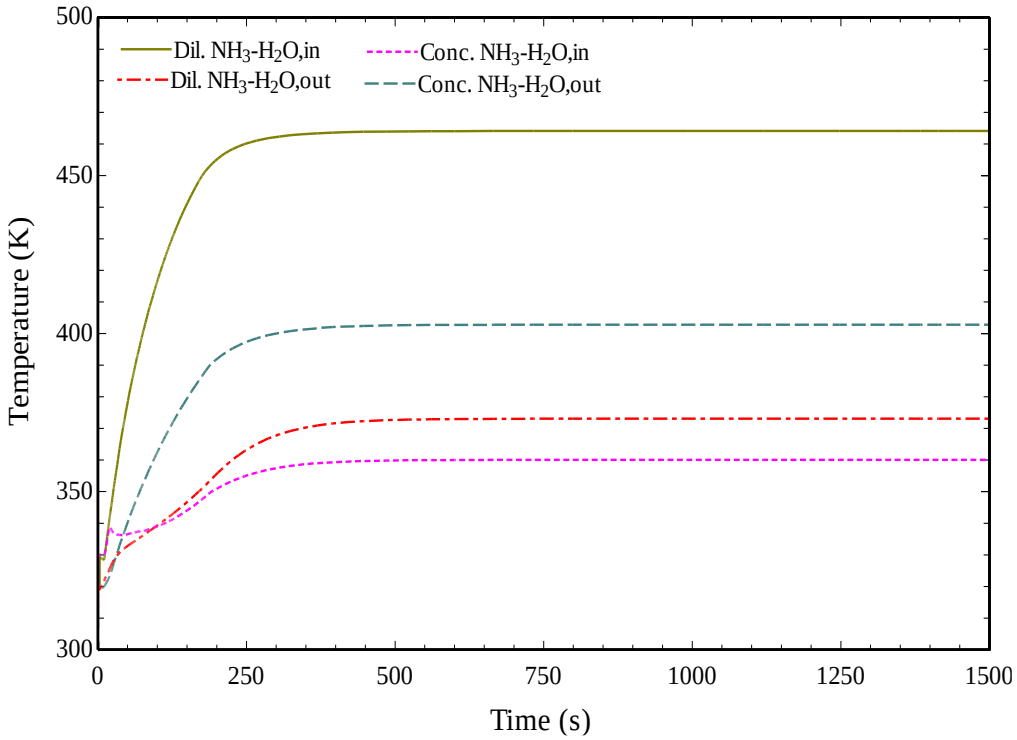

Figure 6-20 : Temperature variation in SHX during pre-cooling phase.

The temperature transient of oil and NH_3-H_2O solution in the desorber is shown in Figure 6-19. The dilute solution exited the desorber at a steady state temperature of 464 K (T_{21}) at 475 s. The concentrated solution entered the desorber (T_{27}) at a steady state temperature of 405 K. Hence; the NH_3-H_2O solution gained approximately 60 K in the desorber. The dilute solution leaving the desorber acted as the heat source for SHX. Therefore, desorber temperature transient greatly affects SHX temperature transients.

The temperature transient of the concentrated solution and dilute solution in the SHX are shown in Figure 6-20.

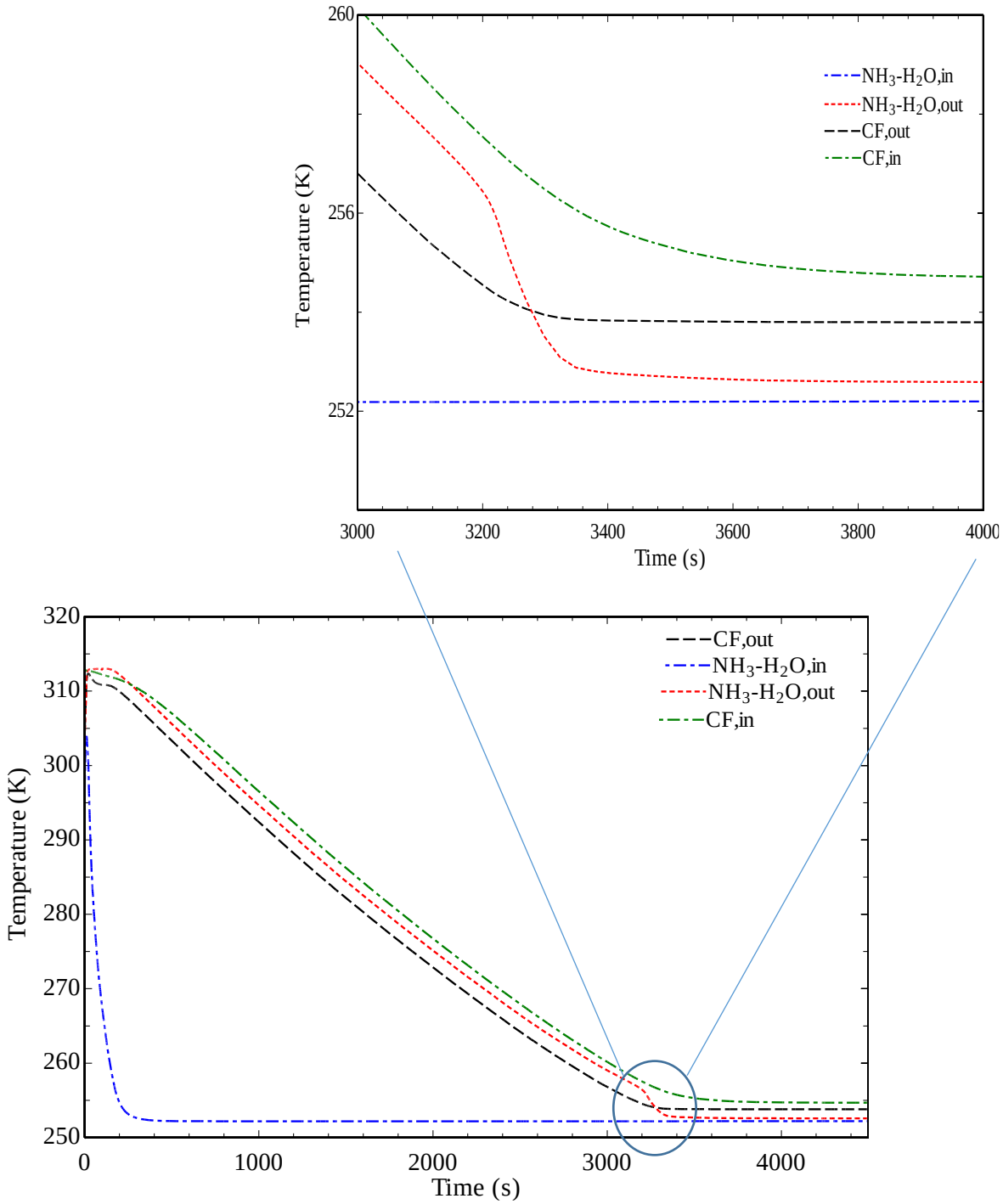

Figure 6-21 : Temperature variation in evaporator during pre-cooling phase.

The temperature evolution of refrigerant and coupling fluid in the evaporator are shown in Figure 6-21. The refrigerant inlet temperature depended upon the low-side pressure evolution in the system. As shown in Figure 6-14, the low side pressure achieved its steady state value at 480 s; hence inlet refrigerant also entered the evaporator at a steady state temperature of 251.7

K (T_{34}) at 480 s. Due to the high thermal capacitance of the refrigerated cabinet, the thermal transient of air (coupling fluid, CF) lasted longer, which also affects the refrigerant outlet temperature transients, which achieved a steady state of 252.8 K (T_{35}) at 3600 s. A remarkable temperature transient was observed with refrigerant evaporator outlet temperature between 3200 s and 3500 s. It can be explained by depicting refrigerant vapour quality at the evaporator outlet, as shown in Figure 6-16. It was observed that the refrigerant vapour quality rapidly decreased from 0.98 to 0.88 from 3200 to 3500 s. The refrigerant quality before 3200 s was approximately 0.98, which meant that refrigerant was in almost vapour phase at the outlet of the evaporator. This was due to a significant temperature difference between air inlet temperature and refrigerant temperature, which evaporated refrigerant completely. However, as the temperature difference between refrigerant temperature and CF temperature reduced, heat transfer also reduces between both fluids. Hence, the refrigerant could not evaporate completely, and its vapour quality also reduces from 0.98 to 0.88.

In this study, the thermal mass of the rectifier was neglected to avoid the complexity involved in the rectifier model. This was the sole reason that the thermal transient of hot NH_3 refrigerant vapour at the condenser inlet progresses to a steady state temperature of 336 K (T_{30}) rapidly within 40 s, as shown in Figure 6-15. The cold coupling fluid entered the condenser at a steady state temperature of 315.5 K (T_{40}) and leaves at 319 (T_{37}) at 285 s. The liquid refrigerant left the condenser at a steady state temperature of 318 K (T_{31}) at 200 s.

The temperature variation inside the RHX during the pre-cooling phase is shown in Figure 6-22. Refrigerant temperature transient after 3200 s in the evaporator also affected the temperature variation in RHX during the pre-cooling phase, which is visible in Figure 6-22. The liquid refrigerant enters RHX from condenser at steady state temperature of 318 K (T_{32}).

Liquid refrigerant outlet temperature encountered long thermal transient due to the thermal response of the evaporator, as explained above.

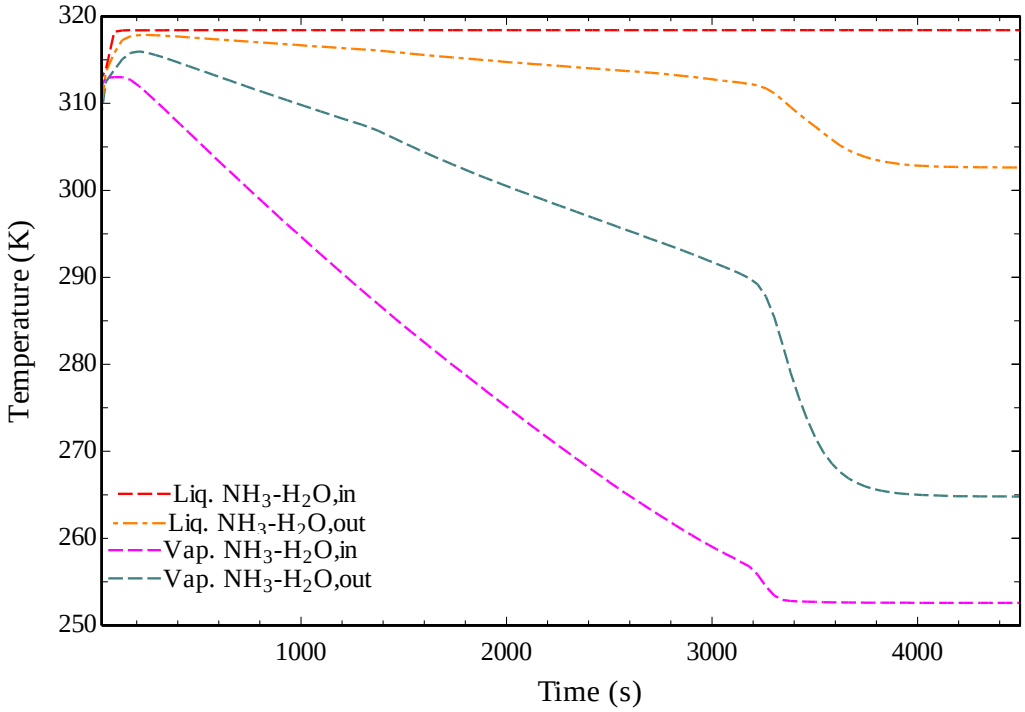

Figure 6-22 : Temperature variation in RHX during pre-cooling phase.

Figure 6-23 depicts the temperature variation in the absorber during the pre-cooling phase of the system. The coupling fluid entered at absorber at a steady state temperature of 315.5 K and left at 323 K (T_{44}) after 425 s. The CF outlet temperature at the absorber outlet was 4 K higher than that of the condenser outlet temperature. This was due to higher amount of heat being rejected in absorber due to the exothermic reaction of mixing refrigerant vapour with the diluted solution. The refrigerant vapour and liquid solution temperature after mixing reached steady state temperature of 351 K at 480 s, and its temperature reduced to 317 K, as shown in Figure 6-23.

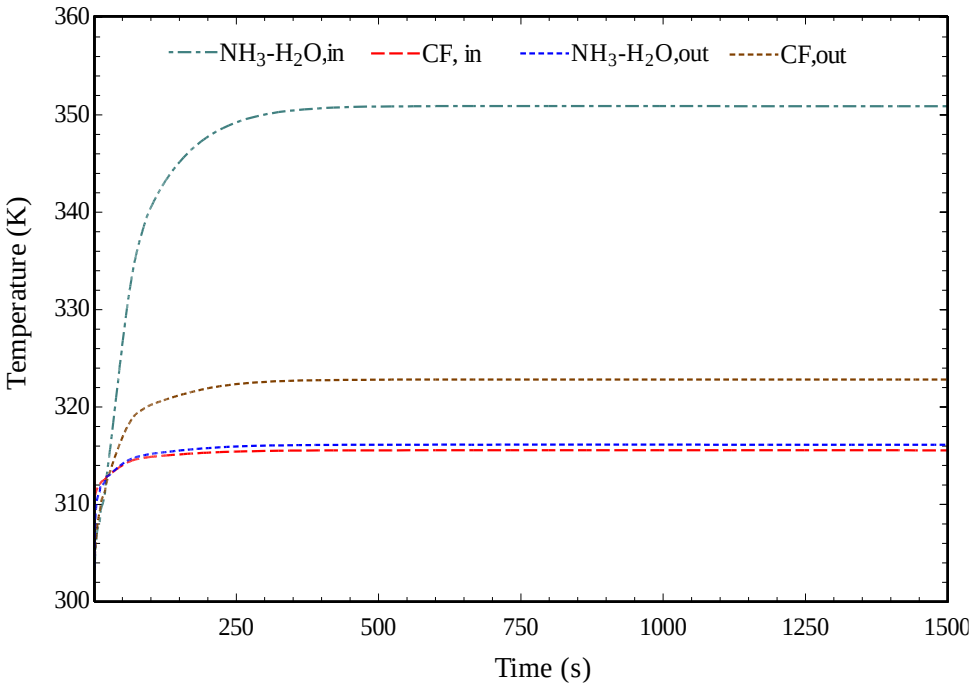

Figure 6-23 : Temperature variation in absorber during pre-cooling phase.

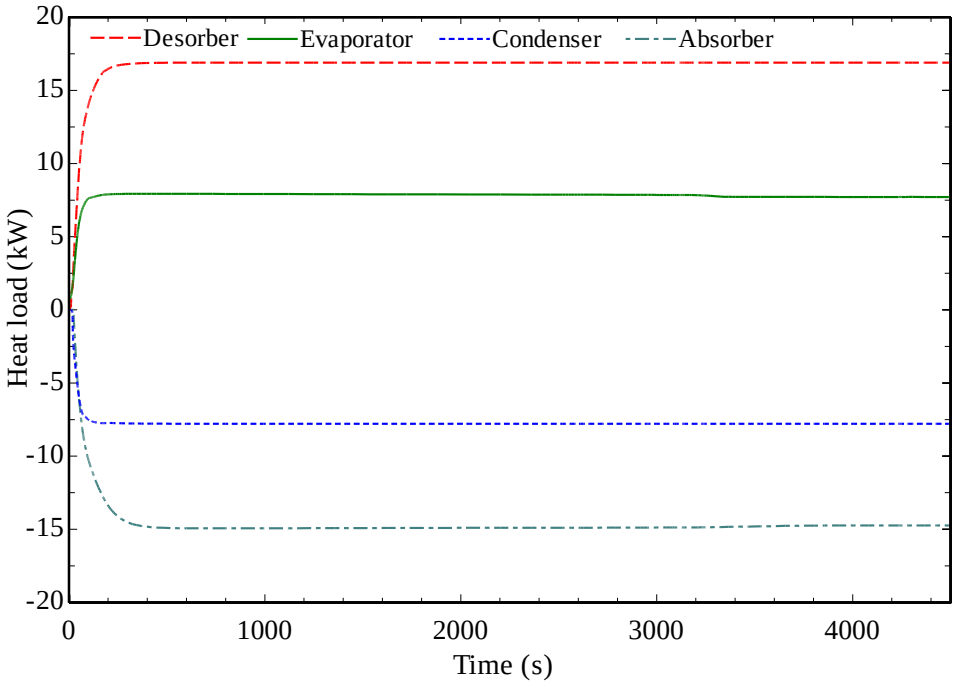

Figure 6-24 : Heat load variation of the VARS components during pre-cooling phase.

Heat load of the components transient depends upon the fluid temperature profile in respective components. Due to the temperature rise in components with time, the heat load of component

rises, as shown in FigureFigure *6-24* and Figure 6-25. Heat was added with hot oil in the desorber; therefore, it showed the highest heat load (16.7 kW), followed by the absorber (15 kW), condenser (7.9 kW) and evaporator (7.7 kW). The condenser heat load transient was found to be fastest compared to other components, mainly due to the condenser rapid temperature transient, as shown in Figure 6-15. The temperature variation in the evaporator after 3200 s, as depicted in FigureFigure *6-21* also affected the heat transfer in an evaporator; between 3200 s and 3500, the evaporator heat load reduces marginally from 7.8 kW to 7.68 kW. Due to its insignificant change, it is challenging to notice in Figure 6-24. RHX and SHX heat load profile is shown in FigureFigure *6-25*. Steady-state SHX and RHX heat loads were 6.9 kW and 1 kW, respectively. The effect of temperature variation after 3200s in RHX, as depicted in FigureFigure *6-22* also influenced heat transfer which can be seen in Figure 6-25.

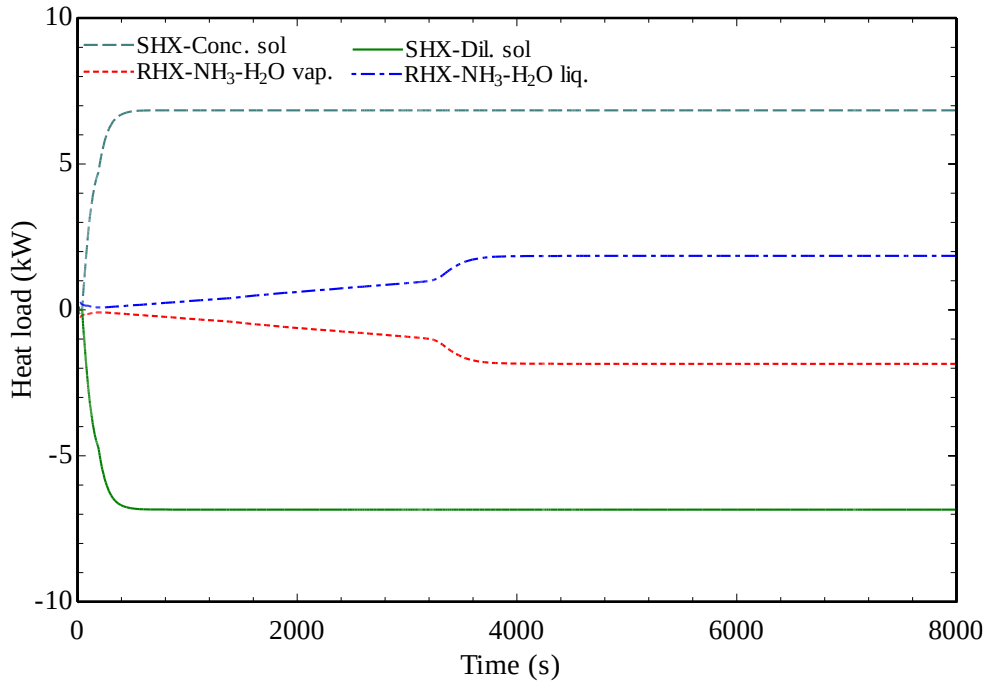

Figure 6-25 : Heat load variation of SHX and RHX during cool-down phase.

6.3 CPOX Operation Transient

It was assumed that the CPOX reformer was heated-up to its light off temperate in the SOFC heat-up phase. Hence, initial temperature of CPOX reformer was assumed 660 K. Figure 6-26 depicts the effect of varying λ_{O2C} on the normalised yield of CPOX reformate at 873 K and 973 K under equilibrium conditions assumption. The trend and values of the graph closely matched studies conducted by Zhu et al [145] and Pukrushpan et al. [144]. Hence, the simplified CPOX model assumptions were reliable and. It was observed that with H_2O yield increased exponentially with λ_{O2C}. A value of λ_{O2C} greater than one generated a significant amount of steam; therefore, CPOX operation at high λ_{O2C} would be useful to switch the operation from CPOX to SOFC start-up quickly, however a high value of λ_{O2C} leads towards high CPOX temperature as it does TOX reaction [147].

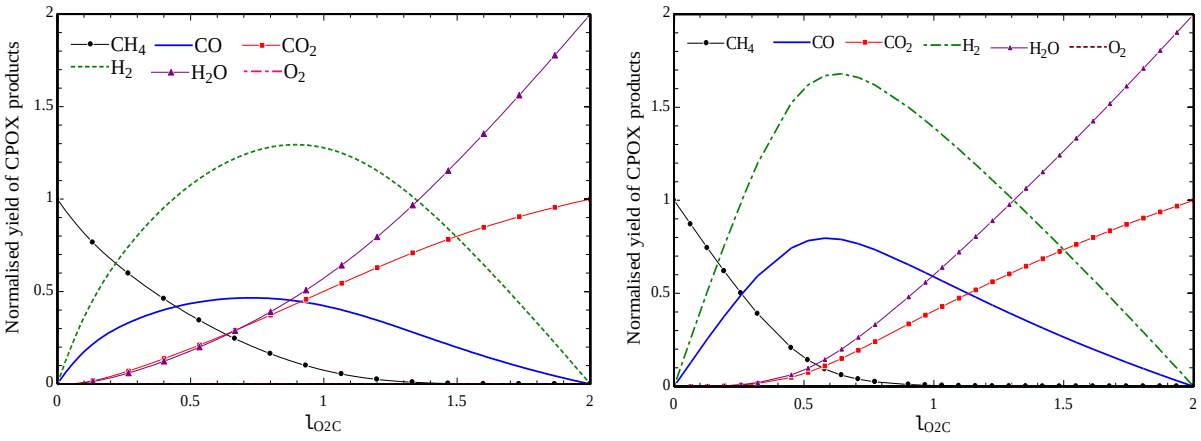

873 K 973 K

Figure 6-26 : Effect of λ_{O2C} on CPOX reformate.

SOFC stack can operate with a maximum 893 K inlet temperature (as shown in Table 5-10). Therefore, operating conditions were selected so that the outlet temperature of the CPOX reformate would not violate the hard limit on the temperature. In addition, CPOX operating

temperature should be close to SOFC temperature at the end of heat-up phase 853 K) to avoid a sudden temperature gradient while switching the operating phase from heat-up to CPOX activation. Therefore, the CPOX reformer should operate between 853 K and 893 K. It was essential to maintain an SC ratio above two to avoid possible carbon deposition on the anode surface during CPOX operation. Stack is not activated in this phase, however stack contains nickel-based anode and carbon deposition might take place on nickel-based anode at such high temperature of stack (close to 853 K) if SC ratio is kept to low (<2). In this analysis, RR was ramped up gradually from 0 to 0.6 within 10 seconds and λ_{O2C} is ramped down gradually from 1 to 0.78 within 20 seconds of the CPOX activation phase, as shown in Figure 6-27 (a). These values were chosen with a trial-and-error method to not to violate above mentioned temperature criteria. In addition, it is also common practice to operate CPOX reformer with λ_{O2C} value between 0.5 and 1 to avoid TOX reaction as shown in Table *3-15*. The CPOX reformate was a hydrogen-rich gas mixture with other combustible gases, such as CH_4 and CO, which enters the burner via stack. The burner temperature may be increased rapidly if it was operated with low amount of air flow. The high airflow rate needed to be supplied during the CPOX operation phase to control burner temperature. Therefore, the burner requires as high as 80 g/s of maximum airflow during CPOX operation phase.

It can be seen from Figure 6-27 (b) that it was possible to obtain enough amount steam from the CPOX reformer to achieve an SC ratio of 2 at the beginning of CPOX activation. However, it is not recommended to switch to the start-up phase immediately after an SC ratio of 2 has been achieved. During the SOFC start-up phase, a low current is drawn, which may produce less steam. It might be possible that the recirculated SOFC off-gas mixture does not contain enough steam to keep the SC ratio above two during the initial phase of the start-up. Hence, achieving a high SC ratio with CPOX operation ensures that the recirculated SOFC off-gas

mixture contains enough steam to maintain the SC ratio above two during the initial phase of the start-up. In this study, CPOX was operated until an SC ratio of 4 is achieved. It was observed that the steady state SC ratio of 4 can be achieved within 100-200 s once the CPOX reformer was activated. It should be noted that even though the minimum SOFC activation temperature is 853 K, the SOFC stack was heated up to 856 K to be in the safe window, as it was expected that the stack temperature may get reduced during the CPOX phase due to endothermic SMR taking place in the SOFC. This took approximately 4100 s (Figure 6-11). Therefore, the CPOX activation phase started at 4100. Thus, the time scale in figures representing CPOX transient phase was started at 4100 s.

During the initial phase of CPOX activation, the CPOX bed temperature increased rapidly, as shown in Figure 6-27 (c), due to higher value of λ_{O2C} during CPOX activation phase. CPOX reformer achieved the steady state temperature of 885 K after 200s of its activation phase. The steady-state temperature of CPOX did not violate the maximum inlet temperature (893 K) that SOFC can sustain, and it was close to the stack activation temperature of 853 K.

The CPOX activation phase only lasted for a short duration of 150-200 s, therefore, the SOFC stack temperature did not show a remarkable deviation. SOFC stack temperature was reduced from 856 K to 853.4 K, as shown in Figure 6-27 (d). It was entirely due to the endothermic SMR reaction inside the stack. It should be noted that even though SOFC was not activated electrically during the CPOX activation phase, SMR and WGS reaction still takes place on the catalytic anode surface. However, the stack temperature was close to its minimum activation temperature (853 K) at the end of the CPOX activation phase.

Air HX1 received the SOFC exhaust at temperature of 430 K (T_{16}). The low-temperature SOFC exhaust could not heat a significant airflow (80 g/s) to high temperature in air HX1 as shown in Figure 6-27 (h). However, air HX2 received SOFC exhaust at significantly high temperatures (above 1000 K (T_{13})). Hence, air pre-heating mainly occurred inside the air HX2 as shown in Figure 6-27 (g). The airflow rate achieved approximately 850 K (T_4) temperature at the end of the CPOX activation phase. The pre-heating temperature of the air and CH_4 mixture affect the CPOX temperature and CH_4 conversion inside the CPOX reformer. Air and CH_4 mixture are usually heated up to 400°C (673 K) before it entered the CPOX reactor [75,184]. The hot SOFC exhaust entered the fuel heat exchanger, and it heated-up the syngas mixture (mixture of fresh fuel and recirculated SOFC off-gas) to a maximum temperature of 700 K (T_8) as shown in Figure 6-27 (f), it mixed with fresh air and temperature reduced to 660 K (T_{18}). In this study, the thermal capacitance of the heat exchanger was added to the hot fluid side; hence hot fluid outlet temperature encounters slower thermal dynamics compared to the cold fluid.

Once enough steam was available from the CPOX operation, the SOFC could be activated and CPOX could be deactivated. As far as VARS operation was concerned during CPOX activation phase, VARS was still operated at its peak load during CPOX activation phase. It was found that during the CPOX phase, SOFC exhaust did not produce enough heat to VARS to operate at its peak load. Therefore, an additional amount of CH_4 was supplied to the burner to deliver sufficient heat to VARS. The variation of additional fuel flow to the burner in the CPOX phase is discussed together with transient SOFC start-up phase in the following sub-section of the chapter (Figure 6-28).

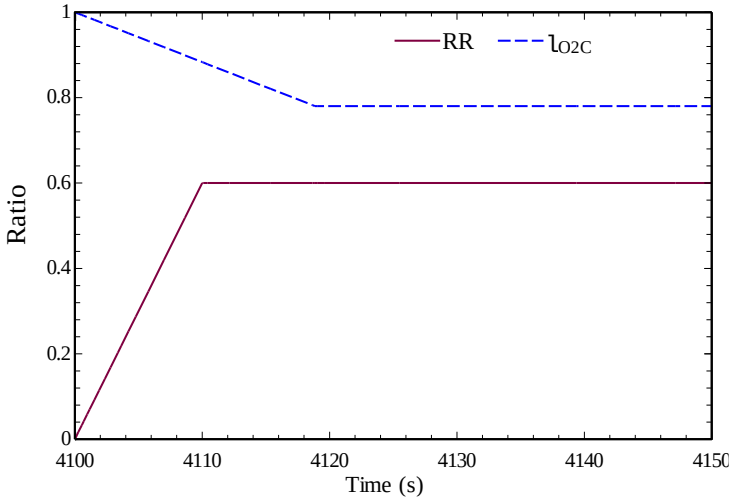

(a) RR and λ_{O2C} development

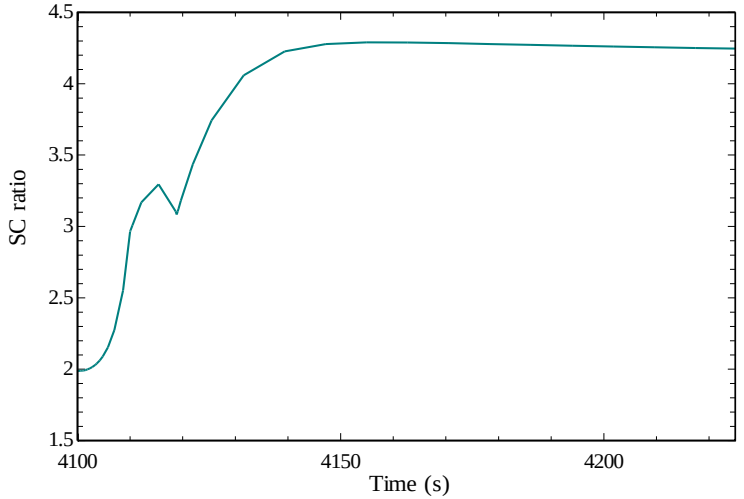

(b) SC ratio development

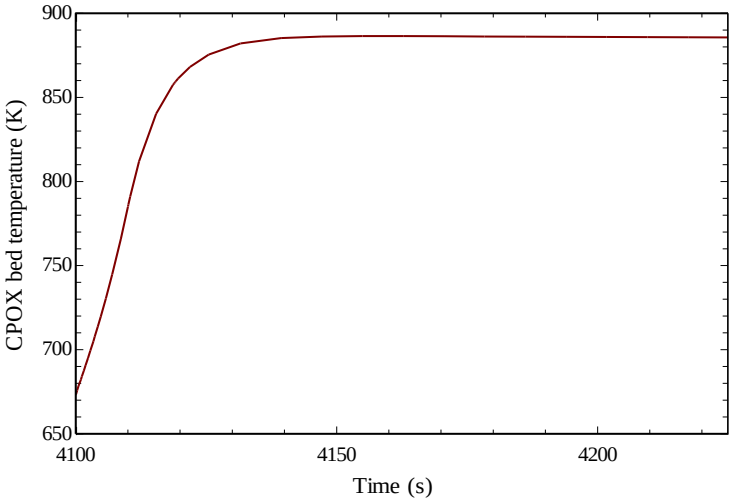

(c) CPOX bed temperature development

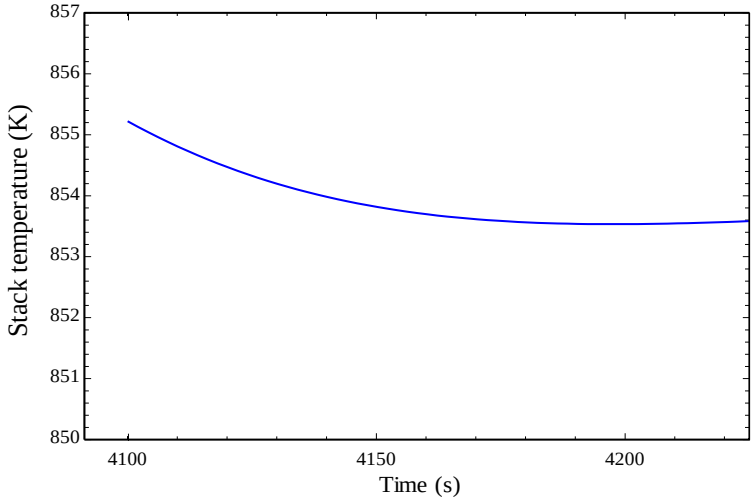

(d) Stack temperature development

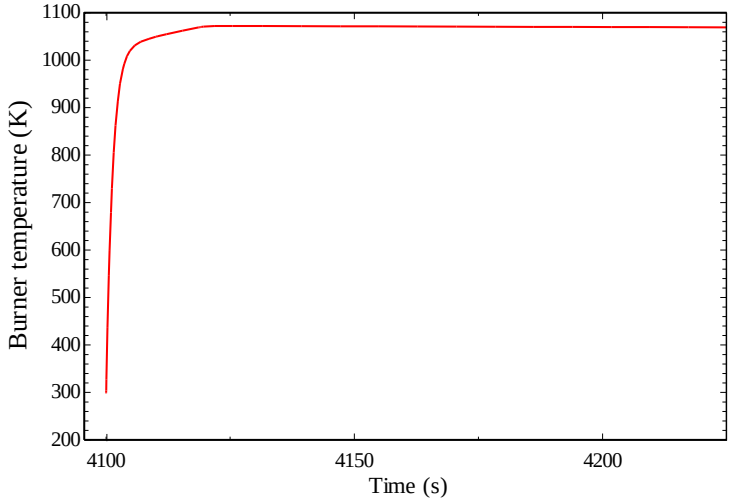

(e) Burner temeprature development

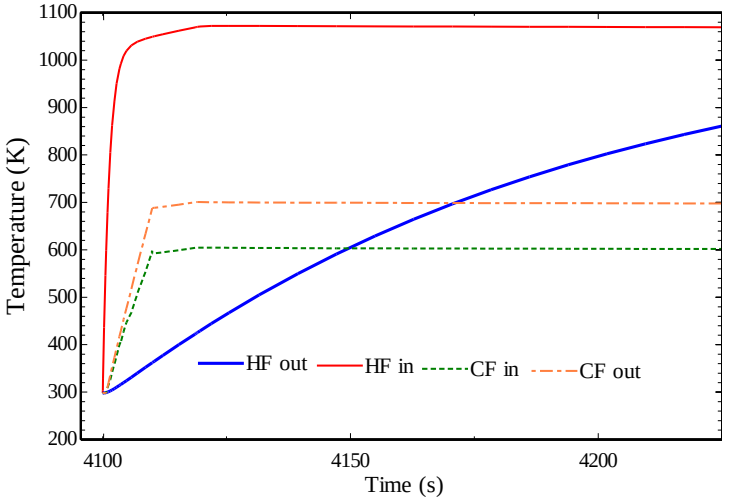

(f) Fuel heat exchanger response

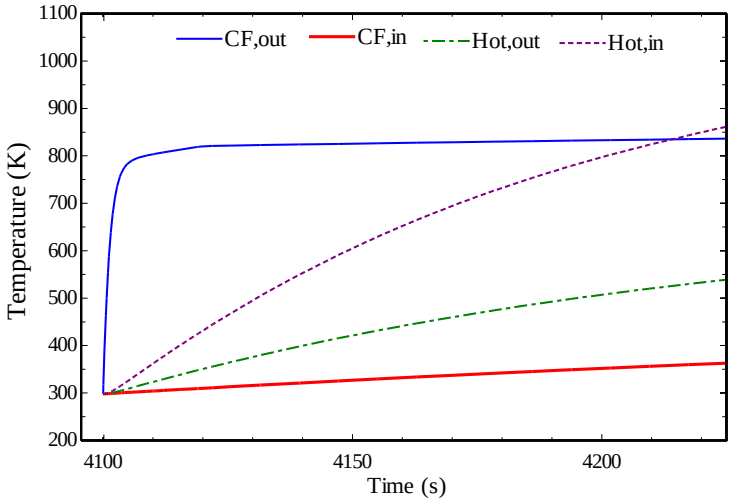

(g) Air heat exchanger-2 response

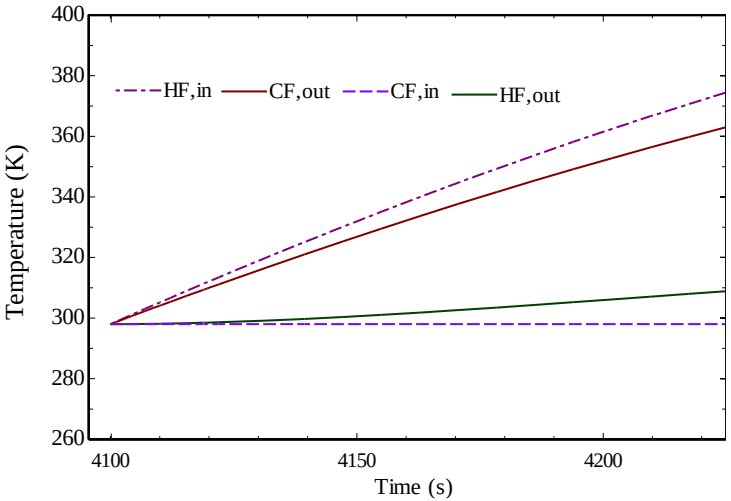

(h) Air heat exchnager-1 response

Figure 6-27 : Transient response of SOFC system during CPOX activation phase.

6.4 SOFC Start-up Phase

In this study, the fuel flow was ramped-up gradually to keep the current ramping-up rate of 600 A/hr at a constant fuel utilisation of 0.75.

If the system fuelled with a high fuel flow during start-up, a significant amount of unreacted fuel could enter burner, which might increase burner temperature rapidly. The fuel flow and air flow varied throughout the SOFC system operation, as shown in Figure 6-28 and Figure 6-29, respectively. The fuel flow to stack was gradually ramped-up from 0.0001 g/s to 0.84 g/s from 4225 s to 5275 s. The airflow rate to stack was gradually ramped up from 0.29 g/s to its nominal value of 60 g/s from 4226 s to 5300 s during the start-up phase, as shown in Figure 6-29. If a high airflow rate was supplied to SOFC during the initial phase of the SOFC start-up, it may cool down the stack. The SOFC exhaust was not able to supply sufficient heat to VARS to operate during the start-up phase. Therefore, an additional amount of CH_4 was supplied to the burner to feed enough heat to the VARS to operate. The amount of additional CH_4 fuel flow to the burner is shown in Figure 6-28 . It was observed that the fuel flow to the burner reduced from 0.01 g/s to 0.008 g/s during the CPOX phase. However, the fuel flow needed to increase from 0.03 g/s at 4225 s and it gradually decreases to 0 g/s at 5500 s again during the current ramp-up period. Fuel flow to the burner reduced with increased fuel flow to the stack. This behaviour was also expected as the burner received a higher SOFC off-gas flow from the stack with the current being ramped up. The SOFC stack was fed with excess air in CPOX and the start-up phase. Therefore, no additional air was needed to supply to the burner during both these phases, which is shown in Figure 6-29.

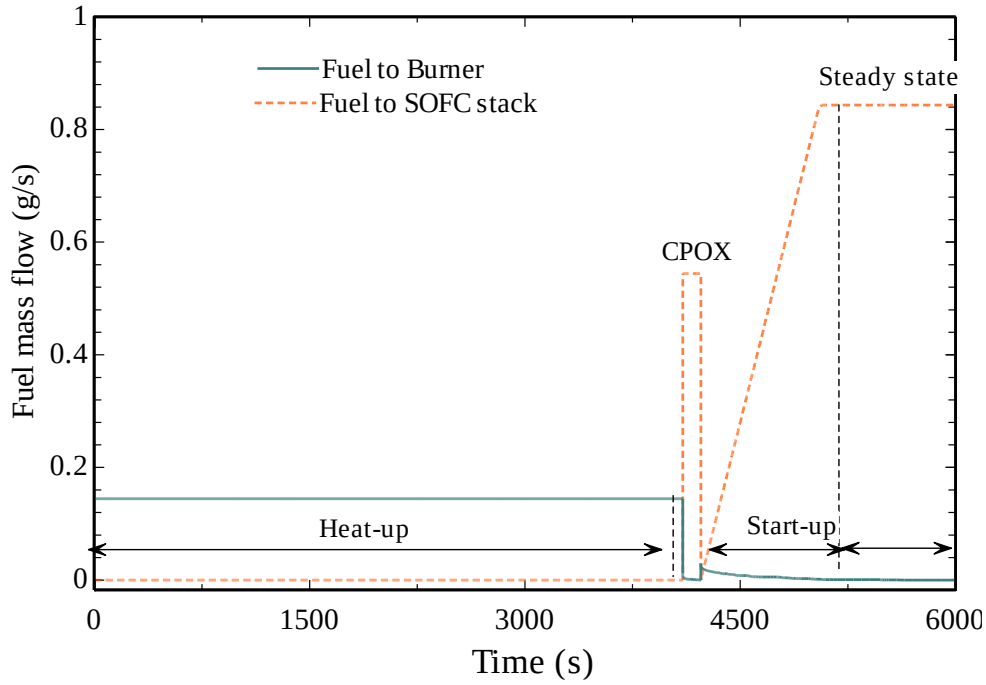

Figure 6-28 : Variation of fuel flow rate during system operation.

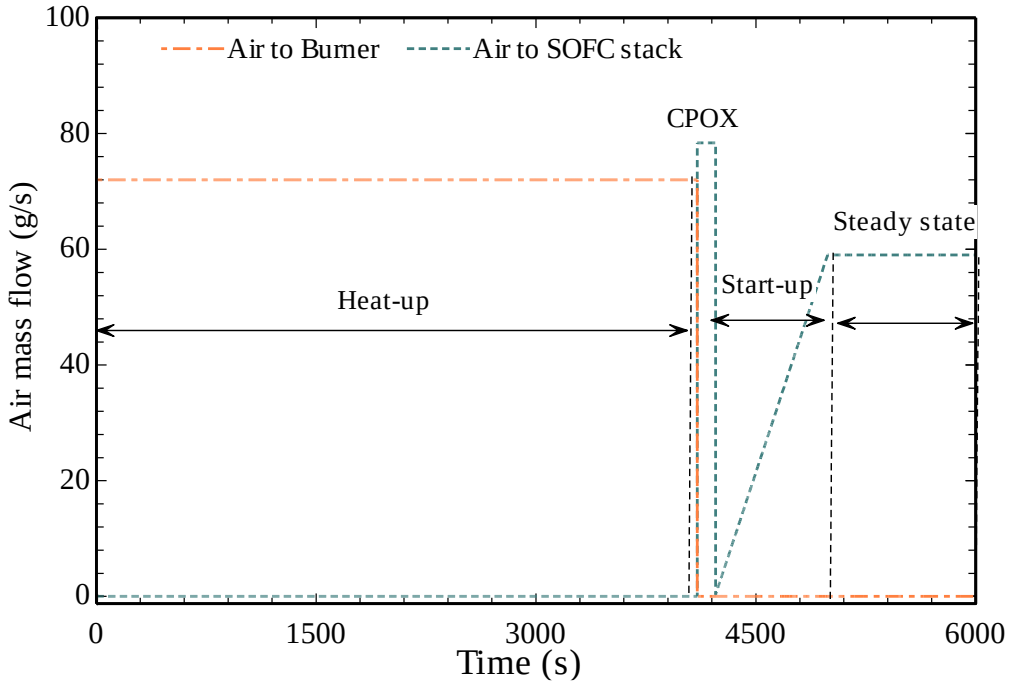

Figure 6-29 : Variation of air flow during system operation.

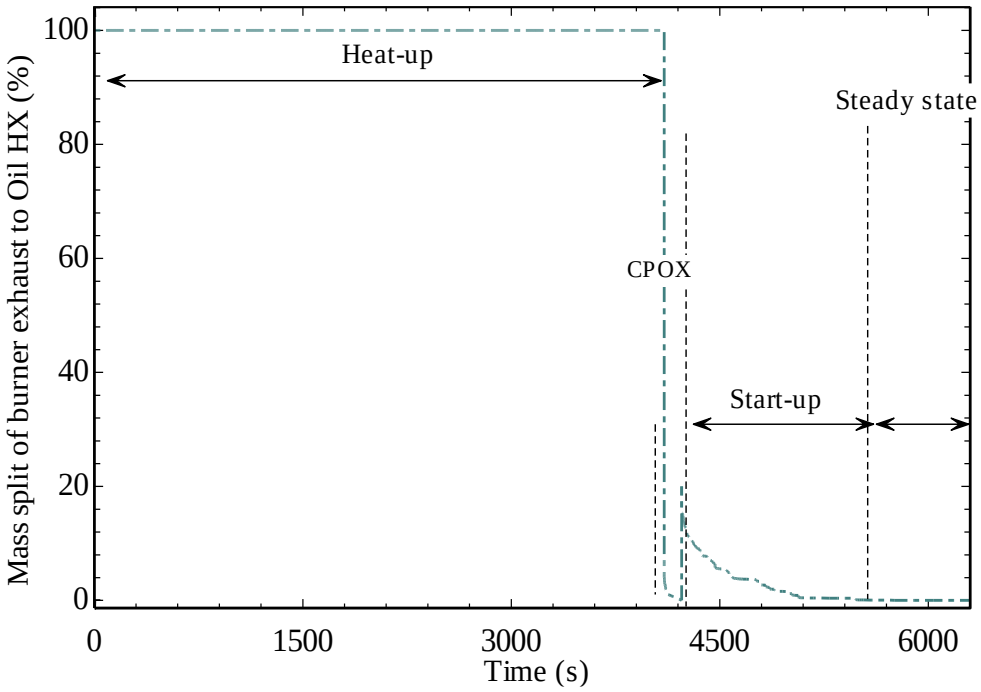

Figure 6-30 : Variation of split of burner exhaust to Oil HX.

The burner exhaust split to Oil HX was one of the essential parameters to vary throughout the system operation. Once pre-cooling of the refrigerated cabinet was achieved, the temperature of the refrigerated cabinet needs to be maintained at 255 K. After pre-cooling of the cabinet, SOFC encountered two operational phases, namely: CPOX activation and start-up phase. During both these phases split need to be controlled to maintain the required oil outlet temperature of 493 K to operate the VARS without any interruption. During SOFC heat-up phase, the VARS was operated solely by a burner. Therefore, during the heat-up and pre-cooling phase, split of the burner exhaust to Oil HX was 100 % as shown in Figure 6-30. During the CPOX phase, the burner exhaust split decreased from 100 % to 8 % and then it reduced gradually reduce to 1.1 % from 4100 s to 4225 s with increased thermal power from SOFC in the CPOX phase. However, the burner exhaust split to Oil HX increased to approximately 20 % at the beginning of the start-up phase. Once the ramp-up period was finished, the split reduced to zero from 4225 s to 5500 s, as SOFC could power VARS after 5500 s.

The CPOX activation phase finished at 4225. Thus, the time scale in figures representing SOFC start-up phase was started at 4225 s. The evaluation of current and current density during the start-up phase is shown in Figure 6-31. The steady state current and current density of 200 A and 0.55 A/cm^2 was achieved within 1200 s of the start-up phase (overall 5425 s). The variation of stack voltage is shown in Figure 6-32. The voltage variation depends upon the current and temperature of the SOFC stack. It is obvious that the voltage decreases with an increased current which is clearly seen in Figure 6-32. At the beginning of the start-up phase, when no current was drawn, t=4225 s, the stack voltage was equal to the stack OCV of 185 V. The stack voltage decreased from 185 V to 79 V from 4225 s to 5200 s due to increased current value. However, after 5200 s, stack voltage increased up to its steady state value of 126 V due to reduced stack ASR with higher stack temperature. Figure 6-33 depicts the stack temperature evolution during the start-up phase. At the beginning of the phase, the stack temperature encountered slight variation. This was due to low current being drawn from the stack, which generated less heat in the SOFC; the stack also received less air flow rate at the beginning of the start-up phase. However, increased current stack produced high exothermic heat, which resulted in an elevated stack temperature. Due to high thermal capacitance of the stack, the SOFC stack thermal transient lasted longer. It was found that the stack achieved a steady state temperature of 993 K at 9500 s (after 5275 s of start-up phase). However, a significant temperature change was observed until 8500 s (within 4275 s of the start-up phase). After 8500 s, stack temperature increased from 990 K to 993 K at 9500 s. It was interesting to note that even though stack temperature increased from 4225 s to 5200 s, stack voltage still decreases due to increased current value during this time window.

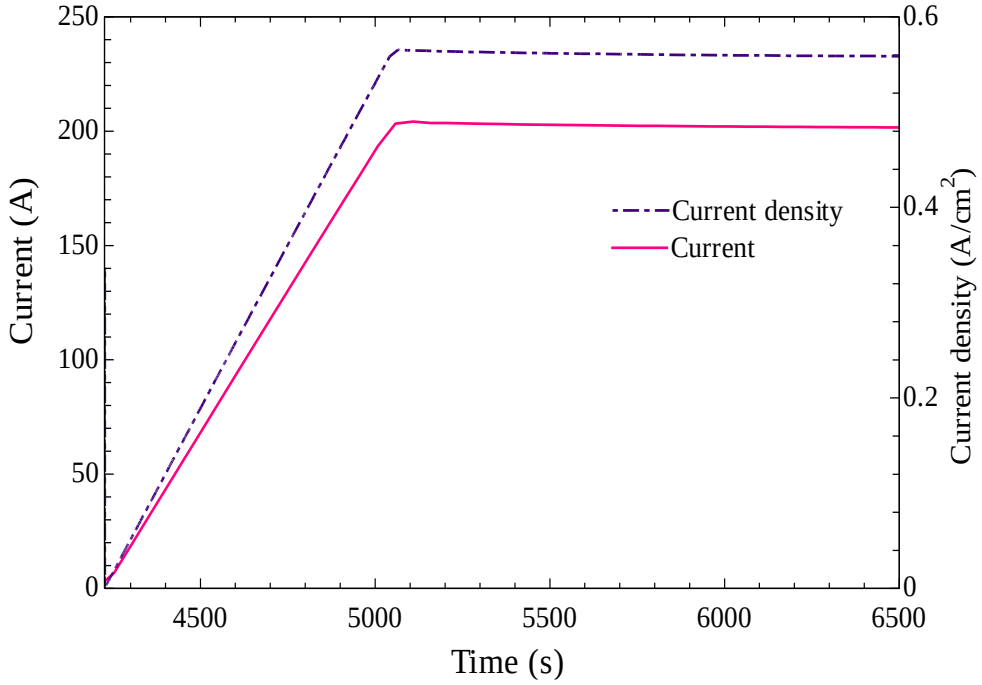

Figure 6-31 : Variation of current and current density during start-up phase.

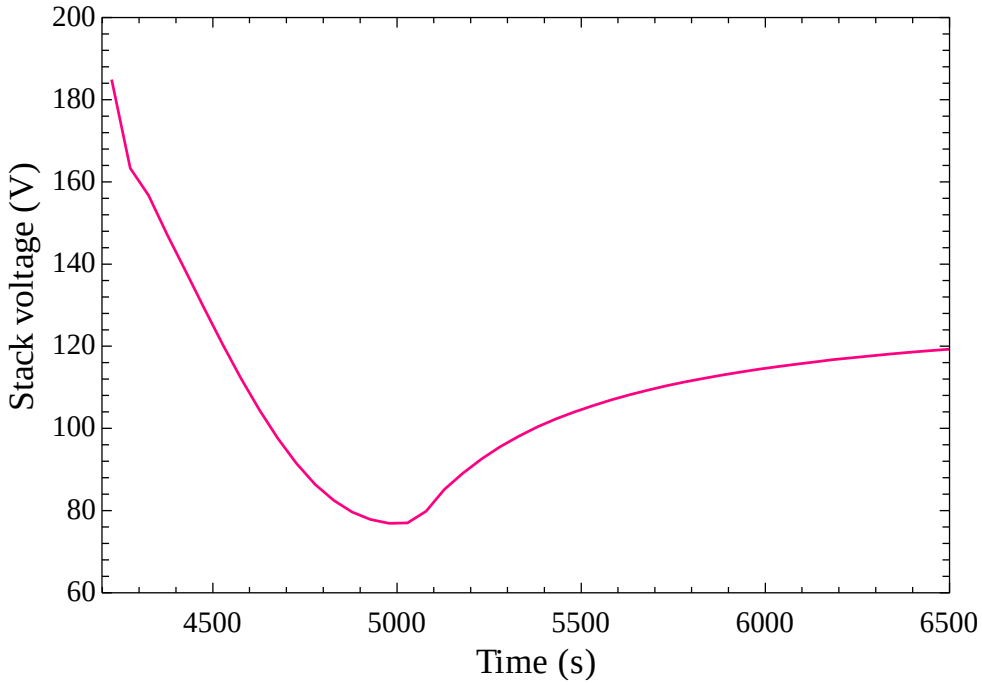

Figure 6-32 : Evolution of stack voltage during the SOFC start-up phase.

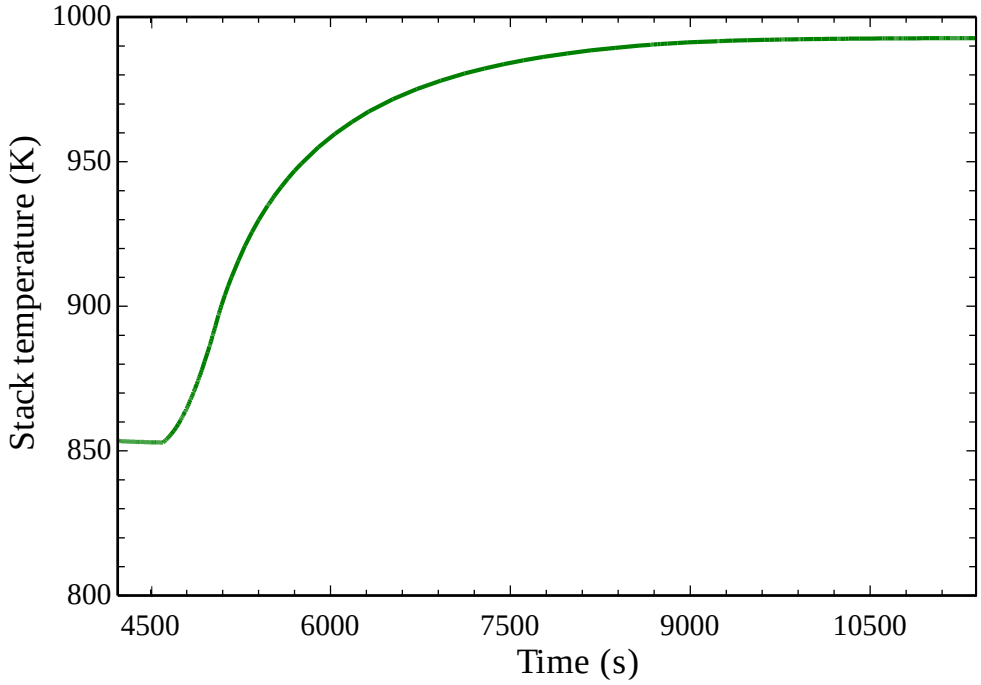

Figure 6-33 : Evolution of stack temperature during start-up phase.

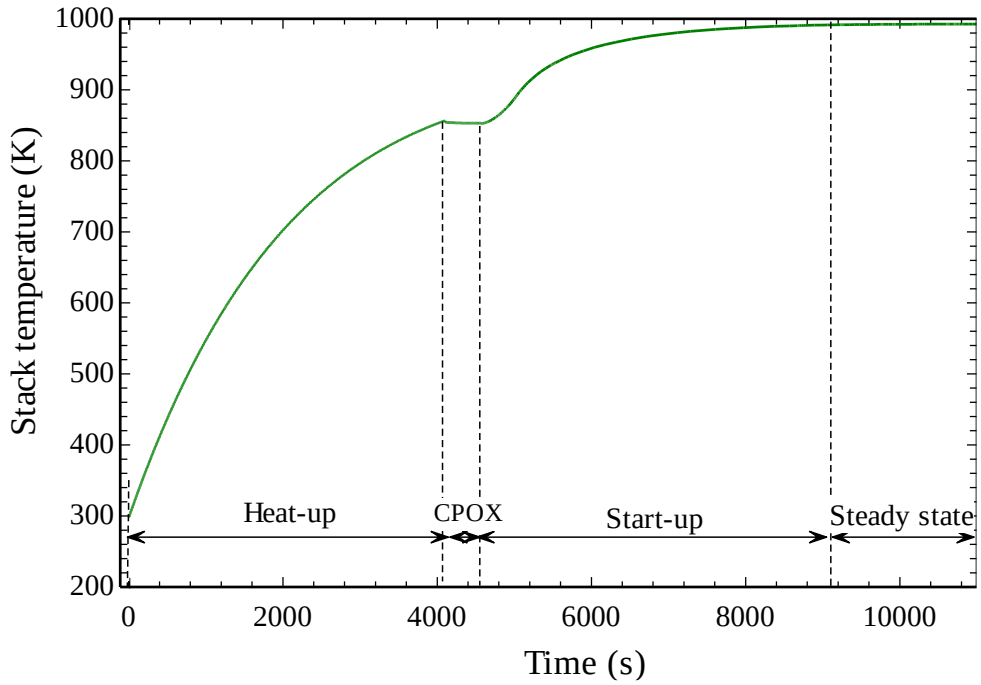

Figure 6-34: Temperature profile of SOFC stack during the different operational phases.

The temperature evolution of the SOFC stack in different operational phase is shown in Figure 6-34. A temperature window during different operational phases is as follows:

1. Heat-up: 303 K to 856 K
2. CPOX phase: 856 K to 853.4 K
3. Start-up phase: 853.4 K to 993 K
4. Steady state: 993 K

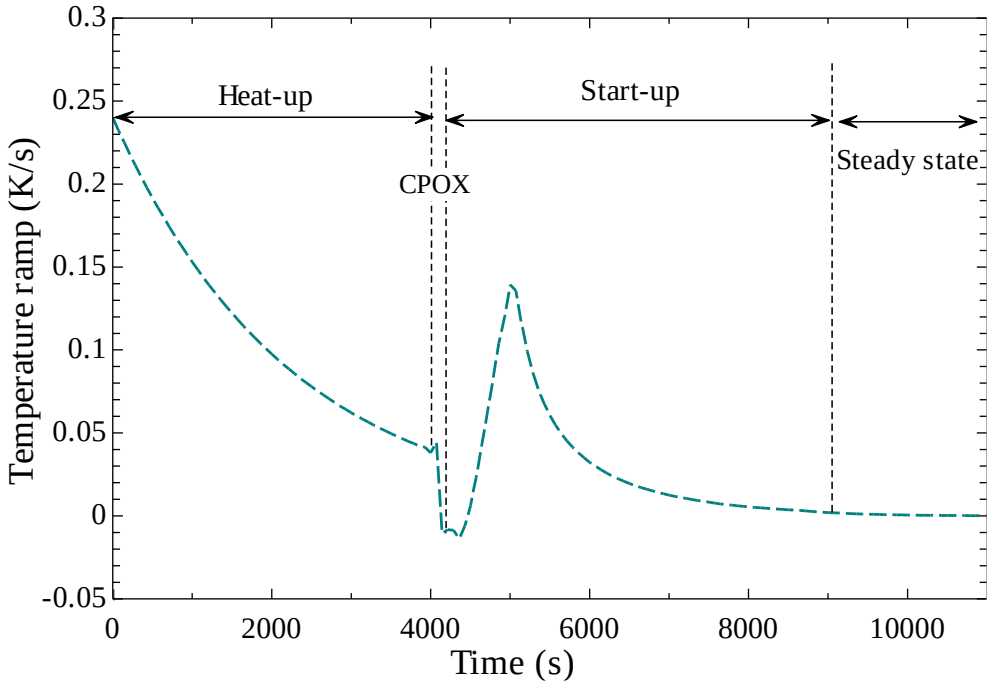

Figure 6-35 : Temperature ramp profile of the SOFC stack during different operational phases.

The temperature ramp is a vital performance parameter affecting stack integrity. An SOFC stack is vulnerable to high temperature ramp; These results from rapid heat-up/cool down of SOFC stack, which generate thermal thermos-mechanical stresses inside the SOFC stack. Therefore, monitoring temperature ramp rates during different SOFC operational phases is important. In a current research study, the operating window during different phases was

selected so that the maximum SOFC stack temperature ramp would not cross the threshold value of ±0.25 K/s (15 K/min). Figure 6-35 shows the temperature ramp of the SOFC stack during the different operational phases. The maximum temperature ramp at the beginning of the heat-up phase was 0.25 K/s which eventually reduced throughout the heat-up phase. Stack temperature reduced from 856 K to 853.4 K during the CPOX phase, resulting in a negative temperature ramp, as shown in Figure 6-35. The maximum temperature ramp value during the start-up phase was 0.142 K/s at 5000 s. However, the temperature ramp of the stack was well below its maximum threshold value of 0.25 K/s during the start-up phase. Hence, it was proved that the current operating envelope protected the SOFC stack.

Electric power produced by stack is a product of current and voltage (eqn.3.46). Therefore, it is evident that the stack power transient depends upon the current and voltage transient. At the beginning of the start-up phase, the stack power was zero as no current was being drawn from the stack. Even though stack current achieved a steady state value by 5425 s, power transient varied with voltage transient. The stack power reached its steady state value of approximately 25 kW, as shown in Figure 6-36. The net power available from SOFC system also increased with stack power. At lower power, system needs less amount of air and fuel flow, hence overall pressure loss in the system is significantly less compared to pressure loss at nominal operation (eqn.*3.62*) which also reduced parasitic losses (air blower and recirculation blower power consumption) of the SOFC system. Therefore, at lower power difference between stack power and system power was not significant as shown in Figure 6-36. The SOFC system achieved net available power of approximately 22.6 kW as shown in Figure 6-36.

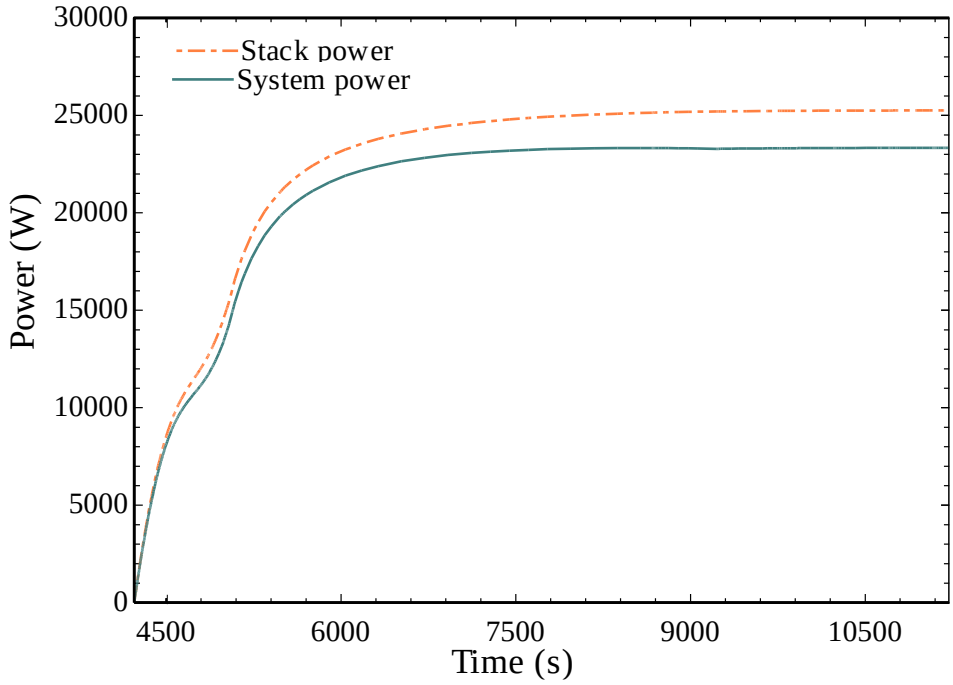

Figure 6-36 : Evaluation of stack and system power during start-up phase.

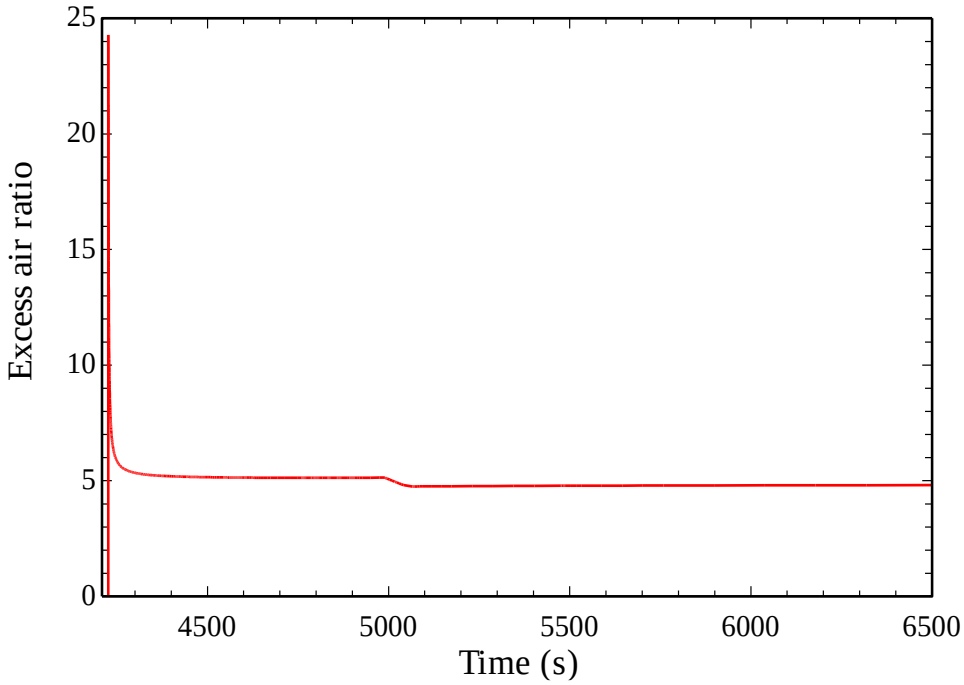

Figure 6-37 : Evolution of excess air ratio during the start-up phase.

The airflow rate was ramped up gradually, affecting the excess air ratio (eqn.3.49). Figure 6-37 outlines the evolution of excess air ratio during the start-up phase. The excess air ratio strongly

depends upon the allowed temperature gain across the stack and current being drawn from SOFC stack. At the beginning of the start-up phase, low current was being drawn which releases less exothermic heat in the stack (lower cooling demand of the stack), which also resulted into high excess air ratio. Higher oxygen amount was utilised inside the stack with the high current drawn from the stack, which also reduced the excess air ratio, as shown in Figure 6-37. Excess air ratio achieved the steady-state value of 4.8 at 5425 s.

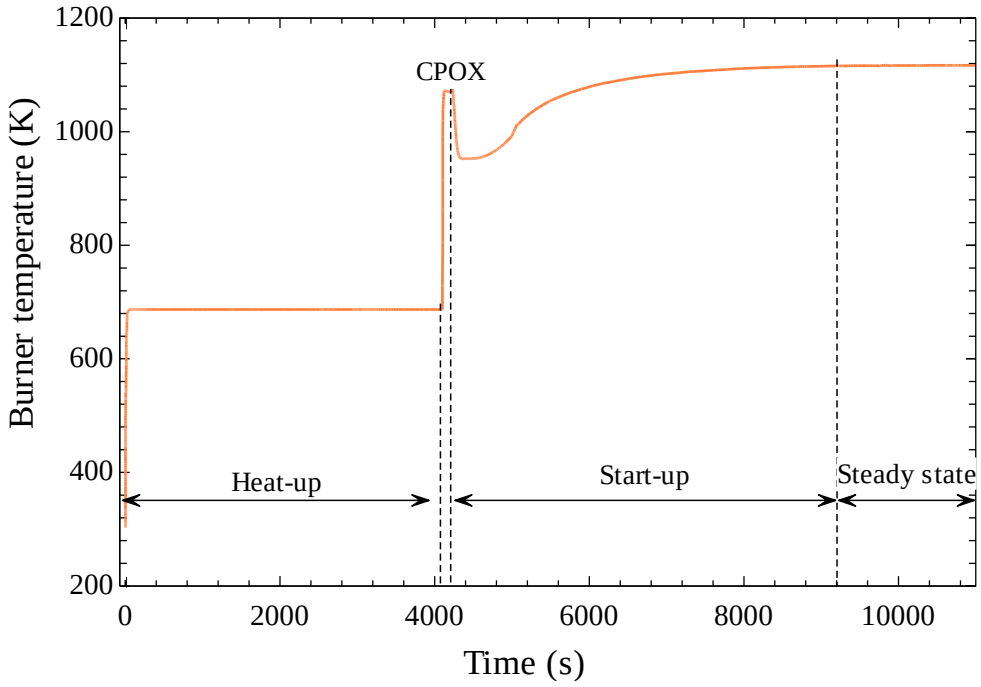

Figure 6-38 : Temperature profile of burner during the different operational phases.

The burner temperature varied throughout different operational phases as it encountered different amounts of fuel and airflow in the distinct operational phase. The development of burner temperature during SOFC system operation is shown in Figure 6-38. The burner encountered the maximum temperature in the SOFC system. Therefore, it needs to ensure that the burner temperature did not cross the maximum temperature limit of 1223 K. The fuel flow rate decreased while switching to the start-up phase from the CPOX phase, as shown in Figure 6-28 ; decreased fuel flow rate also reduced the burner temperature from 1069 K to 953 K

between 4225 s and 4510 s. However, with an increased fuel flow throughout the start phase, burner temperature increased and achieved a steady state temperature of 1117 K.

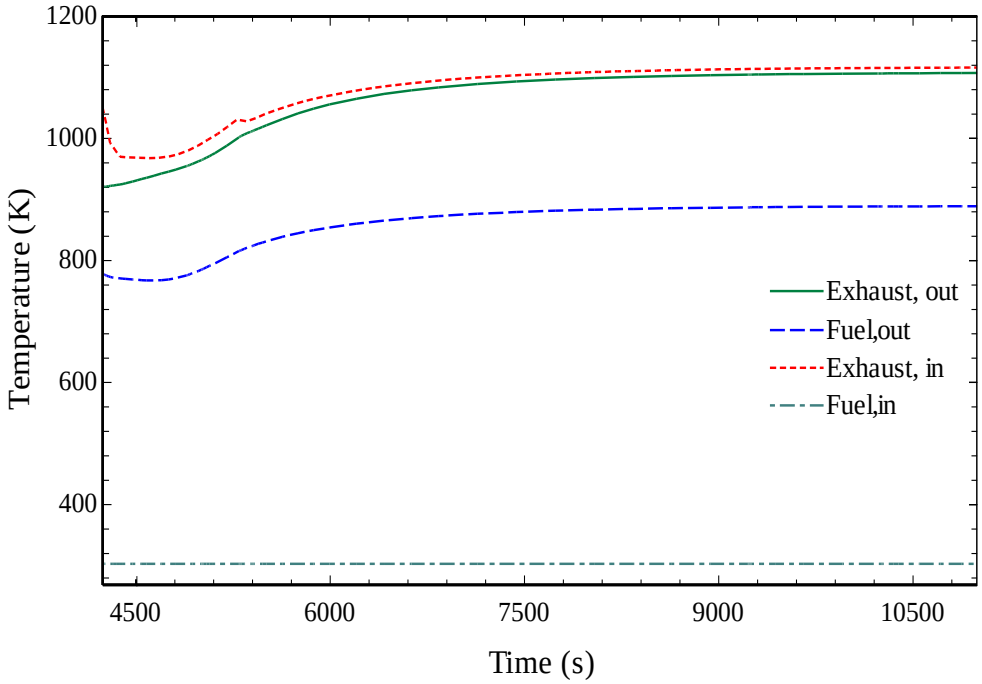

Figure 6-39 : Thermal response of fuel HX during start-up phase.

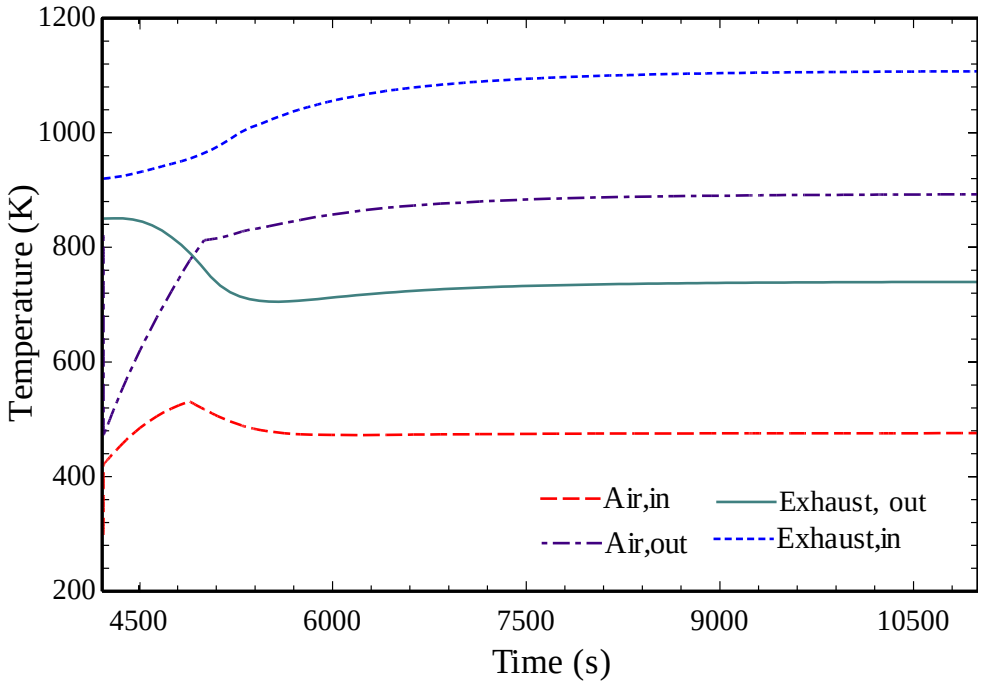

Figure 6-40 : Thermal response of Air HX2 during start-up phase.

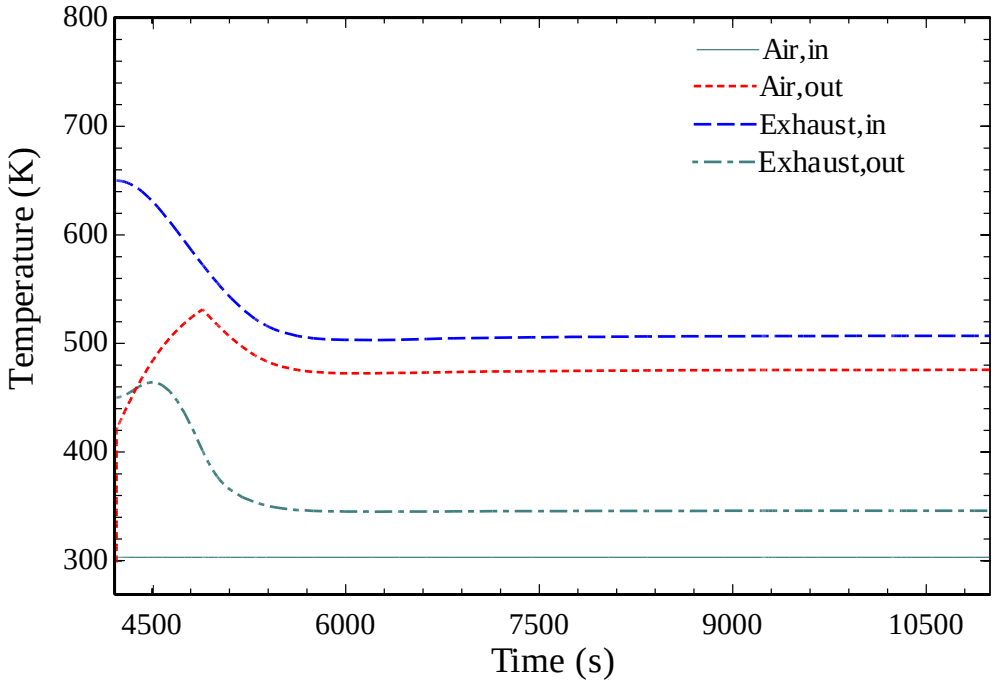

Figure 6-41 : Thermal response of Air HX1 during start-up phase.

Thermal transients of the fuel HX and the two air heat changers are shown in Figure 6-39, Figure 6-40 and Figure 6-41 , respectively. The fuel HX received hot exhaust from the burner. During the CPOX phase, the fuel HX was heated by a hot burner exhaust (1069 K). The fuel flow rate at the beginning of the start-up phase was as low as 0.0001 g/s; hence fuel temperature increased rapidly to 790 K. Fuel inlet temperature gradually increased from 790 K to 892 K from 4226 s to 8000 s, as shown in Figure 6-39. The steady state temperature of burner exhaust was 1108 K at the outlet of fuel HX.

The thermal responses Air HX2 and Air HX1 are shown in Figure 6-40 and Figure 6-41, respectively. Air HX2 received air from heat exchanger 1 and hot exhaust from the fuel heat exchanger. Therefore, the thermal response of the air HX2 depended upon fuel HX and air HX1 thermal response. The air HX2 received air at a higher temperature from 4226 s to 4600 s. Therefore, air temperature in air HX2 increased rapidly during the start-up phase. Air achieved its steady state value of 893 K after 8000 s in air HX2. Air temperature increased

from 303 K to 531 K in air heat exchanger 1 during the initial 4226 s to 4600 s. The airflow rate was increased from 0.29 g/s to 17 g/s from 4226 s to 4600 s, which was significantly less than its steady state value of 60 g/s. Due to less airflow during this temperature window, hot SOFC exhaust rapidly heated-up the cold air in the air HX 1. However, as the start-up phase progressed, heat exchanger 1 encountered a high airflow rate, reducing air outlet temperature and achieving its steady state value of 463 K at 8000 s.

The thermal response of the oil heat exchanger during start-up is shown in Figure 6-42. As explained above, additional fuel flow to the burner and mass split of burner exhaust to oil heat exchanger increased between 4225 s and 5500 s of start-up phase duration. It also increased exhaust inlet temperature in the oil heat exchanger. This strategy worked as expected, as the oil outlet temperature remained at approximately 493 K throughout the start-up phase. It ensured the smooth and uninterrupted operation of the VARS.

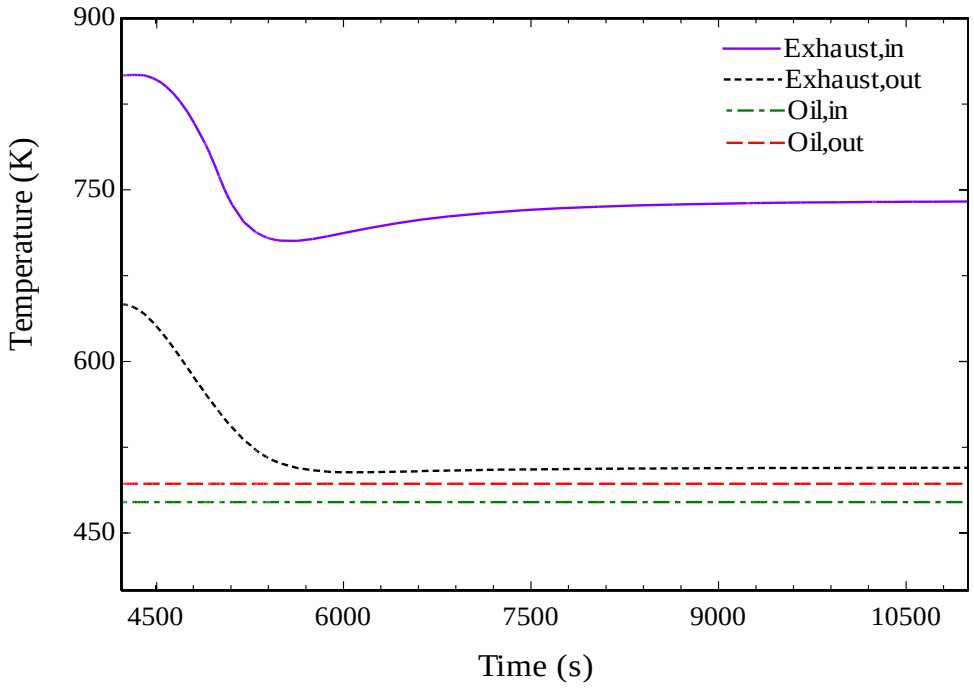

Figure 6-42 : Thermal response of Oil HX during start-up phase.

VARS was operated at its peak load during SOFC heat-up and CPOX phase. However, once the SOFC start-up phase was initiated, VARS was operated at its nominal load of 6 kW. It was smoothly achieved by ramping down the oil flow and solution flow while maintaining the oil inlet temperature to desorber at 493 K. Flow rate, and refrigeration system heat development is depicted in Figure 6-43 and Figure 6-44, respectively. Oil flow and concentrated solution flow rates gradually ramped down from 0.25 kg/s to 0.2 kg/s and 0.024 kg/s to 0.0185 kg/s from 4225 s to 4300 s, respectively. Dilute and refrigerant solution flow followed strong solution flow and reduced from 0.0165 kg/s to 0.0122 kg/s and 0.0068 kg/s to 0.0053 kg/s, respectively. The heat load of all the main components decreased due to the reduced flow rate in the system, as shown in Figure 6-44. Due to smooth transition, VARS did not depict interesting temperature transient during this transition. Therefore, the individual component temperature transient response is not mentioned here to maintain the chapter's brevity.

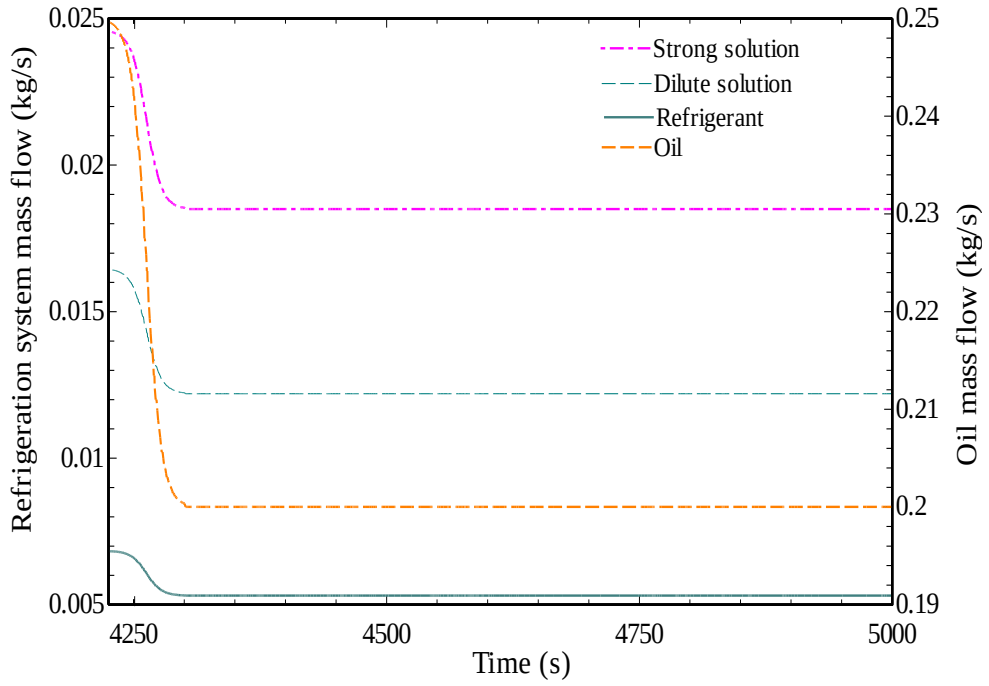

Figure 6-43 : Refrigeration system and oil mass flow variation during the start-up phase.

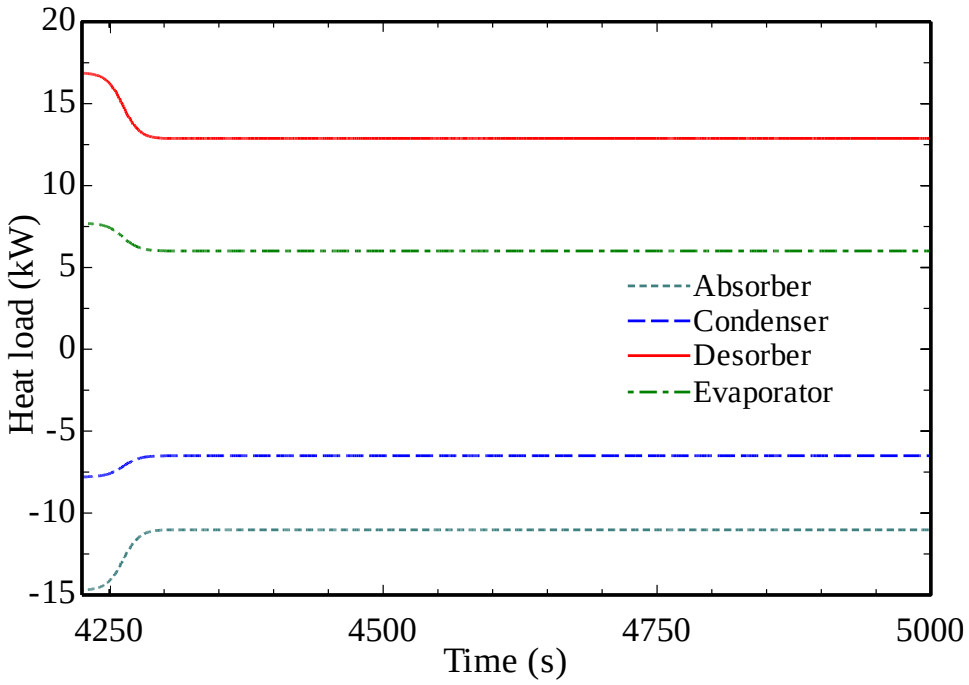

Figure 6-44 : Heat load variations of VARS components during start-up phase.

6.5 System Transient Response during Door Opening

A transient analysis was carried out for a long-distance delivery with the door opening only once to understand the system transient during increased refrigeration load. It was assumed that door opening took place for three minutes at 12000 s. Hence, door was kept opened between 12000 s and 12180 s. If the door was kept open for three minutes, the refrigeration load increased from 6 kW to 7.7 kW (Figure 5-2). The current density needed to increase to get higher thermal power from the SOFC system under increased refrigeration demand.

One of the transient analysis main objectives was to depict the door opening effect on refrigerated cabinet temperature. Therefore, VARS was operated at its nominal point load of 6 kW during door opening. As soon as the door was closed, VARS was operated at its peak load of 7.7 kW to mitigate the effect of a door opening on increased refrigerated cabinet temperature. It should also be noted that refrigeration load demand in the simulation instantaneously

increased to 7.7 kW after 12180 s. This may not represent the actual situation, and in fact, the refrigeration demand load was expected to increase gradually once the door is open. However, detailed analysis was required carry out with fluid dynamics principles, which was included in the scope of the current study.

It should be noted that if SOFC needed to operate at constant power, the burner would need to deal with an increased refrigeration load during door opening. This would be achieved by burning additional fuel to the burner and increasing the mass split of the burner exhaust to the oil heat exchanger. However, the primary motive was to determine whether the SOFC system could mitigate the effect of the door opening without violating any limitations or not. Therefore, the burner was not supplied with additional fuel in this phase.

6.5.1 VARS transient

Figure 6-45 depicts the temperature variation of the refrigerated cabinet during door opening. It is evident that due to the significant amount of infiltration load during door opening, the temperature of the refrigerated cabinet was elevated from 255 K to 259.8 K from 12000 s to 12250 s. Increased refrigeration load by VARS from 6 kW to 7.7 kW also reduced refrigerated cabinet temperature back to the required temperature of 255 K at 13100 s. Hence, it took a total 1000 s to reduce the refrigerated cabinet temperature back to its nominal temperature after door opening.

The mass flow variation in the VARS is shown Figure 6-46. Concentrated solution flow stepped-up from 0.0185 kg/s to 0.0246 kg/s to operate VARS at its peak load of 7.7 kW. Due to the immediate jump in the concentrated solution flow, dilute solution and refrigerant flow rates also showed a sudden jump from 0.012 kg/s to 0.019 kg/s and 0.0053 kg/s to 0.0093 kg/s.

The dilute solution flow and refrigerant flow reduced after a sudden change to their steady-state values of 0.017 kg/s and 0.0067 kg/s, respectively.

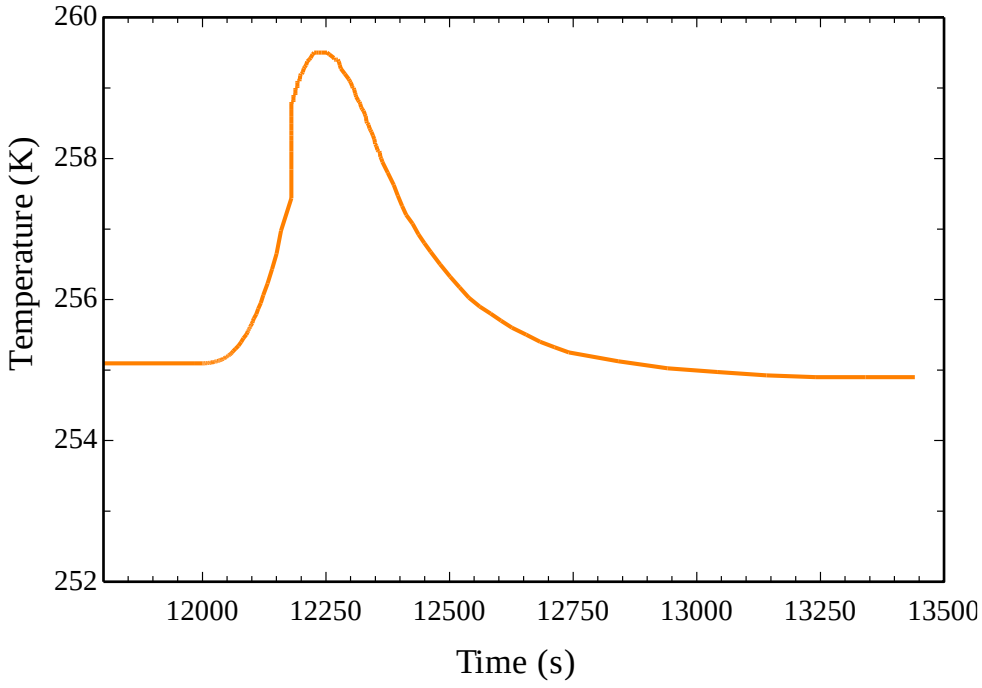

Figure 6-45 : Refrigerated cabinet temperature variation during door opening phase.

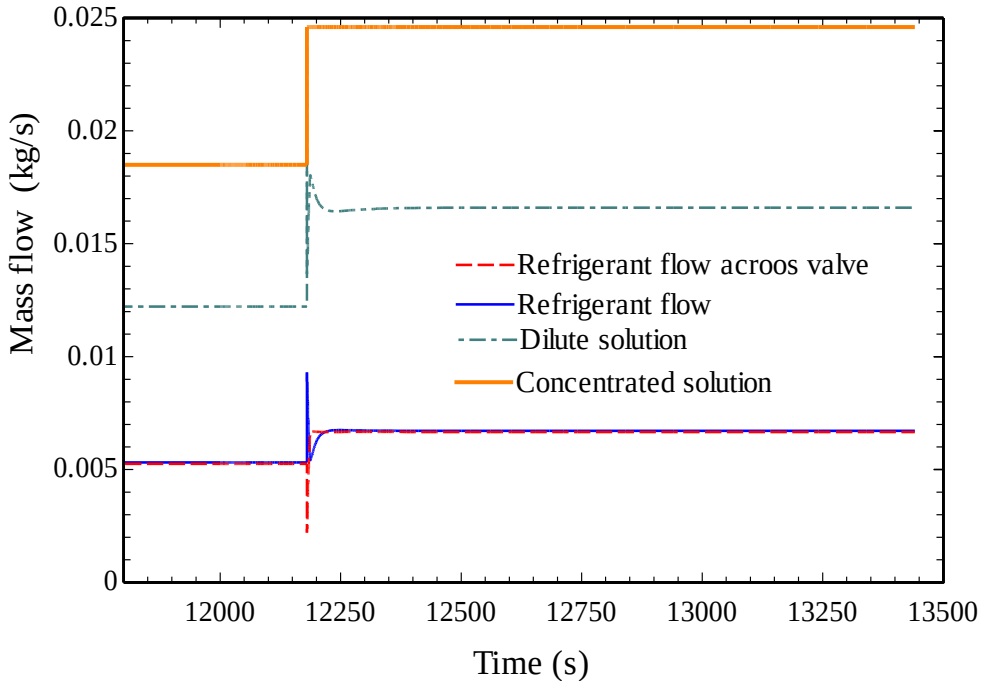

Figure 6-46 : Mass flow rate variation during door opening phase.

Due to the sudden increase of concentrated, and refrigerant flow variation, higher and lower pressure levels in the system are expected to vary. Higher and lower pressure variation of the VARS is shown in Figure 6-47. Higher side pressure increased from 1770 kPa to 1810 kPa as shown in Figure *6-47*. An increase in high side pressure can be explained by a more significant amount of refrigerant vapour generation during due to increased mass flow of concentrated solution. As mentioned above, the refrigerant flow rate started declining after the sudden increase, which means that the refrigerant tank received less refrigerant flow that eventually decreased high side pressure from 1810 kPa to 1798 kPa, as shown in Figure 6-47. Low side pressure rapidly decreased to 160 kPa from 185 kPa due to the sudden increase in concentrated solution flow which reduces ammonia concentration in the solution tank as shown in Figure 6-48. However, gradually ammonia concentration increases which also increased low side pressure from 160 kPa to 179.8 kPa from 12185 s to 13000 s. Interestingly, the refrigerant flow rate through the valve did not encounter significant change, as shown in Figure 6-46, this was due to a low degree of pressure change in the system.

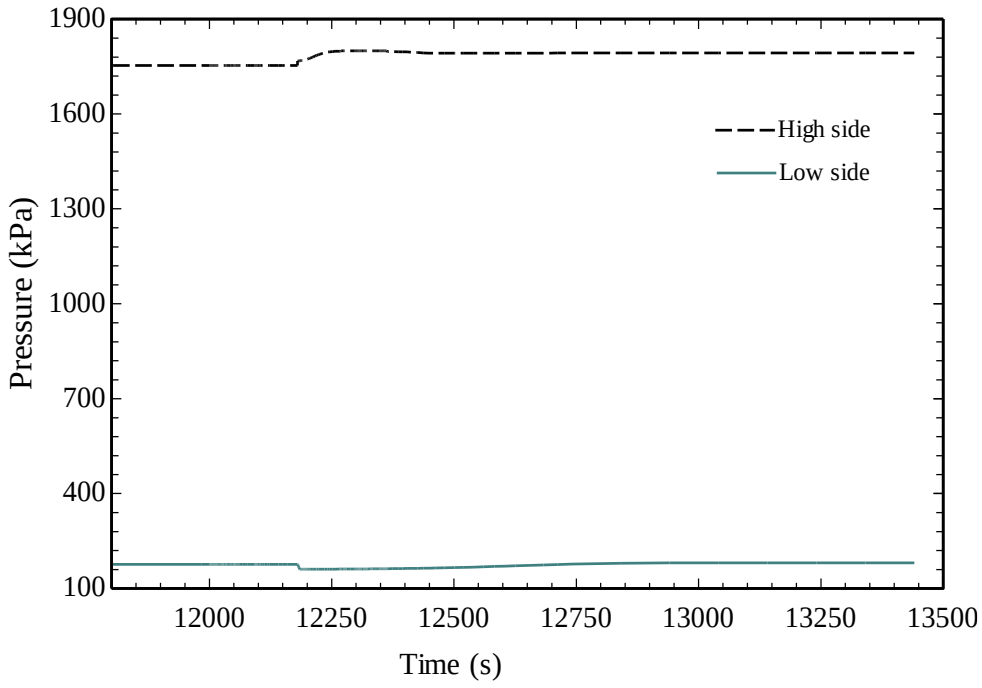

Figure 6-47 : Pressure variation in the VARS system during door opening phase.

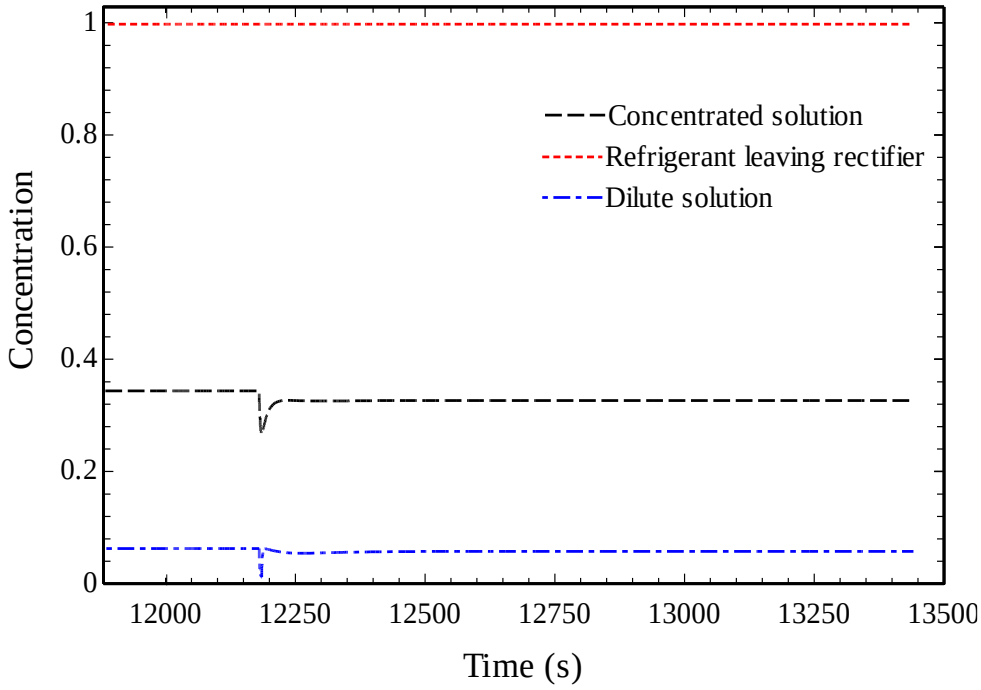

Figure 6-48 : Concentration variation during door opening phase.

Ammonia concentration of concentrated and dilute solution flow variation during the door opening phase Figure 6-48. The ammonia concentration solution decreased to 0.27 from 0.34 due to the sudden increase of the concentrated solution flow to 0.0246 kg/s. After a sudden decrease, it increased again and achieved the steady state value of 0.32. The ammonia concentration of dilute solution also decreased to 0.06 from its previous steady value of 0.1due as shown in Figure 6-48.

Evaporator thermal response to the door opening is shown in Figure 6-49. Once door was opened, refrigerated cabinet temperature increased which also increased return air temperature (coupling fluid). It also increased refrigerant outlet temperature, between 12000 s and 12180 s. The refrigerant outlet temperature increased from 252.9 K to 257.2 K. A sudden increased mass flow in the system also reduced lower side pressure, as shown in Figure 6-47. It also decreased the refrigerant inlet temperature from 251.9 K to 249.8 K which has shown Figure 6-49.

However, with increase in low side pressure, refrigerant inlet temperature started increasing and achieved the steady state temperature of 251.6 K.

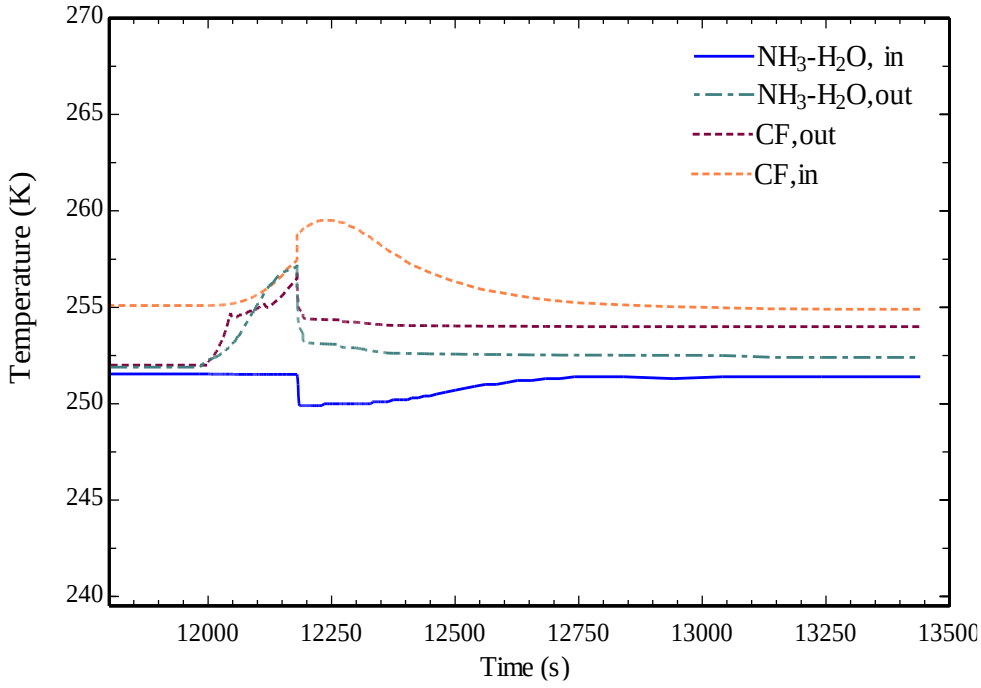

Figure 6-49 : Evaporator thermal response after door opening.

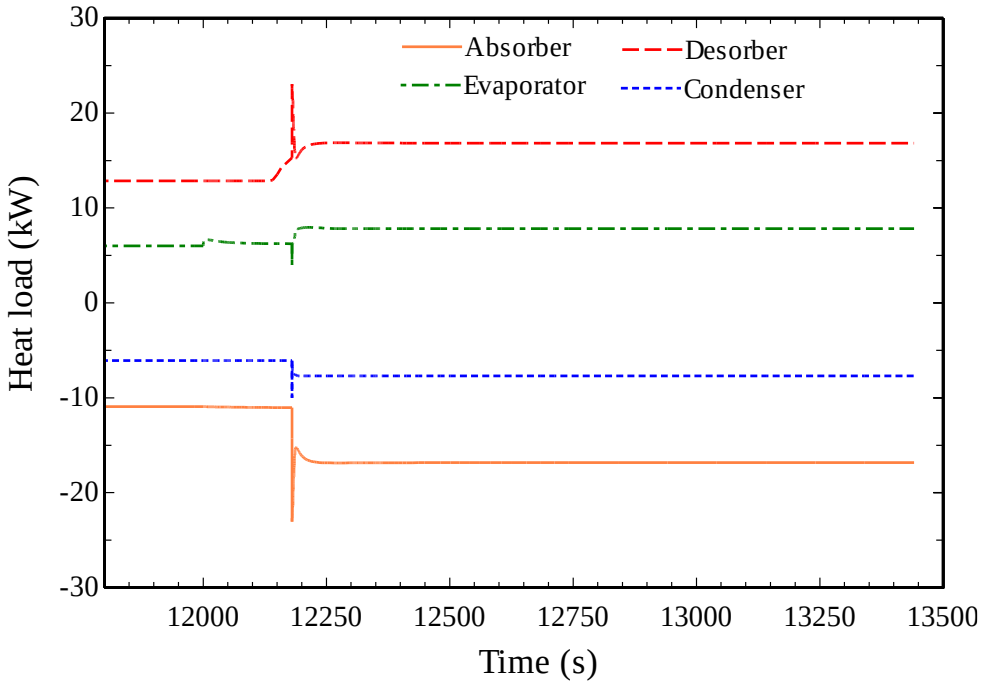

Figure 6-50 : Heat load variation of VARS components during door opening phase.

Figure 6-50 shows heat variation of the main components of the VARS during the door opening phase. At 12180 s, a sudden spike can be observed due to the sudden change in the mass flow in the system, as shown in Figure 6-46. The evaporator heat load spike was less intense than other components heat load. This was due to less variation of refrigerant flow rate through the expansion valve, as depicted in Figure 6-46. It was also observed that the evaporator heat load increased from 6 kW to 6.4 kW within 15 s of door opening (12015 s total) However, it did not significantly affect the remaining components heat load due to their thermal capacitance; hence, it was not noticeable in Figure 6-50. Once the concentrated solution flow was increased (at 12180 s), components achieved their new steady state heat load in approximately 120 s (12300 s in total).

6.5.2 SOFC system transient

The SOFC current was stepped-up immediately from 200 A to 225 A at 12180 s as shown in Figure 6-51 to deliver high amount heat to the VARS to mitigate the effect of door opening.
It is obvious that, stack voltage decreased with increased current. It was observed that the stack voltage reduced from 126 V to approximately 121 V rapidly as shown in Figure 6-52. The Stack voltage further reduced gradually to 120 V due to the thermal response of the stack. This voltage behaviour is in match studies found in the literature [67,185] The thermal response of the stack is shown in Figure 6-53. The stack temperature increased rapidly from 992.7 to 993.5 K due to sudden current step-up. However, airflow was also stepped-up from 60 g/s to 73 g/s, as shown in Figure 6-55. Due to the increased airflow, the stack temperature reduces gradually and achieves its new steady state value of 991 K. SOFC thermal response takes a long time due to its higher thermal mass. It took approximately 4000 s to achieve SOFC new steady state temperature of 991 K. However, the temperature only varied from 992.7 K to 991.

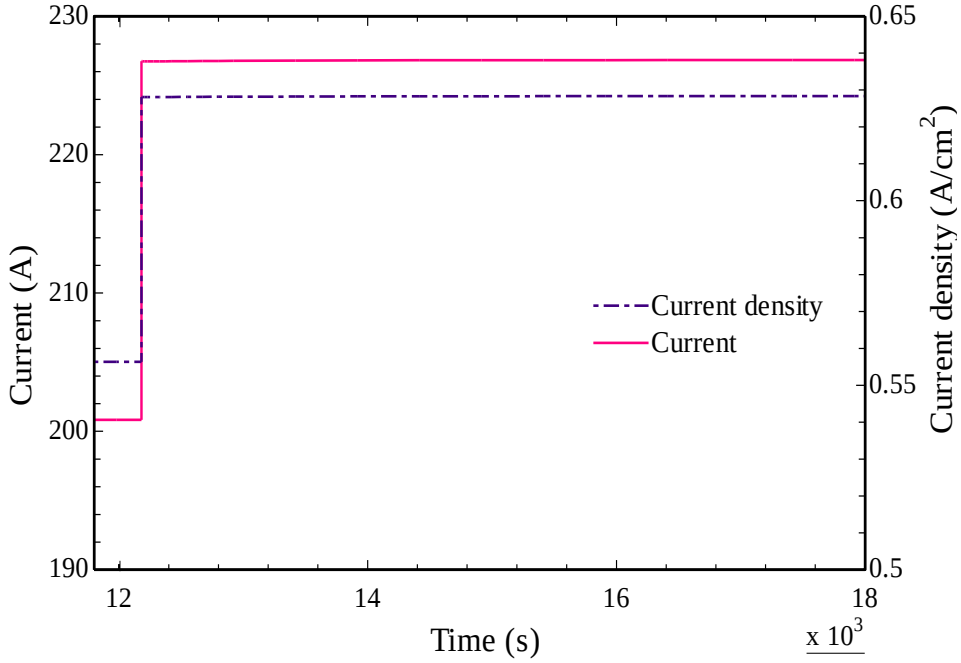

Figure 6-51 : SOFC current and current density evolution in the door opening phase.

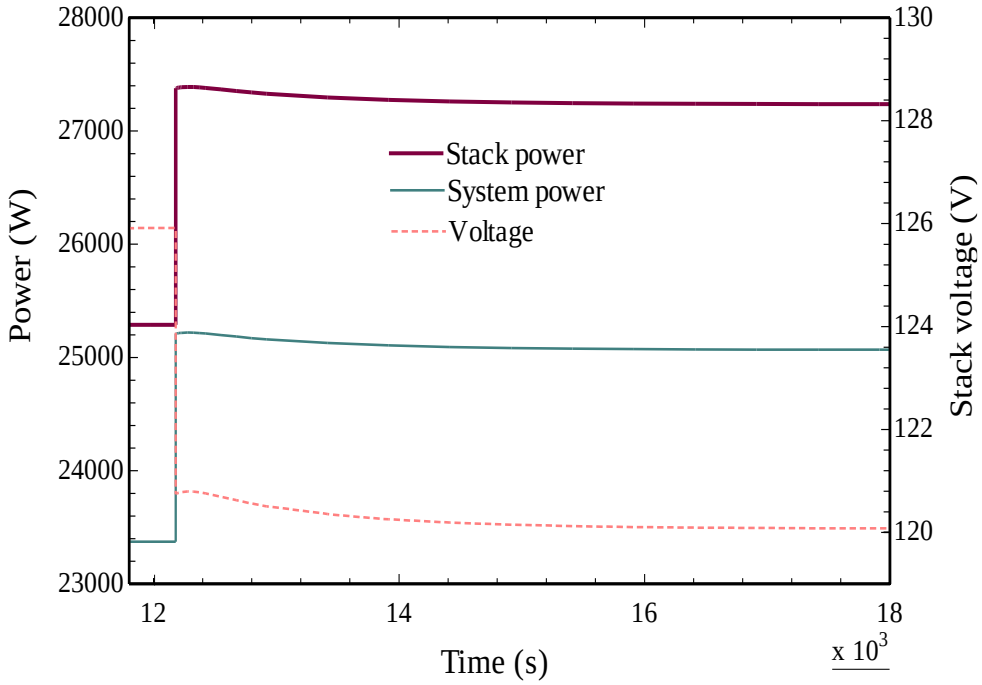

Figure 6-52 : SOFC voltage and power evolution in the door opening phase.

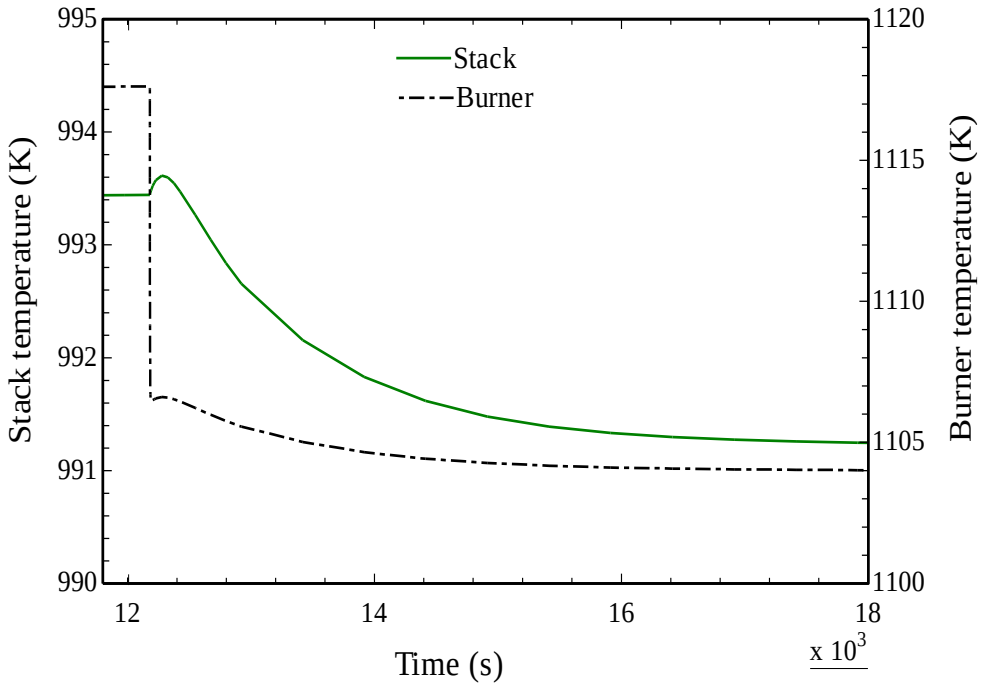

Figure 6-53 : SOFC temperature and burner temperature evolution in the door opening phase.

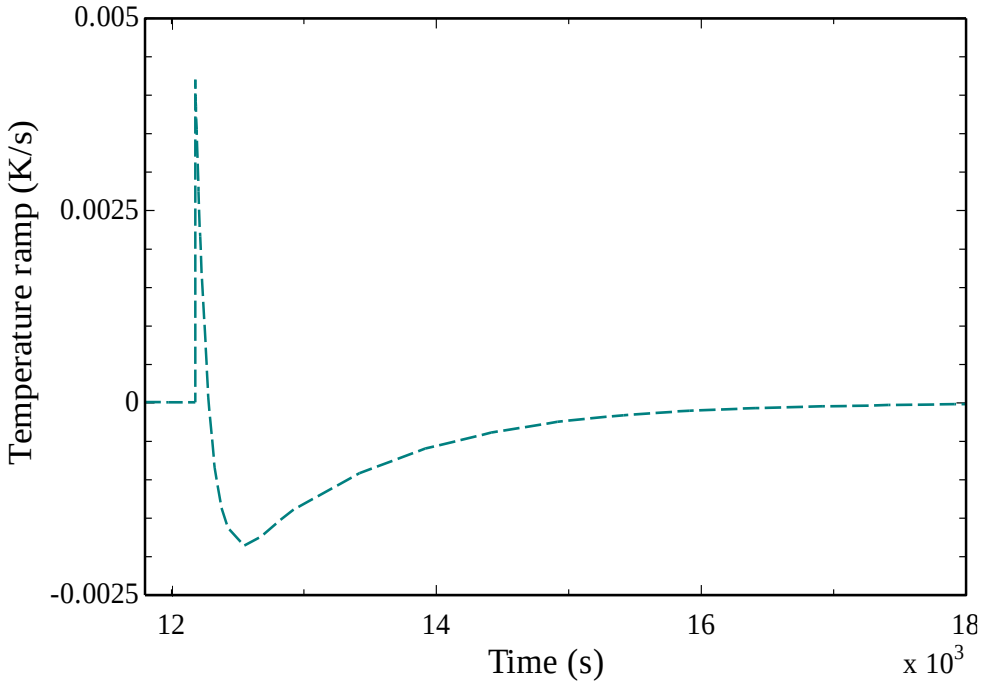

Figure 6-54 : Temperature ramp evolution in the door opening phase.

The stack temperature ramp was supposed to vary due to the current step-up. As highlighted in Figure 6-54, the stack temperature ramp achieved its peak value of 0.048 K/s when the current

was stepped up; however, it reduced gradually and followed the same trend as the stack temperature. The stack temperature ramp did not cross the hard limitation of 0.25 K/s. Therefore, SOFC could counter the door-opening effect without any support from additional devices (burner) to increase the refrigeration load at its peak value.

The airflow was stepped-up to control the maximum stack temperature. The fuel flow needed to increase rapidly from 0.85 g/s to 0.95 g/s at 12180 s as shown in Figure 6-55 to keep the fuel utilisation constant to increase the current value. The SOFC system encountered a higher amount of airflow once current was stepped-up; hence system operated at a high excess air ratio, as shown in Figure 6-56. Excess air ratio value increased from 4.8 to 5.3. SOFC system operation at higher excess air ratio also reduced the burner temperature due to greater amount of air entering the burner, which reduced burner temperature, which is shown in Figure 6-53.

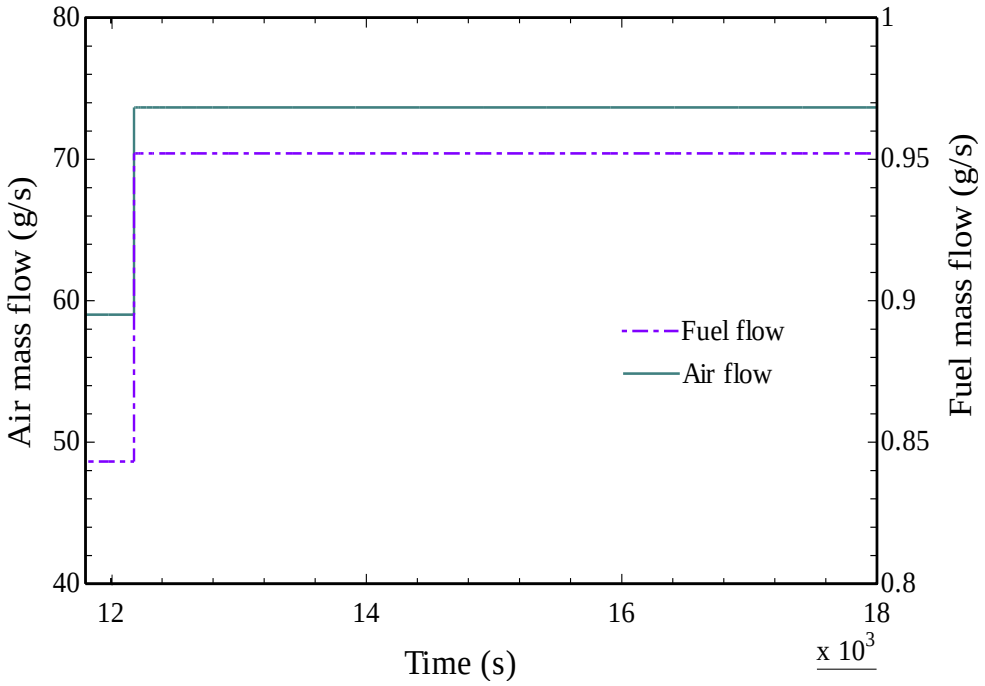

Figure 6-55 : Air and fuel mass flow evolution in the door opening phase.

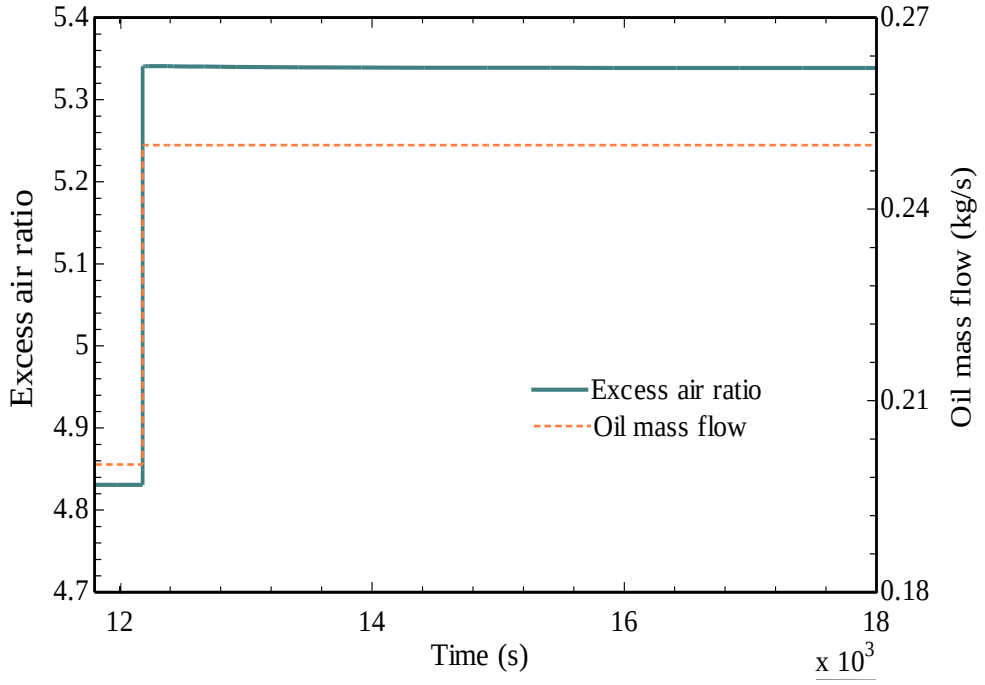

Figure 6-56 : Excess air ratio and oil mass flow evolution in the door opening phase.

Air and fuel heat exchangers also encountered higher flow rate. Therefore, air and fuel inlet temperatures also decreased as shown in Figure 6-57. Air and fuel inlet temperature reduces from 895 K to 886 K and 890 K to 887.5 K, respectively as shown in Figure 6-57. Air and fuel inlet temperature to stack attained their new steady state value at approximately 15250 s; hence it took roughly 3000 s to achieve new steady state values of air and fuel inlet temperature. Stack and system power increased from 25,100 W to 27,300 W and 23,500 W to 25,100 W, respectively as shown in Figure 6-52. This is due to higher current was drawn from the SOFC stack. Oil mass flow was stepped-up immediately for 0.2 kg/s to 0.25 kg/s as shown in Figure 6-56 to deliver high amount of heat to operate VARS.

The oil heat exchanger displayed negligible temperature variations, due to increased heat from the SOFC, oil outlet temperature increased from 493 K to 494 K as shown in Figure 6-58.

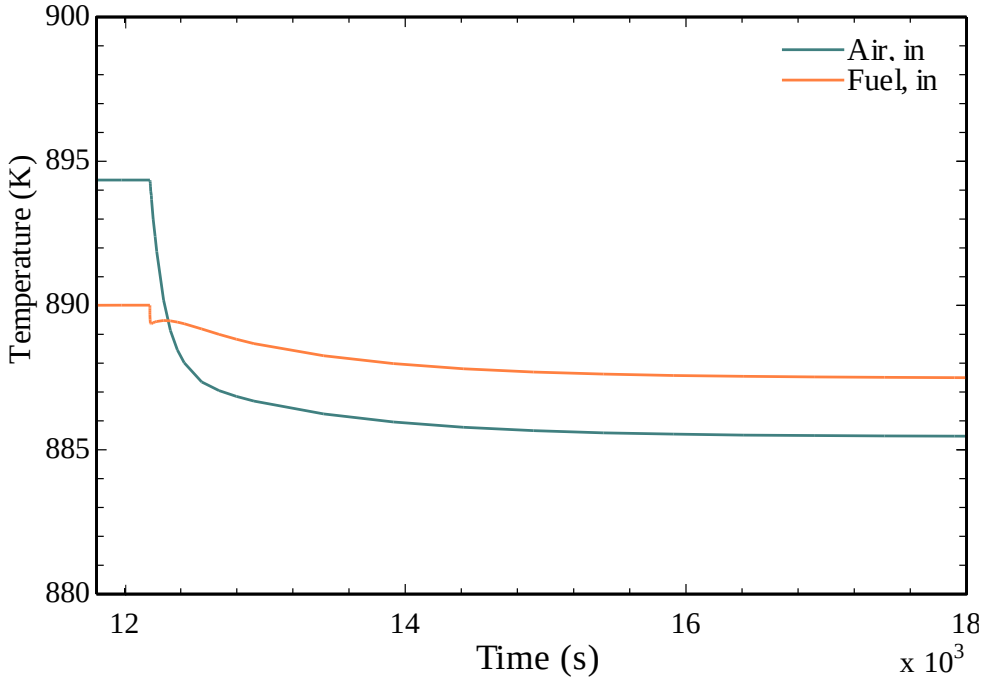

Figure 6-57 : SOFC inlet temperature evolution in the door opening phase.

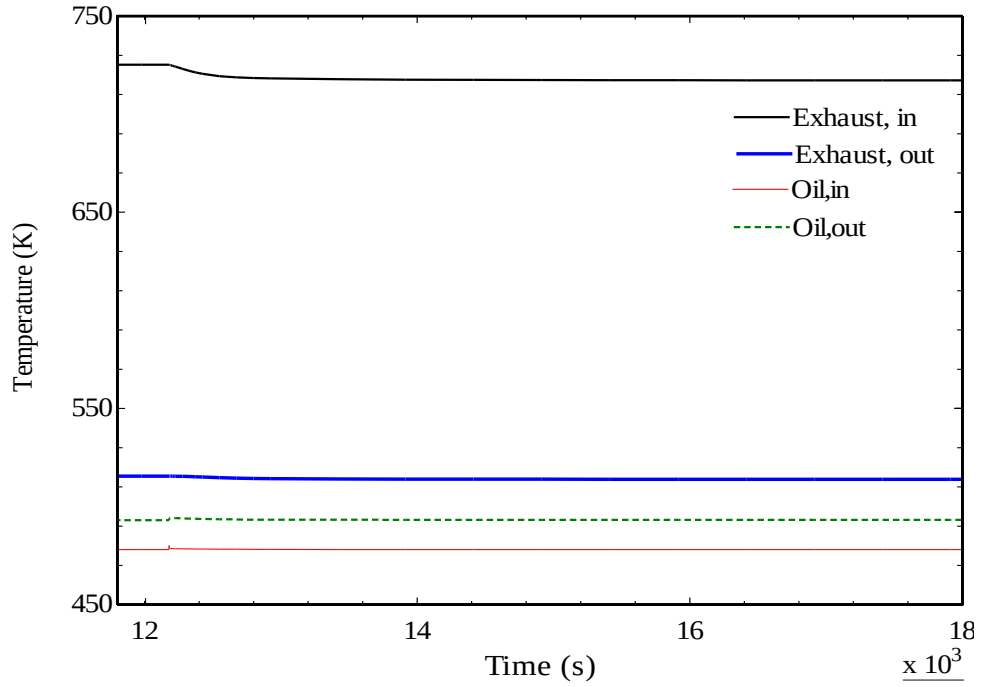

Figure 6-58 : Oil HX thermal response in the door opening phase.

6.6 SOFC non-operative Hours

Temperature transient during cooldown depends upon two quantities, namely (i) the thermal capacitance of the stack and (ii) the thermal conductance of the insulation material (c_{insl}) . A parametric analysis was carried out to establish the effect of the temperature transient during non-operative hours, as shown in Figure 6-59. This was determined by using eqn.6.3.

$$(mc_p)_s \frac{dT_{stack}}{dt} = \dot{Q}_{loss} \qquad 6.3$$

Ambient temperature was assumed 298 K. It was also assumed that during non-operative hours, no fluid stream flow occurred across the SOFC. It was assumed that the stack operated at its nominal design point with a steady state temperature of 993 K before the non-operative period. Therefore, the initial temperature at the start of the non-operative hours was assumed to be 993 K.

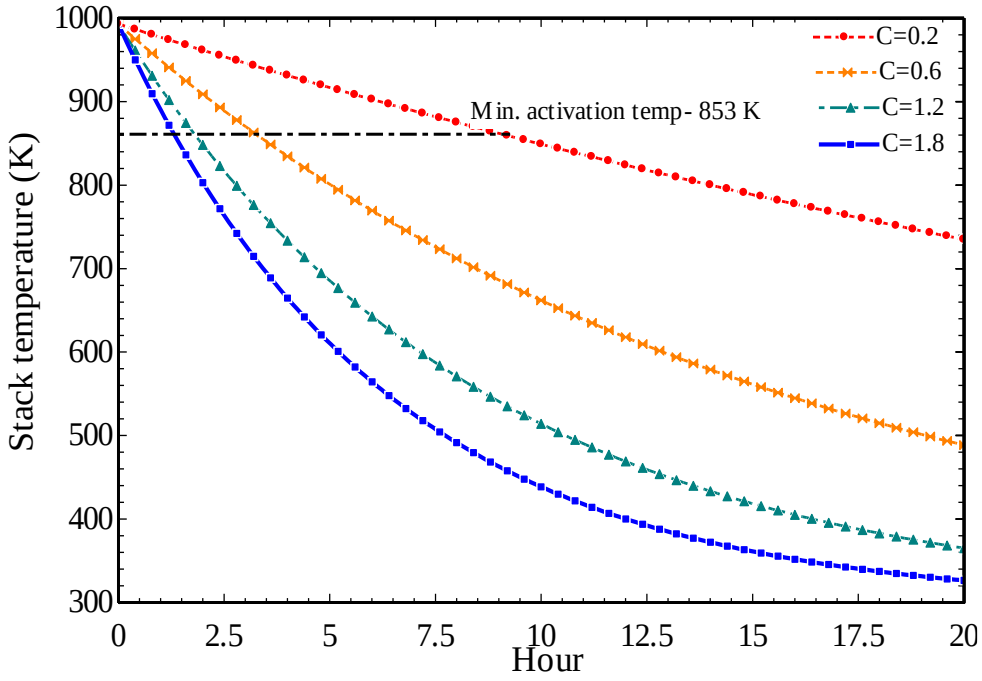

Figure 6-59 : SOFC temperature transient during cooldown.

Figure 6-59 depicts the sensitivity of temperature transient to the thermal conductance (c_{insl}) of the insulation material. The lower the value of c_{insl}, the lower the heat losses, which enabled the SOFC stack to remain at a higher temperature during the non-operative hours. The main interest was to determine the number of hours where SOFC temperature remained above its minimum activation temperature of 853 K. SOFC stack could maintained temperature above 853 K for 9.5 hours, 3.5 hours, 2 hours, 1.5 hours with a value of c_{insl} as 0.2, 0.6, 1.2 and 1.8 W/m^2 K, respectively. As far as truck transportation is concerned, EU regulations demand truck drivers to take a 45 min break after 4.5 hours of driving [186]. However, the truck can operate continuously with an additional driver. Even if the truck journey takes place only with a single driver, it can be seen from Figure 6-59 that it is possible to maintain SOFC temperature above its minimum activation temperature during 45 min break. Therefore, frequent heat-up of SOFC can be easily avoided during short breaks in a single journey. The SOFC stack with c_{insl} value of 0.2 W/m^2 k values can maintain its temperature above minimum activation temperature for 9.5 hours. Therefore, frequent heat-up of the SOFC can be avoided during even for longer non-operative hours of the trucks.

6.7 System Transient Response to Load Following Operation

The next step in the simulation was to determine the system transient response to follow the refrigeration load profile over a driving cycle. The SOFC needs to match the maximum as well as minimum refrigeration demand. As far as range extender application is concerned, SOFC is not expected to encounter any load following conditions. Therefore, no particular load duty profile was considered for the SOFC system in this study. The hottest day and coldest of 2021/2022 calendar year in London were 18 July 2022 and 22 December 2021[187]. These

both days year was chosen to determine the refrigeration demand variation throughout the day. Ambient temperature variation during both these days is shown Figure 6-60.

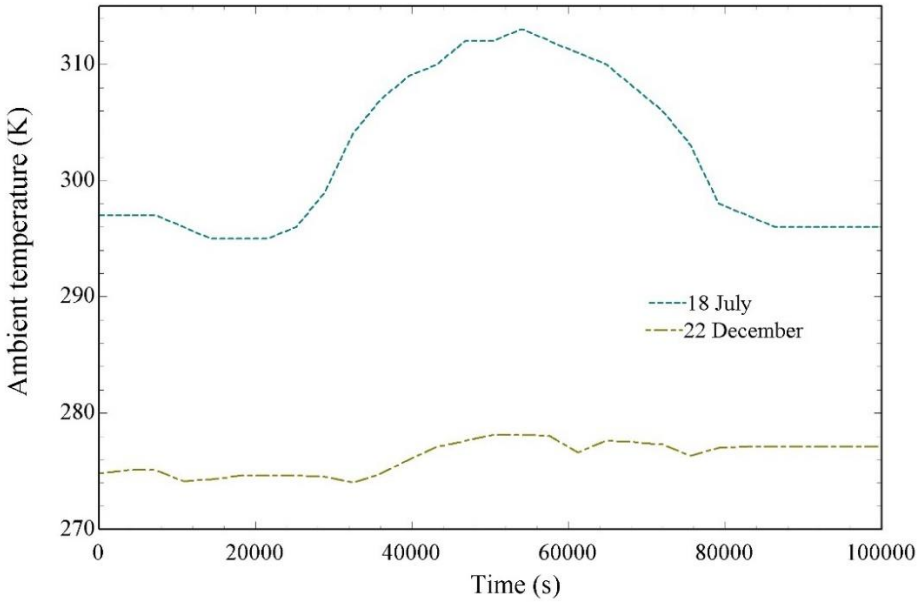

Figure 6-60 : Ambient temperature variation for summer and winter day [187].

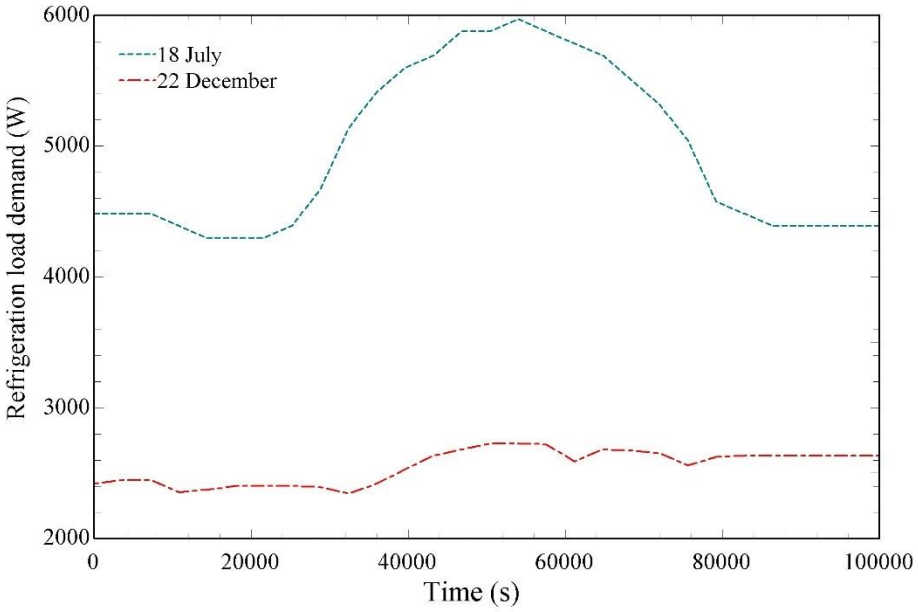

Figure 6-61 : Refrigeration load demand during a journey for summer and winter day.

Figure 6-61 depicts the refrigeration load demand for both days; ambient temperature variation was less for the coldest day. Hence, it is understandable that the refrigeration demand for the coldest day was varied less than for the hottest day. The refrigeration demand varied between 4250 W and 6000 W for the hottest day, while it varied only between 2400 W and 2750 W for the coldest day.

As far as the control aspect to match the refrigeration load demand is concerned, there could be two possibilities to operate the SOFC system:

1. SOFC operation at different operating conditions to meet the refrigeration load demand.
2. Operate SOFC according to electric power demand on-board (constant power generation) and use burner to provide any additional heat to the VARS when SOFC cannot match the refrigeration demand load.

The primary objective of this analysis was to evaluate the feasibility of the SOFC system to match the refrigeration demand load under different weather conditions. Therefore, option 2 was not considered for the transient analysis.

There were several assumptions made as follows to determine SOFC transient characteristics to match refrigeration load following conditions.

- Refrigerated cabinet was already pre-cooled to 255 K before journey starts.
- SOFC stack was heated-up to initial temperature of 893 K.
- The fuel utilisation was kept constant as 0.75 for SOFC system operation.
- Electric power generated from the SOFC under load following conditions was stored in battery on-board of the truck.

- The refrigeration demand load met by VARS with smooth transition of concentrated solution mass flow and oil flow.

It was proved in with Figure 6-43 and Figure 6-44 that the VARS did not encounter significant transient in the performance under smooth transition of load changing. Therefore, the VARS transient characteristic are not included in this section to keep the section short.

The time scale of the whole day is represented in seconds, 0 seconds represents 12 am (mid-night), and it progresses as the day evolves. Variations of current and current density for the hottest day and coldest day are shown Figure 6-62. The current density was higher during summer compared to winter journey due to higher refrigeration load demand. In addition, the current varied from approximately 160 A to 200 A on 18 July. However current variation was significantly reduced on 22 December; it only varied between 106 A to 114 A.

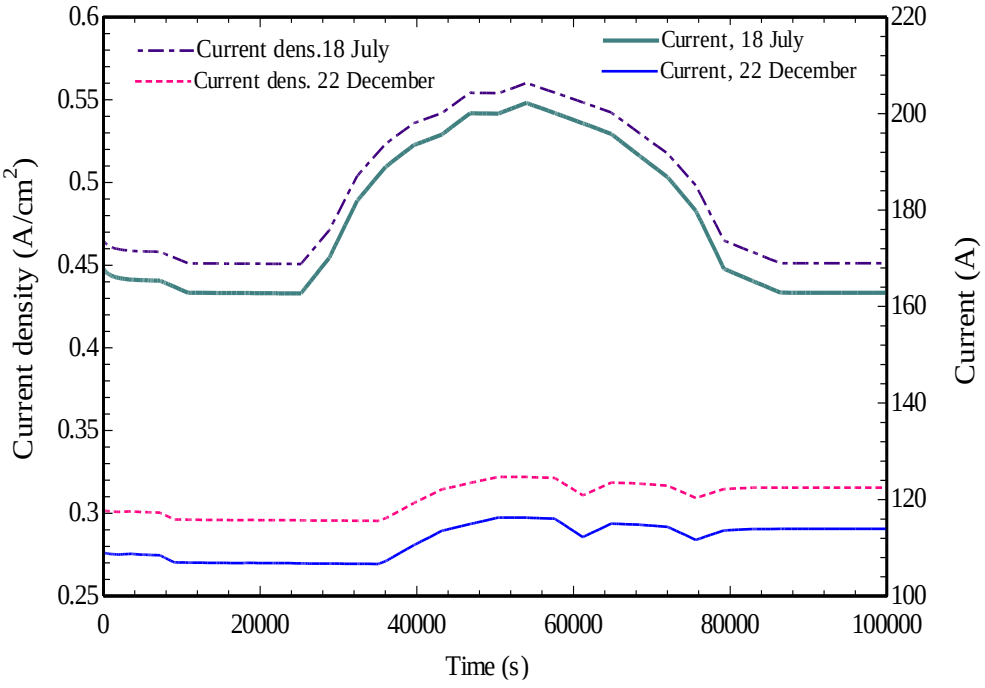

Figure 6-62 : Variation of current during a journey for summer and winter day.

Along with current density, SOFC also needed to be fed with different air flow to keep stack temperature variation value within the threshold value (993 K). Fuel and air variation flow rates for both days are shown in Figure 6-63.

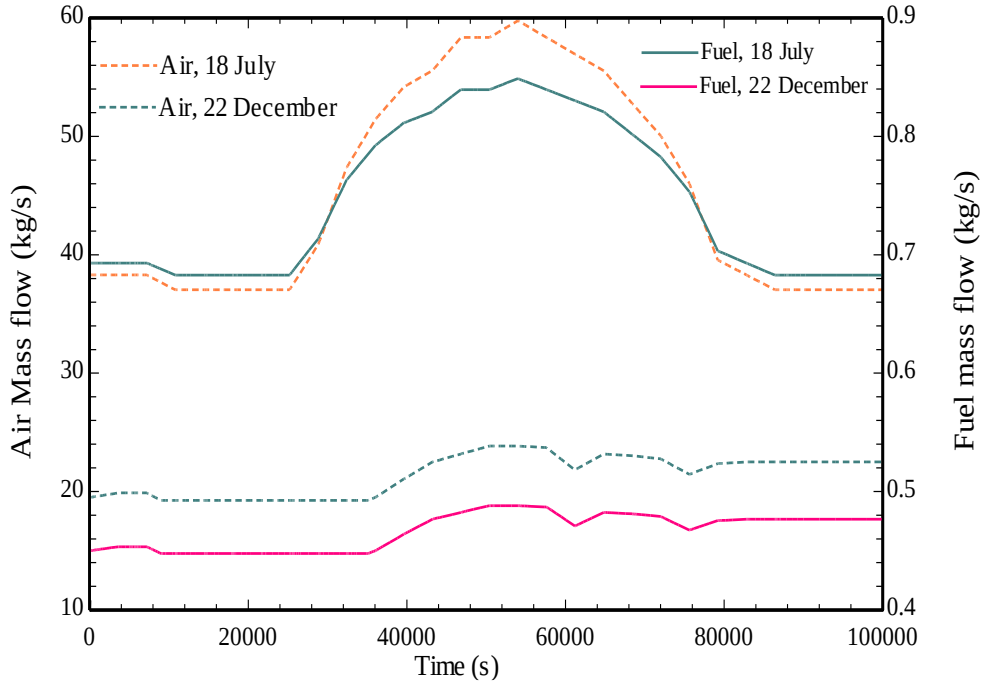

Figure 6-63 : Variation of air and fuel flow during a journey for summer and winter day.

Stack temperature variation for both days is shown in Figure 6-64. It was observed that the SOFC stack temperature never crossed the hard limit of the maximum temperature of 993 K. SOFC achieved the highest temperature close to 993 K. At the same time, refrigeration demand load was highest during both winter and summer journeys. Current density and air flow rate to the stack greatly influenced the SOFC stack temperature. Therefore, stack temperature followed air flow and current density behaviour, as highlighted in Figure 6-63 and Figure 6-62, respectively. The stack temperature ramp variation is the most critical parameter that suggests the SOFC system feasibility in dealing with refrigeration load following conditions. The maximum temperature ramp was observed during the initial phase of the journey, which was expected. However, once the journey was started, temperature ramp variation was not

significant during the load following conditions as shown in Figure 6-64. It was observed that summer day journey encountered higher temperature ramp variation compared to that of the winter journey. However, it was still under allowable temperature ramp variation of 0.25 K/s. Therefore, it was concluded that the SOFC system can deal with the refrigeration load following conditions without the need of any power source (such as burner).

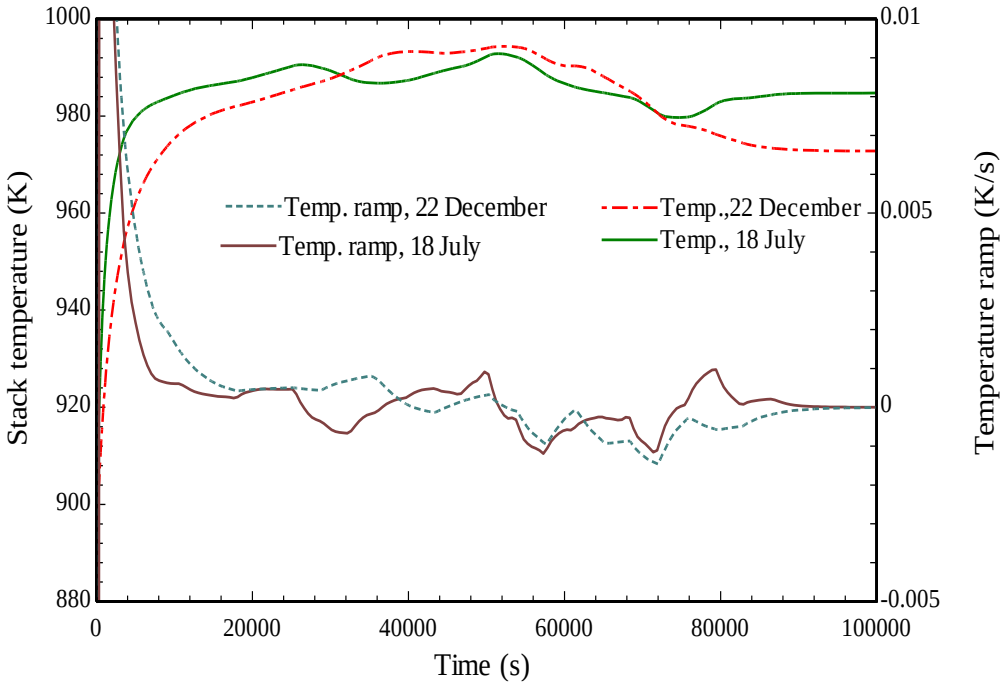

Figure 6-64 : Variation of stack temperature and temperature ramp during a journey for summer and winter day.

The variation of excess air ratio for both days is shown in Figure 6-65. SOFC system needs to operate with higher excess air ratio for summer days compared to winter day, as the system needs more air at a high current density to keep its temperature within the allowable range. At lower currents, the SOFC stack can be operated with lower higher excess air ratio. However, it increased the burner temperature too high; therefore, the SOFC system was operated at slightly higher excess air ratio value even at lower current densities value to keep burner temperature within operating window. Burner temperature variation is shown in Figure 6-65. The SOFC

winter journey experienced higher burner temperatures than the summer journey, which was expected due to the SOFC winter journey running at low excess air ratio.

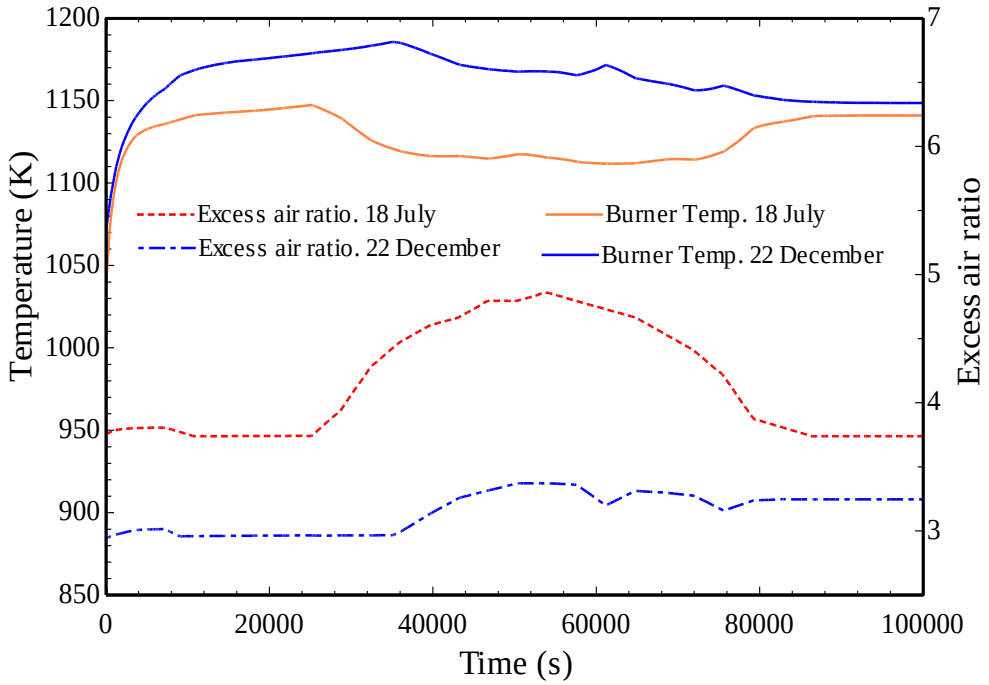

Figure 6-65 : Variation of burner temperature and excess air ratio during a journey for summer and winter day.

The change in stack voltage and system power for both days journey is shown in Figure 6-66. The SOFC system net power followed the refrigeration demand load trend as the SOFC system operating window was chosen according to the refrigeration demand load. The SOFC system power was higher during the summer day journey compared to the winter day journey, due to higher current density operation. The SOFC system power from also affected the overall efficiency of the combined SOFC-VARS system. The change in the combined efficiency of the system is represented in Figure 6-67.

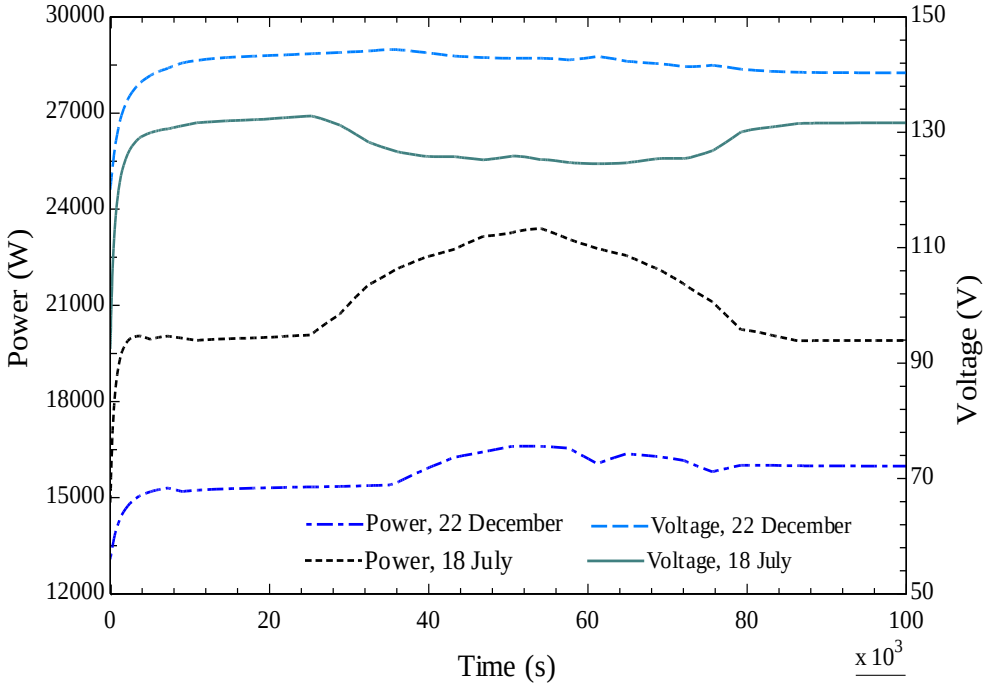

Figure 6-66 : Variation of SOFC voltage and system power during a journey for summer and winter day.

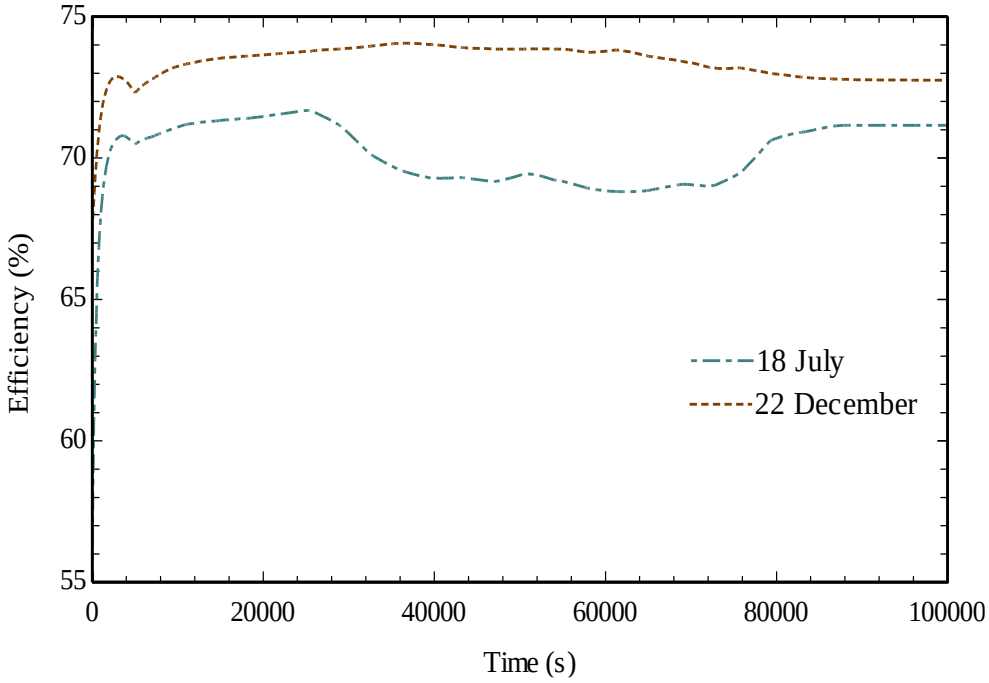

Figure 6-67 : Variation of combined system efficiency during a journey for summer and winter day.

The combined system efficiency improved at low current density (Figure 5-26), therefore winter journey with SOFC system delivered high efficiency. The combined system efficiency showed minor variation along the winter day journey; however, it varied significantly between 67% and 71% during the journey over a summer day.

It is essential to store the electric power generated by the SOFC system on-board. The battery size should be decided such a way that, it would be able to store the electrical power from SOFC throughout the load following conditions under different weather conditions. One of the silent features of this transient analysis is that it also helps to determine the battery size to store electrical power for load following conditions. After assessing the transient performance of the SOFC system subjected to two different weather conditions, it was determined that the SOFC system should be equipped with at least 20 kWh of battery. As mentioned in Table 6-2, the minimum battery size needed for SOFC heat-up with strategy A is 15.1 kWh. Therefore, 20 kWh on-board battery would also fulfil the electrical power during heat-up. The SOFC system with 20 kWh battery can deal with refrigeration load demand up to 6 kW. Hence, it translates into battery size of approximately 3.3 kWh/kW of maximum refrigeration load.

6.8 Conclusion

A detailed transient analysis of the SOFV-VARS combined system was carried out in this chapter. The transient characteristics of the SOFC integrate VARS system were assessed in different operational phases. In addition, SOFC system response to match on-board refrigeration demand load for different weather conditions was also evaluated in detail.

It was found that the schematic of the system needed to be updated for the transient analysis compared to a schematic considered for the steady state analysis to make system operation

feasible in the different operational phase. The SOFC system should be equipped with CPOX reformer to generate steam which would be needed for the SOFC stack operation.

It was possible to carry out the SOFC heat-up and refrigerated cabinet pre-cooling simultaneously. To achieve this, SOFC should be heated-up electrically and VARS should be powered by the burner in the initial operational phase. It was also concluded that the time required to heat up the SOFC heat-up and pre-cool the refrigerated cabinet was approximately similar (~ 4100 s). Hence, longer SOFC heat-up time is no additional burden for the refrigerated transportation application as truck journey cannot begin without the pre-cooling of the refrigerated cabinet.

It was also determined that the SOFC did not generate sufficient heat to power VARS during CPOX reformer and start-up phase. During these phases, VARS was powered by the SOFC and burner. Therefore, burner operation was found essential to power VARS until SOFC achieved its steady state operation conditions.

Based on the transient results obtained, the SOFC did not violate temperature ramp and maximum operation temperature limitations to satisfy load following conditions during door opening phase and under different weather conditions. Therefore, no additional heat source was needed to satisfy the load following conditions during a journey. It proved the feasibility of the SOFC system for the refrigerated transportation application. It was also determined that the SOFC system depicted higher combined system efficiency for a winter journey compared to a summer day. The SOFC system achieved peak combined efficiency of 74 % and 71 % and average combined efficiency of 71 % and 68 % for a winter day and summer day journey, respectively.

The SOFC system should be equipped with approximately 3.33 kWh per kW of maximum refrigeration load to store the electrical power on-board. It would also satisfy the electrical power needed to heat-up the SOFC.

Chapter 7: *Conclusions & Future Work*

This chapter outlines the main findings from the results obtained in the previous chapters. combination of results allows the evaluation of the feasibility of achieving the objectives of this thesis. Finally, the scope of future work is highlighted.

7.1 Summary

A comprehensive literature review of the current status of the SOFC and VARS technologies for automotive transportation was presented. It was proven that even though there is an opportunity to develop SOFC powered VARS for automotive transportation, the feasibility of such a novel concept should be outlined with both experimental setup and simulation approaches. It was proven that sub-zero temperatures can be achieved with the laboratory setup available. A detailed methodology of developing a generic SOFC system model was outlined. Unfortunately, it was not possible to develop a generic transient model for the vapour absorption refrigeration system due to the complexity involved in its operation. Therefore, a detailed discretised 1D model was developed to predict the system performance. SOFCs can generate electrical power with direct internal reforming of methane, enhancing the fuel cell efficiency. In addition, the integration of the SOFC exhaust with a vapour absorption refrigeration system (VARS) increases the overall efficiency further. More specifically, the following contributions were delivered by the current study:

- a simulated SOFC exhaust integration with a VARS was implemented at laboratory scale.
- A comprehensive thermodynamic performance assessment of the combined system was completed to understand the integration of both systems.
- A detailed procedure to select the preferred operating envelope of the SOFC system to power the VARS for different types of application was outlined.
- Transient models were developed for both systems to characterise system response under different operating conditions (including load following).

The developed laboratory setup achieved sub-zero temperatures (down to -8°C) with a maximum COP of 0.26. The setup delivered unsatisfactory performance due to limitations in the way it could be built in the laboratory environment, nevertheless, the desired objective to achieve sub-zero temperatures was fulfilled. Several suggestions were made to obtain improved performance in the future. It was concluded that with the implementation of these improvements, the setup would be able to achieve a COP up to 0.5 and temperature down to -18°C. Nevertheless, the concept proved to be feasible and could in principle be implemented in real world applications. In the next step, steady state and transient simulation models were established to assess the SOFC integrated VARS combined system.

The important findings from the detailed simulation of the combined system to address the research questions stated in the introductory chapter are as follows:

- It was observed that the combined system efficiency was to a high degree sensitive to SOFC system efficiency compared to the VARS COP. This was due to the low COP of the VARS. Hence, the focus should be on optimising the SOFC system performance to enhance the combined system performance.

- The heat exchanger network of the SOFC system was found to be crucial to integrate the SOFC system with the VARS. The cathode air pre-heat exchanger needed to be modified to improve the system performance. It was determined that the air should be heated-up to SOFC operating temperature in two heat exchangers arranged in a series connection to deliver the maximum amount of heat to the VARS. The combined system performance with modified layout showed an improvement of 240% in refrigeration

power density and 15% in refrigeration efficiency compared to the SOFC system conventional layout.

- The SOFC system was operated neither to maximise electric nor heating power. The SOFC system operating envelope was decided with a detailed analysis, considering several performance parameters namely: power density, efficiency and emissions. It was also determined that the SOFC operating envelope greatly depended upon the targeted application.

- If the combined system were be developed as an APU application to match the refrigeration demand load for small and medium trucks, the system efficiency would be close to 50% due to system operation at elevated current density. In that case, a hybrid SOFC-VARS system could be employed on trucks where the VARS would be powered by the SOFC and burner. The SOFC stack could be operated at lower current density to improve the efficiency. An overall efficiency up to 60% could be achieved with such a hybrid SOFC-VARS concept for small and medium trucks. As far as APU application to achieve refrigeration demand for large trucks is concerned, the combined system satisfied the requirements with an efficiency as high as 62%.

- The combined system delivered a maximum efficiency of 68% if the SOFC system were developed as a range extender or prime mover for trucks.

- The SOFC-VARS emitted least amount of GHG emissions compared to cryogenic transportation systems and conventional diesel driven systems. It was concluded that the SOFC-VARS could reduce approximately 25% to 45% emissions from the

refrigerated transportation compared to other technologies. Hence, SOFC system with VARS could decarbonise refrigerated transportation significantly.

- It was concluded that the long SOFC heat-up time was not the bottleneck for the implementation of the SOFC system for refrigerated transportation. It was due likewise the requirement of pre-cooling of the refrigerated cabinet. It was possible to heat-up the SOFC stack within the time required to accomplish the pre-cooling. The SOFC stack was heated by electrical power from a battery and the VARS was powered by the burner during the pre-cooling phase. The SOFC stack required approximately 600 Wh of electrical energy per kW power of stack.

- During SOFC heat-up, start-up and CPOX activation phase, the SOFC could not satisfy the refrigeration load demand. Hence the burner supplied additional heat to the VARS to satisfy the refrigeration load demand. The SOFC delivered the required heat to the VARS after ramping up the current in the start-up phase.

- It was also determined that the SOFC could mitigate the effect of increased refrigeration load due to door opening of the vehicle without violating stack temperature ramp limitations. The current was stepped-up to generate higher thermal power to deliver to VARS.

- The combined system was subjected to refrigeration load following conditions for a typical summer and winter day. The SOFC system was able to follow the refrigeration load without violating maximum working temperature and temperature ramp-up constraints. It was observed that the system showed higher efficiency for a winter

journey compared to summer. The system achieved a peak efficiency of approximately 75% on a winter day, mainly due to the SOFC operation at low current density and improved VARS COP at reduced ambient temperature. The battery was needed to buffer the electrical power generated by the SOFC during load following operations. The SOFC system should be equipped with approximately 3.33 kWh battery capacity per kW of peak refrigeration load.

7.2 Conclusions

The transportation sector is experiencing a technology shift from internal combustion engines to battery-powered electrified systems. However, with limited range and long charging times, battery-powered applications are not attractive for heavy-duty and/or long-haul truck transportation. Fuel cell powered systems offer a promising alternative to truck transportation. Fuel cell technology has already penetrated the heavy-duty/long-haul automotive industry. Harnessing the heat from the fuel cell for use in another application will not only boost the system efficiency but also contribute to maximum recycling of energy within the system rather than wasteful dissipation. It is feasible to develop and employ SOFC-integrated VARS for refrigerated transportation. It makes the refrigerated truck far more efficient than conventional diesel engine-driven truck refrigeration units.

The development of SOFC APU for transportation applications also encourages the possible future design of an entire methane fuelled, SOFC-driven electric vehicle concept where the heat is used for onboard air conditioning and refrigeration. The application of such systems is not restricted to automotive transportation, it can be further extended to stationary applications and other modes of transport to decarbonise the cooling/refrigeration sector.

Ammonia is highly toxic; hence the leakage of ammonia must be avoided and accidental leaks ammonia to the refrigerated cabinet prevented as this will harm the transported goods quality. Leakage chances of ammonia from the system may increase for automobile application due to vibration and acceleration. This safety hazard must be considered in implementing this technology for real world applications.

7.3 Future Work

The outputs of the current thesis provide an operational map of the combined SOFC-VARS system which can deliver further inputs and directions in developing a control methodology for the combined system. A comprehensive control methodology for the SOFC integrated VARS for automotive transportation has not been explored here and is an area that needs to be further explored. A control strategy development would provide further insights into the system operation and would need to take the complex interdependencies of the system operating parameters into account.

A generic model was developed for the SOFC system in this study; however, it was not possible to develop such a generic model for the VARS system. The current VARS transient model requires many details even though it was intended for system level analysis. Therefore, a study needs to be carried out to check the feasibility of developing a generic model for the VARS. This would be a convenient tool in establishing the control methodology of the combined system.

The transient analysis of the combined system under load following conditions was carried out according to UK climate conditions. The refrigeration load demand greatly depends on

climate conditions. Hence, the transient response of the combined system should be evaluated under a range of climate conditions.

The current study did not consider the effect of vehicle vibration on the VARS performance. The vehicle vibration during a journey might affect the absorption and desorption processes in the VARS. The effect of vehicle vibration on the VARS performance could be a future area of analysis.

Methane was considered as a logistic fuel in the current study. It should also be noted that the SOFC can deal with various fuels such as synthetic fuels/LPG/Hydrogen which may be potential logistic fuels for future automotive powertrain. Therefore, the combined system performance should be analysed with different logistic fuels, potentially modifying the SOFC operating envelope according to different fuels.

A setup of the SOFC system powered VARS should be demonstrated on-board a vehicle. This would help to identify and address any issues with the real-world implementation of such systems. The ultimate goal should be the development of SOFC powered automotive powertrain for trucks, where the SOFC would act as a prime mover/range extender/APU to fulfil on-board electrical power requirements, and the SOFC exhaust used for driving a VARS for refrigeration and/or air-conditioning.

Appendix A

Geometrical parameters of experimental set-up components

Table A-1 : Geometrical parameters of the tube-in-tube heat exchanger.

Parameters	Value
Number of fins	4
Fin height (mm)	8
Fin thickness (mm)	4
Length of tube (mm)	500
Inner diameter of inner tube (mm)	29.7
Outer diameter of inner tube (mm)	33.7
Inner diameter of outer tube (mm)	56.3
Outer diameter of outer tube (mm)	60.3
Weight (kg)	7

Table A-2 : Geometrical details of the desorber.

Parameters	Value
Number of plates	27
Height of plate (mm)	300
Width of plate (mm)	50
Thickness of plate (mm)	0.4
Weight(kg)	6

Table A-3 : Geometrical details of the rectifier.

Parameters	Value
Outer tube diameter (mm)	6
Inner tube diameter (mm)	4
Height of cylinder (mm)	400
Helix diameter (mm)	58
Outer diameter of inner cylinder (mm)	42.4
Inner diameter of outer cylinder (mm)	70.3
Weight (kg)	7

Table A-4 : Geometrical parameters of the condenser.

Parameters	Value
Number of fins (N_f)	27
Fin height (mm) (H_f)	400
Fin thickness (mm) (δ_f)	0.3
Length of tube (mm)	410
Inner diameter tube (mm)	29.7
Outer diameter tube (mm)	26.7
Weight (kg)	1.5

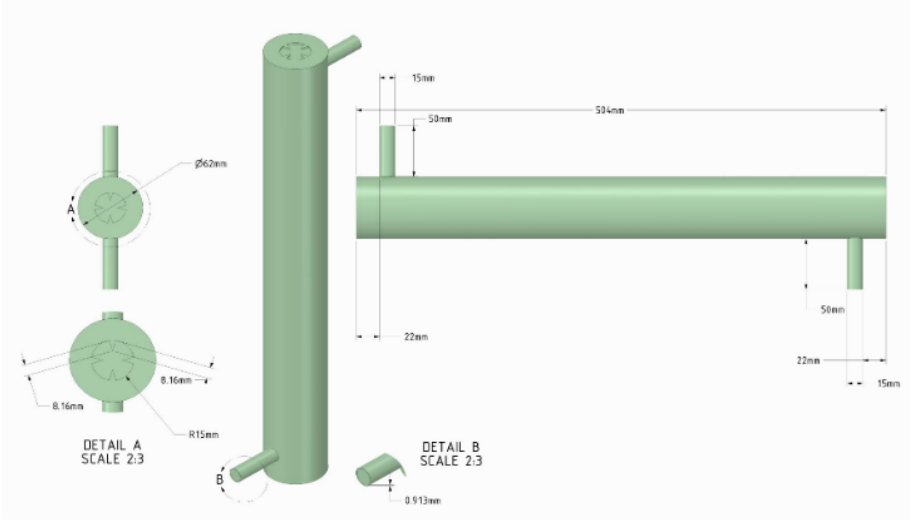

Figure A-1 : CAD drawing of tube-in-tube heat exchanger.

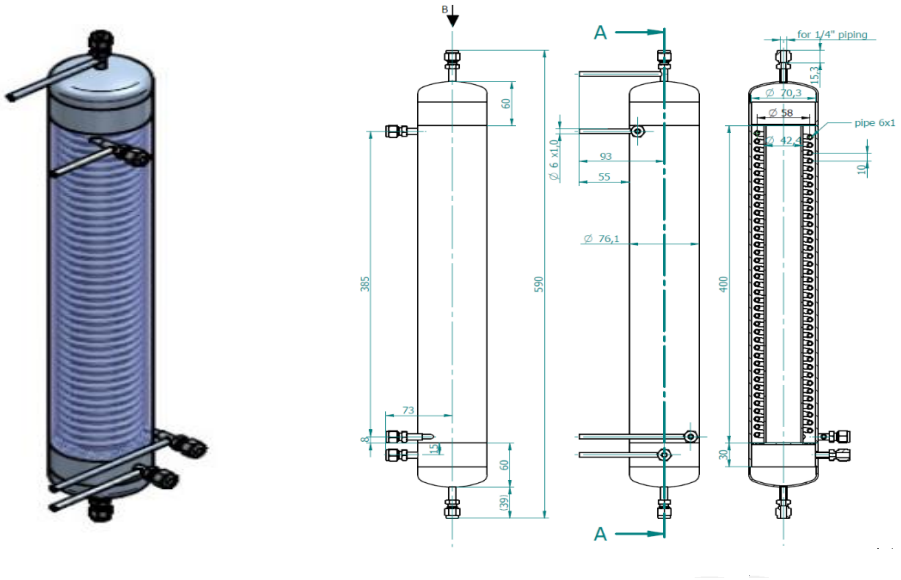

Figure A-2 : Schematic of the rectifier with geometrical details.

Appendix B

Equations used to compute the experimental set-up performance.

Total heat transfer area for the air-oil heat exchanger (A_{oilHX}) was determined by eqn. B.1.

$$A_{oilHX} = A_{fin} + A_{tube} \quad \text{B.1}$$

Where,

A_{fin}	Fin surface area (m^2)
A_{tube}	Un-finned tube area (m^2)

A_{fin} and A_{tube} are determined by eqn.B.2 and eqnB.3, respectively.

$$A_{fin} = 2N_f H_f L_f \quad \text{B.2}$$

$$A_{tube} = \delta_f d_o L_f - N_f L_f \delta_f \quad \text{B.3}$$

Where,

δ_f	Fin thickness (m)
d_o	Outer diameter of inner tube (m)
N_f	Number of fins
H_f	Height of fin (m)
L_f	Length of fin (m)

Table B-1 : Equations used to compute desorber performance of experimental setup.

Equations	Abbreviations	
$\dot{m}_{conc} = \dot{m}_{vap} + \dot{m}_{dil}$	x_{absr}	Ammonia concentration in absorber tank
$\dot{m}_{conc} x_{absr} = \dot{m}_{vap} x_{vap} + \dot{m}_{dil}\, x_{dil}$	$h_{vap,dsrbr}$	Specific enthalpy of refrigerant vapour (kJ/kg)
$\dot{Q}_{dsrbr} = \dot{m}_{vap} h_{vap,dsrbr} + \dot{m}_{dil}\, h_{dil,dsrbr} - \dot{m}_{conc} h_{conc,dsrbr}$	$h_{conc,dsrbr}$	Specific enthalpy of concentrated solution at desorber inlet (kJ/kg)
$h_{conc,dsrbr} = fn(T_{conc,dsrbr}, P_{high}, x_{conc})$	$h_{dilute,dsrbr}$	Specific enthalpy of dilute solution at desorber outlet (kJ/kg)
$h_{vap,dsrbr} = fn(T_{vap,dsrbr}, P_{high}, q = 1)$	$\dot{Q}_{dsrbr}$	Heat load of desorber (W).
$h_{dilute,dsrbr} = fn(T_{dil,dsrbr}, P_{high}, q = 0)$	$T_{vap,dsrbr}$	Temperature of refrigerant vapour at desorber outlet (°C)
$x_{vap} = fn(T_{vap,dsrbr}, P_{high}, q = 1)$	$T_{dil,dsrbr}$	Temperature of dilute solution at desorber outlet (°C)
$x_{dilute} = fn(T_{dilute}, P_{high}, q = 0)$	$T_{conc,dsrbr}$	Temperature of concentrated solution at desorber inlet (°C)
	P_{high}	High side pressure (bar).
	$\dot{m}_{vap}$	Mass flow of refrigerant vapour at desorber outlet (g/s)
	x_{vap}	Ammonia concentration of vapour leaving desorber

Table B-2 : Equations used to compute rectifier performance of experimental setup.

Equations	Abbreviations	
$\dot{Q}_{rect} = \dot{m}_{vap} h_{vap,dsrbr} - \dot{m}_{ref} h_{ref,rect,out} - \dot{m}_{rflx} h_{rflx}$	$h_{ref,rect,out}$	Specific enthalpy of refrigerant vapour at rectifier outlet (kJ/kg)
	h_{rflx}	Specific enthalpy of reflux flow at rectifier outlet (kJ/kg)
	$h_{conc,rect,in}$	Specific enthalpy of concentrated solution at rectifier inlet (kJ/kg)
$\dot{Q}_{rect} = \dot{m}_{conc}(h_{conc,rect,in} - h_{conc,rect,out})$	$h_{conc,rect,out}$	Specific enthalpy of concentrated solution at rectifier outlet (kJ/kg)
$\dot{m}_{vap} = \dot{m}_{ref} + \dot{m}_{rflx}$	$T_{conc,rect,in}$	Temperature of concentrated solution at rectifier inlet (°C)
$\dot{m}_{vap} x_{vap} = \dot{m}_{ref} x_{ref} + \dot{m}_{rflx} x_{rflx}$	$T_{ref,rect,out}$	Temperature of refrigerant vapour at rectifier outlet (°C).
$h_{conc,rect,out} = h_{conc,dsrbr}$	$h_{ref,rect,out}$	Specific enthalpy of refrigerant vapour at rectifier outlet (kJ/kg)
$h_{conc,rect,in} = fn(T_{conc,rect,in}, P_{high}, x_{absr})$	h_{rflx}	Specific enthalpy of reflux flow at rectifier outlet (kJ/kg)
$x_{ref} = fn(T_{ref,rect,out}, P_{high}, q = 1)$	$h_{conc,rect,in}$	Specific enthalpy of concentrated solution at rectifier inlet (kJ/kg)
$h_{ref,rect,out} = fn(T_{ref,rect,out}, P_{high}, q = 1)$	$\dot{m}_{ref}$	Mass flow of refrigerant vapour at rectifier outlet (g/s)
$x_{rflx} = fn(T_{conc,rect,in}, P_{high}, q = 0)$	x_{ref}	Ammonia concentration of vapour leaving rectifier
$h_{rflx} = fn(T_{conc,rect,in}, P_{high}, q = 0)$	x_{rflx}	Ammonia concentration of reflux leaving rectifier
	$\dot{m}_{rflx}$	Mass flow of reflux at rectifier outlet (g/s)
	$\dot{Q}_{rect}$	Rectifier heat load (W)

Table B-3 : Equation used to compute condenser and evaporator performance of experimental setup.

Equations	Abbreviations	
$\dot{Q}_{cond} = \dot{m}_{ref}(h_{ref,rect,out} - h_{condenser,out})$	$h_{cond,out}$	Specific enthalpy of refrigerant at condenser outlet (kJ/kg)
$h_{cond,out} = fn(T_{cond,out}, P_{high}, x_{ref})$	$T_{cond,out}$	Refrigerant temperature at condenser outlet (°C)
$q_{cond,out} = fn(T_{cond,out}, P_{high}, x_{ref})$	$q_{cond,out}$	Vapour mass fraction of refrigerant at condenser outlet
$\dot{Q}_{evp} = \dot{m}_{ref}(h_{evp,in} - h_{evp,out})$	$h_{evp,in}$ & $h_{evp,out}$	Specific enthalpy of the refrigerant at evaporator inlet and outlet (kJ/kg)
$h_{evp,in} = fn(T_{evp,in}, P_{low}, x_{ref})$	$T_{evp,in}$ & $T_{evp,out}$	Temperature of refrigerant at evaporator inlet and outlet (°C)
$h_{evp,out} = fn(T_{evp,out}, P_{high}, x_{ref})$	P_{low}	Low side pressure (bar)
	$\dot{Q}_{cond}$ & $\dot{Q}_{evp}$	Heat load of condenser and evaporator (W)

Table B-4 : Equation used to compute absorber performance of experimental setup.

Equations	Abbreviations	
$\dot{m}_{absr} = \dot{m}_{ref} + \dot{m}_{dil}$	$\dot{m}_{absr}$	Incoming mass flow of fluid in absorber (g/s)
$\dot{m}_{absr}x_{absr} = \dot{m}_{ref}x_{ref} + \dot{m}_{dil}\,x_{dil}$	$h_{absr,in}$	Specific enthalpy of solution at absorber inlet (kJ/kg)
$\dot{m}_{absr}h_{absr,in} = \dot{m}_{ref}h_{evp,out} + \dot{m}_{dil}\,h_{dil}$	$T_{absr,in}$	Solution temperature in absorber after mixing (°C)
$T_{absr,in} = fn(P_{low}, x_{absr}, h_{absr,in})$	$\dot{Q}_{absr}$	Heat load of absorber (W)
$\dot{Q}_{absr} = \dot{m}_{absr}(h_{absr,in} - h_{absr,out})$		
$h_{absr,out} = fn(T_{absr,out}, P_{low}, x_{absr})$		

Appendix C

Refrigeration load calculation

The ASHRAE thermal load calculation methodology. divides the refrigeration load of the refrigerated vehicle into five categories, namely: transmission load ($\dot{Q}_{TL}$), infiltration load ($\dot{Q}_{IL}$), product load ($\dot{Q}_{PL}$), precooling load ($\dot{Q}_{PRL}$) and miscellaneous load ($\dot{Q}_{ML}$) as shown in Figure C-1. Hence, total cooling load of the vehicle is summation of all these five different types of loads as shown in eqn.C.1.

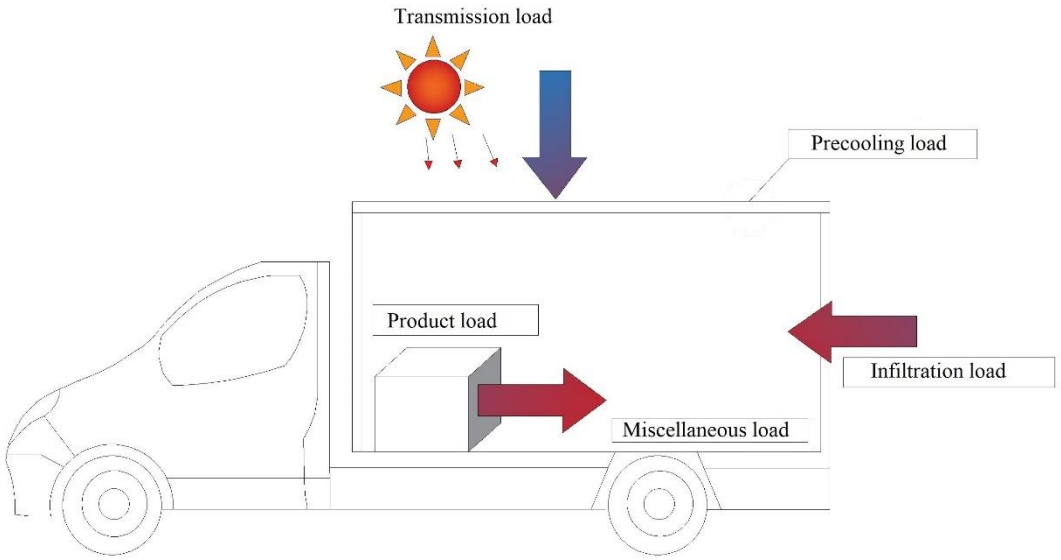

Figure C-1 : Different refrigeration load of the refrigerated vehicle.

$$\dot{Q}_{refrigeration-load} = \dot{Q}_{TL} + \dot{Q}_{IL} + \dot{Q}_{PL} + \dot{Q}_{PRL} + \dot{Q}_{ML} \quad \text{C.1}$$

Transmission load is the heat penetration into the refrigerated cabinet through the surface of solid body (via convection or conduction heat transfer). Transmission load ($\dot{Q}_{TL}$) is expressed based on the Fourier's law [1] as shown in eqn.C.2.

$$\dot{Q}_{TL} = UA\Delta T \qquad \text{C.2}$$

Where,

ΔT Difference between ambient temperature and refrigerated cabinet temperature (ºC)

The overall heat transfer coefficient (U) in eqn.C.2 was calculated using eqn. C.3

$$U = \frac{1}{\frac{1}{h_i} + \frac{x_{ins}}{k_{ins}} + \frac{1}{h_o}} \qquad \text{C.3}$$

where,

h_i	Inner surface heat transfer coefficient (W/m^2 K)
h_o	Outer surface heat transfer coefficient (W/m^2 K)
x_{ins}	Thickness of the insulation (m)
k_{ins}	Conductivity of the insulation material (W/m K)

For still air, h_i and h_o values were taken as 9.1 W/m^2 K, but if refrigerated cabinet is exposed to wind more than 25 km/h, h_o value increased to 34 W/m^2 K [1].

Allowance for the temperature difference (ΔT) to consider solar heat gain is taken from ASHRAE guideline [1] and it is shown in Table C-1.

Table C-1 : Temperature allowance to consider solar heat gain.

Type of cabinet surface	East wall (K)	South wall (K)	West wall (K)	Flat roof (K)
Dark coloured	5	3	5	11
Medium coloured	4	3	4	9
Light coloured	3	2	3	5

Infiltration load is the thermal load entering the refrigerated cabinet due to door opening, it was determined using eqn. C.4. The magnitude of the Infiltration load depends upon the dimensions of the door and frequency of the door opening [1]. Heat gain due to infiltration is significant

for short delivery journey where frequent door openings take place, however for longer journey (end point to end point), it is not that significant as door opening does not take place often.

$$\dot{Q}_{IL} = \frac{t_0}{3600} q_{IL} \quad \text{C.4}$$

Where

t_0 Door opening time per hour (s)
q_{IL} Heat gain during door openings (kW)

Heat gain during door openings can be determined using eqn.C.5.

$$q_{IL} = 0.577 W H^{1.5} \left(\frac{q_s}{A}\right)\left(\frac{1}{R_S}\right) \quad \text{C.5}$$

Where,
W Door width (m)
H Door height (m)
$\frac{q_s}{A}$ Sensible heat load of infiltration air per square metre of door opening (kW/m^2)
R_S Sensible heat ratio for infiltration from ambient to refrigerated cabinet (kW/m^2)

Values of $\frac{q_s}{A}$ and R_S for infiltration from ambient to different types of trucks were taken from the ASHRAE guideline [1].

Product load is the heat released by the food present in the refrigerated cabinet. Precooling load is the energy needed to cool down the refrigerated cabinet to the settling temperature before loading of the products. Miscellaneous load includes the heat released by internal sources, human and equipment related load. However, miscellaneous load and product load are always negligible compared to infiltration load, precooling load and transmission load [1].

The roof, doors and walls consist of 60mm polyurethane foam (0.0228 w/m K thermal conductivity) [1]

Effect of door opening for small truck

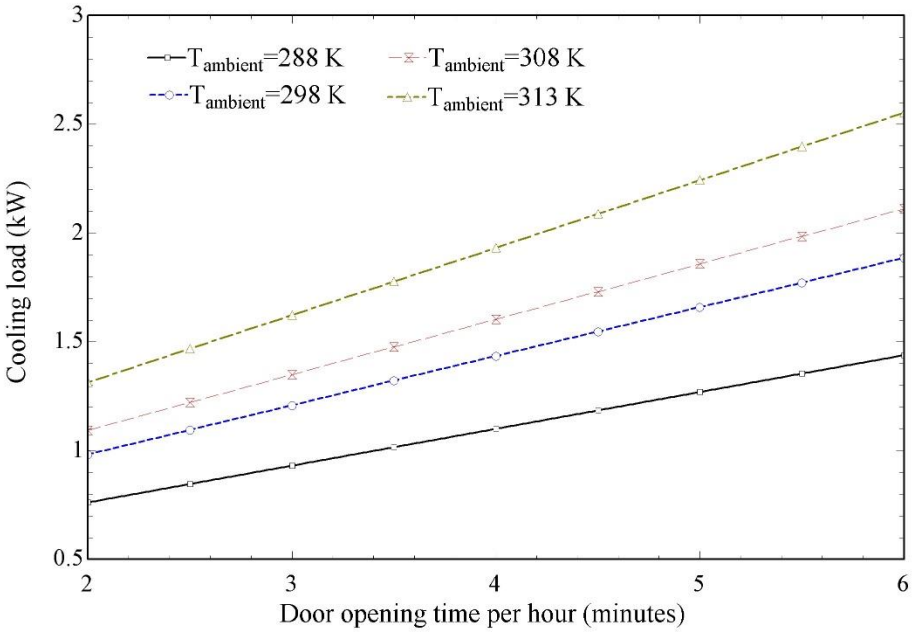

Figure C-2 : Effect of door opening time on refrigeration load of small truck.

The small, refrigerated vans/trucks used for short delivery route and urban area delivery route where frequent door opening take place, hence infiltration load was significant. Therefore, door opening time during journey is vital factor to compute cooling load for the small-refrigerated trucks and vans. Door opening time per hour was varied from 2 minutes to 6 minutes. The longer the doors are kept open, the more ambient air entered the refrigerated cabinet which increased the demand load

References

1. ASHRAE, 2018. Chapter 24. Refrigerated-facility loads. 2018 ASHRAE Handbook – Refrigeration, SI edition.

Appendix D

Desorber iterative solver

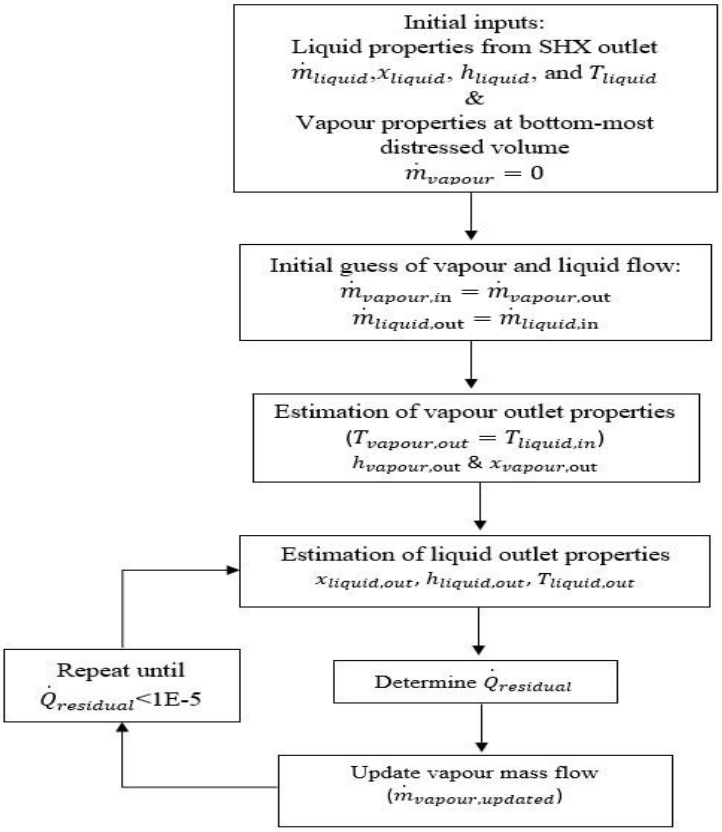

Figure D-1 : Iterative desorber solver.

To solve the model of the desorber, inlet conditions of liquid solution ($\dot{m}_{liquid}$,x_{liquid}, h_{liquid}, and T_{liquid}) at the top most discretised volume were determined from the SHX outlet whilst mass flow of vapour ($\dot{m}_{vapour,0}$) at bottom-most discretised volume was zero as no amount of vapour entered into desorber from the bottom. There were eight unknowns for each discretised volume namely: $\dot{m}_{vapour,i}$,$x_{vapour,i}$,$h_{vapour,i}$, $T_{vapour,i}$, $\dot{m}_{liquid,i}$,$T_{liquid,i}$,$x_{liquid,i}$, and $h_{liquid,i}$. However, there were only five equations for each discretised volume. Therefore, it was

required to develop iterative solver for the desorber modelling. A pictorial presentation of various steps involved in the iterative desorber solver is depicted in Figure D-1.

First step required to solve the iterative desorber model was to guess initial mass flow of the liquid solution ($\dot{m}_{liquid,i}$) and refrigerant vapour ($\dot{m}_{vapour,i}$) in each discretised volume which was assumed to be the inflow values.

$$\dot{m}_{liquid,i} = \dot{m}_{liquid,i+1}$$

$$\dot{m}_{vapour,i} = \dot{m}_{vapour,i-1}$$

The liquid-vapour phase equilibrium was assumed, which also determined the vapour outlet temperature at the outlet of each discretised volume with following assumption.

$$T_{vapour,i} = T_{liquid,i+1}.$$

Hence, saturated vapour enthalpy ($h_{vapour,i}$) and concentration ($x_{vapour,i}$) can be determined with known $T_{vapour,i}$ and high-side pressure.

$$h_{vapour,i}=fcn(T_{vapour,i}, P_{high}, q = 1)$$

$$x_{vapour,i}=fcn(T_{vapour,i}, P_{high}, q = 1)$$

q is a vapour quality. q=0 suggest that vapour content in the mixture is zero (i.e., saturated liquid/sub-cooled liquid) and q=1 implies saturated vapour mixture.

The liquid solution concentration ($x_{liquid,i}$) was determined by using initial two equations mentioned mass and species conservation equations with known values of $x_{vapour,i}$, $\dot{m}_{vapour,i}$and $\dot{m}_{liquid,i}$. Saturated liquid temperature ($T_{liquid,i}$) and enthalpy ($h_{liquid,i}$) were determined by following equations.

$$T_{liquid,i}=fcn(P_{high}, x_{liqud,i}, q = 0)$$

$$h_{liquid,i}=fcn(P_{high}, x_{liqud,i}, q = 0)$$

In the final step, the residual energy is derived in each discretised control volume to update the vapour mass flow rate as shown below.

$$\dot{Q}_{residual} = \dot{m}_{liquid,i+1}h_{liquid,i+1} + \dot{m}_{vapour,i-1}h_{vapour,i-1} - \dot{m}_{liquid,i}h_{liquid,i} - \dot{m}_{vapour,i}h_{vapour,i} + (UA)_{liquid,i}(T_{w,i} - T_{liquid,i})$$

$$\dot{m}_{vapour,updated} = \frac{\dot{Q}_{residual}}{h_{vapour,i} - h_{liquid,i}}$$

Energy, mass, and species conservation equations were carried out until the convergence criterion of $\dot{Q}_{residual}$<1E-5 was achieved.

Refrigerant and storage tanks equations

Table D-1 : Equations used to determine temperature and pressure in storage tanks.

Equations	Abbreviations	
$P_{low} = fcn(x_{sol.tank}, v_{sol.tank}, U_{sol.tank})$	$v_{sol.tank}$ & $v_{ref.tank}$	Specific volume of the working fluid in solution and refrigerant tank (m^3/kg).
$P_{high} = fcn(x_{ref.tank}, v_{ref.tank}, U_{ref.tank})$	$x_{sol.tank}$ & $x_{ref.tank}$	Ammonia concentration of the working fluid in solution and refrigerant tank.
$T_{sol.tank,out} = fcn(x_{sol.tank}, v_{sol.tank}, U_{sol.tank})$	$U_{sol.tank}$ & $U_{ref.tank}$	Specific internal energy of the working fluid in solution and refrigerant tank, respectively (kJ/kg).
$T_{ref.tank,out} = fcn(x_{ref.tank}, v_{ref.tank}, U_{ref.tank})$	$T_{sol.tank}$ & $T_{ref.tank}$	Temperature of the working fluid in solution and refrigerant tank (K).

Appendix E

Cryogenic refrigerated transportation systems

The working principle for cryogenic transport is the same, independent of the actual cooling fluid, such as liquid nitrogen (LN_2) or liquefied carbon dioxide (LCO_2). LN_2 or LCO_2 are stored in a large vacuum insulated tank mounted underneath the vehicle chassis. The fluids stored in the tank are at high pressure and low temperature (LN_2 at 3 bar and -196°C and LCO_2 at 8.6 bar and -57°C). As shown in Figure E-1, a pump forces the cryogenic fluid to enter an evaporator where the heat exchange takes place between ambient air and cryogenic fluid. Then the cooled air is passed into the refrigerated cabinet of the truck.

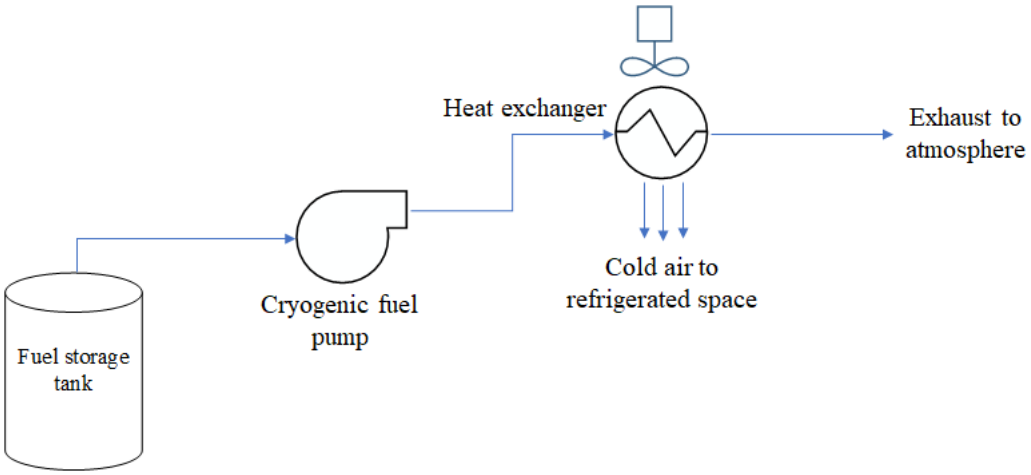

Figure E-1 : Cryogenic refrigeration systems using LN_2 and LCO_2.

Bibliography

1. Environmental Dangers of Global Refrigerated Transport Studied - Global Fleet - Automotive Fleet. [accessed 2 April 2020]; Available from: https://www.automotive-fleet.com/129394/environmental-danger-of-global-use-of-refrigerated
2. Refrigerated Transport Market Research Report: Market size, Industry outlook, Market Forecast, Demand Analysis,Market Share, Market Report 2019-2025. [accessed 16 January 2021]; Available from: https://www.industryarc.com/Report/15136/refrigerated-transport-market.html
3. Rai A, Tassou SA. Environmental impacts of vapour compression and cryogenic transport refrigeration technologies for temperature controlled food distribution. Energy Convers Manag. 2017;150(2137)pp.:914–23. DOI: 10.1016/j.enconman.2017.05.024
4. Bengherbi Z, Wagner F, Teyssandier E, Ayres M, Owen N, Peters T, Strahan D, Butterfield Vb. Liquid Air on the European Highway- The economic and environmental impact of zero-emission transport refrigeration. Dearman; 2015.
5. Grupp D, Dwyer HA, Kulkarni C, Solomon M, Miller M. Design, testing, and demonstration of a hybrid fuel cell powered APU/TRU system. SAE Tech Pap. 2007;(724). DOI: 10.4271/2007-01-0699
6. Technology assessment: transport refrigerators, California Environmental Protection Agency, Air Resources Board., State of California. 2015.
7. Pedolsky H, Bau R La, Labau R. Reintroduction of Cryogenic Refrigeration for Cold Transport. In: International Refrigeration and Air Conditioning Conference, Paper 1021. Purdue; 2010. DOI: http://docs.lib.purdue.edu/iracc/1021

8. Yoshida T, Kojima K. Toyota MIRAI fuel cell vehicle and progress toward a future hydrogen society. Electrochem Soc Interface. 2015 Jan 1;24(2)pp.:45–9. DOI: 10.1149/2.F03152if

9. Kast J, Vijayagopal R, Gangloff JJ, Marcinkoski J. Clean commercial transportation: Medium and heavy duty fuel cell electric trucks. Int J Hydrogen Energy. 2017;42(7)pp.:4508–17. DOI: 10.1016/j.ijhydene.2016.12.129

10. Braun RJ. Optimal design and operation of solid oxide fuel cell systems for small-scale stationary applications [thesis]. University of Wisconsin –Madison; 2002.

11. Fuel cell market | FCHObservatory. [accessed 12 February 2021]; Available from: https://www.fchobservatory.eu/observatory/technology-and-market/fc-market-fc-type

12. Biert L. Solid oxide fuel cells for ships System integration concepts with reforming and thermal cycles [thesis]. TU Delft University. 2019. DOI: 10.4233/uuid

13. Srikhirin P, Aphornratana S, Chungpaibulpatana S. A review of absorption refrigeration technologies. Vol. 5, Renewable and Sustainable Energy Reviews. 2000. pp. 343–72. DOI: 10.1016/S1364-0321(01)00003-X

14. Lang M, Bohn C, Henke M, Schiller G, Willich C, Hauler F. Understanding the Current-Voltage Behavior of High Temperature Solid Oxide Fuel Cell Stacks. J Electrochem Soc. 2017;164(13)pp.:F1460–70. DOI: 10.1149/2.1541713jes

15. Wilberforce T, Alaswad A, Palumbo A, Dassisti M, Olabi AG. Advances in stationary and portable fuel cell applications. Int J Hydrogen Energy. 2016 Oct 5;41(37)pp.:16509–22. DOI: 10.1016/j.ijhydene.2016.02.057

16. Marra D, Pianese C, Polverino P, Sorrentino M. Models for Solid Oxide Fuel Cell Systems- Exploitation of Models Hierarchy for Industrial Design of Control and Diagnosis Strategies. Springer; 2016.

17. Mogensen D, Grunwaldt JD, Hendriksen P V., Dam-Johansen K, Nielsen JU. Internal

steam reforming in solid oxide fuel cells: Status and opportunities of kinetic studies and their impact on modelling. J Power Sources. 2011 Jan 1;196pp.:25–38. DOI: 10.1016/j.jpowsour.2010.06.091

18. Mastropasqua L, Campanari S, Brouwer J. Solid oxide fuel cell short stack performance testing - Part A: Experimental analysis and M-combined heat and power unit comparison. J Power Sources. 2017 Dec 15;371pp.:225–37. DOI: 10.1016/j.jpowsour.2017.10.028
19. Xu H, Dang Z, Bai BF. Analysis of a 1 kW residential combined heating and power system based on solid oxide fuel cell. Appl Therm Eng. 2013;50(1)pp.:1101–10. DOI: 10.1016/j.applthermaleng.2012.07.004
20. Bentrcia M, Alshitawi M, Omar H. Developmens of alternative systems for automotive air conditioning-A review †. J Mech Sci Technol. 2018;32(4)pp.:1857–67. DOI: 10.1007/s12206-018-0342-2
21. Ibrahim NI, Al-Sulaiman FA, Ani FN. Solar absorption systems with integrated absorption energy storage–A review. Renew Sustain Energy Rev. 2018;82(November 2016)pp.:1602–10. DOI: 10.1016/j.rser.2017.07.005
22. Venkataraman V. Coupling of a Solid Oxide Fuel Cell with a Vapour Absorption Refrigeration System for refrigerated truck application [thesis]. University of Birmingham; 2017.
23. Tassou SA, De-Lille G, Ge YT. Food transport refrigeration - Approaches to reduce energy consumption and environmental impacts of road transport. Appl Therm Eng. 2009;29(8–9)pp.:1467–77. DOI: 10.1016/j.applthermaleng.2008.06.027
24. Venkataraman V, El-Kharouf A, Pandya B, Amakiri E, Steinberger-Wilckens R. Coupling of engine exhaust and fuel cell exhaust with vapour absorption refrigeration/air conditioning systems for transport applications: A review. Therm Sci

Eng Prog. 2020 Aug 1;18p.:100550. DOI: 10.1016/j.tsep.2020.100550

25. Fuel cell handbook—seventh edition. U.S. Department of Energy. 2004. DOI: 10.5860/choice.26-6292

26. Sharaf OZ, Orhan MF. An overview of fuel cell technology: Fundamentals and applications. Vol. 32, Renewable and Sustainable Energy Reviews. 2014. pp. 810–53. DOI: 10.1016/j.rser.2014.01.012

27. Christian, Mitchell M, Kenis PJA. Ceramic microreactors for on-site hydrogen production from high temperature steam reforming of propane. Lab Chip. 2006 Sep 26;6(10)pp.:1328–37. DOI: 10.1039/b607552e

28. Dissanayake D, Rosynek MP, Kharas KCC, Lunsford JH. Partial oxidation of methane to carbon monoxide and hydrogen over a Ni/Al2O3 catalyst. J Catal. 1991 Nov 1;132(1)pp.:117–27. DOI: 10.1016/0021-9517(91)90252-Y

29. Leah RT, Bone A, Hammer E, Selcuk A, Rahman M, Clare A, Rees L, Lawrence N, Ballard A, Domanski T, Mukerjee S, Selby M. Development of High Efficiency Steel Cell Technology for Multiple Applications. ECS Trans. 2017;78(1)pp.:2005–14. DOI: 10.1149/07801.2005ecst

30. Peters R, Riensche E, Cremer P. Pre-reforming of natural gas in solid oxide fuel-cell systems. J Power Sources. 2000 Mar 1;86(1)pp.:432–41. DOI: 10.1016/S0378-7753(99)00440-1

31. Lamp P, Tachtler J, Finkenwirth O, Mukerjee S, Shaffer S. Development of an Auxiliary Power Unit with Solid Oxide Fuel Cells for Automotive Applications. Fuel Cells. 2003;3(3)pp.:146–52. DOI: 10.1002/fuce.200332107

32. Lawrence J, Boltze M. Auxiliary power unit based on a solid oxide fuel cell and fuelled with diesel. J Power Sources. 2006 Mar 21;154(2)pp.:479–88. DOI: 10.1016/j.jpowsour.2005.10.036

33. Delphi demos SOFC tech for truck APU. Fuel Cells Bulletin. 2010 Dec; DOI: 10.1016/S1464-2859(10)70334-5

34. Morris K, Hennessy DT, Ho D, Peterson D. Solid Oxide Fuel Cell Development for Auxiliary Power in Heavy Duty Vehicle Applications. Delphi Automotive System; 2010.

35. Rechberger J, Kaupert A, Hagerskans J, Blum L. Demonstration of the First European SOFC APU on a Heavy Duty Truck. Transp Res Procedia. 2016;14pp.:3676–85. DOI: 10.1016/j.trpro.2016.05.442

36. Kendall K, Newton J, Kendall M. Microtubular SOFC (mSOFC) System in Truck APU Application. ECS Trans. 2015 Jul 17;68(1)pp.:187–92. DOI: 10.1149/06801.0187ecst

37. Nissan unveils world's first FCEV with SOFC running on bioethanol. Fuel Cells Bulletin. 2016 Sep 1; DOI: 10.1016/s1464-2859(16)30231-0

38. Running on e-Bio: Nissan's Solid Oxide Fuel Cell System. [accessed 7 March 2020]; Available from: https://blog.nissan-global.com/EN/?p=14144

39. Benveniste G, Pucciarelli M, Torrell M, Kendall M, Tarancón A. Life Cycle Assessment of microtubular solid oxide fuel cell based auxiliary power unit systems for recreational vehicles. J Clean Prod. 2017 Nov 1;165pp.:312–22. DOI: 10.1016/j.jclepro.2017.07.130

40. Ballard A, Domanski T, Rees L, Nobbs C, Lawrence N, Heffer K, Harman J, Evans C, Barnard P, Mukerjee S, Selby M. Development of the 5kW e SteelCell® Technology Platform for Stationary Power and Transport Applications . ECS Trans. 2019;91(1)pp.:117–22. DOI: 10.1149/09101.0117ecst

41. Udomsilp D, Rechberger J, Neubauer R, Bischof C, Thaler F, Schafbauer W, Menzler NH, de Haart LGJ, Nenning A, Opitz AK, Guillon O, Bram M. Metal-Supported Solid

Oxide Fuel Cells with Exceptionally High Power Density for Range Extender Systems. Cell Reports Phys Sci. 2020 Jun 24;1(6)p.:100072. DOI: 10.1016/j.xcrp.2020.100072

42. Pirou S, Talic B, Brodersen K, Hauch A, Frandsen HL, Skafte TL, et al. Production of a monolithic fuel cell stack with high power density. Nat Commun. 2022;13(1). DOI: 10.1038/s41467-022-28970-w

43. Williams MC. Fuel Cell Program Annual Report, National Energy Technology Laboratory. 2004.

44. Dogdibegovic E, Fukuyama Y, Tucker MC. Ethanol internal reforming in solid oxide fuel cells: A path toward high performance metal-supported cells for vehicular applications. J Power Sources. 2020 Feb 15;449p.:227598. DOI: 10.1016/j.jpowsour.2019.227598

45. Determan MD, Garimella S. Design, fabrication, and experimental demonstration of a microscale monolithic modular absorption heat pump. Appl Therm Eng. 2012 Dec 5;47pp.:119–25. DOI: 10.1016/j.applthermaleng.2011.10.043

46. Staedter MA, Garimella S. Development of a micro-scale heat exchanger based, residential capacity ammonia–water absorption chiller. Int J Refrig. 2018 May 1;89pp.:93–103. DOI: 10.1016/j.ijrefrig.2018.02.016

47. Du S, Wang RZ, Chen X. Development and experimental study of an ammonia water absorption refrigeration prototype driven by diesel engine exhaust heat. Energy. 2017 Jul;130pp.:420–32. DOI: 10.1016/j.energy.2017.05.006

48. Ramanathan A, Gunasekaran P. Simulation of absorption refrigeration system for automobile application. Therm Sci. 2008;12(3)pp.:5–13. DOI: 10.2298/TSCI0803005R

49. Keinath CM, Delahanty JC, Garimella S, Garrabrant MA. Diesel Engine Waste-Heat Driven Ammonia-Water Absorption System for Space-Conditioning Applications. In:

International Refrigeration and Air Conditioning Conference 2012, Paper 1318. pp. 1–10.

50. Talbi M, Agnew B. Energy recovery from diesel engine exhaust gases for performance enhancement and air conditioning. Appl Therm Eng. 2002 Apr 1;22(6)pp.:693–702. DOI: 10.1016/S1359-4311(01)00120-X

51. Mostafavi M, Agnew B. Thermodynamic analysis of combined diesel engine and absorption refrigeration unit - Naturally aspirated engine with precooling. Appl Therm Eng. 1997 Jun 1;17(6)pp.:593–9. DOI: 10.1016/s1359-4311(96)00037-3

52. Koehler J, Tegethoff WJ, Westphalen D, Sonnekalb M. Absorption refrigeration system for mobile applications utilizing exhaust qases. Heat Mass Transf. 1997;32(5)pp.:333–40. DOI: 10.1007/s002310050130

53. Aly WIA, Abdo M, Bedair G, Hassaneen AE. Thermal performance of a diffusion absorption refrigeration system driven by waste heat from diesel engine exhaust gases. Appl Therm Eng. 2017 Mar;114pp.:621–30. DOI: 10.1016/j.applthermaleng.2016.12.019

54. Novella R, Dolz V, Martín J, Royo-Pascual L. Thermodynamic analysis of an absorption refrigeration system used to cool down the intake air in an Internal Combustion Engine. Appl Therm Eng. 2017 Jan;111pp.:257–70. DOI: 10.1016/j.applthermaleng.2016.09.084

55. Hanriot S, Brito P, Maia C, Rêgo A. Analysis of working parameters for an ammonia-water absorption refrigeration system powered by automotive exhaust gas. Case Stud Therm Eng. 2019 Mar;13p.:100406. DOI: 10.1016/j.csite.2019.100406

56. Cao T, Lee H, Hwang Y, Radermacher R, Chun H hwan. Performance investigation of engine waste heat powered absorption cycle cooling system for shipboard applications. Appl Therm Eng. 2015;90pp.:820–30. DOI: 10.1016/j.applthermaleng.2015.07.070

57. Brodrick CJ, Dwyer HA, Farshchi M, Bruce Harris D, King Jr FG. Effects of Engine Speed and Accessory Load on Idling Emissions from Heavy-Duty Diesel Truck Engines. J Air Waste Manage Assoc. 2002;52(9)pp.:1026–31. DOI: 10.1080/10473289.2002.10470838

58. Venkataraman V, Pacek AW, Steinberger-Wilckens R. Coupling of a Solid Oxide Fuel Cell Auxiliary Power Unit with a Vapour Absorption Refrigeration System for Refrigerated Truck Application. Fuel Cells. 2016;16(3)pp.:273–93. DOI: 10.1002/fuce.201500124

59. Amakiri EL. Coupling a Solid Oxide Fuel Cell Exhaust with a Vapour Absorption Refrigeration System for Refrigerated Truck : Modelling and Experimental Investigation [thesis]. University of Birmingham; 2020.

60. Hauth M, Seidl M, Sallai C, Soukup N, Postl A, Rieberer R, Albert J. Development of a Solid Oxide Fuel Cell System Towards Flexible Production of Electricity, Heat and Cooling Power for Transport Applications. In: 7th Transport Research Arena. Vienna; 2018.

61. Zabihian F, Fung A. A Review on Modeling of Hybrid Solid Oxide Fuel Cell Systems. Int J Eng. 2009;(2)pp.:85–119.

62. Bao C, Wang Y, Feng D, Jiang Z, Zhang X. Macroscopic modeling of solid oxide fuel cell (SOFC) and model-based control of SOFC and gas turbine hybrid system. Prog Energy Combust Sci. 2018;66(5)pp.:83–140. DOI: 10.1016/j.pecs.2017.12.002

63. Wang K, Hissel D, Péra MC, Steiner N, Marra D, Sorrentino M, Pianese C, Monteverde M, Cardone P, Saarinen J. A Review on solid oxide fuel cell models. Int J Hydrogen Energy. 2011 Jun 1;36(12)pp.:7212–28. DOI: 10.1016/j.ijhydene.2011.03.051

64. Bove R, Ubertini S. Modeling solid oxide fuel cell operation: Approaches, techniques

and results. J Power Sources. 2006 Sep 13;159pp.:543–59. DOI: 10.1016/j.jpowsour.2005.11.045

65. Romijn R, Özkan L, Weiland S, Ludlage J, Marquardt W. A grey-box modeling approach for the reduction of nonlinear systems. J Process Control. 2008 Oct 1;18(9)pp.:906–14. DOI: 10.1016/j.jprocont.2008.06.007

66. Marra D, Sorrentino M, Pianese C, Jensen KJNL. Control-Oriented Modeling of Non-Adiabatic Solid Oxide Fuel Cell Stacks. Fuel Cells. 2017;17(3)pp.:328–43. DOI: 10.1002/fuce.201600150

67. Sorrentino M, Pianese C, Guezennec YG. A hierarchical modeling approach to the simulation and control of planar solid oxide fuel cells. J Power Sources. 2008;180(1)pp.:380–92. DOI: 10.1016/j.jpowsour.2008.02.021

68. Saarinen J, Halinen M, Ylijoki J, Noponen M, Simell P, Kiviaho J. Dynamic model of 5 kW SOFC CHP test station. J Fuel Cell Sci Technol. 2007;4(4)pp.:397–405. DOI: 10.1115/1.2759502

69. Sorrentino M, Pianese C. Grey-Box Modeling of SOFC Unit for Design, Control and Diagnostics Applications. In: Proceedings of the European Fuel Cell Forum 2009. Lucerne; 2009. pp. 1–12.

70. Gallo M, Marra D, Sorrentino M, Pianese C, Au SF. A versatile computational tool for model-based design, control and diagnosis of a generic Solid Oxide Fuel Cell Integrated Stack Module. Energy Convers Manag. 2018 Sep 1;171pp.:1514–28. DOI: 10.1016/j.enconman.2018.06.062

71. Marra D, Sorrentino M, Pohjoranta A, Pianese C, Kiviaho J. A Lumped Dynamic Modelling Approach for Model-Based Control and Diagnosis of Solid Oxide Fuel Cell System with Anode Off-Gas Recycling. ECS Trans. 2015;68(1)pp.:3095–106. DOI: 10.1149/06801.3095ecst

72. Wu CC, Chen TL. Design and dynamics simulations of small scale solid oxide fuel cell tri-generation system. Energy Convers Manag X. 2019 Jan;1pp.:1–14. DOI: 10.1016/j.ecmx.2018.100001

73. KANG Y, LI J, CAO G, TU H, LI J, YANG J. One-dimensional Dynamic Modeling and Simulation of a Planar Direct Internal Reforming Solid Oxide Fuel Cell. Chinese J Chem Eng. 2009;17(2)pp.:304–17. DOI: 10.1016/S1004-9541(08)60209-8

74. Xi H, Sun J. A low-order dynamic model for planar solid oxide fuel cells using online iterative computation. J Fuel Cell Sci Technol. 2008;5(4)pp.:1–12. DOI: 10.1115/1.2931491

75. Uva P, Biert L Van, Mestemaker BTW. Dynamic Modelling of a Solid Oxide Fuel Cell System for Maritime Applications considering Balance of Plant components. In: Third international conference on modelling and optimisation of ship energy systems. 2021. pp. 1–12.

76. Murshed AM, Huang B, Nandakumar K. Control relevant modeling of planer solid oxide fuel cell system. J Power Sources. 2007 Jan 1;163(2)pp.:830–45. DOI: 10.1016/j.jpowsour.2006.09.080

77. Goyal A. Dynamics and control of ammonia-water absorption heat pumps [thesis]. Georgia Institute of Technology; 2018.

78. Tiji AE, Ramiar A, Ebrahimnataj MR. Investigation of the launch time of NH3-H2O absorption chiller under different working condition. Proc IMechE Part E J Process Mech Eng. 2020;234(1)pp.:15–28. DOI: 10.1177/0954408919879871

79. Kim B, Park J. Dynamic simulation of a single-effect ammonia-water absorption chiller. Int J Refrig. 2007 May;30(3)pp.:535–45. DOI: 10.1016/j.ijrefrig.2006.07.004

80. Adjibade MIS, Thiam A, Awanto C, Ndiogou BA, Sambou V. Dynamic investigation of the diffusion absorption refrigeration system NH3-H2O-H2. Case Stud Therm Eng.

2017 Sep 1;10pp.:468–74. DOI: 10.1016/j.csite.2017.10.006

81. Castaing-Lasvignottes J, Belhani M, Alaphilippe M. Modeling and experimental validation of the dynamic behaviour of a liquid absorption chiller. In: HPC 2004 – 3rd International Conference on Heat Powered Cycles. 2004. pp. 11–5.

82. Kaushik S, Delhi N. Dynamic Simulation of an Ammonia- Water Absorption Cycle Solar Heat Pump with Integral Refrigerant Storage. J Heat Recover Syst Vol. 1985;5(2)pp.:101–16.

83. Fu DG, Poncia G, Lu Z. Implementation of an object-oriented dynamic modeling library for absorption refrigeration systems. Appl Therm Eng. 2006 Feb 1;26(2–3)pp.:217–25. DOI: 10.1016/j.applthermaleng.2005.05.008

84. Viswanathan VK, Rattner AS, Determan MD, Garimella S. Dynamic model for a small-capacity ammonia-water absorption chiller. In: HVAC and R Research. 2013. pp. 865–81. DOI: 10.1080/10789669.2013.833974

85. Viswanathan VK. Dynamic model for small-capacity ammonia-water absorption chiller [thesis]. Georgia Institute of Technology; 2013.

86. Martinho LCS, Vargas JVC, Balmant W, Ordonez JC. A single stage absorption refrigeration system dynamic mathematical modeling, adjustment and experimental validation. Int J Refrig. 2016 Aug 1;68pp.:130–44. DOI: 10.1016/j.ijrefrig.2016.04.023

87. Wen H, Wu A, Liu Z, Shang Y. A State-Space Model for Dynamic Simulation of a Single-Effect LiBr/H2O Absorption Chiller. IEEE Access. 2019;7pp.:57251–8. DOI: 10.1109/ACCESS.2019.2913657

88. Paratherm^{TM} NF Heat Transfer Fluid | Paratherm. [accessed 18 October 2021]; Available from: https://www.paratherm.com/heat-transfer-fluids/paratherm-nf-heat-transfer-fluid/

89. Viswanathan VK, Rattner AS, Determan MD, Garimella S. Dynamic model for a small-capacity ammonia-water absorption chiller. In: HVAC and R Research. 2013. pp. 865–81. DOI: 10.1080/10789669.2013.833974

90. Dehghan B B, Aprile M, Pistocchini L, Toppi T, Motta M. Transient behavior assessments of a single-effect ammonia-water absorption heat pump system: Development of an efficient experimentally validated numerical framework. Int J Heat Mass Transf. 2021 Oct 1;177p.:121252. DOI: 10.1016/j.ijheatmasstransfer.2021.121252

91. Kreith F, Manglik RM. Principles of heat transfer. Cengage learning; 2016.

92. Çengel YA, Boles MA. Thermodynamics: An Engineering Approach. Eighth. McGraw-Hill Education; 2015.

93. Bell IH, Quoilin S, Georges E, Braun JE, Groll EA, Horton WT, Lemort V. A generalized moving-boundary algorithm to predict the heat transfer rate of counterflow heat exchangers for any phase configuration. Appl Therm Eng. 2015 Mar 25;79pp.:192–201. DOI: 10.1016/j.applthermaleng.2014.12.028

94. Chapter 24. Refrigerated-facility loads. In: Ashrae Handbook. 2018. pp. 24.1-24.10.

95. Tassou SA, Hadawey A, Ge YT, Lagroy De Groutte B. Carbon Dioxide Cryogenic Transport refrigeration Systems. The Centre for Energy and Built Environment Research, Brunel University. Uxbridge; 2009.

96. Staedter MA, Garimella S. Direct-coupled desorption for small capacity ammonia-water absorption systems. Int J Heat Mass Transf. 2018;127pp.:196–205. DOI: 10.1016/j.ijheatmasstransfer.2018.06.118

97. Staedter MA, Garimella S. Experimental investigation of a compact thermal compressor for an ammonia-water absorption heat pump. Appl Therm Eng. 2018;143(April)pp.:550–60. DOI: 10.1016/j.applthermaleng.2018.07.120

98. Garimella S, Determan MD, Meacham JM, Lee S, Ernst TC. Microchannel component technology for system-wide application in ammonia/water absorption heat pumps. In: International Journal of Refrigeration. 2011. pp. 1184–96. DOI: 10.1016/j.ijrefrig.2011.03.005

99. Goyal A, Staedter MA, Hoysall DC, Ponkala MJ, Garimella S. Experimental evaluation of a small-capacity, waste-heat driven ammonia-water absorption chiller. Int J Refrig. 2017;79pp.:89–100. DOI: 10.1016/j.ijrefrig.2017.04.006

100. Chandrasekaran S, Hughes M, Kini G, Garimella S. A Microchannel Shell-And-Tube Absorber for Ammonia-Water Absorption. Appl Therm Eng. 2020 Nov 13;p.:116321. DOI: 10.1016/j.applthermaleng.2020.116321

101. Goyal A, Garimella S. Multivariable feedback control of small-capacity ammonia-water absorption systems. Energy Convers Manag. 2019;191(November 2018)pp.:159–73. DOI: 10.1016/j.enconman.2019.03.080

102. Artuso P, Rossetti A, Minetto S, Marinetti S, Moro L, Col D Del. Dynamic modeling and thermal performance analysis of a refrigerated truck body during operation. Int J Refrig. 2019 Mar;99pp.:288–99. DOI: 10.1016/j.ijrefrig.2018.12.014

103. 2018 Ashrae Handbook-Refrigeration. Ashrae. 2018.

104. Forinash D. Novel air-coupled heat exchangers for waste heat-driven absorption heat pumps [thesis]. Georgia Institute of Technology; 2015.

105. Yunus AC. Heat transfer: a practical approach. WBC McGraw-Hill; 1998.

106. Staedter M. Optimal Thermal Compressors for Miniaturized Ammonia-Water Absorption Systems [thesis]. Georgia Institute of Technology; 2018.

107. Bove R, Ubertini S. Modeling Solid Oxide Fuel Cells. Springer Science & Business Media. 2008.

108. Khotseng L. Fuel Cell Thermodynamics. In: Thermodynamics and Energy

Engineering. IntechOpen; 2020. pp. 25–75. DOI: 10.5772/intechopen.90141

109. Bavarsad PG. Energy and exergy analysis of internal reforming solid oxide fuel cell-gas turbine hybrid system. Int J Hydrogen Energy. 2007 Dec 1;32(17)pp.:4591–9. DOI: 10.1016/j.ijhydene.2007.08.004

110. Ni M, Leung MKH, Leung DYC. Parametric study of solid oxide fuel cell performance. Energy Convers Manag. 2007 May;48(5)pp.:1525–35. DOI: 10.1016/J.ENCONMAN.2006.11.016

111. Pirkandi J, Ghassemi M, Hamedi MH, Mohammadi R. Electrochemical and thermodynamic modeling of a CHP system using tubular solid oxide fuel cell (SOFC-CHP). J Clean Prod. 2012;29–30pp.:151–62. DOI: 10.1016/j.jclepro.2012.01.038

112. Sadeghi M, Chitsaz A, Mahmoudi SMS, Rosen MA. Thermoeconomic optimization using an evolutionary algorithm of a trigeneration system driven by a solid oxide fuel cell. Energy. 2015 Sep 1;89pp.:191–204. DOI: 10.1016/J.ENERGY.2015.07.067

113. Peters R, Deja R, Blum L, Pennanen J, Kiviaho J, Hakala T. Analysis of solid oxide fuel cell system concepts with anode recycling. Int J Hydrogen Energy. 2013;38(16)pp.:6809–20. DOI: 10.1016/j.ijhydene.2013.03.110

114. Noponen M, Torri P, Göös J, Puranen J, Lehtinen T, Pylypko S, Ounpuu E. Progress of SOC Development at Elcogen. ECS Trans. 2021 Jul 9;103(1)pp.:267–74. DOI: 10.1149/10301.0267ECST/XML

115. Lim TH, Song RH, Shin DR, Yang J Il, Jung H, Vinke IC, Yang SS. Operating characteristics of a 5 kW class anode-supported planar SOFC stack for a fuel cell/gas turbine hybrid system. Int J Hydrogen Energy. 2008 Feb 1;33(3)pp.:1076–83. DOI: 10.1016/j.ijhydene.2007.11.017

116. Gubner A. Non-isothermal and dynamic sofc voltage-current behavior. In: Proceedings - Electrochemical Society. 2005. pp. 814–26. DOI: 10.1149/200507.0814pv

117. Klotz D. Characterization and Modeling of Electrochemical Energy Conversion Systems by Impedance Techniques. KIT Sci Publ. 2012;p.:190.

118. Hauth M, Sallai C, Weißensteiner S, Pickelberger S, Thonhofer P, Obernberger I, Benesch C, Heschl C, Stelzer R, Heitzinger D, Megel S, Rothe S, Schnetter J, Kusnezoff M, Mai A, Moritz Becker, Stauch S. Results of 5 kW SOFC CHP system development in the SOFC5-60 project. In: 14th European SOFC & SOE Forum, 20-23 Oct, Lucerne Switzerland. 2020. pp. 594–604.

119. Lawrence J. Staxera GmbH- SOFC stack modules for decentralized power generation. 2013.

120. Mai A, Fleischhauer F, Denzler R, Grolig JG, Dold M, Schuler A. HEXIS Galileo 1000 N and HEXIS' next Generation SOFC System. In: 13th European SOFC & SOE Forum, July 2018, Lucerne/Switzerland. pp. 6–13.

121. Mai A, Grolig JG, Sarda V, Dold M, Schuler A. Status of HEXIS' SOFC Module Development. In: 14th European SOFC & SOE Forum, 20-23 Oct, Lucerne Switzerland. pp. 47–54.

122. Geipel C, Herbrig K, Mittmann F, Pötschke M, Reichel L, Strohbach T, Surrey A, Walter C. Stack Development and Industrial Scale-Up. In: 13th European SOFC & SOE Forum, July 2018, Lucerne/Switzerland. pp. 25–31.

123. Frimodt C, Mygind KF. Integration of solid oxide fuel cells and absorption cooling units [thesis]. Denmark Technical University; 2010.

124. Engelbracht M, Peters R, Blum L, Stolten D. Analysis of a Solid Oxide Fuel Cell System with Low Temperature Anode Off-Gas Recirculation. J Electrochem Soc. 2015;162(9)pp.:F982–7. DOI: 10.1149/2.0371509jes

125. Fang Q, Blum L, Peters R, Peksen M, Batfalsky P, Stolten D. SOFC stack performance under high fuel utilization. Int J Hydrogen Energy. 2015 Jan 12;40(2)pp.:1128–36.

DOI: 10.1016/j.ijhydene.2014.11.094

126. Gubner A. Modelling of High Temperature Fuel Cells : The Thermal , Chemical , Electrochemical and Fluidmechanical Behaviour of Solid Oxide Fuel Cells Operating with Internal Reforming of Methane [thesis]. University of Portsmouth; 1996.

127. Chitsaz A, Sadeghi M, Sadeghi M, Ghanbarloo E. Exergoenvironmental comparison of internal reforming against external reforming in a cogeneration system based on solid oxide fuel cell using an evolutionary algorithm. Energy. 2018 Feb;144pp.:420–31. DOI: 10.1016/j.energy.2017.12.008

128. Achenbach E. Three-dimensional and time-dependent simulation of a planar solid oxide fuel cell stack. J Power Sources. 1994;49(1–3)pp.:333–48. DOI: 10.1016/0378-7753(93)01833-4

129. Achenbach E, Riensche E. Methane/steam reforming kinetics for solid oxide fuel cells. J Power Sources. 1994 Dec 1;52(2)pp.:283–8. DOI: 10.1016/0378-7753(94)02146-5

130. Theo A. A novel SOFC tri-generation system for building applications. [thesis]. University of Nottingham; 2015. DOI: 10.1007/978-3-319-46966-9

131. Chan SH, Ho HK, Tian Y. Modelling of simple hybrid solid oxide fuel cell and gas turbine power plant. J Power Sources. 2002 Jun 15;109(1)pp.:111–20. DOI: 10.1016/S0378-7753(02)00051-4

132. Chitsaz A, S. Mahmoudi SM, Rosen MA. Greenhouse gas emission and exergy analyses of an integrated trigeneration system driven by a solid oxide fuel cell. Appl Therm Eng. 2015;86pp.:81–90. DOI: 10.1016/j.applthermaleng.2015.04.040

133. Gholamian E, Zare V. A comparative thermodynamic investigation with environmental analysis of SOFC waste heat to power conversion employing Kalina and Organic Rankine Cycles. Energy Convers Manag. 2016;117pp.:150–61. DOI: 10.1016/j.enconman.2016.03.011

134. Baghernejad A, Yaghoubi M, Jafarpur K. Exergoeconomic comparison of three novel trigeneration systems using SOFC, biomass and solar energies. Appl Therm Eng. 2016;104pp.:534–55. DOI: 10.1016/j.applthermaleng.2016.05.032

135. Chitsaz A, Hosseinpour J, Assadi M. Effect of recycling on the thermodynamic and thermoeconomic performances of SOFC based on trigeneration systems; A comparative study. Energy. 2017;124pp.:613–24. DOI: 10.1016/j.energy.2017.02.019

136. Slippey AJ. Dynamic Modeling and Analysis of Multiple SOFC System Configurations [thesis]. Rochester Institute of Technology; 2009.

137. Holtappels P, Mehling H, Roehlich S, Liebermann SS, Stimming U. SOFC system operating strategies for mobile applications. Fuel Cells. 2005;5(4)pp.:499–508. DOI: 10.1002/fuce.200400088

138. Petruzzi L, Cocchi S, Fineschi F. A global thermo-electrochemical model for SOFC systems design and engineering. J Power Sources. 2003;118(1–2)pp.:96–107. DOI: 10.1016/S0378-7753(03)00067-3

139. Petruzzi L, Cocchi S, Fineschi F. A global thermo-electrochemical model for SOFC systems design and engineering. In: Journal of Power Sources. Elsevier; 2003. pp. 96–107. DOI: 10.1016/S0378-7753(03)00067-3

140. Cirici RC. Process Simulations for Multi-Fuel SOFC CHP concept [thesis]. FH Joanneum, Kapfenberg; 2014.

141. Braun RJ, Klein SA, Reindl DT. Evaluation of system configurations for solid oxide fuel cell-based micro-combined heat and power generators in residential applications. J Power Sources. 2006;158(2 SPEC. ISS.)pp.:1290–305. DOI: 10.1016/j.jpowsour.2005.10.064

142. Heshmat H, Cordova JL. Ultra High Temperature Anode Recycle Blower for Solid Oxide Fuel Cell, Mohawk Innovative Technology, Inc. 2019;

143. van Biert L, Godjevac M, Visser K, Aravind P V. A review of fuel cell systems for maritime applications. Vol. 327, Journal of Power Sources. Elsevier B.V.; 2016. pp. 345–64. DOI: 10.1016/j.jpowsour.2016.07.007

144. Pukrushpan J, Stefanopoulou A, Varigonda S, Eborn J, Haugstetter C. Control-oriented model of fuel processor for hydrogen generation in fuel cell applications. Control Eng Pract. 2006;14(3 SPEC. ISS.)pp.:277–93. DOI: 10.1016/j.conengprac.2005.04.014

145. Zhu J, Zhang D, King KD. Reforming of CH4 by partial oxidation: Thermodynamic and kinetic analyses. Fuel. 2001;80(7)pp.:899–905. DOI: 10.1016/S0016-2361(00)00165-4

146. Pianko-Oprych P, Hosseini SM, Jaworski Z. Model development of integrated CPOx reformer and SOFC stack system. Polish J Chem Technol. 2016 Dec 1;18(4)pp.:41–6. DOI: 10.1515/pjct-2016-0069

147. Pianko-Oprych P, Hosseini SM, Pianko-Oprych P, Hosseini SM. Dynamic Analysis of Load Operations of Two-Stage SOFC Stacks Power Generation System. Energies. 2017 Dec 11;10(12)p.:2103. DOI: 10.3390/en10122103

148. Holtappels P, Mehling H, Roehlich S, Liebermann SS, Stimming U. SOFC system operating strategies for mobile applications. Fuel Cells. 2005;5(4)pp.:499–508. DOI: 10.1002/fuce.200400088

149. Ataer ÖE, Ileri A, Göğüş Y. Transient behaviour of finned-tube cross-flow heat exchangers. Int J Refrig. 1995 Mar 1;18(3)pp.:153–60. DOI: 10.1016/0140-7007(94)00002-F

150. Barelli L, Bidini G, Ciupăgeanu DA, Pianese C, Polverino P, Sorrentino M. Stochastic power management approach for a hybrid solid oxide fuel cell/battery auxiliary power unit for heavy duty vehicle applications. Energy Convers Manag. 2020 Oct

1;221p.:113197. DOI: 10.1016/j.enconman.2020.113197

151. Electrical Generation for More-Electric Aircraft using Solid Oxide Fuel Cells GA Whyatt LA Chick. 2012.

152. Wu X long, Xu Y wu, Li D, Zheng Y, Li J, Sorrentino M, Yu Y, Wan X, Hu L, Zou C, Li X. Afterburner temperature safety assessment for solid oxide fuel cell system based on computational fluid dynamics. J Power Sources. 2021 Jun 1;496p.:229837. DOI: 10.1016/j.jpowsour.2021.229837

153. Park YJ, Min G, Hong J. Comparative study of solid oxide fuel cell-combined heat and power system designs for optimal thermal integration. Energy Convers Manag. 2019 Feb;182pp.:351–68. DOI: 10.1016/j.enconman.2018.12.068

154. Little AD. Conceptual Design of POX / SOFC 5kW net System Final Report, Department of Energy, National Energy Technology Laboratory, Morgantown, WV. 2001.

155. Wu W, Wang B, Shi W, Li X. An overview of ammonia-based absorption chillers and heat pumps. Vol. 31, Renewable and Sustainable Energy Reviews. Elsevier Ltd; 2014. pp. 681–707. DOI: 10.1016/j.rser.2013.12.021

156. Deng J, Wang RZ, Han GY. A review of thermally activated cooling technologies for combined cooling, heating and power systems. Vol. 37, Progress in Energy and Combustion Science. 2011. pp. 172–203. DOI: 10.1016/j.pecs.2010.05.003

157. Garimella S, Keinath CM, Delahanty JC, Hoysall DC, Staedter MA, Goyal A, Garrabrant MA. Development and demonstration of a compact ammonia-water absorption heat pump prototype with microscale features for space-conditioning applications. Appl Therm Eng. 2016;102pp.:557–64. DOI: 10.1016/j.applthermaleng.2016.03.169

158. Pandya B, El-Kharouf A, Venkataraman V, Steinberger-Wilckens R. Comparative

study of solid oxide fuel cell coupled absorption refrigeration system for green and sustainable refrigerated transportation. Appl Therm Eng. 2020 Jun 1;179p.:115597. DOI: 10.1016/j.applthermaleng.2020.115597

159. Kakaç S, Shah RK, Aung W. Handbook of single-phase convective heat transfer. John Wiley and Sons Inc.,New York, NY; 1987.

160. van Biert L, Visser K, Aravind P V. Intrinsic methane steam reforming kinetics on nickel-ceria solid oxide fuel cell anodes. J Power Sources. 2019 Dec 15;443p.:227261. DOI: 10.1016/j.jpowsour.2019.227261

161. Solid Oxide cell stack | Products | Elcogen. [accessed 2 July 2022]; Available from: https://elcogen.com/products/solid-oxide-cell-stacks/

162. Zhang W, Croiset E, Douglas PL, Fowler MW, Entchev E. Simulation of a tubular solid oxide fuel cell stack using AspenPlus^{TM} unit operation models. Energy Convers Manag. 2005 Jan;46(2)pp.:181–96. DOI: 10.1016/j.enconman.2004.03.002

163. Chitsaz A, Hosseinpour J, Assadi M. Effect of recycling on the thermodynamic and thermoeconomic performances of SOFC based on trigeneration systems; A comparative study. Energy. 2017 Apr 1;124pp.:613–24. DOI: 10.1016/j.energy.2017.02.019

164. Tsai TI. Carbon Formation in Solid Oxide Fuel Cells During internal Reforming and Anode Off-Gas Recirculation [thesis]. University of Birmingham; 2015.

165. Krishnan VV. Recent developments in metal-supported solid oxide fuel cells. Wiley Interdiscip Rev Energy Environ. 2017;6(5). DOI: 10.1002/wene.246

166. Elmer T. A novel SOFC tri-generation system for building applications [thesis]. University of Nottingham;

167. Virden J, Howden K. The 21 st Century Truck Partnership Fuel Cell Technologies for Auxiliary Power Research Partnership. Pacific Northwest National Laboratory. Des

Moines, Iowa; 2004.

168. Lee SB, Lim TH, Song RH, Shin DR, Dong SK. Development of a 700 W anode-supported micro-tubular SOFC stack for APU applications. Int J Hydrogen Energy. 2008 May 1;33(9)pp.:2330–6. DOI: 10.1016/j.ijhydene.2008.02.034

169. Choudhury A, Chandra H, Arora A. Application of solid oxide fuel cell technology for power generation - A review. Vol. 20, Renewable and Sustainable Energy Reviews. Pergamon; 2013. pp. 430–42. DOI: 10.1016/j.rser.2012.11.031

170. Rai A. Energy demand and environmental impacts of food transport refrigeration and energy reduction methods during temperature-controlled distribution [thesis]. Brunel University London; 2019.

171. Koronaki IP, Cowan D, Maidment G, Beerman K, Schreurs M, Kaar K, Chaer I, Gontarz G, Christodoulaki RI, Cazauran X. Refrigerant emissions and leakage prevention across Europe - Results from the RealSkillsEurope project. Energy. 2012;45(1)pp.:71–80. DOI: 10.1016/j.energy.2012.05.040

172. Lemmon EW, McLinden MO, Friend and DG. NIST Chemistry WebBook, NIST Standard Reference Database. NIST Chemistry WebBook. 2017. 20899 pp. DOI: 10.18434/T4D303

173. Energy Cost Savings with the Frigoblock Alternator Drive System. FRIGOBLOCK Grosskopf GmbH. Essen; 2016.

174. Eriksson M, Ahlgren S. LCAs of petrol and diesel: a literature review. Department of Energy and Technology, Swedish University of Agricultural Sciences. 2013.

175. R452A (Opteon XP44) | Linde Gas. [accessed 7 April 2020]; Available from: https://www.linde-gas.com/en/products_and_supply/refrigerants/hfo_refrigerants/r452a/index.html

176. Rai A, Tassou SA. Energy demand and environmental impacts of alternative food

transport refrigeration systems. Energy Procedia. 2017;123pp.:113–20. DOI: 10.1016/j.egypro.2017.07.267

177. European Commission. Ener, D.G. Study on Actual GHG Data for Diesel, Petrol, Kerosene and Natural Gas. European Commission, Directorate-General for Energy. 2014.

178. Bicer Y, Dincer I, Zamfirescu C, Vezina G, Raso F. Comparative life cycle assessment of various ammonia production methods. J Clean Prod. 2016;135pp.:1379–95. DOI: 10.1016/j.jclepro.2016.07.023

179. R717 (Ammonia) | Linde Gas. [accessed 22 May 2020]; Available from: https://www.linde-gas.com/en/products_and_supply/refrigerants/natural_refrigerants/r717_ammonia/index.html

180. Pandya B, El-Kharouf A, Steinberger-Wilckens R. Transient analysis of a solid oxide fuel cell coupled with an absorption refrigeration system for refrigerated transportation. In: 14th European SOFC & SOE Forum, 20-23 Oct, Lucerne Switzerland. 2020. pp. 277–86.

181. Goyal A, Garimella S. Computing thermodynamic properties of ammonia–water mixtures using artificial neural networks. Int J Refrig. 2019 Apr 1;100pp.:315–25. DOI: 10.1016/j.ijrefrig.2019.02.011

182. Khanafer K, Al-Masri A, Vafai K, Preethichandra P. Heat up impact on thermal stresses in SOFC for mobile APU applications: Thermo-structural analysis. Sustain Energy Technol Assessments. 2022 Aug 1;52p.:102159. DOI: 10.1016/j.seta.2022.102159

183. Bossel U. Rapid startup SOFC modules. In: Energy Procedia. 2012. pp. 48–56. DOI: 10.1016/j.egypro.2012.08.039

184. Di Filippi A. Development and experimental validation of CPOx reforming dynamic model for fault detection and isolation in SOFC systems [thesis]. University of Salerno; 2015.

185. Sorrentino M, Pianese C. Model-based development of low-level control strategies for transient operation of solid oxide fuel cell systems. J Power Sources. 2011;196(21)pp.:9036–45. DOI: 10.1016/j.jpowsour.2011.01.023

186. Goel A, Vidal T, Adrianus ·, Kok L, Kok AL. To team up or not: single versus team driving in European road freight transport. 2021;33pp.:879–913. DOI: 10.1007/s10696-020-09398-0

187. Historical weather data for London,UK | Visual Crossing. [accessed 26 November 2022]; Available from: https://www.visualcrossing.com/weather-history/London,UK/metric/2022-07-19/2022-07-19